

# Exploration and Optimization of Novel Piezoelectric Devices

by

**Christopher Andrew Petroff**

Bachelor of Science, Boston College, 2015

Submitted to the Graduate Faculty of the  
Kenneth P. Dietrich School of Arts and Sciences  
in partial fulfillment  
of the requirements for the degree of  
**Doctor of Philosophy**

University of Pittsburgh

2021

UNIVERSITY OF PITTSBURGH  
KENNETH P. DIETRICH SCHOOL OF ARTS AND SCIENCES

This dissertation was presented

by

**Christopher Andrew Petroff**

It was defended on

2021-07-15

and approved by

Tara Y. Meyer, Professor, Department of Chemistry

Jennifer E. Laaser, Assistant Professor, Department of Chemistry

M. Ravi Shankar, Professor, Department of Industrial Engineering,  
John A. Swanson School of Engineering

Dissertation Director:

Geoffrey R. Hutchison, Associate Professor, Department of Chemistry

Copyright © by Christopher Andrew Petroff

2021

This work is released under a Creative Commons Attribution 4.0 International License.

# Exploration and Optimization of Novel Piezoelectric Devices

Christopher Andrew Petroff, Ph.D.

University of Pittsburgh, 2021

Piezoelectricity, the linear interconversion of mechanical work and electrical potential, is utilized in a variety of transducers, sensors, actuators, and energy harvesting devices. It consists of a direct effect, where mechanical force leads to buildup of electrical charge and a converse effect, where an applied electrical potential produces a mechanical deformation. While traditional piezoelectric devices rely upon crystalline and ceramic materials that are often hard and brittle, there is an growing body of research on soft, flexible, and biocompatible devices. This dissertation focuses on the exploration and optimization of novel piezoelectric devices developed through a rational design approach. An array of piezoelectric devices are presented, based off of two different tunable scaffolds. Utilizing polar, small organic molecule dopants or oligopeptide self-assembled monolayers, these molecularly engineered piezoelectrics show great potential in energy harvesting and sensing applications.

A semi-automated system was developed to test and analyze the piezoelectric direct effect of devices in a quasi-static manner. It was then deployed for the study of piezoelectric foams based on an array of different polar, small organic molecules deposited on a poly(dimethylsiloxane) foam scaffold; the dopant molecules were electrically poled into polar alignment. This system allows for the independent tuning of the piezoelectric response through changes in either the mechanical properties of the foam's modulus or the electrical properties stemming from the dopant. Next, oligopeptide based devices are examined. As their polar order stems from the

self-assembly of the monolayer, they are intrinsically piezoelectric and poling free. These devices are easily produced through solution processing and hold great potential as sensors due to their exceptionally large piezoelectric voltage constant. Work has begun on examining these oligopeptides, using piezo force microscopy and computational methods, to better understand the mechanisms behind their piezoelectric nature and, hopefully, molecularly engineer improved devices.

# Table of Contents

<b>List of Tables</b>	<b>xi</b>
<b>List of Figures</b>	<b>xii</b>
<b>Preface</b>	<b>xvii</b>
<b>1.0 Introduction</b>	<b>1</b>
1.1 Electrostatics, Electric Polarization, and Electromechanical Coupling . . .	1
1.2 Mechanical Properties of Materials . . . . .	3
1.3 Piezoelectricity . . . . .	4
1.3.1 A Brief History . . . . .	4
1.3.2 Origins of Piezoelectricity . . . . .	5
1.3.3 Piezoelectric Constants and Figures of Merit . . . . .	5
1.3.4 Electrical Poling . . . . .	10
1.3.5 Piezoelectric Measurements . . . . .	12
1.3.6 Piezoelectric Single Crystals . . . . .	13
1.3.7 Piezoelectric Ceramics . . . . .	14
1.3.8 Polymers . . . . .	16
1.3.9 Novel and Composite Devices . . . . .	17
1.4 Other Forms of Electromechanical Coupling and Relevant Related Phenomena	17
1.4.1 Flexoelectricity . . . . .	18
1.4.2 Ferroelectricity . . . . .	18
1.4.3 Electrostriction . . . . .	19
1.4.4 Pyroelectricity . . . . .	19
1.4.5 Triboelectricity . . . . .	20
1.5 Piezoelectric Energy Harvesting . . . . .	20
1.6 Piezoelectric Sensing . . . . .	22

1.7	Rational Design of Materials . . . . .	24
1.7.1	Overview . . . . .	24
1.7.2	Small Organic Molecules as Dopants . . . . .	25
1.7.3	Oligopeptide Self-Assembled Monolayers . . . . .	25
1.8	Dissertation Overview . . . . .	26
<b>2.0</b>	<b>Development of Measurement System</b>	<b>27</b>
2.1	Piezoelectric Measurement Methods . . . . .	27
2.2	Testing Hardware and Setup . . . . .	30
2.3	Data Processing . . . . .	32
2.4	Piezoelectric Polyurethane Foams: A Test Case . . . . .	34
2.4.1	Experimental Methods . . . . .	34
2.4.2	Results . . . . .	36
<b>3.0</b>	<b>Highly Tunable Molecularly Doped Flexible Poly(dimethylsiloxane) Foam</b>	
	<b>Piezoelectric Energy Harvesters</b>	<b>38</b>
3.1	Summary . . . . .	38
3.2	Introduction . . . . .	39
3.3	Experimental Methods . . . . .	41
3.3.1	Materials . . . . .	41
3.3.2	PDMS Foam Preparation . . . . .	42
3.3.3	Device Preparation and Electrical Poling . . . . .	43
3.3.4	Device Testing and Characterization . . . . .	43
3.4	Results and Discussion . . . . .	45
3.5	Conclusions . . . . .	51
3.6	Acknowledgement . . . . .	51
<b>4.0</b>	<b>Intrinsically Polar Piezoelectric Self-Assembled Oligopeptide Monolayers</b>	<b>52</b>
4.1	Summary . . . . .	52

4.2	Introduction . . . . .	53
4.3	Promise of Piezoelectric Self-Assembled Monolayers . . . . .	54
4.4	Piezoelectric Charge Constant . . . . .	55
4.5	Piezoelectric Voltage Constant . . . . .	59
4.6	Device Stability . . . . .	63
4.7	Flexible Device Prototype . . . . .	63
4.8	Conclusions and Outlook . . . . .	65
4.9	Experimental Section . . . . .	65
4.9.1	Materials . . . . .	65
4.9.2	Device Preparation . . . . .	66
4.9.3	Device Testing and Characterization . . . . .	67
4.9.4	<i>Ab Initio</i> Molecular Dynamics Simulations . . . . .	68
4.10	Acknowledgment . . . . .	70
<b>5.0</b>	<b>Oligopeptide-Based Piezoelectric Materials: Understanding Electromechanical Coupling in Molecules</b>	<b>71</b>
5.1	Introduction . . . . .	71
5.2	Background . . . . .	74
5.3	Model Oligopeptide System . . . . .	85
5.4	Device Scale Characterization . . . . .	85
5.5	Piezo-Force Microscopy . . . . .	90
5.6	Computational Investigations . . . . .	91
<b>6.0</b>	<b>Double-Wave Method Ferroelectric Measurements of a Corannulene Derivative</b>	<b>96</b>
6.1	Introduction . . . . .	96
6.1.1	Single-Molecule Ferroelectric Bowls . . . . .	99
6.1.2	Double-Wave Method . . . . .	101



6.1.3	EGaIn Electrodes . . . . .	103
6.2	Materials and Methods . . . . .	103
6.2.1	Materials . . . . .	103
6.2.2	Sample Preparation . . . . .	104
6.2.3	Measurement Setup . . . . .	104
6.2.4	Ferroelectric Measurements . . . . .	105
6.3	Results and Discussion . . . . .	106
6.4	Conclusions . . . . .	115
6.5	Acknowledgment . . . . .	118
<b>7.0</b>	<b>Conclusions and Future Directions</b>	<b>119</b>
7.1	Conclusions . . . . .	119
7.2	Future Directions . . . . .	123
 <b>Appendix A: Supplementary Information for Highly Tunable Molecularly</b>		
<b>Doped Flexible Poly(dimethylsiloxane) Foam Piezoelectric Energy Har-</b>		
<b>vesters</b>		<b>126</b>
A.1	Supplementary Figures . . . . .	126
A.2	Peak Finding Python Script . . . . .	130
 <b>Appendix B: Supplementary Information for Intrinsically Polar Piezoelec-</b>		
<b>tric Self-Assembled Oligopeptide Monolayers</b>		<b>139</b>
B.1	ANOVA . . . . .	139
B.2	Supplementary Figures on Piezoelectric Response . . . . .	144
B.3	Supplementary Note: Computational Details and Discussion . . . . .	149
B.4	AFM Images of PCB Substrate . . . . .	154
B.5	Minimum Working Example of Voltage Peak Finding Python Script . . . .	154

<b>Appendix C: Supplementary Information for Oligopeptide-Based Piezoelec-</b>	
<b>tric Materials: Understanding Electromechanical Coupling in Molecules</b>	<b>157</b>
C.1 Materials and Methods . . . . .	157
C.1.1 Peptide Devices . . . . .	157
C.1.2 PFM Measurements . . . . .	158
C.1.3 Computational Methods . . . . .	158
C.2 Supporting Figures . . . . .	159
<b>Appendix D: Supplementary Information for Double-Wave Method Ferro-</b>	
<b>electric Measurements of a Corannulene Derivative</b>	<b>166</b>
D.1 Minimum Working Example of Ferroelectric Analysis Python Script . . . .	166
<b>Bibliography</b>	<b>170</b>

## List of Tables

Table 1.1	Piezoelectric charge constants of common materials . . . . .	8
Table 1.2	Piezoelectric voltage constants of common materials . . . . .	10
Table 5.1	Piezoelectric coefficients of organic materials . . . . .	81
Table B.1	ANOVA charge constant results for DDT-PU PCBs . . . . .	139
Table B.2	ANOVA charge constant results for PU PCBs . . . . .	140
Table B.3	ANOVA charge constant results for thin PU PCBs . . . . .	140
Table B.4	ANOVA charge constant results for carboxylate-terminated versus amide-terminated peptides . . . . .	140
Table B.5	ANOVA charge constant results for carboxylate-terminated peptides . . .	141
Table B.6	ANOVA charge constant results for amide-terminated peptides . . . . .	141
Table B.7	ANOVA charge constant results for DDT-PU versus PU coated PCBs . .	141
Table B.8	ANOVA charge constant results for normal thickness versus thinner thickness PU coated PCBs . . . . .	142
Table B.9	ANOVA voltage constant results for DDT-PU PCBs . . . . .	142
Table B.10	ANOVA voltage constant results for PU PCBs . . . . .	142
Table B.11	ANOVA voltage constant results for thin PU PCBs . . . . .	143
Table B.12	ANOVA voltage constant results for normal thickness versus thinner thickness PU coated PCBs . . . . .	143

# List of Figures

Figure 1.1	The perovskite structure of lead zirconium titanate (PZT) . . . . .	6
Figure 1.2	Cartesian coordinate system axes numbering. . . . .	7
Figure 1.3	Piezoelectric measurement axes . . . . .	8
Figure 1.4	Electrical poling of piezoelectric ceramics . . . . .	11
Figure 1.5	Schematic of poly(vinylidene difluoride) (PVDF) . . . . .	16
Figure 1.6	Piezoelectric cantilever vibrational energy harvesters . . . . .	21
Figure 2.1	Equivalent circuit of a piezoelectric vibrator near fundamental resonance	29
Figure 2.2	Measurement system setup . . . . .	31
Figure 2.3	Printed circuit board (PCB) electrodes . . . . .	32
Figure 2.4	Piezoelectric polyurethane foam poling setup . . . . .	35
Figure 2.5	Piezoelectric polyurethane foam testing setup . . . . .	35
Figure 2.6	Piezoelectric response of polyurethane foams as a function of poling voltage	36
Figure 2.7	Piezoelectric response of polyurethane foams as a function of foam thickness	37
Figure 3.1	General overview of devices and measurements . . . . .	46
Figure 3.2	Effect of dopant concentration and poling field on piezoelectric response	48
Figure 3.3	Effect of dopant on piezoelectric response . . . . .	48
Figure 3.4	Effect of modulus on piezoelectric response . . . . .	49
Figure 3.5	Voltage drop over various resistances and the resulting generated power density . . . . .	50
Figure 4.1	Generalized scheme outlining PSAM devices studied . . . . .	56
Figure 4.2	Piezoelectric charge constant response . . . . .	57
Figure 4.3	Piezoelectric voltage constant response . . . . .	60

Figure 4.4	Thickness effect on piezoelectric response . . . . .	62
Figure 4.5	Flexible sealed PSAM device (CA12-NH <sub>2</sub> /DDT-PU) fabricated on gold-coated plastic substrates . . . . .	64
Figure 5.1	Schematic of the piezoelectric effect . . . . .	72
Figure 5.2	Unit cells of $\alpha$ -, $\beta$ -, and $\gamma$ -polymorphs of glycine . . . . .	76
Figure 5.3	Schematic diagram of oligopeptides studied in model oligopeptide system . . . . .	86
Figure 5.4	Model of oligopeptide SAM on gold substrate . . . . .	87
Figure 5.5	Measured direct piezoelectric constants of model oligopeptide system measured on the device scale . . . . .	89
Figure 5.6	Measured converse piezoelectric constants of model oligopeptide system measured using DART-PFM . . . . .	91
Figure 5.7	Correlation of piezoelectric response between PFM measurements and device scale measurements . . . . .	92
Figure 5.8	Converse piezoelectric constants of model oligopeptide system calculated using DFT . . . . .	93
Figure 5.9	Correlation of piezoelectric response between DFT calculations and device scale measurements . . . . .	94
Figure 5.10	Correlation of piezoelectric response between DFT calculations and PFM measurements . . . . .	95
Figure 6.1	Types of polarization-electric field curves . . . . .	97
Figure 6.2	Schematic of corannulene bowl-to-bowl inversion . . . . .	100
Figure 6.3	Double-wave method example . . . . .	102
Figure 6.4	EGaIn electrode measurement setup . . . . .	105
Figure 6.5	4,4',4'',4'''-(Dibenzo[ <i>ghi,mno</i> ]fluoranthene-1,2,5,6-tetrayl)tetrabenzoic acid (H <sub>4</sub> DFT) structure . . . . .	107

Figure 6.6	1-Pyrenecarboxylic acid (PCA) structure . . . . .	107
Figure 6.7	Sample current–voltage and charge–voltage curves for H <sub>4</sub> DFT up to 10 V	108
Figure 6.8	Sample current–voltage and charge–voltage curves for PCA control . . .	109
Figure 6.9	Sample current–voltage and charge–voltage curves for H <sub>4</sub> DFT up to 20 V	109
Figure 6.10	Sample charge–voltage curves for H <sub>4</sub> DFT at different temperatures . . .	111
Figure 6.11	Effect of pulse speed on H <sub>4</sub> DFT measurements . . . . .	112
Figure 6.12	Sample current–time traces for H <sub>4</sub> DFT under different pulse sequences .	114
Figure 6.13	Sample current behavior for H <sub>4</sub> DFT over time . . . . .	115
Figure 6.14	Current–voltage and charge–voltage curves for H <sub>4</sub> DFT measured under inert conditions . . . . .	116
Figure 6.15	Current–voltage and charge–voltage curves for PCA control measured under inert conditions . . . . .	117
Figure A.1	Evaporation rate of acetonitrile in PDMS foam . . . . .	126
Figure A.2	Effect of dopant concentration and poling field on piezoelectric response up to 10 N . . . . .	127
Figure A.3	Effect of dopant on piezoelectric response up to 10 N . . . . .	127
Figure A.4	Stress–strain curve for sugar templated PDMS foam . . . . .	128
Figure A.5	Stress–strain curve for a salt templated PDMS foam cured at room tem- perature . . . . .	128
Figure A.6	Decay in piezoelectric response over time . . . . .	129
Figure B.1	Process by which the piezoelectric charge constant ( $d_{33}$ ) is obtained . . .	144
Figure B.2	Process by which the piezoelectric voltage constant ( $g_{33}$ ) is obtained . .	145
Figure B.3	Piezoelectric charge constant ( $d_{33}$ ) values for 1-dodecanethiol (DDT) control PSAM devices . . . . .	146

Figure B.4	Piezoelectric voltage constant ( $g_{33}$ ) values for 1-dodecanethiol (DDT)	
	control PSAM devices . . . . .	146
Figure B.5	Long term storage stability of samples . . . . .	147
Figure B.6	The piezoelectric voltage constants ( $g_{33}$ ) of sealed PSAM devices . . . .	147
Figure B.7	Stability of sealed PSAM devices . . . . .	148
Figure B.8	Atomistic visualization of the carboxylate-terminated peptide CA <sub>6</sub> in liquid water from room-temperature <i>ab initio</i> molecular dynamics simulations .	149
Figure B.9	Probability distributions of the lengths of the four H-bonds characterizing the $\alpha$ -helix structure . . . . .	151
Figure B.10	Probability distributions of the lengths of the four H-bonds characterizing the $\alpha$ -helix structure of the carboxylate-terminated peptide CA <sub>6</sub> . . . . .	152
Figure B.11	Probability distributions of the lengths of the four H-bonds characterizing the $\alpha$ -helix structure of the amide-terminated peptide CA <sub>6</sub> -NH <sub>2</sub> . . . . .	153
Figure B.12	AFM amplitude scans of PCBs . . . . .	154
Figure C.1	Relationship between measured piezoelectric charge and voltage constants for peptide self-assembled monolayer (PSAM) devices . . . . .	159
Figure C.2	Correlation between calculations made using the different measurement reference points . . . . .	160
Figure C.3	Correlation of piezoelectric response between PFM measurements and device scale measurements . . . . .	160
Figure C.4	Correlation of piezoelectric response between DFT calculations and device scale measurements . . . . .	161
Figure C.5	Atomistic visualization of the amide-terminated peptide CA <sub>7</sub> -NH <sub>2</sub> in liquid water from room-temperature <i>ab initio</i> molecular dynamics simulations . . . .	162
Figure C.6	Probability distributions of the length of the structure of the amide- terminated peptide CA <sub>7</sub> -NH <sub>2</sub> . . . . .	163

Figure C.7	Probability distributions of the length of the structure of the amide-terminated peptide CA <sub>6</sub> F-NH <sub>2</sub>	163
Figure C.8	Probability distributions of the length of the structure of the amide-terminated peptide CFA <sub>6</sub> -NH <sub>2</sub>	164
Figure C.9	Probability distributions of the length of the structure of the amide-terminated peptide CA <sub>6</sub> Y-NH <sub>2</sub>	164
Figure C.10	Probability distributions of the length of the structure of the amide-terminated peptide CYA <sub>6</sub> -NH <sub>2</sub>	165



# Preface

With my time at Pitt coming to a close, I find myself sitting here musing about what has been and what is to come. During these last six years I made countless friends, learned a ton, and grew as a chemist and a person.

With the COVID-19 pandemic ravaging the world, the past year and a half has been far from normal. Despite the uncertainty that it has brought, science must go on. I want to pause for a moment to remember all those affected by this pandemic. I know, from personal experience, the toll that even minor symptoms can bring. COVID-19 is a terrible disease that has brought all too much suffering and death. In particular, I want to take time to remember Dr. Frank Tsung, my undergraduate research advisor at Boston College, who passed this January, at just 44, after a lengthy battle with COVID-19. Your passing is a great loss to the scientific community, and your friendship, kindness, and insight are sorely missed by all those that had the pleasure of knowing you. An article remembering Frank and highlighting his work was recently published in *ACS Applied Materials & Interfaces*.<sup>1</sup>

I want to take some time to thank those who got me to where I am today. I thank my high school chemistry teacher at the Taft School, Mr. David Hostage, for sparking my love of chemistry. From my undergraduate years at Boston College, I thank my professors, especially Dr. Ken Metz and the late Dr. Frank Tsung. I thank everyone in the Tsung group, especially my graduate student mentor, Dr. Randy Chou. I also thank all my friends in the chemistry department, especially Dr. Joey Palomba and Dr. Lauren Yablon.

At Pitt, first and foremost, I thank my advisor Dr. Geoff Hutchison for all his help and support. Without his guidance, I would not be here today. Next, I thank my committee, Dr. Tara Meyer, Dr. Jenny Laaser, and Dr. Ravi Shankar, for their time and expertise. I thank everyone in the Hutchison group—past and present—for their assistance and friendship over the years, especially Dr. Nate Miller and Dakota Folmsbee. I also thank the two

undergraduate students who worked with me over the years—Thomas Bina and Jeremy Stundon—for all their assistance. Outside the lab, I thank the members of the club cross country team, past and present, for the camaraderie and running. You helped raise my running to the next level, which allowed me to set new PRs across the board. My time on the team was an integral part of my Pitt experience and helped really make this place feel like home.

To my family, thank you for all you have done for me over the years. I thank my parents, Dr. Genevieve O’Connell and Dr. Ognen Petroff, for everything. Your love, kindness, humility, and knowledge have made me the man—and scientist—I am today. I thank my brother, Dr. Matthew Petroff, for all his insights over the years. Whether it was an electrical, electronics, physics, or yet another programming question, thank you for taking the time to listen to me ramble and for offering your best suggestions.

Finally, to my girlfriend Jess Uhrin, thank you for all your love and support. Thank you for adopting Mango and gracing our lives with the most adorable adventure kitty out there. Thank you for maybe even allowing some of the chemistry to rub off on you.

PITTSBURGH, JULY 2021

C. PETROFF

# 1.0 Introduction

Piezoelectricity is the linear interconversion of mechanical force and electrical potential. In the direct effect, applied force is converted to electrical potential, while in the converse effect, an applied electric field results in the mechanical deformation of the material. Traditional piezoelectric devices are mainly hard, brittle ceramics with applications that range from ultrasonic transducers to pressure sensors to energy harvesters. Numerous ideas have been proposed to make piezoelectrics soft, flexible, and biocompatible; unfortunately, many of these devices suffer from considerably lower piezoelectric response. The goal of this work is to present a framework for understanding piezoelectricity on a molecular level and its application in soft, flexible devices.

This introductory chapter starts with an overview of relevant basic electrical and mechanical concepts, before diving into a summary of piezoelectricity. Next, other related phenomena are reviewed before piezoelectric energy harvesting and sensing are discussed. It concludes with some remarks on the rational design of novel piezoelectric materials and an overview of the rest of the dissertation.

## 1.1 Electrostatics, Electric Polarization, and Electromechanical Coupling

Electrostatics is the general study of electric charges at rest and is a foundation to the study of most electrical phenomena. These electric charges can be positive or negative in nature, where like charges repel and unlike charges attract. When positive and negative charges are separated from each other, a material becomes electrically polarized. Since unlike charges

attract, separated charges have the tendency to flow as current to minimize the imbalance; the interactions between these charges and currents is known as electromagnetism and are summarized, as a unified theory, by Maxwell's equations. A conductor is a material where charge flows freely, whereas an insulator is a material that inhibits the flow of charge. The vector that runs between areas of positive and negative charge in a system of zero net charge is known as the dipole moment; in chemistry, the convention is that it points from positive charge to negative charge.<sup>2</sup> The force experienced by a charge due to surrounding charges is known as the electric field ( $\vec{E}$ ). The polarization ( $\vec{P}$ ) is the amount that charges are moved by the influence of  $\vec{E}$ ; in dielectrics—which are polarizable insulators—this displacement is very small as the electrons do not flow since they are bound to the nuclei.<sup>2</sup> The relative permittivity ( $\epsilon_r$ ), or dielectric constant, is the ratio relating the dielectric displacement ( $\vec{D}$ ) to the applied electric field such that  $\vec{D} = \epsilon_r \vec{E}$  and is a measure of the charge stored in a dielectric placed between two conductors.<sup>2,3</sup>

A material's dielectric properties are of particular importance to piezoelectric applications, as movement of internal dipoles is the origin of the effect. For many piezoelectric materials, the various polar domains are aligned and locked in by heating above the point of polar disorder, the Curie temperature ( $T_C$ ), and then applying an electric field to align the dipoles and maintaining it as the material is cooled. Several equations relate to this process. The polarizability ( $\alpha$ ) of a material—the extent to which it polarizes in response to an applied electric field—is related to  $\epsilon$  by the Clausius–Mossotti equation:

$$\frac{\epsilon - 1}{\epsilon + 2} = \frac{4\pi}{3} N \alpha \quad (1.1)$$

where  $\epsilon$  is the permittivity,  $N$  is the number of particles per unit volume, and  $\alpha$  is the polarizability.<sup>\*2,4</sup> For a single molecule, the induced polarization ( $P_\alpha$ ) is related to the electric

---

<sup>\*</sup>The  $4\pi/3$  constant applies for isotropic materials or those with cubic symmetry. It differs but is within the same order of magnitude for crystals with lower symmetry.<sup>4</sup>

field as follows:

$$\vec{P}_\alpha = N\alpha\vec{E}_i \quad (1.2)$$

where  $N$  is the number of particles per unit volume and  $\vec{E}_i$  is average electric field strength acting on the molecule.<sup>2</sup> Debye adapted Langevin's theory on paramagnetism to dielectrics; a generalized approximation of the Langevin function can determine the dipole alignment in a material based on the polarization:

$$\frac{\bar{\mu}}{\mu} = \frac{\vec{P}}{N\mu} \quad (1.3)$$

where  $\bar{\mu}$  is the average dipole moment,  $\mu$  is the individual dipole moment,  $\vec{P}$  is the polarization, and  $N$  is the number of particles per unit volume.<sup>4</sup> These equations relate the dielectric properties of the material and the applied electric field to the degree of dipole alignment and the magnitude of the piezoelectric response.

## 1.2 Mechanical Properties of Materials

Since the piezoelectric effect interconverts mechanical and electrical energy, there are several mechanical properties relevant to piezoelectric materials. Two key concepts needed to discuss the mechanical properties of materials are stress and strain.<sup>5</sup> Stress is applied force divided by area, whereas strain is the resulting deformation of the material. There are two types of stress: direct and shear. Direct stress is a uniaxial stress applied in one direction. For shear stress, different faces are stressed in different directions.<sup>5,6</sup> Direct stress ( $\sigma$ ) produces direct strain ( $\varepsilon$ ), while shear stress ( $\tau$ ) produces shear strain ( $\gamma$ ).<sup>6</sup> A deformation is considered to be elastic if the sample fully recovers its original shape once the stress is removed.<sup>5</sup> Several moduli—such as Young's, shear, and bulk—are used to quantify the response of materials to applied stress. The Young's (or elastic) modulus ( $E_Y$ ) relates a material's uniaxial stress to

its deformation along that axis as follows:<sup>6</sup>

$$E_Y = \frac{\sigma}{\varepsilon} \quad (1.4)$$

The shear modulus ( $G = \frac{\tau}{\gamma}$ ) is the analogue for shear stress and shear strain, while the bulk modulus ( $K = \frac{\text{volumetric stress}}{\text{volumetric strain}}$ ) applies to cases where stress is equally applied in all directions, such as from hydrostatic pressure.<sup>5,6</sup> The Poisson effect details how the cross-sectional area of materials increases under compressive loads.<sup>6</sup> Of the moduli, Young's modulus is the most relevant for direct piezoelectric coefficients, whilst the shear modulus is relevant for shear coefficients. For most materials, small values of stress and strain are linearly related by Hooke's law ( $\sigma = E_Y \varepsilon$ ); Young's modulus can therefore be determined by taking the slope of the stress-strain curve.<sup>5,6</sup> Hard materials such as steel (200 GPa) have very high Young's moduli whereas softer materials such as nylon (30 GPa), polyurethane rubber (<0.06 GPa), natural rubber (0.002 GPa), and poly(dimethylsiloxane) (PDMS) (0.0008 GPa) have much lower values.<sup>7-9</sup> When materials are made into foams, for example, their moduli can be lowered from that of the bulk material.<sup>9</sup>

## 1.3 Piezoelectricity

### 1.3.1 A Brief History

Piezoelectricity was first discovered in 1880 by Pierre and Jacques Curie when they showed that charge appeared on the surfaces of certain crystals in direct proportion to applied force.<sup>4,10</sup> Wilhelm Hankel then asserted that the observed phenomenon was distinct from pyroelectric effects and suggested the name piezoelectricity.<sup>11,12</sup> Based on thermodynamic principles, Gabriel Lippmann postulated that a converse piezoelectric effect must also exist;<sup>12,13</sup> this was

verified by the Curies in 1881. The theoretical underlyings of piezoelectricity were developed over the next couple decades, most fully by Woldemar Voigt in 1894 and culminating in his 1910 work *Lehrbuch der Kristallphysik*.<sup>4,14</sup> The next significant advances in piezoelectricity came during the First World War with Paul Langevin proposing early ultrasonic sonar. Around the same time, Walter Cady developed the piezoelectric resonator which helped make modern radio possible via direct frequency control.<sup>15</sup> Numerous other applications were invented over the next several decades including microphones and phonograph pickups. By the 1940s, piezoelectric ceramics were discovered.<sup>3</sup> Finally, in 1945, the Institute of Radio Engineers published the first standard of piezoelectric crystals;<sup>16</sup> this was followed by a revised, expanded standard in 1949.<sup>17</sup>

### 1.3.2 Origins of Piezoelectricity

Traditional piezoelectricity originates from force induced changes in non-centrosymmetric crystals. In these crystals, an applied force leads to an asymmetric change resulting in the production or change of a dipole moment. As an example, the tetragonal crystal structure of lead zirconium titanate (PZT) is shown in Figure 1.1. More generally, piezoelectricity emerges from changes in the dipole moment density, allowing for polymers and other noncrystalline materials containing aligned dipoles to serve as piezoelectric devices. Chapter 3 discusses piezoelectric devices based on polar small organic molecules embedded in PDMS foams, while Chapter 4 covers piezoelectric devices based on self-assembled monolayers (SAMs) of oligopeptides.

### 1.3.3 Piezoelectric Constants and Figures of Merit

There are a total of 18 piezoelectric constants deriving from the six possible components of stress and the three possible components of electric polarization in piezoelectric crystals.<sup>4</sup> In

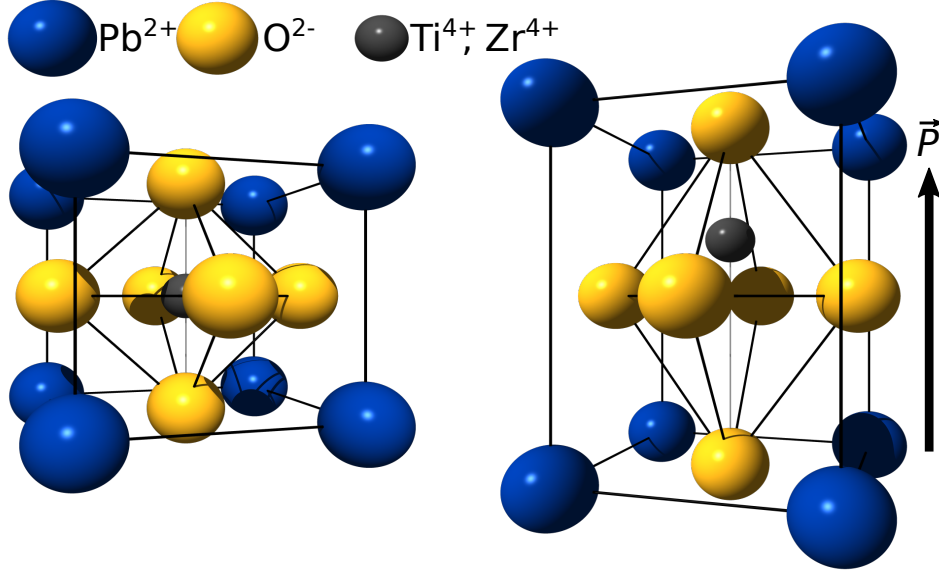


Figure 1.1: The perovskite structure of lead zirconium titanate (PZT).<sup>†</sup> The cubic structure (left) is present above the Curie temperature while tetragonal (right) or rhombohedral structures with bulk polarization are present at lower temperatures, depending on the ratio of titanium to zirconium.<sup>18</sup> These non-centrosymmetric structures give rise to the piezoelectric response. Note that the lattice stretch for the tetragonal structure is exaggerated; the actual stretch is 1 %–2 %.<sup>19</sup>

a Cartesian coordinate system, this relates to polarization about each of the three axes as well as both linear and shear stress about each of the three axes. In many crystal classes, several of these orientations are degenerate, resulting in fewer unique constants. The coefficients can take the form of the piezoelectric charge ( $d$ ), voltage ( $g$ ), and permittivity ( $\epsilon$ ) constants.

A key figure of merit used to quantitate the piezoelectric effect is the piezoelectric charge constant,  $d_{ij}$ . It is a measure of both the charge produced per unit of applied force (pC/N)—the direct effect—and the mechanical deformation as a function of an applied electric field (pm/V)—the converse effect. Both sets of units are equivalent; this is shown by the following series of unit conversions

$$\frac{\text{pC}}{\text{N}} = \frac{\text{V} \cdot \text{pF}}{\text{N}} = \frac{\cancel{\text{N}} \cdot \text{pJ}}{\cancel{\text{N}} \cdot \cancel{\text{V}}^2} = \frac{\text{pJ}}{\text{N} \cdot \text{V}} = \frac{\cancel{\text{N}} \cdot \text{pm}}{\cancel{\text{N}} \cdot \text{V}} = \frac{\text{pm}}{\text{V}} \quad (1.5)$$

---

<sup>†</sup>Figure adapted from reference [20].



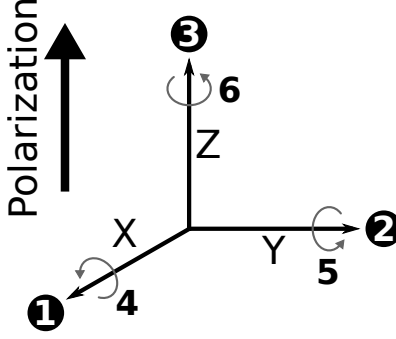


Figure 1.2: Cartesian coordinate system axes numbering. Polarization is aligned to the positive  $Z$ -direction. The first subscript of the piezoelectric constants refers to the direction of induced polarization or applied electric field, while the second subscript refers to the direction of applied stress or induced strain.

where  $C$  is coulomb,  $N$  is newton,  $V$  is volt,  $F$  is farad,  $J$  is joule, and  $m$  is meter. The units used generally coincide with the type of effect being measured. The subscripts,  $i$  and  $j$ , describe the poling and testing axes, respectively. As shown in Figure 1.2, the numbers 1, 2, and 3 refer to the  $X$ ,  $Y$ , and  $Z$  axes, respectively, while the numbers 4, 5, and 6 refer to shear about those axes. Normally, polarization is aligned to the positive  $Z$ -direction for non-single crystalline materials. The first subscript,  $i$ , refers to the direction of induced polarization in the stressed material or the direction of the applied field, while the second subscript,  $j$ , refers to the direction of applied stress or induced strain. For example, to determine the  $d_{33}$  piezoelectric constant of a material, induced polarization is measured along the  $Z$ -axis, while stress is also applied along the  $Z$ -axis; to determine the  $d_{31}$  piezoelectric constant of a material, induced polarization is measured along the  $Z$ -axis, while stress is applied perpendicular to the  $Z$ -axis (parallel to the  $XY$ -plane) (Figure 1.3). Charge constants for common piezoelectric materials are given in Table 1.1.

Piezoelectric materials can be defined as those whose polarization changes with applied stress such that:

$$\Delta P = d_{ij}\sigma \quad (1.6)$$

where  $\Delta P$  is the change in polarization due to stress,  $\sigma$  is the applied stress, and  $d_{ij}$  is the

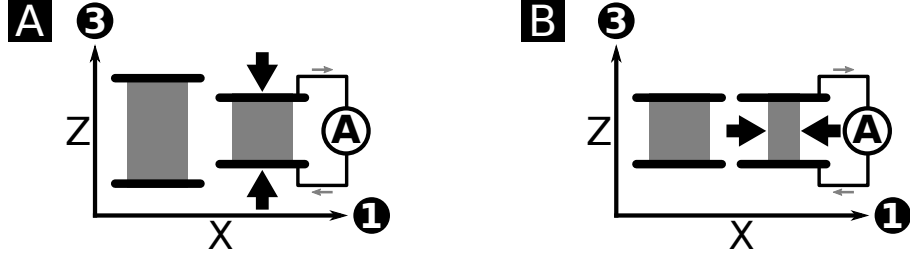


Figure 1.3: Piezoelectric measurement axes. (A) For  $d_{33}$ , current is measured along the  $Z$ -axis while force is applied along the  $Z$ -axis. (B) For  $d_{31}$ , current is measured along the  $Z$ -axis while force is applied along the  $X$ -axis.

Table 1.1: Piezoelectric charge constants of common materials.

Material	Piezoelectric Charge Constant	Ref.
$\alpha$ -Quartz	$d_{11} = -2.3 \text{ pC/N}$	[4, 21]
Bone	$d_{\text{eff}} = \sim 8 \text{ pC/N}$	[22]
Lead Zirconium Titanate (PZT)	$d_{33} = 200 \text{ pC/N} - 600 \text{ pC/N}$	[3, 21, 23]
Barium Titanate	$d_{33} = 149 \text{ pC/N}$	[21, 23]
Poly(vinylidene difluoride) (PVDF)	$d_{33} = -33 \text{ pC/N}$	[21]

piezoelectric coefficient.<sup>24</sup> This shows that the piezoelectric effect is linear in uniform materials. In a centrosymmetric crystal, all the components of the piezoelectric coefficient cancel to zero due to symmetry.<sup>24</sup> While some piezoelectric materials become polarized only when stressed, most have nearly permanent dipole moments and are known as electrets.<sup>24</sup> Electrets are the electrical analogue of a permanent magnet. The electromechanical coupling factor ( $k$ ) quantifies the efficiency of electrical and mechanical energy conversion in a piezoelectric such that:<sup>3</sup>

$$k^2 = \frac{\text{electrical energy converted to mechanical energy}}{\text{input electrical energy}} = \frac{\text{mechanical energy converted to electrical energy}}{\text{input mechanical energy}} \quad (1.7)$$

where  $k$  must be between 0 and 1. The remaining input energy is either stored elastically, stored dielectrically, or dissipated. It is not a measure of the overall power conversion efficiency of a piezoelectric transducer, however, as it does not take into account the dissipation factor of the input.<sup>3</sup>

While the piezoelectric charge constant is an ideal figure of merit for energy harvesting and actuation applications, the piezoelectric voltage constant ( $g_{ij}$ ) is preferred for sensing applications. Large voltage constants, with units of mVm/N, mean that a large, easily detectable voltage is generated, which is easier to detect than current. The piezoelectric charge and voltage constants are related by the permittivity such that:

$$g_{33} = \frac{d_{33}}{\varepsilon_r \varepsilon_0} \quad (1.8)$$

where  $\varepsilon_r$  is the relative permittivity of the material and  $\varepsilon_0$  is the vacuum permittivity.<sup>25</sup> Other figures of merit may include non-piezoelectric properties of a material, depending on the intended application. The piezoelectric constants allow for standardized comparison of

Table 1.2: Piezoelectric voltage constants of common materials.

Material	Piezoelectric Voltage Constant	Ref.
$\alpha$ -Quartz	$g_{11} = 57 \text{ mVm/N}$	[26, 27]
Lead Zirconium Titanate (PZT)	$g_{33} = \sim 40 \text{ mVm/N}$	[3]
Barium Titanate	$g_{33} = 11.4 \text{ mVm/N}$	[28]
Poly(Vinylidene Difluoride) (PVDF)	$g_{33} = 160 \text{ mVm/N}$	[29]
$\gamma$ -Glycine Film	$g_{\text{eff}} = 47 \text{ mVm/N}$	[30]

materials, and the specific constant selected as the key figure of merit should be based on the intended use of the material. Voltage constants for common piezoelectric materials are given in Table 1.2.

#### 1.3.4 Electrical Poling

Certain materials are naturally piezoelectric, namely non-centrosymmetric single crystals, whereas most must be electrically poled through the application of a high voltage electric field. The vast majority of commonly used piezoelectric materials—including ceramics and polymers—are not found as single crystals and, consequently, must be electrically poled to achieve bulk polarization. Many common ceramic piezoelectric materials—such as PZT—are polycrystalline perovskites, which spontaneously fragment into randomly oriented, polarized ferroelectric domains as they cool to below the Curie temperature,  $T_C$ .<sup>18</sup> To achieve bulk polarization and piezoelectricity, these materials must be heated to near the Curie temperature—the temperature at which polarization is lost—and then be allowed to cool while under a high voltage electric field; the electric field must be above that of the coercive field—the voltage at which domain alignment is influenced.<sup>3</sup> The field aligns the domains, which are locked in place as the material is cooled, leaving a remanent polarization after

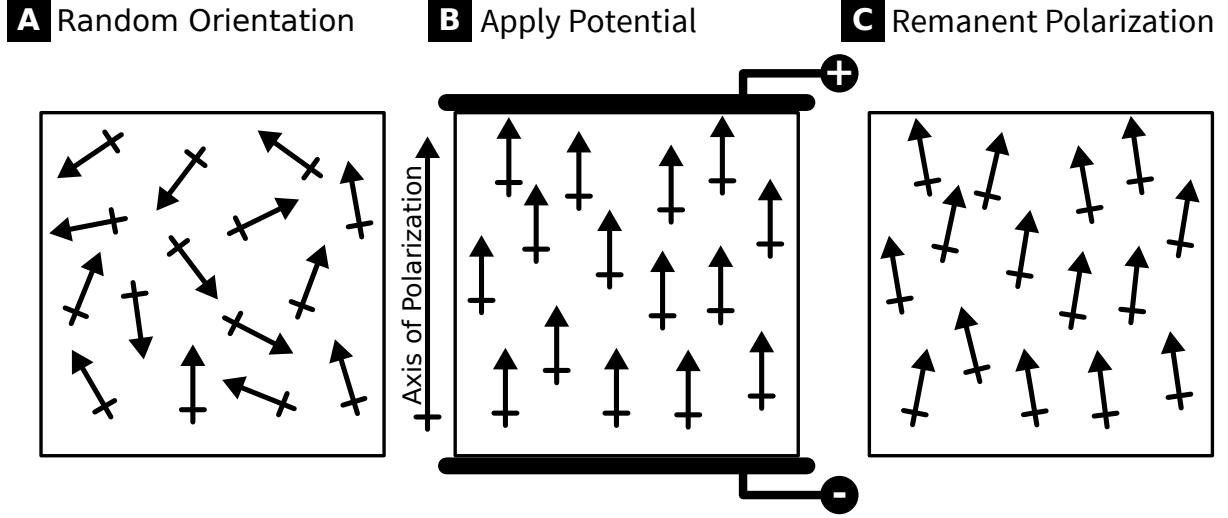


Figure 1.4: Electrical poling of piezoelectric ceramics, taking place at high voltage and temperature, aligns polar crystal domains.

the field is removed (Figure 1.4).<sup>18</sup> The final remanent polarization does not have quite the same degree of alignment as the material had while under the poling field because of dipole relaxation.

As predicted by application of the Langevin function, the polarization induced in poled piezoelectrics by the applied electric field increases with poling voltage.<sup>24,31</sup> The function relates the total equilibrium polarization as follows:<sup>31,32</sup>

$$P = N\mu \cdot \left( \coth \left( \frac{\mu E_{\text{local}}}{k_B T} \right) - \frac{k_B T}{\mu E_{\text{local}}} \right) \quad (1.9)$$

where  $N$  is the dipole number density,  $\mu$  is the dipole moment,  $E_{\text{local}}$  is the local poling field,  $k_B$  is the Boltzmann constant, and  $T$  is a finite temperature. For low poling fields and temperatures ( $<1$  MV/mm at room temperature) used for certain materials such as polymers, the function is approximately linear:<sup>2</sup>

$$P \approx N\mu \cdot \left( \frac{\mu E_{\text{local}}}{3k_B T} \right) \quad (1.10)$$

Since a high degree of alignment is desirable, most piezoelectrics are poled to the maximum

extent that equipment and material properties permit. Dielectric breakdown is the limiting factor in the maximum poling voltage that can be applied to many materials; for ceramics, this is often minimized by poling within an oil bath, which eliminates problems caused by the breakdown of air.<sup>3</sup>

Numerous factors affect the poling field required, including composition, temperature, and shape. For ceramics, common poling fields are in excess of 1 kV/mm and are applied for anywhere from a few seconds to an hour or more at temperatures  $>100^{\circ}\text{C}$ .<sup>3,33</sup> Different compositions of the same ceramic differ widely in the poling field required.<sup>3</sup> Generally, the coercive field required decreases with increased temperature and can be somewhat overcome by increased poling duration. The dielectric breakdown field decreases with increased sample thickness and cross-sectional area, likely due, in part, to an increased probability of defects; therefore, smaller samples are generally easier to reliably pole than larger ones.<sup>3</sup> Larger samples, especially those with greater piezoelectric response, are also more vulnerable to strain induced mechanical failure due to deformations caused by the poling field.

### **1.3.5 Piezoelectric Measurements**

In the simplest sense, piezoelectric constants are determined by applying a force and measuring a charge or voltage for the direct effect, and applying a potential and measuring a deformation for the converse effect. Getting accurate measurements is a bit more complicated, however. The electric displacement vector must be related to the second-order stress tensor to obtain the third-order piezoelectric tensor. Originally, piezoelectric constants were measured statically by placing weights on samples and measuring the resultant charge or voltage. Static measurements have largely been abandoned for quasi-static or dynamic ones. Quasi-static measurements improve accuracy by increasing measurement speed to reduce leakage effects and, simultaneously, greatly increasing the number of points averaged. Dynamic measurements are based on piezoelectric resonance and employ impedance spectroscopy; this is the

preferred method for piezoelectric transducers but is incompatible with many soft, hybrid devices. A more comprehensive overview of piezoelectric measurement methods is presented in Chapter 2, alongside a summary of the measurement system developed to analyze the devices in Chapters 3, 4, and 5.

### 1.3.6 Piezoelectric Single Crystals

The first report of what is now known as the piezoelectric effect, by the Curie brothers, was on the electrical response of naturally occurring single crystals, including quartz and Rochelle salt (sodium potassium tartrate) which were to be the most studied.<sup>4,10</sup> Quartz, for example, is naturally piezoelectric and is found in single crystals of its trigonal  $\alpha$ -quartz state.<sup>34</sup> A piezoelectric crystal can be prepared for piezoelectric use simply by making the correct crystallographic cut such that electrodes can be applied across the desired axis. Generally, crystals are cut either into plates or bars. Plates are electroded on their top and bottom surfaces and excited along the perpendicular axis (i.e., through the plates). Bars are normally electroded lengthwise and excited parallel to the electrodes, as electroding the ends would result in a much greater electrode separation and, therefore, a diminished field.<sup>4</sup>

Piezoelectric crystals are commonly used as resonators (and transducers). The resonant frequency is excited in the crystal via the converse effect by means of an AC electric field. The crystal's vibrations then lead to charge feedback on the drive circuit via an amplifier, keeping it in resonance. Due to its stability and near temperature–frequency independence, quartz crystal resonators have seen widespread use in time keeping and frequency control since their invention in 1921.<sup>15</sup> In addition, oblique cuts of quartz allow it to be tuned to almost any frequency.<sup>4</sup> While fully electroded surfaces excite the resonance frequency, the frequency of a crystalline bar can be boosted to harmonic values by splitting the electrodes

into segments of alternating polarity. Modern quartz wristwatches, for example, use the flexural resonances of a doubly electroded tuning-fork-shaped crystal to minimize size and improve reliability.<sup>35</sup>

While, historically, most piezoelectric research involved inorganic crystals, certain organic crystals have since been found to also be piezoelectric. For example, single crystals of amino acids, including *DL*-alanine and  $\beta$ -glycine, have been shown to be piezoelectrically active.<sup>36,37</sup> An advantage of soft biological materials is their low dielectric constants, which, despite their relatively meager charge constants, allow for large piezoelectric voltage constants, on par with inorganic materials. While these organic crystals are unlikely to have practical applications in their single crystalline form, polycrystalline films show promise as biologically compatible sensors.<sup>37–39</sup>

### 1.3.7 Piezoelectric Ceramics

Due to their often superior properties and ease of manufacture, piezoelectric ceramics, since their discovery in the 1940s, quickly surpassed single crystals in breadth of use.<sup>3</sup> Common piezoelectric ceramics, such as PZT and barium titanate, are members of a class of materials known as perovskites. Members of this class are of the composition  $ABX_3$  and adopt the same structure as the mineral perovskite.<sup>40</sup> The archetypal perovskite is a cubic, centrosymmetric structure of the  $Pm\bar{3}m$  space group.<sup>40</sup> This structure is not piezoelectrically active, but most perovskites—PZT and barium titanate included—spontaneously adopt distortions to this structure, when cooled below their Curie points, which remove the center of symmetry (Figure 1.1, page 6).<sup>3</sup> The polar crystal grains of these ceramics are aligned by poling to create bulk polarization. When these poled ceramics are stressed, the strain alters the unit cell, leading to a change in polarization, which results in a piezoelectric response.<sup>40</sup> Below its Curie temperature, PZT adopts either a tetragonal structure (<52% zirconium at 0 °C) or a rhombohedral structure (>52% zirconium at 0 °C) depending on composition.<sup>18</sup>



Barium titanate transitions from a cubic structure through tetragonal, orthorhombic, and rhombohedral configurations with decreasing temperature and pressure.<sup>40</sup> Depending on the ceramic and its composition, electrical poling occurs at temperatures from 100 °C to 400 °C while under electric fields of 1 kV/mm to 4 kV/mm;<sup>3,33</sup> generally, higher temperatures and voltages lead to more complete polarization.<sup>3</sup> Piezoelectric ceramics are normally divided by their ferroelectric behavior into electrically “hard” and electrically “soft” categories, where hard ceramics have low domain mobility and soft ceramics have high domain mobility.<sup>41</sup> The hardness characteristics of piezoelectric ceramics are tuned through doping. Hard ceramics contain oxygen vacancies, are hard to polarize, have low dielectric losses, and can be subjected to large electrical and mechanical stresses for use in high-power resonators. Soft ceramics, however, contain A site lattice vacancies, are easy to polarize, have large piezoelectric charge constants, and have applications as sensors and actuators.<sup>41</sup> While piezoelectric ceramics have found use in many applications, they have several drawbacks in that they have a limited range of motion, are liable to crack, and are often lead containing.<sup>21,42–44</sup>

Piezoelectric ceramics are prepared as as a solid solution.<sup>3</sup> Powders of the constituents are milled together to ensure intimate, uniform contact. The material is then calcined to remove water, carbon dioxide, and volatile impurities. After calcination, it is milled further and then formed into the desired shape under pressure.<sup>33</sup> Next, the ceramic is fired at temperatures reaching 1200 °C or more. Finally, the ceramic is ground to its final dimensions, electroded, and electrically poled, turning it into a piezoelectric. The ceramic manufacturing process allows, with ease, for the near infinite tuning of piezoelectric ceramic properties from composition to poling conditions to dimensions and more. Manufacturing simplicity, combined with high piezoelectric constants, has led to many practical applications of piezoelectric ceramics, including microphones, transducers, ultrasounds, frequency filters, actuators, energy harvesters, and sensors.<sup>3,33</sup>

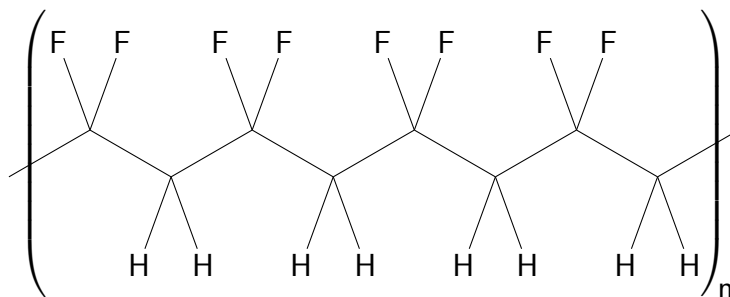


Figure 1.5: Schematic of poly(vinylidene difluoride) (PVDF). In the semicrystalline piezoelectric  $\beta$ -phase of PVDF, the polymer backbone adopts a planar zigzag conformation with negative fluorine atoms on one side and positive hydrogen atoms on the other.<sup>24,48</sup>

### 1.3.8 Polymers

Polymer based piezoelectric materials are an increasingly used alternative to ceramics. Of these, most early research and applications revolved around poly(vinylidene difluoride) (PVDF) (Figure 1.5).<sup>24,45</sup> It is commonly used in flexible sensors and is being studied for use in other flexible electronics.<sup>45</sup> PVDF is normally electrically poled at a temperature of  $>80^{\circ}\text{C}$  and an electric field of  $>3\text{ kV/mm}$  and then uniaxially stretched.<sup>24</sup> The piezoelectric effect in PVDF arises from the poled oriented dipoles of the polymer's semicrystalline regions.<sup>24</sup> While it has received a disproportionately large research focus, PVDF is just one of many polymers in which dipoles can be locked into alignment. It has the advantages of being flexible, lead-free, and biocompatible, but it suffers from a piezoelectric response an order of magnitude below that of top ceramics such as PZT and barium titanate.<sup>21,46</sup> The theories and techniques developed for PVDF should be widely applicable to other polymers. Behind PVDF, the next most commercialized is P(VDF-TrFE), a copolymer of PVDF and trifluoroethylene. On the biological front, poly( $\gamma$ -benzyl-L-glutamate) has received considerable interest.<sup>47</sup> Despite considerable scientific interest, polymer based piezoelectrics still come up short on many metrics when compared to ceramics. As a result, many investigators have turned to hybrid and composite devices in hopes of bringing ceramic-like response to flexible devices.

### **1.3.9 Novel and Composite Devices**

A wide array of approaches have been investigated in hopes of developing durable, flexible piezoelectric devices with response on par or better than that of common ceramics. These range from embedding ceramic particles in polymer matrices to nanoribbon or nanowire devices to viral capsid based films and more.<sup>49,50</sup> In a standard particle/matrix composite device, small particles of a piezoelectric ceramic are embedded in a pliable polymer matrix. They are designed to take advantage of the piezoelectric properties of the ceramic while simultaneously enjoying the soft, flexible properties of the polymer matrix. Increasing the filler content usually increases the piezoelectric response but to the detriment of the mechanical properties.<sup>49</sup> Potential downsides of these devices include incompatibilities between the poling fields required for complete polarization of the ceramic particles and the dielectric breakdown of the polymer matrix as well as losses in transmitting mechanical forces through the matrix to the particle. Certain approaches to help solve the latter problem involve depositing thin films of piezoelectric ceramics on polymer ribbons or using novel geometries to better transmit force in a efficient manner while maintaining flexibility.<sup>51</sup> Other approaches rely on using unusual new piezoelectric materials.

## **1.4 Other Forms of Electromechanical Coupling and Relevant Related Phenomena**

Besides piezoelectricity, other closely related phenomena interconvert mechanical and electrical energy including flexoelectricity, ferroelectricity, and electrostriction. Another closely

associated effect, pyroelectricity, relates temperature changes with electrical potential. These other effects are present, to varying extents, in most piezoelectrics. Triboelectricity, a type of contact electrification, is also omnipresent.

#### **1.4.1 Flexoelectricity**

Flexoelectricity is the linear electromechanical coupling of inhomogeneous strain to electrical polarization. It is the closely related inhomogeneous analogue of piezoelectricity and its homogeneous strain.<sup>52</sup> Flexoelectricity is manifest as the bending of a material where the inside of the bend undergoes compressive strain, while the outside of the bend experiences tensile strain. Piezoelectricity relies on noncentrosymmetric point groups, as its homogeneous strain cannot change a material's symmetry; the inhomogeneous strain of flexoelectricity, however, breaks a material's symmetry, which makes it universal to all point groups.<sup>52</sup> Similar to the piezoelectric effect, it has a direct and converse effect; however, it is generally much weaker at bulk scales. The flexoelectric effect is considerably greater at the nanoscale and in high dielectric constant materials. Many flexible piezoelectric devices undoubtedly have contributions from flexoelectricity, and the effect can be exploited using geometry considerations to make pseudo-piezoelectric devices.<sup>52</sup>

#### **1.4.2 Ferroelectricity**

Ferroelectricity is a property of materials such that their spontaneous electric polarization can be reversed by application of an electric field.<sup>3,53</sup> It is often complimentary to piezoelectricity and found in nearly all piezoelectric ceramics. It occurs in a subset of pyroelectric crystals (themselves the subset of permanently polarized piezoelectric crystals) where the dipole can be flipped by means of an applied electric field. Ferroelectrics exhibit memory due to the energy required to reverse the domains and, therefore, exhibit hysteresis in a voltage

sweep. Ferroelectrics near their Curie temperature often exhibit exceptional piezoelectric and dielectric properties. Ferroelectricity can be exploited directly in memory devices, but ferroelectric materials are most often used in applications where the ferroelectric nature enhances other properties. In Chapter 6, ferroelectricity is discussed in greater detail.

### 1.4.3 Electrostriction

Electrostriction is the direction independent interaction of mechanical deformation and electric field. It is proportional to the square of the electric field and is present in small amounts in all materials.<sup>4</sup> The deformation is the same no matter the polarity of the applied electric field and scales with even powers of the field.<sup>3</sup> It is proportional to strain ( $x$ ) and applied electric field ( $E$ ) such that:

$$x = ME^2 \tag{1.11}$$

where  $M$  is the electrostrictive coefficient, a fourth-rank tensor.<sup>33,53</sup> Electrostriction is caused by the anharmonicity of the spring-like lattice interactions between ions.<sup>53</sup> Generally, the electrostrictive effect is very weak, but it can be large enough to be of interest in high dielectric materials, such as ferroelectrics just above their Curie point.<sup>3</sup> The converse electrostrictive effect is due to stress dependent changes in permittivity and can be exploited for use in stress sensors.<sup>53</sup> In most piezoelectric applications, electrostriction can be safely ignored due to its comparatively very weak nature and its easily identifiable quadratic relation.

### 1.4.4 Pyroelectricity

Pyroelectricity relates temperature changes in materials with reversible changes in spontaneous electrical polarization, and it is present in all permanently polarized piezoelectric crystals with one unique axis of electrical polarization.<sup>33,54</sup> The change in polarization results in buildup of surface charges that can be detected by an induced current produced in an external

circuit. Identification of primary pyroelectricity is often complicated by secondary and tertiary pyroelectric effects—piezoelectric effects arising from thermal expansion/contraction of unconstrained crystals and strain gradients due to uneven heating, respectively.<sup>54</sup> The converse pyroelectric effect, also known as the electrocaloric effect, causes a temperature change in a crystal upon application of an electric field; this is unique from resistive heating arising from leakage currents. Pyroelectrics have applications as temperature and infrared light sensors.<sup>53</sup>

#### **1.4.5 Triboelectricity**

Triboelectricity is a charging that occurs when two dielectrics come in contact with each other. It can be generated kinetically due to the asymmetric rubbing of like materials or through contact electrification from the static contact of unlike materials.<sup>55</sup> This charging occurs based on the triboelectric series. Despite its ubiquitous nature, the triboelectric effect is poorly understood, but it is believed to originate from direct electron transfer between materials.<sup>55,56</sup> There is mounting evidence that ion transfer may also play a role.<sup>57</sup> No matter the underlying mechanism, triboelectric generators are able to exploit the effect to generate electricity. It is important to minimize contributions from the triboelectric effect when characterizing piezoelectric materials. This is commonly accomplished in quasi-static direct effect measurements by keeping a minimum preload force applied to the sample during testing to ensure all surfaces remain in contact.

### **1.5 Piezoelectric Energy Harvesting**

Piezoelectric energy harvesters convert mechanical energy to usable electrical energy by means of the piezoelectric effect. They have the potential to power small, low power electronic devices

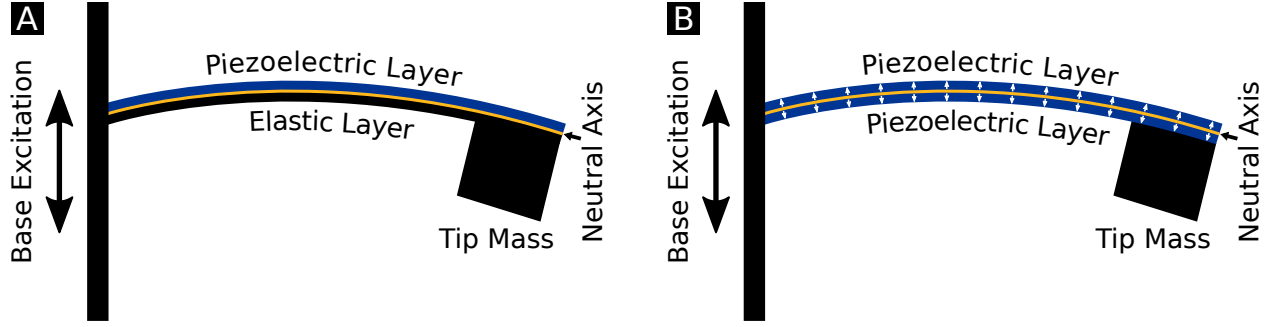


Figure 1.6: Piezoelectric cantilever vibrational energy harvesters.<sup>‡</sup> (A) Unimorph and (B) bimorph designs are shown. The base is excited up and down causing the cantilever to bend due to the inertia holding the tip mass relatively stationary.

in situations where battery based devices are impractical. They can be split into two main categories: inertial and kinematic. Inertial energy harvesters convert vibrations to electrical energy by means of a mass and spring model.<sup>21</sup> They generally consist of a piezoelectric cantilever that is fixed on one end and is attached to a mass on the other end. When vibrations oscillate the base, the inertial mass of the weight resists movement thereby bending the piezoelectric cantilever to produce electricity. Since bending motion in a piezoelectric device cancels, a unimorph or bimorph cantilever is employed.<sup>21</sup> In a unimorph, the piezoelectric layer is attached to an elastic nonpiezoelectric such that the neutral bending axis is outside the piezoelectric layer. In a bimorph, two oppositely poled piezoelectric layers that meet at the neutral axis are used. Figure 1.6 shows unimorph and bimorph piezoelectric cantilever vibrational energy harvesters. These devices are normally operated at or near resonance, as power output quickly decreases as the vibrational frequency strays from the resonant one.<sup>21</sup> Unlike electromagnetic energy harvesters, piezoelectric energy harvesters are solid state and can be relatively easily miniaturized since aluminum nitride devices, for example, are compatible with MEMS (microelectromechanical systems) fabrication methods.<sup>21</sup>

The other major type of piezoelectric energy harvesters are kinematic based devices in which the device is directly coupled to motions. These devices are generally larger than inertial

---

<sup>‡</sup>Figure adapted from reference [21].

based harvesters and are anchored on two sides so that motions can be transferred through them. They operate at slower, off-resonance frequencies by means of bending, stretching, or compressing. This means that electromechanical coupling plays a larger role in their efficiency.<sup>21</sup> Most piezoelectric energy harvesters based on novel materials and structures function kinematically. One challenge in developing these compliant harvesters—especially stretchable ones—is ensuring reliable, flexible electrical connections to the piezoelectric elements. This can be accomplished using spring-like or meandering electrical traces, using inherently stretchable conductors, or relying on percolation via high loadings of conductive particles.<sup>49</sup> Novel piezoelectric energy harvesters use a range of flexible piezoelectric elements such as nanowires, electrospun fibers, and embedded particles as active elements.<sup>49</sup> No matter the mechanism used, optimizing piezoelectric energy harvester is a complicated problem. The overall efficiency is based on the overarching system, including power conversion electronics and load; it is not merely dependent on the piezoelectric transducer.<sup>21</sup> Due to the complicated coupling and numerous losses at every stage, typical piezoelectric energy harvesters only obtain around 20 % power conversion efficiency in real world applications.<sup>21</sup>

## 1.6 Piezoelectric Sensing

While similar in many ways to piezoelectric energy harvesting, the figures of merit for piezoelectric sensing do differ somewhat. In order to achieve good sensitivity over background noise, a piezoelectric force sensor must produce sufficient open circuit voltage.<sup>58</sup> The piezoelectric voltage constant ( $g_{33}$ ), discussed previously in Section 1.3.3, is a key figure of merit for sensing applications, as it relates the voltage response of a material to the applied force. As shown previously in Equation 1.8 on page 9, it is related to the piezoelectric charge constant by the permittivity. It follows that high charge constants paired with low permittivities lead to high voltage constants. While many piezoelectric ceramics have large charge constants, they also



have large relative permittivities ( $\sim 1000$ ), which somewhat hinders their sensing abilities.<sup>58</sup> While lower relative permittivities are generally desirable, very low values can complicate overall device design due to cable losses from impedance mismatches.<sup>58,59</sup>

For several decades, considerable piezoelectric sensor research focused on hydrophones for underwater listening. Since hydrophones are much smaller in dimension than the wavelengths they sense and are surrounded on all sides by the water, hydrostatic piezoelectric coefficients ( $d_h$  and  $g_h$ ) apply (where  $g_{31} + g_{32} + g_{33} = g_h$ ). Unfortunately, the hydrostatic coefficients of ceramics are generally very low as, for PZT,  $g_{33} \approx -(g_{31} + g_{32})$ . As a result, work commenced on developing methods for decoupling the piezoelectric modes; this ultimately led to some of the first piezoelectric ceramic-polymer composites.<sup>58</sup> These composites also had the added benefit of better matching the device impedance with that of water. It was eventually discovered that parallel ceramic rods in a polymer matrix (so called 1-3 composites) gave the best results, as they kept the  $g_{33}$  component while eliminating the cancellations due to the  $g_{31}$  and  $g_{32}$  components.<sup>58</sup> Research continued on improving the sensitivity of this design by addressing several pitfalls such as  $g_{31}$  contributions caused by the polymer bulging when compressed due to the Poisson effect.<sup>58</sup>

The naming convention for ceramic-polymer composites, developed by Newnham, conveys the connectivity of the active and passive phases.<sup>58,60,61</sup> It is of the format *connectivity of the active phase-connectivity of the passive phase* where the connectivity ranges from 0 for no connectivity to 3 for connectivity in the  $X$ ,  $Y$ , and  $Z$  directions. For example, piezoelectric particles (0-D connectivity) in an interconnected matrix (3-D connectivity) are 0-3 composites while a layered structure of alternating piezoelectrically active material (2-D connectivity) and polymer matrix (2-D connectivity) is a 2-2 composite. These naming conventions are no longer common in the literature, even for applicable composite devices such as ceramic particles in a matrix (0-3), parallelly aligned nanowires or nanorods in a matrix (1-3), or thin piezoelectric films with an insulator layer to prevent charge leakage (2-2). Contemporary piezoelectric sensor research has turned more towards the development of flexible sensors, often for the

monitoring of low-frequency stimuli such as heart rate or touch. Despite the considerable research interest, a majority of recent articles in the literature do not provide adequate data for meaningful comparisons and often focus on figures of merit only tangential to their stated target applications. It is uncommon that the piezoelectric voltage constant is reported, and, when it is, it is often converted from the charge constant using a permittivity value measured at a frequency several orders of magnitude greater than that of the piezoelectric measurement.

## 1.7 Rational Design of Materials

### 1.7.1 Overview

While piezoelectric materials have long been an area of considerable research interest, few attempts have been made at the rational design of these materials from the ground up with the goal of maximizing their piezoelectric response and efficiency. The electromechanical coupling factor ( $k$ ), introduced earlier in Section 1.3.3, is of interest when considering fundamental piezoelectric design.<sup>62</sup> It states that the general coupling efficiency of a piezoelectric material is:<sup>32,63</sup>

$$k = d \sqrt{\frac{E_Y}{\varepsilon_r}} \quad (1.12)$$

where  $k$  is the coupling efficiency,  $d$  is the piezoelectric coefficient,  $E_Y$  is the Young's modulus, and  $\varepsilon_r$  is the dielectric constant. Since perfect efficiency cannot be reached, it follows that:<sup>32</sup>

$$d < \sqrt{\frac{\varepsilon_r}{E_Y}} \quad (1.13)$$

This means that, so long as the piezoelectrically active element can be decoupled from its matrix, the individual components of efficiency can be tuned independently. The Young's modulus, or stiffness of the material, can be tuned by altering the matrix's composition,

while the permittivity can be altered, for example, by changing the identity of the piezoelectrically active component. It is known that lowering the modulus of a material increases its piezoelectric response,<sup>64</sup> but, by separating the two factors, this can be more fully exploited.

### **1.7.2 Small Organic Molecules as Dopants**

One approach carried out towards the rational design of piezoelectric materials was to dope a polymer matrix with electrically poled polar small organic molecules.<sup>65</sup> Dopants were dispersively adhered to the surfaces of an open-cell PDMS foam. The components of the piezoelectric response could then be independently tuned by varying the dopant or matrix properties. Piezoelectric measurements were carried out that demonstrated that the charge constant increased with increasing dopant dipole moment, increasing dopant concentration, increasing poling field, and decreasing matrix modulus. The complete work is presented in Chapter 3.

### **1.7.3 Oligopeptide Self-Assembled Monolayers**

SAMs are ordered molecular assemblies spontaneously formed by adsorption of active solution molecules onto a solid surface.<sup>66</sup> These molecules often take the form of functionalized long-chain hydrocarbons, but many other moieties are possible. As an example, thiol-containing molecules will self-assemble on gold surfaces. Adsorption kinetics are often split into two distinct regimes with a fast diffusion controlled adsorption step taking only a few minutes followed by a slow reorganization step taking several hours or more, during which time the SAM develops its final properties.<sup>66</sup> SAMs are a versatile tool for surface modification as a uniform, well formed film can be easily and reliably grown simply by placing a substrate in solution for a day or so.

On a rational design basis, SAMs are a helpful mechanism for determining, on an atom-by-atom level, the relationship between molecular sequence and piezoelectric response in organics. SAMs of various thiol-containing oligopeptides were grown on gold surfaces and subsequently electromechanically characterized, to help elucidate the effect of amino acid sequence on piezoelectric response.<sup>67</sup> Device assemblies were produced by placing the oligopeptide SAM against a second polyurethane coated electrode that had either bare gold or gold functionalized with an alkanethiol SAM underneath. While sequence effects were somewhat unclear, the devices produced outstanding piezoelectric charge constant responses up to 2 Vm/N and a prototype flexible device produced nearly 6 V of open-circuit voltage in response to gentle bending motions. The complete work is presented in Chapter 4.

## 1.8 Dissertation Overview

This chapter provided an introduction to piezoelectricity and related phenomena relevant to the work presented in this dissertation. The following is a summary of the remainder: Chapter 2 outlines piezoelectric measurements in detail, the development of the measurement and analysis framework used in the remainder of the work, and a test case using polar small organic molecule doped piezoelectric polyurethane foams; Chapter 3 presents published work on using PDMS foams as a framework to develop piezoelectric devices using polar small organic molecule dopants; Chapter 4 presents published work on piezoelectric devices based on polar SAMs of oligopeptides; Chapter 5 provides a perspective on using oligopeptide-based piezoelectric materials as a framework for understanding electromechanical coupling in molecules; Chapter 6 provides an overview of ferroelectricity, the double-wave method of measuring ferroelectric hysteresis loops, and results from measurements on SAMs of a bowl-like corannulene derivative; and, finally, Chapter 7 provides concluding remarks and insights on future research directions.

## 2.0 Development of Measurement System

### 2.1 Piezoelectric Measurement Methods

Piezoelectric constants are an important tool for characterizing new piezoelectric materials and can be measured using an array of methods. Some of these methods are explained in a series of IRE/IEEE standards (now withdrawn).<sup>25,62,68–70</sup> The methods can be divided into two main categories: those for measuring the direct effect and those for measuring the converse effect. The direct effect is determined using static or quasi-static loading in which weights or forces are applied to the material and the resultant charge or voltage is measured. Charge is measured for determining the piezoelectric charge constant ( $d_{ij}$ )—relevant for transducer and energy harvesting applications—whilst voltage is measured (and converted to induced electric field) for piezoelectric voltage constant ( $g_{ij}$ ) measurements—of interest for sensing applications. While these methods have largely been phased out in favor of resonance based ones for ceramic transducers, they are still applicable in many cases where resonance based methods are impractical or undesirable, such as with very soft materials. In the resonance based approaches, the converse piezoelectric constants are determined from the frequency dependence of the electrical impedance.<sup>25</sup> At the nanoscale, the converse effect is measured using piezo force microscopy (PFM) which directly measures the physical deformation of a material in response to an applied electric field. Strain gauge and laser interferometry based converse measurements are also possible. Measurement techniques are also divided between static (including quasi-static) and dynamic (resonance) measurements; it is important that the measurement technique matches the regime of the material’s intended application. While

resonance based approaches are the most common in traditional piezoelectric materials, other methods are often needed for novel materials and devices where the material properties differ from those of traditional single-crystalline and ceramic piezoelectrics.

Characterization of the direct piezoelectric effect is important for sensing and energy harvesting applications. While the direct and converse constants should be equal in theory, this is not always the case under real-world conditions.<sup>71–74</sup> Early on, piezoelectric measurements were carried out using the static method. Weights were placed on the material and the resultant charge was measured as the voltage across a capacitor; since the weights must be slowly and carefully placed, this method results in loss due to charge leaks. The method can be modified to minimize this error by, instead, quickly removing a weight.<sup>75</sup> More modern approaches to measuring the direct effect are quasi-static in nature. A known force is applied to the sample using a mechanical actuator at a frequency up to one order of magnitude below any piezoelectrically active resonance.<sup>75</sup> Commercial devices—known as  $d_{33}$  or Berlincourt meters—are available for this type of testing. Generally, they apply a 10 N preload force followed by 0.25 N compressions as a frequency of  $\sim 100$  Hz.<sup>76,77</sup> Preload forces are applied to help minimize electrostatic effects. While these instruments are easy, convenient, and work well for ceramics, soft materials that need a lower preload force and/or slower compression frequency due to slow elastic recovery rates are incompatible. Luckily, stepper motors or other actuators with sufficient travel can be used to make a series of compressions of differing force at a selectable rate; a linear regression of the resulting data can help minimize errors associated with leakage due to the slower speeds. Regardless of the test method chosen, it is important to ensure that it is compatible with the material properties of the device under test.

Dynamic resonance measurements of the converse piezoelectric effect are considered the most accurate and reliable for traditional materials; this is especially true for use as transducers. Typically, a resonance method is carried out by measuring the impedance spectrum. The resonance ( $f_r$ ) and antiresonance ( $f_a$ ) frequencies can be determined based

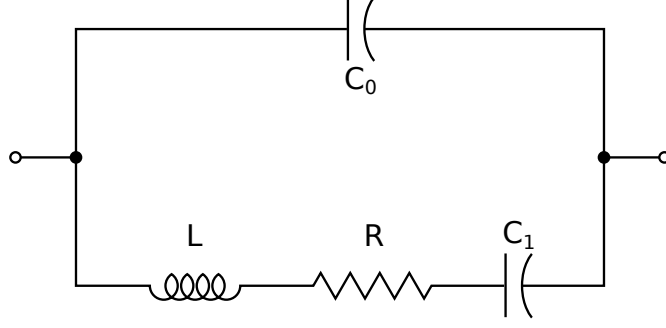


Figure 2.1: Equivalent circuit of a piezoelectric vibrator near fundamental resonance.  $L$ ,  $R$ , and  $C_1$  are the motional inductance, resistance, and capacitance respectively.  $C_0$  is the shunt capacitance.

on the equivalent circuit (Figure 2.1).<sup>3</sup> The minimum impedance is approximately equal to  $f_r$  while the maximum impedance is approximately equal to  $f_a$ .<sup>78</sup> The resonance and antiresonance frequencies, along with the density ( $\rho$ ) and off resonance permittivity ( $\varepsilon_{33}^X$ ), can be used to calculate the piezoelectric constant.<sup>3,25,79</sup> First, the elastic compliance ( $s_{33}^E$ ) is calculated:

$$s_{33}^E = \frac{1}{4\rho h^2 f_r^2} \quad (2.1)$$

where  $\rho$  is the sample density,  $h$  is the sample height, and  $f_r$  is the sample resonance frequency. Next, the electromechanical coupling factor ( $k_{33}$ ) is calculated:

$$k_{33} = \sqrt{\frac{\pi}{2} \frac{f_r}{f_a} \tan\left(\frac{\pi}{2} \frac{f_a - f_r}{f_a}\right)} \quad (2.2)$$

Finally, the piezoelectric constant can be computed:

$$d_{33} = k_{33} \sqrt{s_{33}^E \varepsilon_{33}^X} \quad (2.3)$$

Similar equations are used for determining the other piezoelectric constants. These equations are only valid when their various underlying assumptions are true. While resonance based measurement methods are useful and accurate for traditional ceramics and crystals for transducers, they cannot be used for many novel polymer, hybrid, or biological based devices.

The converse piezoelectric effect of a surface can be measured at the nanoscale using PFM. It works by generating a piezoelectric response in the surface using an AC field applied through the tip and measuring the amplitude response.<sup>80</sup> The sensitivity of this technique was improved through use of dual AC resonance tracking (DART-PFM) which allows for the tip to be reliably operated at resonance.<sup>81</sup> It works by bracketing two drive resonances about the tip's resonant frequency; this allows for tracking and maintenance of tip resonance as it shifts due to surface changes. Overall sensitivity is improved by maintaining tip resonance. One potential drawback of DART-PFM is that the measured effective piezoelectric constants are due to both piezoelectric and tip-sample electrostatic response. This is often overcome through the use of high spring constant levers; while this often works well for hard materials, the stiff lever will greatly deform soft surfaces and reduce sensitivity.<sup>82</sup> Our group solved this issue through the creation of a DC-sweep DART-PFM technique which allows for the use of soft, low spring constant levers by sweeping the DC bias voltage with fixed AC field to determine and correct for the electrostatic contributions.<sup>82</sup> When properly implemented, PFM techniques allow for reliable determination of piezoelectric constants at the nanoscale.

## 2.2 Testing Hardware and Setup

A semi-automated quasi-static direct piezoelectric measurement system (Figure 2.2) was developed to study the piezoelectric foams presented in Chapter 3 and the piezoelectric self-assembled monolayers (SAMs) of oligopeptides presented in Chapters 4 and 5; its function is described in the following sections. A computer running a custom Python script controls a stepper motor to apply compressions to a sample and controls a source measure unit (SMU) to measure applied force and resultant current or voltage. The stepper motor is controlled via a script running on an Arduino Uno microcontroller board. Once triggered by the control computer via a serial command sent over a serial-to-USB interface, the Arduino sends 5 V



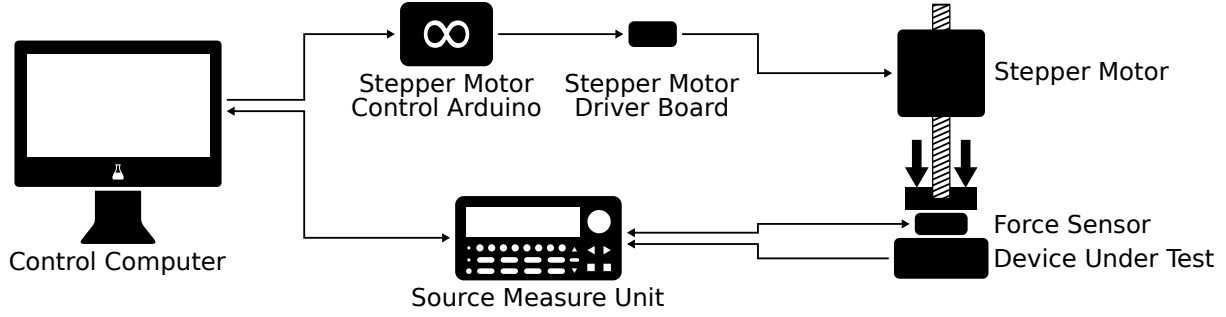


Figure 2.2: Measurement system setup. A computer controls the stepper motor via an Arduino Uno microcontroller board coupled to a stepper motor driver board. It also controls the source measure unit which measures piezoelectric response current or voltage. The source measure unit also applies voltage to and measures resistance on the force sensor.

digital voltage pulses at correct intervals for each step to the stepper motor driver board (EasyDriver v4.5, Brian Schmalz/SparkFun Electronics); it also sends either a 0 V or 5 V digital signal to the driver board direction pin to set the stepper motor rotation direction. The driver board then sends power to the stepper motor to step it as needed. Simultaneously, the control computer sends Lua-based code to the SMU (Keithley SourceMeter Model 2614B) over the VXI-11 protocol via Ethernet.<sup>§</sup> The code directs the SMU to run the resistive force sensor (Tekscan FlexiForce A201) (by applying voltage and measuring resistance) on one channel while measuring the short circuit current or open circuit voltage across the device under test on the other. The SMU then feeds the data back to the control computer.

In practical use, an approximate preload force was set manually when mounting the sample, followed by running a script on the control computer to fine tune the preload force. The preload force serves to minimize triboelectric and other electrostatic responses in the signal. The script would measure the average force applied to the sample for 10 s before instructing the stepper motor to increase or decrease the preload force as needed; this process was automatically repeated until the preload force was in the desired range. With the preload force set, another script could be run to measure the piezoelectric response as desired.

<sup>§</sup>The initial iteration used an Ethernet/VISA/GPIB interface to send the code to an older Keithley SourceMeter Model 2612 SMU.

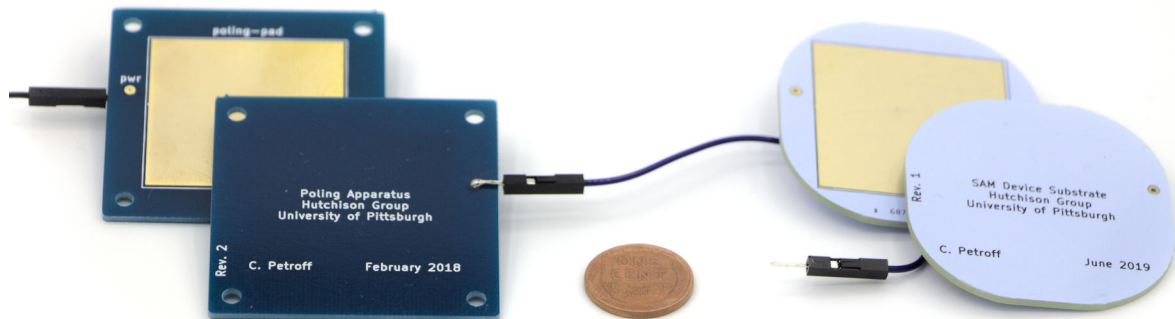


Figure 2.3: Printed circuit board (PCB) electrodes.  $5\text{ cm} \times 5\text{ cm}$  PCBs with  $3.5\text{ cm} \times 3.5\text{ cm}$  electroless nickel immersion gold (ENIG) pads were used as rigid electrodes for piezoelectric measurements. The original PCBs (left) were used for electrical poling and testing of piezoelectric foams as well as for growth and testing of oligopeptide self-assembled monolayers (SAMs). Redesigned PCBs (right) fit inside smaller Petri dishes and allowed for SAMs to be grown from a smaller volume of solution. A United States penny is shown for scale (center).

Generally, three sets of measurements were run consecutively and the resultant piezoelectric response averaged. For piezoelectric charge constant measurements, short circuit current was recorded, while for piezoelectric voltage constant measurements, open circuit voltage was recorded. Custom printed circuit boards (PCBs) were designed and purchased for use as electrodes (Figure 2.3); they were used both to electrically pole and to test the piezoelectric foams while the piezoelectric oligopeptide SAMs were grown directly on their gold surfaces and then tested.

## 2.3 Data Processing

Data processing is a key step of any measurement workflow. The resistance, current, and voltage data—all as a function of time—received by the control computer need to be converted into piezoelectric constants. This was carried out in a semi-automated fashion through use of Python scripts (see Appendices A.2 and B.5). First, resistance is converted into applied

force through use of a linear calibration regression. Next, the force baseline—the preload force—is determined by averaging the first 25 data points ( $\sim 1$  s) of the force measurement for piezoelectric charge constant measurements and averaging data points 30 to 530 ( $\sim 5$  s for most measurements) for piezoelectric voltage constant measurements; this baseline is later subtracted from the height of the force peaks. Force peaks are identified as regions where the force value exceeds  $a\sigma + b$  where  $\sigma$  is the standard deviation in the force over baseline determination region and  $a$  and  $b$  are constants that were normally set to 3 and 0.2, respectively, with good results.

For piezoelectric charge constant calculations, the current in the region corresponding to each force peak is examined. The current baseline is determined by averaging the first 25 data points of the measurement. The start of a current peak is set as five data points before the start of the force peak, while the end is set as when the average of three current values has crossed the baseline. Currents are integrated into charge via the trapezoidal method.

For piezoelectric voltage constant measurements, the voltage baseline is first corrected using the average slope over data points 30 to 530 ( $\sim 5$  s for most measurements). Voltage peaks corresponding to force peaks are then determined using the peak finding algorithm of SciPy’s signal processing submodule. Force is converted to external stress by dividing by sample area, and voltage is converted to induced electric field by dividing by sample thickness. The piezoelectric charge constant is determined as the slope of the linear regression of the charge–force plot, while the piezoelectric voltage constant is determined as the slope of the linear regression of the induced electric field–external stress plot;<sup>¶</sup> additional details on piezoelectric charge and voltage constant determination are provided in Chapters 3 and 4, respectively.

---

<sup>¶</sup>A standard linear regression was originally used, but it was later changed to a robust linear regression to minimize the influence of outliers.

## 2.4 Piezoelectric Polyurethane Foams: A Test Case

The measurement system and analysis framework discussed in the previous two sections was developed around the testing of piezoelectric polyurethane foams. These foams, based on previous work in the group by Michael J. Moody,<sup>32</sup> involve the use of polar, small organic molecule dopants to generate the piezoelectric response, similar to what is discussed in Chapter 3 for poly(dimethylsiloxane) (PDMS) foams. Along with efforts to improve the sample-to-sample foam consistency, the measurement system presented here greatly improved the consistency and reliability of the piezoelectric measurements. The results of these experiments are presented in the remainder of this chapter.

### 2.4.1 Experimental Methods

2-Chloro-4-nitroaniline (>98 %) (CNA) was obtained from TCI. Polytek Development Corp. PolyFoam F-3 two-part (part A: methylene bis(phenylisocyanate); part B: polyether polyol and proprietary copolymer) polyurethane foam system was obtained from Brick in the Yard Mold Supply. All chemicals were used as received.

Polyurethane foam samples were prepared from a two-part commercial polyurethane system. First, the CNA dopant was dissolved in the polyol component. Dopant concentration was calculated based off the total volume of both parts of the unreacted foam. Next, the isocyanate component was added to the polyol/dopant mixture and the components were mixed, allowed to dwell, and then scraped onto the poling slides. The top poling slide was lowered into place, and the poling field was applied for two hours during which time the mixture foamed, reaching and expanding across the top poling slide. For poling, samples were placed between PCBs discussed in Section 2.2; polyimide tape was applied to the PCBs for protection. Samples were poled at 0kV–5kV. During poling, the PCBs had a fixed spacing of 3 mm–12 mm. The poling plates were held in place using screws and wing-nuts,



Figure 2.4: Piezoelectric polyurethane foam poling setup. The foam sample was placed between two parallel plates of fixed separation across which a potential was applied.

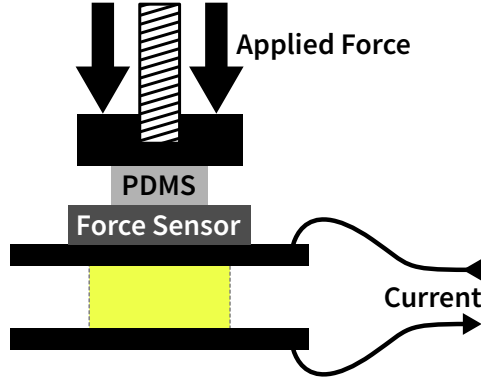


Figure 2.5: Piezoelectric polyurethane foam testing setup. The foam sample was placed between two plates with force applied along the Z-axis.

and separation was maintained through the use of aluminum spacers. The poling setup is depicted in Figure 2.4. After poling was completed, a 20 mm diameter circular core was taken from each sample using a punch. The samples were then tested, and the piezoelectric response was calculated.

Samples were tested in a quasi-static manner. For testing, samples were placed between two PCBs identical to those used for poling. The sandwich was then positioned in a testing apparatus consisting of a movable plastic block below a threaded rod (Figure 2.5). A force sensor (Texscan FlexiForce A201), with a PDMS spacer on top, rested above the sample sandwich and below the plastic block. A slight pressure was applied using the threaded rod to minimize triboelectric charge generation. Using the apparatus, compressions of varying force were applied along the Z-axis every few seconds; measurements were recorded for 70 s using a Keithley 2612 SourceMeter. The system was tested on quartz and PVDF; test results agree with literature values. Data was then processed as discussed above in Section 2.3.

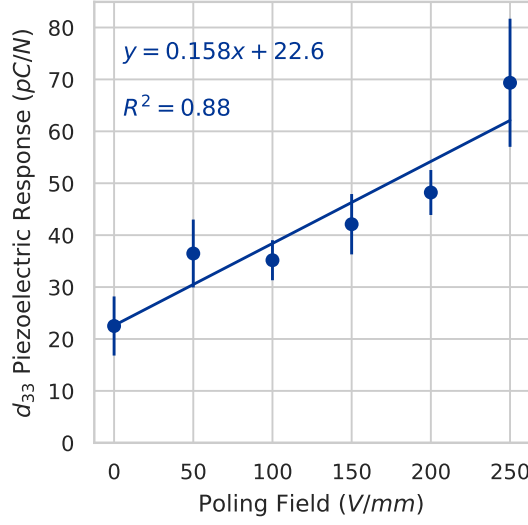


Figure 2.6: Piezoelectric response of polyurethane foams as a function of poling voltage. The response of 0.2 M CNA doped, 5 mm thick polyurethane foams increased linearly with poling voltage.

#### 2.4.2 Results

The effects of poling voltage and foam thickness were examined for the CNA doped piezoelectric polyurethane foams. The poling voltage applied to the samples was varied from 0 V/mm to 1000 V/mm. The piezoelectric response was seen to increase with poling voltage until a breakdown point was reached and the piezoelectric response collapsed to near that of unpoled samples (not shown). As seen in Figure 2.6, before the breakdown voltage, the piezoelectric response of the samples increased linearly with poling voltage. The cause of the breakdown is not known as it occurs at a much lower voltage than the dielectric breakdown voltage of polyurethane foam ( $>3000$  V/mm).<sup>83</sup> The region prior to the breakdown shows that the bulk polarization increases linearly with increased poling voltage. As the piezoelectric effect in the samples is believed to arise from the alignment of the individual dipole moments of the dopant molecules, the linear increase is expected.

The thickness of the polyurethane foam was varied from 3 mm to 10 mm. Figure 2.7 shows that the piezoelectric response of the polyurethane foams increased with increasing thickness.

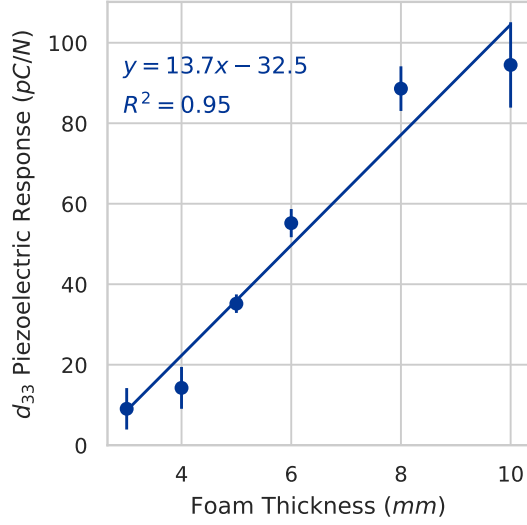


Figure 2.7: Piezoelectric response of polyurethane foams as a function of foam thickness. The response of 0.2 M CNA doped polyurethane foams poled at 100 V/mm increased with foam thickness.

This large effect is likely a property of the matrix. Qualitatively, the thicker foams are softer; all foams can be compressed approximately 50 % when 10 N of force is applied. This indicates that an edge effect remains for the top and bottom of the foam samples, where the material is stiffer. While these piezoelectric polyurethane foams helped with the development of and demonstrated the utility of the measurement system presented in this chapter, shortcomings including foam inconsistencies and dopant incompatibility caused the polyurethane system to be abandoned in favor of the piezoelectric PDMS foams presented in the next chapter.

### 3.0 Highly Tunable Molecularly Doped Flexible Poly(dimethylsiloxane) Foam Piezoelectric Energy Harvesters

This chapter is adapted from:

Petroff, C. A.; Bina, T.; Hutchison, G. R. Highly Tunable Molecularly Doped Flexible Poly(dimethylsiloxane) Foam Piezoelectric Energy Harvesters. *ChemRxiv:7562456.v3* **2019**. DOI: 10.26434/chemrxiv.7562456.v3

which is also published as:

Petroff, C. A.; Bina, T. F.; Hutchison, G. R. Highly Tunable Molecularly Doped Flexible Poly(dimethylsiloxane) Foam Piezoelectric Energy Harvesters. *ACS Appl. Energy Mater.* **2019**, 2, 9, 6484–6489. DOI: 10.1021/acsaem.9b01061.

It is a collaborative effort in which I designed the testing system, revised the analysis script, carried out the experiments and data analysis, generated the figures, and wrote the manuscript; T.F.B. wrote the initial version of the analysis script under my direction; and G.R.H conceived and directed the project.

### 3.1 Summary

Despite considerable research interest in developing piezoelectric materials, little work has focused on the fundamental design of these materials from the ground up. Herein, we present a general, versatile method for producing tunable, flexible piezoelectric energy harvesters



(PEHs) with excellent piezoelectric response. Using a poly(dimethylsiloxane) (PDMS) foam derived from a sugar template, we separate the electrical and mechanical properties of the PEH, thereby allowing us to optimize them separately. The electrical properties were tuned by varying the poling field, the polar dopant, and the dopant concentration. The mechanical properties were tuned by varying foam preparation and thus the compressive modulus. Through the careful tuning of these properties, we are able to achieve a maximum piezoelectric response of 153 pC/N—considerably higher than most other reported flexible PEHs. Combined with our previous work, we demonstrate that doping polymer foams with polar dopants is a highly general strategy and has the potential to lead to materials with considerably higher piezoelectric responses.

### 3.2 Introduction

Piezoelectric energy harvesters (PEHs) have the potential to self-power a growing class of small, low-power electronic devices such as remote or wearable sensors or Internet of Things devices.<sup>84</sup> Based on the direct piezoelectric effect, these devices have the ability to generate electricity scavenged from the environment or the human body to power devices indefinitely and to eliminate the environmental and labor costs of battery replacements.<sup>51,85</sup> The vast majority of piezoelectric materials are hard ceramics (Young’s modulus,  $E_Y > 100$  GPa)<sup>86,87</sup> such as lead zirconium titanate (PZT).<sup>21,88</sup> As such, these hard, brittle materials are only able to withstand a very limited range of deformations, limiting their application in many situations.<sup>21,42,44</sup> Most current polymer piezoelectric materials, such as poly(vinylidene fluoride) (PVDF) ( $d_{33}$  of 20–30 pC/N), have a piezoelectric response an order of magnitude or more below that of PZT ( $> 200$  pC/N).<sup>21</sup> Consequently, there is a need for intrinsically flexible materials with high electromechanical response.

A variety of approaches towards new flexible piezoelectric materials have been developed, including peptide nanotubes,<sup>89</sup> sponge-like ceramic-polymer composites,<sup>90</sup> quantum dot-polymer composites,<sup>91</sup> nanoparticle-polymer composites,<sup>92</sup> and sugar-nanofiber composites.<sup>93</sup> Despite long being an area of considerable research interest, few attempts have been made at the rational design of these materials from the ground up to maximize their piezoelectric response and efficiency. A key figure of merit is the  $d$  piezoelectric tensor, as well as the electromechanical coupling factor,  $k$ , which is a quantitative measure of the efficiency of piezoelectric materials at interconverting electrical and mechanical energy.<sup>62</sup> The general coupling efficiency of a piezoelectric material is<sup>32,63</sup>

$$k = d\sqrt{\frac{E_Y}{\epsilon}} \quad (3.1)$$

where  $k$  is the coupling efficiency,  $d$  is the piezoelectric coefficient,  $E_Y$  is the Young's modulus, and  $\epsilon$  is the relative permittivity. Since perfect efficiency cannot be reached, it follows that:<sup>32</sup>

$$d < \sqrt{\frac{\epsilon}{E_Y}} \quad (3.2)$$

As the relative permittivity is directly related to the dipole moment,<sup>2</sup> this relation shows that, if the material polarization is generated separately from the matrix, each property can be separately tuned for desired parameters. The bulk dipole moment can be tuned by incorporating different polar dopants and by the degree of polar alignment. The Young's modulus is a measure of the stiffness of a material along the axis of deformation and can be tuned by changing the properties of the matrix. It is known that lowering the modulus of a material increases its piezoelectric response, but, by separating the two factors, this can be more fully exploited.<sup>32,64</sup>

In this study, building on our previously published work,<sup>32</sup> we present a highly tunable, flexible PEH that demonstrates the effect of both the bulk dipole moment and the modulus on piezoelectric response. While the maximum piezoelectric response we report here is somewhat

lower than our previous work, we have vastly improved the consistency and tailorability of our system, while simultaneously showing that our method is broadly applicable and not derived from matrix specific effects. By doping poly(dimethylsiloxane) (PDMS) foam with varying amounts of highly polar small organic molecules and electrically poling at a range of voltages, we are able to control the bulk polarization of our PEH; similarly, by varying the curing temperature of our PDMS matrix, we are able to tune the modulus of our PEH. Our results demonstrate that each method can modulate the overall piezoelectric response as expected.

### 3.3 Experimental Methods

#### 3.3.1 Materials

2-Chloro-4-nitroaniline (>98 %) (CNA) and 4-nitro-1,2-phenylenediamine (>97.0 %) were obtained from TCI. 2-Methyl-4-nitroaniline (99 %) (MNA) and 3-aminobenzoic acid (99+%) were obtained from Acros Organics. *N,N*-Dimethyl-4-nitroaniline (>98 %), 4-nitroacetanilide (98 %), and acetanilide (98 %) were obtained from Alfa Aesar. Benzoic acid (99.5 %) was obtained from J.T. Baker. Acetonitrile ( $\geq 99.9$  %) and 1,4-dibromobenzene (98 %) were obtained from Sigma-Aldrich. Sodium chloride (certified ACS, crystalline) was obtained from Fisher Chemical. Sylgard 184 silicone elastomer system (polydimethylsiloxane; PDMS) was obtained from Dow Corning. Granulated sugar was obtained from Domino Foods. All chemicals were used as received. Ultrapure water (18.2 M $\Omega$  cm) was generated using a Millipore Synergy system.

### 3.3.2 PDMS Foam Preparation

PDMS foams were produced from a sugar template using a procedure adapted from the literature.<sup>9</sup> To prepare the sugar template, 5.2 g of white granulated sugar was mixed with 300  $\mu$ L of ultrapure water and pressed into a 30 mm diameter, 6 mm high mold using medium-firm pressure; excess sugar was scraped off the top to leave a level surface. After several hours, the sugar template was removed from the mold and allowed to continue drying for a total of at least 24 h. PDMS was prepared according to the manufacturer’s directions by mixing 10 g elastomer base with 1 g curing agent. After mixing, the PDMS mixture was added to a 9 cm diameter Petri dish containing four sugar templates. The Petri dish was placed under vacuum (40 kPa) for a total of 5 h. After 4 h, the vacuum oven was switched on, and, over the course of the last hour, the samples were heated to 80 °C. After heating, the samples were removed from the vacuum oven. The sugar was then removed by washing with ultrapure water under ultrasonication. Excess water was squeezed from the polymer foams, and the samples were placed in a 130 °C oven for 1 h to dry. They were then removed from the Petri dish, and a 20 mm diameter circular punch was taken from each sample. The average size of the sugar granules used to produce the template was approximately 0.3 mm; therefore, we expect the template to produce open-cell foams with a similar pore size. Sugar granule size was measured from optical microscopy images taken on an Olympus BH2 microscope and analyzed with the ImageJ software package (Version 1.48k).

To vary the modulus of the foams, a similar procedure was followed by substituting sodium chloride templates, while varying the curing temperature. For the template, 5.3 g of sodium chloride was mixed with 250  $\mu$ L of ultrapure water. Freshly mixed PDMS was added, and the samples were placed in a vacuum desiccator for 4 h. They were then removed from the desiccator and either left on the bench top at room temperature for 48 h or placed

in a 100 °C or 200 °C oven for 1 h; this produced three different sets—each with a different modulus. After curing and washing, excess water was squeezed from the foams, and they were placed in a vacuum desiccator to dry.

### 3.3.3 Device Preparation and Electrical Poling

In the second step of the process, dopant molecules were dissolved in acetonitrile. Foam samples were placed on the poling slides (described below), and 1 mL of the dopant solution was added to the foam sponge using a micropipet (e.g. 0.3 M CNA samples had 1 mL of 0.3 M CNA/acetonitrile solution added to them). All solvent evaporated from the foams within 2 h leaving the dopant coating the pores of the PDMS foam (Figure A.1). Samples were then electrically poled for 48 h; shorter poling times led to inconsistent results whereas longer poling times (up to longest tested of 5 d) were consistent with poling for 48 h. All samples were 20 mm diameter, 6 mm thick circular disks.

For poling, samples were placed between two 5 cm  $\times$  5 cm custom designed and manufactured printed circuit boards (PCBs) (Where Labs/DirtyPCBs.com) with 3.5 cm  $\times$  3.5 cm electroless nickel immersion gold (ENIG) finished copper pads; polyimide tape was applied to the PCBs for protection. Samples were poled under a DC potential of 0 kV–5 kV. During poling, the PCBs had a fixed spacing of 6 mm. The poling slides were held in place using screws and wing-nuts, and separation was maintained through the use of aluminum spacers.

### 3.3.4 Device Testing and Characterization

After poling was completed, the samples were tested in a quasi-static manner, and the piezoelectric response was calculated. For testing, samples were placed between two PCBs identical to those used for poling; polyimide tape was not used as it was found to produce erroneous electrostatic signals. The sandwich was then positioned in a testing apparatus

consisting of a threaded rod controlled by a stepper motor. A force sensor (Tekscan FlexiForce A201), with a PDMS spacer on top, rested above the sample sandwich and below the rod. A slight preload pressure ( $\approx 0.3$  N) was applied using the threaded rod to minimize triboelectric charge generation; higher preload forces were seen to reduce the piezoelectric response. Using the apparatus, compressions of varying force (up to 10 N) were applied along the Z-axis every few seconds; the rate of compression was held constant at approximately 1.7 mm/s. Force and current measurements were recorded for 70 s using either a Keithley 2612 SourceMeter or a Keithley 2614B SourceMeter; results were consistent between instruments. To ensure accuracy, the system was tested on commercial ceramic samples of PZT-4 (Steiner & Martins SM121) and barium titanate (Steiner & Martins SM511); the measured piezoelectric responses of  $316 \pm 13$  pC/N for PZT-4 and  $134 \pm 5$  pC/N for barium titanate agree favorably with the manufacturer’s specifications of 300 pC/N and 140 pC/N, respectively. A preload force of 10 N was used when testing the ceramics.

The collected data are simply the applied force and measured current—both as a function of time. To calculate the piezoelectric coefficient ( $d_{33}$ ), force versus charge was plotted for each compression, and the slope of the linear best fit was calculated. A custom Python script was used to compute charge by integrating the current peaks over time. The script identifies force peaks and subtracts off any baseline force; it then looks for the corresponding current peak and integrates it to calculate the corresponding charge during the period of increasing applied force.

Compression testing was performed using an Anton Paar MCR 302 rheometer. Applied force was increased from 0.2 N to 12.0 N over the course of 350 s. As no linear region was observed for the sugar templated samples, the modulus was approximated by taking the secant of the stress–strain curve for strains corresponding to 0.2 N–10.0 N of applied force.<sup>94</sup> For the sodium chloride templated samples, the slope of the linear region of the stress–strain curve was used. Masses were measured using a Denver Instrument SI-234 Summit Series analytical balance.

### 3.4 Results and Discussion

PDMS foams were produced from a sugar mold; doped with a solution of a polar, small organic molecule in acetonitrile; and electrically poled. This new system has several key advantages over our previously published polyurethane system: improved consistency and increased tailorability.<sup>32</sup> The use of a sugar template allows for much more consistent foams to be produced; the foams have a more uniform pore size, density, and, thus, compressive modulus. As the polyurethane system was limited to dopants that could be dissolved in the polyol, the use of acetonitrile (or numerous other organic solvents) allows for a much wider array of dopants and dopant concentrations to be used. While we find a somewhat lower maximum piezoelectric response than in our previous report, this is likely due, in part, to the switch from flexible copper tape electrodes to smooth, rigid PCBs; wrinkles in the tape could amplify the response but lead to more inconsistent data. Additionally, in the present work, dopants are only able to coat the voids in the PDMS whereas they were more fully incorporated into the polyurethane. The PCBs, combined with smooth, consistent compressions driven by a stepper motor, have allowed us to greatly reduce error and produce smooth, tight charge–force curves from which to determine the piezoelectric response. Future applications could use flexible electrodes to obtain higher electrical response.

Figure 3.1A illustrates a schematic diagram of the testing procedure. As the foam is compressed by the stepper motor, the dipole concentration in the foam increases, causing charge to build up on either side and current to flow. The resulting force and current is measured simultaneously (Figure 3.1B); for each force peak, the corresponding current is integrated to compute the resultant charge. Note that the peak current remains constant with varying force since the rate of compression is intentionally held constant. Charge is plotted as a function of force (Figure 3.1C); the slope of the linear fit is the piezoelectric response,  $d_{33}$ . The results presented here are calculated from applied forces of up to 4 N, as this was the most linear region of the charge–force curve; an analysis using applied forces of

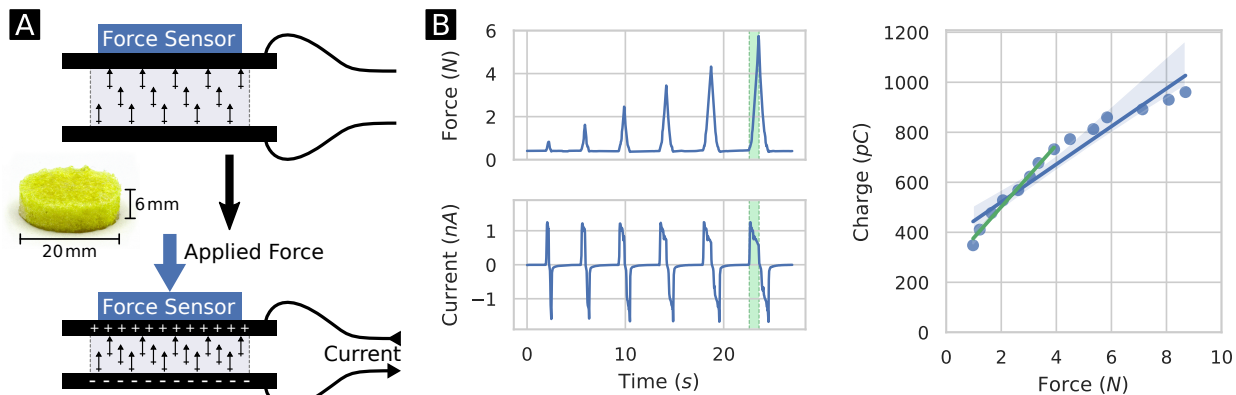


Figure 3.1: General overview of devices and measurements. (A) Schematic diagram showing an applied force compressing the sample, increasing the dipole concentration, and leading to the buildup of charge and subsequent flow of current. Photograph of a representative foam with dimensions labeled (inset). (B) Simultaneous measurement of force and current over time. The green shading represents the time over which the current is integrated to calculate charge. (C) Charge–force plot of a 0.2 M CNA doped sample poled at 800 V/mm. Primary analysis uses forces up to 4 N (green line).

up to 10 N can be found in Appendix A.1. At higher forces (above 5 N–6 N), the resultant charges increased sublinearly—likely due to the elastic properties of the foams. When higher forces are included in the analysis, the piezoelectric response is smaller, but the same trends are observed as discussed below (Figures A.2 and A.3). While other electrostatic effects may also be present, the linear/sublinear charge-force curve demonstrates that the measured response is primarily piezoelectric.

In Figure 3.2A, the piezoelectric response is plotted as a function of the concentration of the added CNA dopant solution over a variety of poling fields while in Figure 3.2B, a subset of the data is presented showing the piezoelectric response as a function of the poling field. The response was tuned by varying the concentration of the added CNA dopant solution and by varying the poling voltage; it should be noted that the solvent evaporates early in the poling process leaving the dopant coating the foam’s pores. For lower poling voltages ( $\leq 400$  V/mm), the piezoelectric response increased slightly (average piezoelectric response increase of 20 % per 0.1 M increase in dopant solution concentration) with increased



dopant solution concentration. For higher poling voltages ( $\geq 600$  V/mm), the piezoelectric response peaked at a dopant solution concentration of 0.1 M–0.2 M before decreasing with higher concentrations; on average, the piezoelectric response of these samples increased by 34 % per 200 V/mm increase in poling field. A maximum piezoelectric response of 153 pC/N was observed for 0.1 M CNA doped samples poled at 800 V/mm. The observed piezoelectric response increases with increased poling field as the molecular dipole moments become more aligned (Figure 3.2B). We were not able to test poling fields above 800 V/mm due to power supply limitations, but the piezoelectric response will increase until dielectric breakdown is reached or full polar alignment is achieved. The dielectric strength of PDMS is 19 kV/mm, but we expect the dielectric strength of our foams to be lower due to air present in the voids.<sup>95</sup> The piezoelectric response does not always increase with increased dopant concentration, possibly due to interactions between the dopant and the PDMS matrix to which it adheres. PDMS is known to have an innate electrical response, although the mechanism behind it has been debated.<sup>96–98</sup>

As shown in Figure 3.3, the piezoelectric response varies as a function of dopant molecule dipole moment; the structures, names, and dipole moments of the dopants used are also given. The bulk piezoelectric response does not correlate directly with the dipole moment, but seems to initially increase before plateauing for dopants with dipoles above 4 D; on average, the piezoelectric response for dopants with dipole moments above 4 D is 12 % higher than those with smaller dipole moments and 75 % higher than undoped foams. These data additionally demonstrate that the response cannot be attributed to the presence of piezoelectric crystals, since benzoic acid, 3-aminobenzoic acid, acetanilide, and 4'-nitroacetanilide form centrosymmetric crystals whereas the other dopants used do not;<sup>99–103</sup> no trend is seen between the two categories of crystals. While we expected piezoelectric response to increase linearly with increased dopant dipole moment, interactions between the dopant and the PDMS matrix likely increasingly hinder full alignment of larger dipoles.

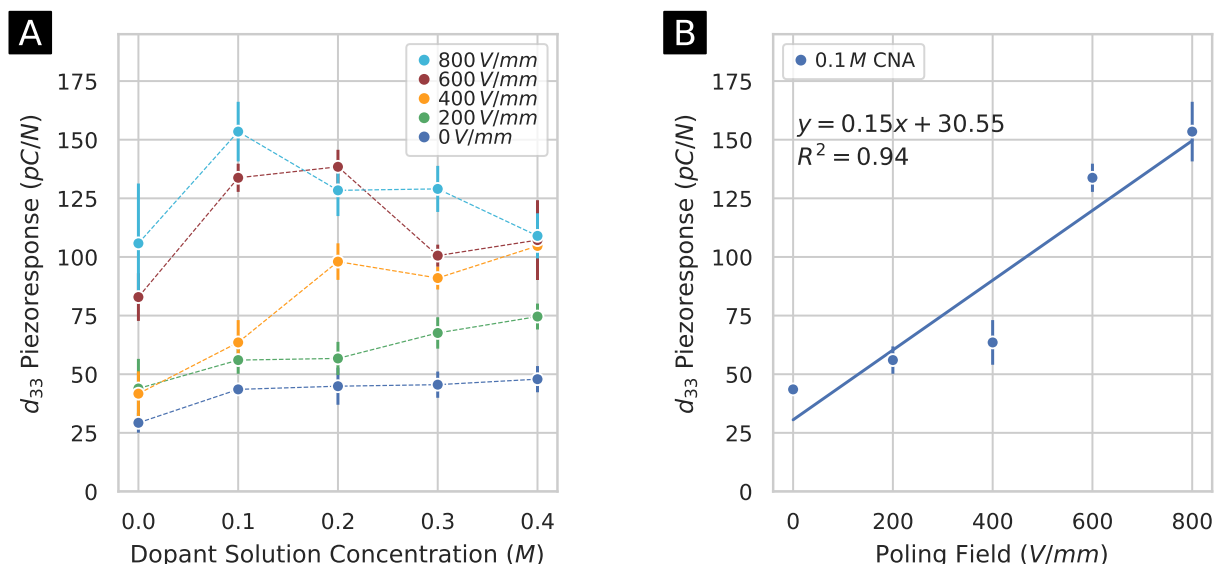


Figure 3.2: Effect of dopant concentration and poling field on piezoelectric response. (A) The piezoelectric response as a function of added CNA dopant solution concentration over an array of poling fields. (B) The 0.1 M CNA dopant solution subset showing the piezoelectric response increasing as a function of poling field. Error bars represent standard error across at least four samples.

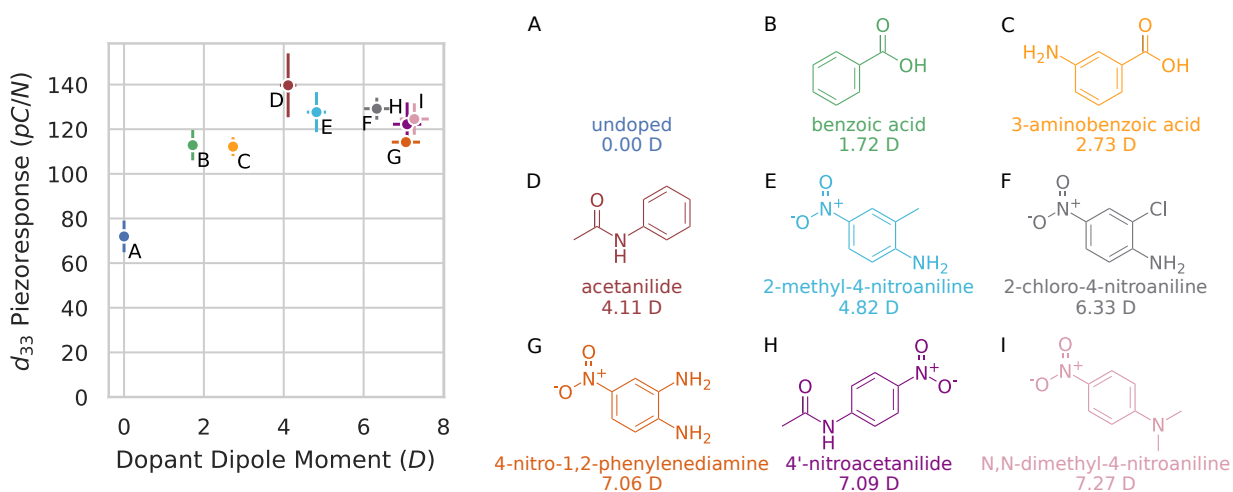


Figure 3.3: Effect of dopant on piezoelectric response. (A–I) Piezoelectric response as a function of dopant dipole moment for samples poled at 600 V/mm after being doped with a 0.1 M solution. Dipole moments are experimental values in dioxane taken from the literature.<sup>104–107</sup> X-axis error bars are 5%; Y-axis error bars represent standard error across at least four samples.

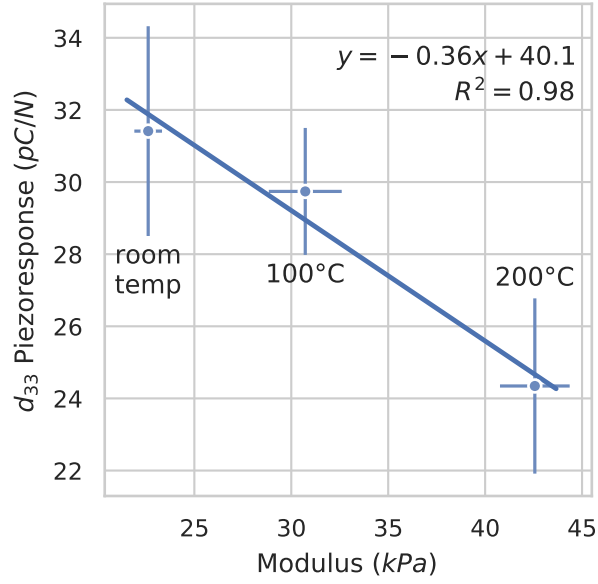


Figure 3.4: Effect of modulus on piezoelectric response. Piezoelectric response as a function of compressive modulus for sodium chloride templated foams doped with 0.1 M CNA and poled at 800 V/mm. Foams were cured at room temperature, 100 °C, and 200 °C (as labeled). Error bars represent standard error; modulus was measured for a subset of four samples in each set.

The compressive modulus of the PDMS foams is  $9.24 \pm 0.14$  kPa; the secant of the stress-strain curves (for strains corresponding to applied forces up to 10 N) was used as no linear region was observed (Figure A.1). As a result, the modulus for lesser forces is lower than the reported value. In order to evaluate the effect of modulus on piezoelectric response, the modulus of the foam needed to be varied without altering its structure. To accomplish this, the PDMS was cured at several temperatures (room temperature, 100 °C, and 200 °C);<sup>108</sup> a switch to a sodium chloride mold was necessary to accommodate the needed temperature range. These data are not directly comparable to the rest of this work as the foam structure is different; as these foams exhibit a linear stress-strain curve, the modulus can be determined by the slope of the linear region (Figure A.5). Figure 3.4 displays the piezoelectric response as a function of modulus. Increasing the foam modulus lead to a decrease in the resultant piezoelectric response, as expected (see Equation 2 and our previous work<sup>32</sup>).

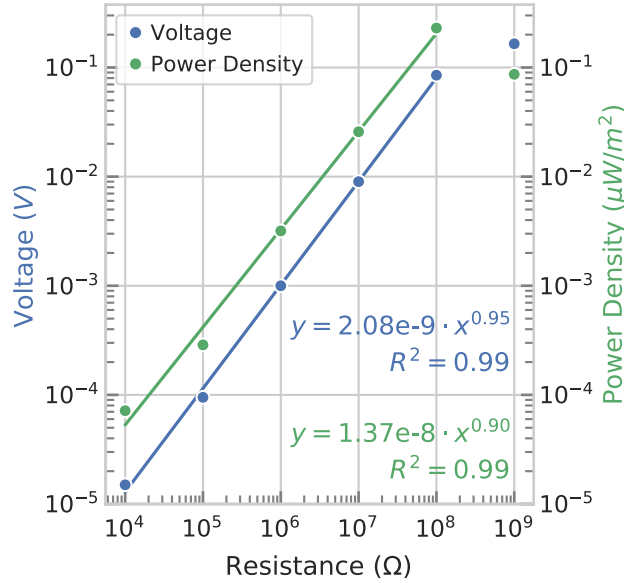


Figure 3.5: Voltage drop over various resistances and the resulting generated power density for a 0.1 M CNA doped sample poled at 800 V/mm. Note the log scales.

Several additional properties of the PDMS foams were studied. In Figure 3.5, the voltage drop and resulting generated power density are plotted as a function of resistance. The voltage and power density increase logarithmically until a peak voltage of 85 mV and power density of 0.23  $\mu\text{W}/\text{m}^2$ —both corresponding to a resistance of 100 M $\Omega$ . The stability of the piezoelectric response is poor as it decayed back to baseline after just two days (Figure A.6); repoling samples boosted their piezoelectric response back to near initial levels. The piezoelectric response appears to decay in a double exponential fashion, but the decay kinetics are beyond the scope of this study. The decay in piezoelectric response is likely due to thermal randomizations as repoling restores the electrical response while mechanical properties remain constant; this decay is expected because the PDMS matrix has been fully cured prior to poling and the dopant is only dispersively adhered to the matrix surface—there is nothing to lock the dipoles in place. A key challenge for future work is to improve the stability of the piezoelectric response and to incorporate higher concentrations of dopant molecules into the polymer matrix itself—instead of just coating the foam voids.

### 3.5 Conclusions

We have demonstrated that the piezoelectric response of our PDMS foam PEH can be successfully tuned through changes to both its relative permittivity and its compressive modulus. By changing the poling field, the dopant (and its dipole moment), or the dopant concentration, we are able to vary the electrical properties of our PEH and optimize its piezoelectric response. We are similarly able to optimize the piezoelectric response by changing the mechanical properties through variations in the foam’s compressive modulus. While the ideal dopant concentration varied by poling field, increasing the poling field generally produced the largest piezoelectric response. Our maximum measured piezoelectric response, a remarkable 153 pC/N, was from a foam doped with 0.1 M CNA and poled under an electric field of 800 V/mm. Mechanically, softer foams produced the highest piezoelectric response. Combined with our previous work with polyurethane foams, we have presented a highly tunable system that is general to a wide range of polymer matrices and polar dopants. Going forward, we aim to further improve the piezoelectric response of our materials and their stability by incorporating polar molecules directly into the polymer matrix through covalent attachment.

### 3.6 Acknowledgement

I thank Julia Cuthbert for assistance with taking compression measurements and Tomasz Kowalewski for use of the rheometer. Software used in this chapter includes, in part, Matplotlib,<sup>109</sup> NumPy,<sup>110</sup> pandas,<sup>111</sup> pySerial, SciPy,<sup>112</sup> and Python-VXI11.

## 4.0 Intrinsically Polar Piezoelectric Self-Assembled Oligopeptide Monolayers

This chapter is adapted from:

Petroff, C. A.; Cassone, G.; Šponer, J.; Hutchison, G. R. Intrinsically Polar Piezoelectric Self-Assembled Oligopeptide Monolayers. *ChemRxiv:13151069.v1* **2021**. DOI: 10.26434/chemrxiv.13151069.v1

which is also published as:

Petroff, C. A.; Cassone, G.; Šponer, J.; Hutchison, G. R. Intrinsically Polar Piezoelectric Self-Assembled Oligopeptide Monolayers. *Adv. Mater.* **2021**, 2007486. DOI: 10.1002/adma.202007486.

It is a collaborative effort in which I designed the testing system, carried out the experiments and data analysis, generated a majority of the figures, and wrote the bulk of the manuscript; G.C. and J.Š. designed the *ab initio* molecular dynamics simulations; G.C. executed the *ab initio* molecular dynamics simulations; and G.R.H. conceived and directed the project.

### 4.1 Summary

Flexible, bio-compatible piezoelectric materials are of considerable research interest for a variety of applications, but many suffer from low response or high cost to manufacture. Herein, novel piezoelectric force and touch sensors based on self-assembled monolayers of oligopeptides are presented which produce large piezoelectric voltage response and are easily manufactured without the need for electrical poling. While the devices generate modest piezoelectric charge

constants ( $d_{33}$ ) of up to 9.8 pC/N, they exhibit immense piezoelectric voltage constants ( $g_{33}$ ) up to 2 Vm/N. Furthermore, a flexible device prototype is demonstrated that produces open-circuit voltages of nearly 6 V under gentle bending motion. Improvements in peptide selection and device construction promise to further improve the already outstanding voltage response and open the door to numerous practical applications.

## 4.2 Introduction

Piezoelectric materials find use in a wide range of applications from touch and vibration sensors<sup>58</sup> to energy harvesters<sup>113</sup> to micromechanical actuators.<sup>114</sup> These devices rely on the piezoelectric effect to interconvert mechanical stress and electrical charge. In the direct piezoelectric effect, an applied force produces a resultant charge, whereas, in the converse effect, an applied voltage causes a mechanical deformation. Most existing piezoelectric materials are hard, brittle, lead-containing ceramics such as lead zirconium titanate (PZT).<sup>115</sup> As such, these materials have limited ranges of motion, are liable to crack, and are not bio-compatible. While there is a large research focus on developing flexible, bio-compatible piezoelectric materials,<sup>38</sup> much of this work has involved placing traditional piezoelectrics on or into flexible substrates, often sacrificing electrical performance for added flexibility and ease of manufacturing (i.e.,  $d$ -values <200 pC/N instead of 500 pC/N–600 pC/N for PZT).<sup>51,113,116</sup> In addition to well known piezoelectric polymers such as semi-crystalline poly(vinylidene fluoride) (PVDF), researchers have begun to develop fundamentally new piezoelectric materials such as helicenes, amino acids, viruses, and peptides.<sup>37,38,50,89,117,118</sup>

While the most commonly reported piezoelectric constant is the piezoelectric charge constant,  $d$ , the piezoelectric voltage constant,  $g$ , is perhaps more meaningful for sensing applications, since large voltages can be easily and accurately detected.<sup>30,37,58,59,119</sup> Despite its importance, there are few examples of the voltage constant reported in the literature,

making device comparisons difficult (see Guerin et al.<sup>30</sup> and Chen et al.<sup>120</sup> as examples). When both polarization and stress are along the Z-axis, the subscript 33 is used (i.e.,  $d_{33}$  and  $g_{33}$ ). The piezoelectric charge and voltage constants are related by the relative permittivity such that  $g_{33} = \frac{d_{33}}{\varepsilon_r \varepsilon_0}$ , where  $\varepsilon_r$  is the relative permittivity of the material and  $\varepsilon_0$  is the vacuum permittivity.<sup>25</sup> As such, low dielectric constant organics have the potential to produce high-response piezoelectric sensors.<sup>30</sup> The piezoelectric voltage constant is often calculated from the piezoelectric charge constant, or it can be measured directly from applied stress and resulting electric field. Direct measurements—while lacking in the literature—are perhaps more meaningful for low-frequency sensing applications such as from human touch, as conversions are often calculated using the relative permittivity for a higher frequency, which may or may not translate to real-world use at lower frequencies. The relative permittivity of many piezoelectric polymer composites is shown to increase at lower frequencies,<sup>121–123</sup> which would lead to a decreased piezoelectric voltage constant at those frequencies.

Piezoelectricity occurs naturally in the body and plays an important role in processes such as bone growth.<sup>38</sup> This phenomenon has allowed for the production of piezoelectric nanogenerators made from tissue harvested from both plants<sup>124,125</sup> and animals.<sup>126,127</sup> While it has been demonstrated that amino acids and peptides are piezo-active,<sup>38</sup> significant challenges exist in applying them to usable devices, including aligning the materials or crystals to produce a bulk piezoelectric response by means of an external high-voltage electric field.<sup>38</sup>

### 4.3 Promise of Piezoelectric Self-Assembled Monolayers

We find self-assembled monolayers (SAMs) to be a promising approach to bulk alignment of piezoelectric molecules<sup>82,128</sup> and thus present piezoelectric SAM (PSAM) devices based on self-assembled oligopeptide monolayers. SAMs have been widely studied, and thiol-containing



molecules are known to form uniform, stable monolayers on gold substrates.<sup>129</sup> Self-assembled piezoelectric devices present significant advantages over more traditional approaches as they are intrinsically polar and can be easily produced through solution processing.

SAMs of thiol-containing oligopeptides, ranging in length from seven to thirteen amino acids were formed from solution on the gold-coated surface of printed circuit boards (PCBs). The peptide sequences, shown in Figure 4.1(A), consist of cysteine (C) and six, nine, or twelve alanines (A); both carboxylate-terminated and amide-terminated forms were studied for most sequences. These sequences were chosen as they are short, helical, thiol-containing oligopeptides that are similar except for their varying lengths and end groups. As illustrated in Figure 4.1(B), assemblies of a peptide functionalized PCB facing a polyurethane (PU) coated PCB (with optional 1-dodecanethiol (DDT) coating) were tested in a quasi-static manner using an automated system. Piezoelectric constants were subsequently calculated from these data. Moreover, state-of-the-art *ab initio* molecular dynamics (AIMD) simulations were carried out in order to help interpret, on a microscopic basis, some of the experimental results.

## 4.4 Piezoelectric Charge Constant

The peptides used are helical and should act as “molecular springs”<sup>128,130,131</sup> when compressed, leading to much greater length changes than similar linear molecules such as the DDT used as a control. As the length of each peptide changes, so too does its dipole; therefore, when a force is applied to compress these “springs,” charge builds up on the surface, leading to a measurable piezoelectric response.<sup>128,130,131</sup> The piezoelectric charge constant ( $d_{33}$ ) is calculated by integrating the measured current and plotting the resultant charge versus the applied force (Figure B.1); since there is no convention for defining the positive  $Z$ -axis in our self-assembled, non-crystalline materials, we used the absolute value of charge. Figure 4.2(A)

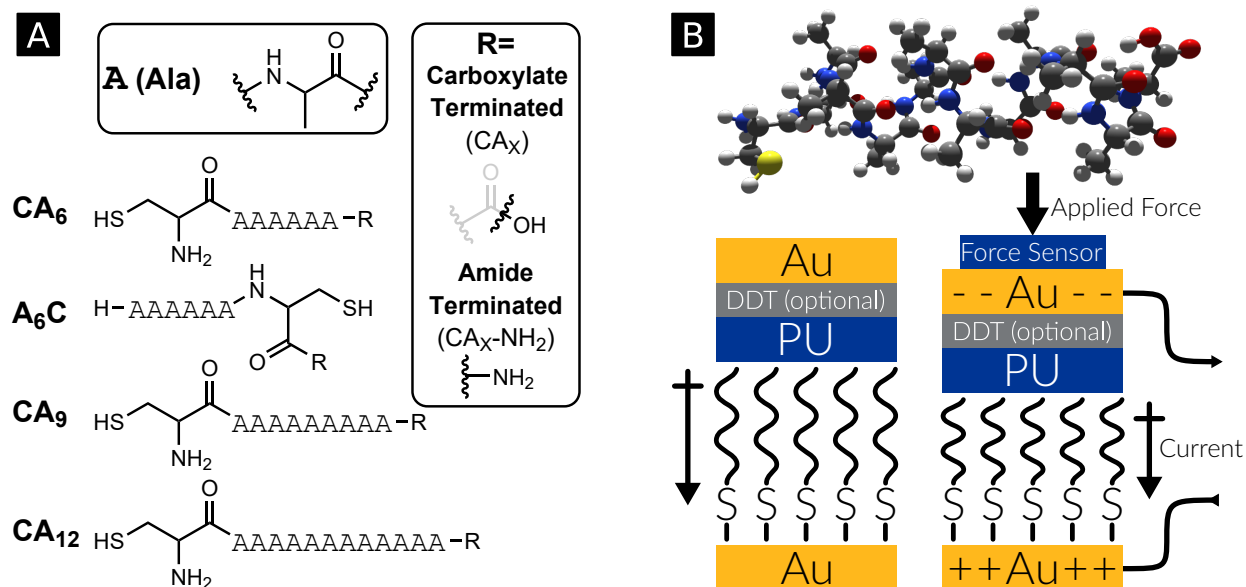


Figure 4.1: Generalized scheme outlining PSAM devices studied. (A) Chemical structures of peptides used. (B) 3D structure of  $\alpha$ -helical peptide CA<sub>12</sub> (top). Schematic diagram showing an applied force compressing a PSAM device, changing the dipole moment, and leading to the buildup of charge and subsequent flow of current (bottom).

and (B) presents a summary of  $d_{33}$  values obtained for our PSAM devices. Computed  $d_{33}$  values for peptide assemblies are consistently higher than those of the alkanethiol controls (Figure B.3). A small piezoelectric response is expected for DDT because SAMs contain an interface and are, therefore, inherently piezoelectric.<sup>132</sup> A maximum value of  $(9.8 \pm 1.5)$  pC/N is obtained for the assembly consisting of amide-terminated CA<sub>6</sub> functionalized PCBs opposing PU coated DDT functionalized PCBs (CA<sub>6</sub>-NH<sub>2</sub>/DDT-PU). On average, peak current values of 80 pA–100 pA were observed at the maximum applied force of  $\sim 6$  N. On average, the PSAM device assemblies had a resistance of  $(56.9 \pm 1.8)$  M $\Omega$  and a capacitance (measured at  $\sim 0.7$  MHz) of  $(428 \pm 14)$  pF; the only observed trend is that, generally, the capacitance slightly increased with increased chain length.

We experimentally examined several variations of our PSAM devices and used analysis of variance (ANOVA) to look and see how and if these changes affect the piezoelectric response in a statistically significant fashion (see Tables B.1–B.12). Firstly, we varied the PCB opposing

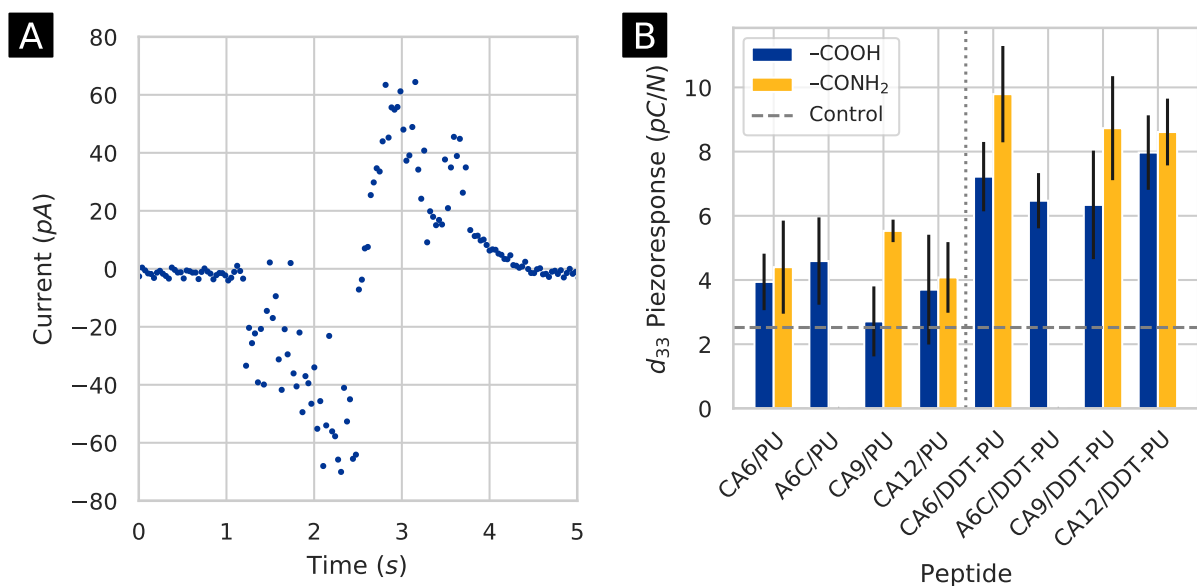


Figure 4.2: Piezoelectric charge constant response. (A) Representative short-circuit current measurement for one compression of a PSAM device. (B) The piezoelectric charge constants ( $d_{33}$ ) of PSAM devices containing PU coated DDT PCBs are greater than those containing PU coated unfunctionalized PCBs. Amide-terminated peptides present higher responses than carboxylate-terminated ones. Peptide responses are greater than those of DDT controls (dashed line; see Figure B.3).

the peptide PCB in the device. These PCBs were coated in PU, and we looked at both unfunctionalized and DDT functionalized versions. With nearly double the response, peptides tested against PCBs where the PU layer coats a DDT monolayer (average  $d_{33}$  of 7.9 pC/N) produced statistically higher responses than peptides tested against PCBs where the PU layer coats bare gold (average  $d_{33}$  of 4.1 pC/N). While this difference in piezoelectric response is somewhat unexpected, we theorize the DDT may affect the organization and properties of the PU layer, thereby altering the piezoelectric responses of the devices.

Next, we analyzed the difference in piezoelectric response between carboxylate-terminated and amide-terminated peptides. The amide-terminated peptides appear to produce (P-value  $<0.05$ ) statistically greater piezoelectric responses than carboxylate-terminated peptides do; this is counter intuitive at first, as the amide-terminated form should have a smaller dipole moment, but the amide-termination may also affect the tilt angle of the SAM or the stability and rigidity of the  $\alpha$ -helix. If the amide causes the SAM to stand more perpendicular to the surface, this can counteract the effect of a smaller dipole by increasing the effective dipole in the  $Z$ -direction. Additionally, if the  $\alpha$ -helices of the amide-terminated peptides are less rigid, they will deform more easily under compression, leading to a greater change in dipole and, therefore, greater piezoelectric response.

Finally, we looked at varying the peptide sequence to alter its length; we tested CA<sub>6</sub>, A<sub>6</sub>C, CA<sub>9</sub>, and CA<sub>12</sub> sequences. Somewhat surprisingly, the length of the peptide did not statistically alter the measured response despite the length-dictated dipole differences. Several explanations exist for the analogous values: they are similar because the longer peptides may not stand as straight on the surface, leading to a lower response in the  $Z$ -direction; the SAMs of the longer peptides may pack less densely, leading to lower response per unit area; and/or the responses are dominated by the hydrogen bonding of the  $\alpha$ -helices of the peptide backbone, which may be invariant of the peptide length. Indeed, previous computational work in our group on similar peptides showed no clear length effect on piezoelectric response.<sup>133</sup>

We turned to AIMD simulations to help explain our experimental results. We examined the carboxylate-terminated CA<sub>6</sub> sequence and the corresponding amide-terminated CA<sub>6</sub>-NH<sub>2</sub> sequence. The modeling shows that the piezoelectric responses of our peptides are largely dependent on the strength of the hydrogen bonds in the  $\alpha$ -helices of the peptide backbones. The backbone of the carboxylate-terminated peptides was found to be more stable and rigid than its amide-terminated counterpart. Furthermore, higher applied electric fields were needed before the carboxylate-terminated peptide deformed. These data agree favorably with our experimental results, which show that the amide-terminated peptides produce higher response than the carboxylate-terminated peptides and suggest that the length of the peptide plays a relatively minor role in the overall piezoelectric response. For a more detailed, quantitative discussion of the AIMD results, see the Supplementary Note (Appendix B.3) and Figures B.8–B.11.

## 4.5 Piezoelectric Voltage Constant

Our PSAM devices show great potential as piezoelectric sensors as demonstrated by their high piezoelectric voltage constants ( $g_{33}$ ). These voltage constants are calculated by plotting induced electric field (measured voltage divided by sample thickness) against external stress (applied force divided by sample area) and determining the linear fit (Figure B.2). As shown in Figure 4.3(A) and (B),  $g_{33}$  values up to  $(750 \pm 150)$  mVm/N were obtained; for comparison, this is an order of magnitude greater than the  $g_{33}$  value of  $<40$  mVm/N for PZT<sup>134,135</sup> and is also greater than the predicted  $g_{33}$  value of  $\sim 480$  mVm/N for a racemic alanine crystal.<sup>37</sup> As expected, the measured  $g_{33}$  values are greater than those obtained for alkanethiol controls (Figure B.4). While the oft reported peak voltage produced by piezoelectric devices is important for showing their potential practical use, the voltage value is affected by many factors including the device area and thickness as well as the force applied, making it difficult

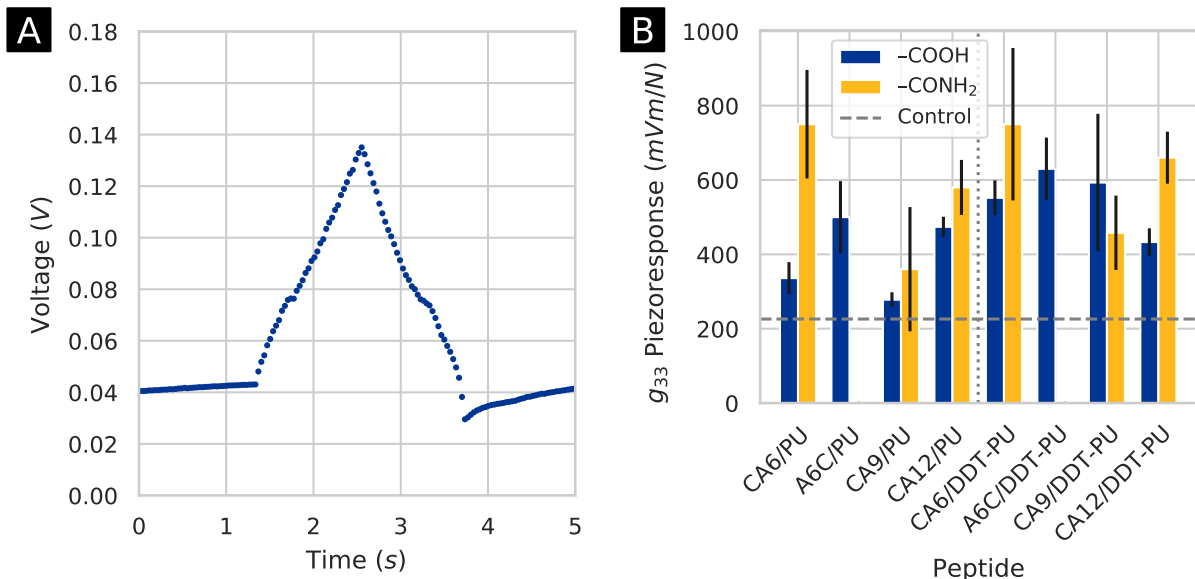


Figure 4.3: Piezoelectric voltage constant response. (A) Representative open-circuit voltage measurement for one compression of a PSAM device. Note that the baseline has been corrected. (B) The piezoelectric voltage constants ( $g_{33}$ ) of PSAM devices. Peptide responses are greater than those of DDT controls (dashed line; see Figure B.4). Error bars represent standard error across multiple samples.

to compare devices reported in the literature. For example, we saw, on average, a peak voltage of  $\sim 0.2$  V at the maximum applied force of 6 N, but if we had only applied 3 N of force, the maximum voltage would have been merely  $\sim 0.1$  V. In contrast, the piezoelectric voltage constant ( $g$ )—the voltage analog of the ubiquitous piezoelectric charge constant ( $d$ )—allows for meaningful comparisons of sensing potential but is, unfortunately, largely absent from the literature.

While we initially planned to examine the voltage response of our PSAM devices analogously to our approach for the charge response, the results are more varied and less conclusive. Although the same trends—greater DDT-PU response, greater amide-termination response, and no length effect—are present, they are not statistically significant. To help explain this incongruity, we examined the difference in response between individual PU and DDT-PU PCBs. While the different PCBs within each category were statistically similar for values

of the piezoelectric charge constant, the piezoelectric voltage constant values obtained for individual DDT-PU PCBs were statistically different. This lack of uniformity is likely because capacitive and leakage effects hold a greater role in the voltage measurements and quite possibly vary PCB to PCB due to defects in the dielectric layer.

The induced electric field plays a critical role in the magnitude of the piezoelectric voltage constant; it is dependent on both the measured voltage and the device thickness. For our PSAM devices, we calculated the induced electric field based on the distance between the electrodes; this distance is almost entirely dictated by the thickness of our PU dielectric layer, whereas the absolute voltage should be largely independent of thickness. Accordingly, we looked to increase our induced electric field and piezoelectric voltage constant by decreasing the PU thickness. We accomplished this by diluting our uncured PU with petroleum ether before spin-coating and drying. When we tested our peptides against these thinner dielectric layers, we observed a much greater piezoelectric voltage response (Figure 4.4(A) and (B)); unexpectedly, we also saw an increase in the piezoelectric charge response. It is unknown how the petroleum ether used to reduce the PU thickness affected the spin coating, drying, and final properties of the PU dielectric layer; the PCBs with the thinner PU coating were less consistent, as we observed statistical differences between the individual PCBs in both the piezoelectric charge and voltage constants. We suspect that changes to the PU dielectric layer resulted in the statistically greater piezoelectric charge constant ( $d_{33}$ ) values for PSAM devices containing these thinner PU PCBs; the charge constant should be largely independent of the thickness of the dielectric layer. Nonetheless, the  $g_{33}$  values obtained for thin PU PSAM devices are considerably greater than the change in  $d_{33}$  values alone can account for. Since the thin PU layer is nearly half the thickness of the normal PU layer, we expect the resultant PSAM devices (including DDT controls) to have almost twice the voltage response. Indeed, the  $g_{33}$  values of up to  $(2000 \pm 600)$  mVm/N observed for the thin PU PSAM devices agree, within error, to those expected from the combination of the  $d_{33}$  increase and the PU thickness decrease; on average, the  $g_{33}$  values for the PSAM devices containing PCBs with

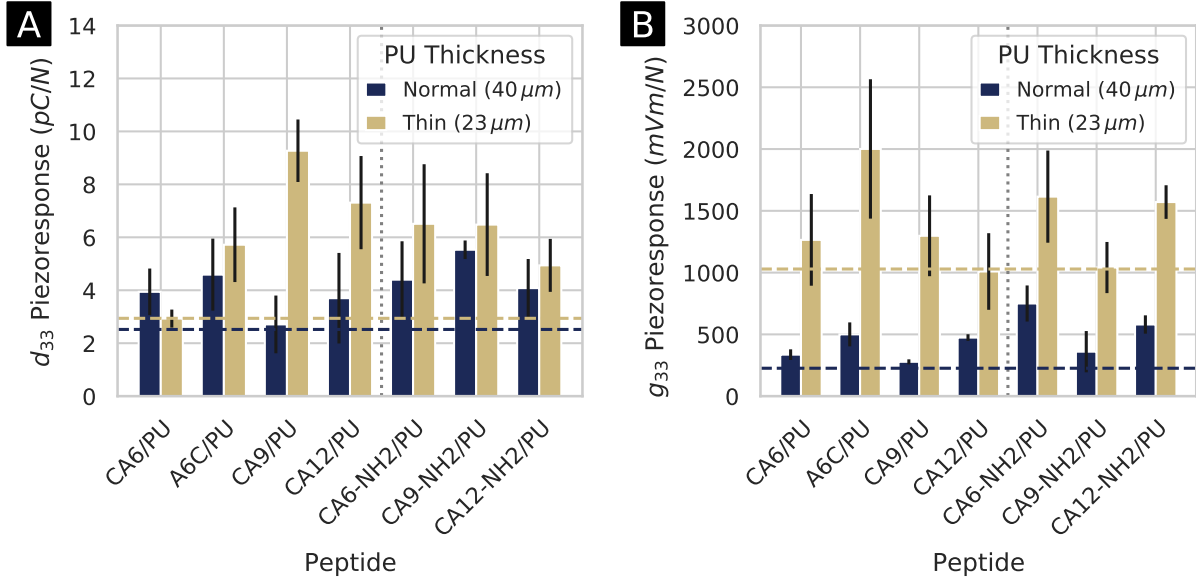


Figure 4.4: Thickness effect on piezoelectric response. (A) The piezoelectric charge constants ( $d_{33}$ ) of PSAM devices using normal thickness PU (40  $\mu\text{m}$ ) compared with those using thinner PU (23  $\mu\text{m}$ ). (B) The piezoelectric voltage constants ( $g_{33}$ ) of PSAM devices using normal thickness PU compared with those using thinner PU. The dashed lines show the piezoelectric response of DDT controls (see Figure B.3 and B.4) where navy corresponds to the normal thickness and gold corresponds to the thinner thickness.

the thinner PU coating were  $(220 \pm 40) \%$  greater than those with the normal thickness PU, whereas the expected increase based on the combination of  $d_{33}$  increase  $(60 \pm 30) \%$  and thickness decrease  $(74 \pm 2) \%$  is  $(180 \pm 60) \%$ . We suspect that the PU dielectric layer is key to the devices' large voltage responses as it allows for the large voltages to be produced without shorting across the SAM. The maximum  $g_{33}$  value of 2 Vm/N is quite remarkable and, to the best of our knowledge, is the highest experimental value reported to date in the literature.



## 4.6 Device Stability

The long-term stability of piezoelectric devices is of importance to their practical adoption; as such, we measured the stability of the piezoelectric response of our devices in multiple ways. Our PSAM devices show remarkable stability and retain their initial piezoelectric response for at least three months when stored away from light in a vacuum desiccator (Figure B.5); this is in line with the expected stability of SAMs under these storage conditions. While the long-term storage stability is adequate, the response of our normal PSAM devices decays over a matter of hours when exposed to ambient conditions. In order to solve this problem, we produced sealed PSAM devices where we placed the two PCBs together before the PU dried. The active layer of these sealed PSAM devices is protected from the atmosphere. When we tested these devices, we found that, while the charge response was much lower, the voltage response was similar to that of our normal PSAM devices due to the thinner PU layer (Figure B.6). On the stability front, the response actually increased over several weeks of testing (Figure B.7). Some of the observed increase in response is due to the slight decrease in preload force over time due to the nature of our testing setup; the rest of the increase might be due to organizing effects in the monolayer over time. These results show that, with improved manufacturing methods, our PSAM devices have real potential in practical applications.

## 4.7 Flexible Device Prototype

To further demonstrate the potential practical application of our PSAM devices, we constructed a sealed device made using flexible, gold-coated substrates. When tested using our normal method, we measured a  $d_{33}$  value of  $(3.68 \pm 0.08)$  pC/N and a  $g_{33}$  value of  $(35 \pm 4)$  mVm/N (the PU layer is an order of magnitude thicker, but its thickness and

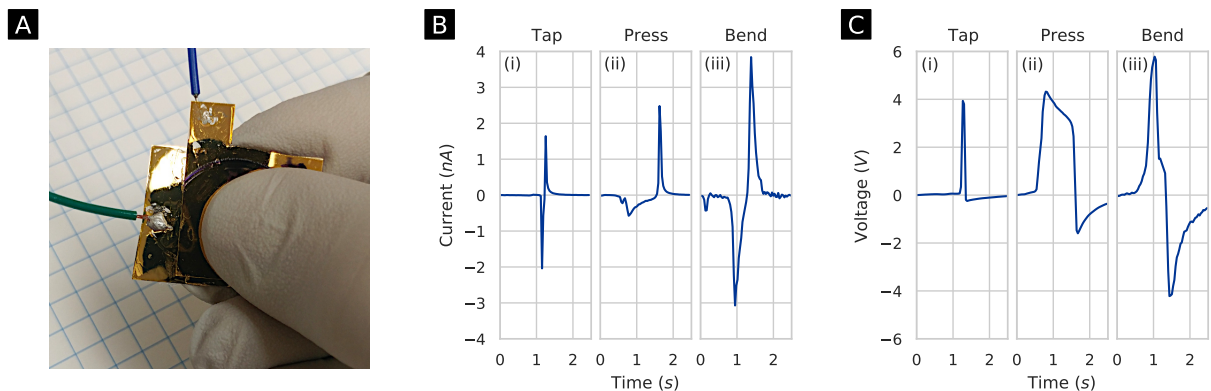


Figure 4.5: Flexible sealed PSAM device (CA12-NH<sub>2</sub>/DDT-PU) fabricated on gold-coated plastic substrates. (A) Image of device being tested. (B) Current response of flexible device. (C) Voltage response of flexible device. Current and voltage responses were measured due to (i) light finger taps while mounted, (ii) firm finger presses while mounted, and (iii) bending while held between three fingers. The device produced nearly 4 nA of short-circuit current and 6 V of open-circuit voltage when subject to gentle bending motion.

uniformity are somewhat uncertain). In addition, we examined our flexible device under more practical conditions by measuring its current and voltage in response to finger taps, presses, and bends (Figure 4.5). The finger taps and presses led to maximum currents of approximately 2 nA and voltages of approximately 4 V, whereas the bends produced almost 4 nA and 6 V. These values are much greater than those obtained when the device is tested normally (0.006 nA/0.06 V) and are likely due to the more localized nature of the force. The measured voltage response is much greater than that of most flexible devices reported in the literature while simultaneously being considerably easier to manufacture, making it a formidable candidate for potential practical applications.

## 4.8 Conclusions and Outlook

We present an innovative new method of producing thin, flexible, non-crystalline organic piezoelectric devices based on SAMs that show great potential for practical applications. The devices are simple, easy to manufacture due to their self-assembled nature that negates the need for electrical poling, and produce large voltage responses important for potential sensing applications. Furthermore, their peptide nature makes them fully biocompatible and easily modifiable. Future work in tuning the sequence and functionalization of the amino acids as well as use of better dielectrics and more precise manufacturing methods holds the potential for large increases to the already outstanding voltage response of our PSAM devices.

## 4.9 Experimental Section

### 4.9.1 Materials

Peptides CA<sub>6</sub> and A<sub>6</sub>C were obtained from Sigma-Genosys. All other peptides were obtained from AnaSpec. Ethanol (200 proof) was obtained from Decon Labs. Acetonitrile ( $\geq 99.9\%$ ) and 1-dodecanethiol ( $\geq 98\%$ ) were obtained from Sigma-Aldrich. Petroleum ether (certified ACS) was obtained from Fisher Scientific. Liquid conformal polyurethane coating was obtained from MG Chemicals (Urethane Conformal Coating; Cat. No. 4223-55ML). Spray conformal polyurethane coating was obtained from Techspray (Fine-L-Kote UR Conformal Coating; Cat. No. 2104-12S). All chemicals were used as received. Ultrapure water ( $18.2\text{ M}\Omega\text{ cm}$ ) was generated using a Millipore Synergy system.

### 4.9.2 Device Preparation

Self-assembled monolayers (SAMs) were formed on the outer gold surface of  $5\text{ cm} \times 5\text{ cm}$  custom designed and manufactured printed circuit boards (PCBs) (Where Labs/DirtyPCBs.com) with  $3.5\text{ cm} \times 3.5\text{ cm}$  electroless nickel immersion gold (ENIG) finished copper pads. The PCBs were first cleaned by ultrasonically cleaning them in ethanol for at least 30 min; rinsing sequentially with ethanol, water, and ethanol; and then drying them under a stream of nitrogen gas. Monolayers were formed by submerging the PCBs in a  $0.5\text{ mM}$ – $1\text{ mM}$  solution of the desired chemical or peptide for 48 h under ambient conditions to ensure uniformity. Solutions were prepared with either ethanol, water, acetonitrile, or a combination of the solvents depending on solubility; the solvent should not influence the resulting SAM and is not present in the final device.<sup>129</sup> After SAM formation, PCBs were removed from solution and washed using the same procedure as above before being wrapped in aluminum foil and stored in a vacuum desiccator. Topography images taken with an atomic force microscope (AFM) (Asylum Research MFP-3D, AC mode, AC240TS-R3 cantilever) show SAM uniformity (Figure B.12). Wires were soldered onto the PCBs for testing.

In order to obtain consistent, reproducible contact between the PCBs, a commercial conformal polyurethane (PU) coating was applied to the surface of some PCBs using a spin coater (Chemat Technology Spin Coater KW-4A, 1 mL PU, 1000 rpm for 6 s increasing to 6000 rpm for 10 s). A thinner PU coating was obtained by mixing the PU with petroleum ether (50/50 v/v) before spin coating. The thickness of the PU coating was measured using calipers ( $0.040 \pm 0.004\text{ mm}$  normal coating;  $0.023 \pm 0.003\text{ mm}$  thinner coating).

Sealed piezoelectric self-assembled monolayer (PSAM) devices were prepared by spraying one PCB with an aerosol can of commercial conformal PU, placing the other PCB and a 1 kg weight on top, and allowing the PU to dry. The PU thickness is  $\sim 0.01\text{ mm}$ . A flexible sealed PSAM device was prepared by depositing a 10 nm titanium adhesion layer followed by a 100 nm gold layer on flexible Nunc Thermanox Plastic Coverslips (Thermo Scientific) using

an electron beam evaporation system (Plassys Electron Beam Evaporator MEB550S); the flexible sealed PSAM device was then prepared similarly to the PCB sealed PSAM devices except that liquid PU was drop cast to form the dielectric layer ( $\sim 0.42$  mm thickness). The flexible sealed PSAM device has an active area of  $2.5\text{ cm} \times 2.5\text{ cm}$ .

### 4.9.3 Device Testing and Characterization

Samples were removed from the desiccator at least 1 h prior to testing, as inconsistent results were obtained when testing was performed sooner. PSAM devices consisting of one PU coated PCB facing one uncoated, SAM functionalized PCB were tested in a quasi-static manner before the piezoelectric response was calculated. Similar to our previous work,<sup>65</sup> the PSAM device was positioned in a testing apparatus where force was applied using a stepper motor controlled threaded rod. A force sensor (Tekscan FlexiForce A201), with a poly(dimethylsiloxane) spacer on top, rested between the rod and the device under test. In order to reduce triboelectric charge generation, a preload force of  $\sim 1$  N was applied using the threaded rod before compressions of varying force (up to  $\sim 6$  N) were applied along the Z-axis at a rate of approximately 0.17 mm/s. Force and short-circuit current or open-circuit voltage measurements were recorded for 70 s and 90 s, respectively, using a Keithley 2614B SourceMeter. Each recorded measurement is the average of the values computed from three sequential, undisturbed test sequences, and each sample was tested at least five times with the PCBs of the PSAM device separated between measurements; sealed PSAM devices were not separated, but the preload force was removed and reapplied. As reported in our previous work, the system was tested on commercial ceramic piezoelectric materials to ensure accuracy.<sup>65</sup>

The collected data are simply the applied force and measured current or voltage—both as a function of time. To calculate the piezoelectric charge constant ( $d_{33}$ ), force versus charge was plotted for each compression and the slope of the linear best fit was calculated using a robust linear regression (Figure B.1). A custom Python script was used to compute charge

by integrating the current peaks over time;<sup>65</sup> we modified our previous script to optimize the peak finding sensitivity and to use a robust linear regression. The script identifies force peaks and subtracts off any baseline force; it then looks for the corresponding current peak and integrates it to calculate the resultant charge during the period of increasing applied force. The piezoelectric voltage constant ( $g_{33}$ ) was calculated in a similar manner except that, after the force and voltage peaks were identified, voltage was converted to induced electric field by dividing by sample thickness and force was converted to external stress by dividing by electrode area (see Figure B.2 and minimum working example Python script in Appendix B.5). Resistance was measured using a Keithley 2614B SourceMeter. Capacitance was measured using a Zhengzhou Minghe Electronic Technology LC100-A inductance capacitance meter.

#### 4.9.4 *Ab Initio* Molecular Dynamics Simulations

We used the software package CP2K,<sup>136,137</sup> based on the Born–Oppenheimer approach, to perform *ab initio* molecular dynamics (AIMD) simulations of samples containing carboxylate-terminated peptide CA<sub>6</sub> or amide-terminated peptide CA<sub>6</sub>-NH<sub>2</sub> solvated in liquid water; both were under the action of static and homogeneous electric fields applied along a given direction (corresponding to the Z-axis). The implementation of an external field in numerical codes based on Density Functional Theory (DFT) can be achieved by exploiting the Modern Theory of Polarization and Berry’s phases<sup>138–140</sup> (see, *e.g.*, Ref.<sup>141</sup>). The CA<sub>6</sub>-containing numerical sample was composed of one CA<sub>6</sub> peptide solvated by 253 H<sub>2</sub>O molecules (*i.e.*, 833 atoms) arranged in a cubic cell with edge equal to 20.4 Å, so as to reproduce the liquid water experimental density of 1.00 g cm<sup>-3</sup> at room temperature. Similarly, the CA<sub>6</sub>-NH<sub>2</sub>-containing numerical sample was composed of one CA<sub>6</sub>-NH<sub>2</sub> peptide solvated by 253 H<sub>2</sub>O molecules (*i.e.*, 835 atoms) arranged in a cubic cell with edge equal to 20.4 Å. As usual, in order to minimize nonphysical surface effects, all structures were replicated in space by employing periodic boundary conditions. The intensity of the electric field was gradually increased with

a step increment of  $0.5 \text{ V nm}^{-1}$  from zero up to a maximum of  $1.0 \text{ V nm}^{-1}$ . In the zero-field cases, we performed dynamics of 50 ps for each investigated sample whereas, for each other value of the field intensity, we ran dynamics of 20 ps, thus accumulating a global simulation time equal to 180 ps where a time-step of 0.5 fs was chosen. Additional tests employing different atomistic configurations of the initial structures and/or assigning diverse initial atomic velocities were executed in order to exclude biases stemming from specific initial molecular arrangements.

Wavefunctions of the atomic species were expanded in the triple-zeta valence plus polarization (TZVP) basis set with Goedecker-Teter-Hutter pseudopotentials using the GPW method.<sup>142</sup> A plane-wave cutoff of 400 Ry was imposed. Exchange and correlation (XC) effects were treated with the Becke-Lee-Yang-Parr (BLYP)<sup>143</sup> density functional. Moreover, in order to take into account dispersion interactions, we employed the dispersion-corrected version of BLYP (*i.e.*, BLYP-D3).<sup>144,145</sup> The adoption of the BLYP-D3 functional has been dictated by the widespread evidence that such a functional, when dispersion corrections are taken into account, offers one of the best adherences with the experimental results related to water among the standard GGA functionals.<sup>146,147</sup> It is well-known that neglecting dispersion corrections leads to a severely over-structured liquid (see, *e.g.*, Ref.<sup>148</sup> and references therein). In order to counteract the overstructuring of intermolecular interactions typically induced by GGA XC functionals, all simulations were executed at a temperature of 350 K. The dynamics of nuclei were simulated classically within a constant number, volume, and temperature (NVT) ensemble using the Verlet algorithm whereas the canonical sampling was executed by employing a canonical-sampling-through-velocity-rescaling thermostat<sup>149</sup> set with a time constant equal to 10 fs.

## 4.10 Acknowledgment

I thank Z. N. Georgieva for assistance with spin coating and Dr. N. C. Miller for assistance in preparing the flexible substrates. Software used in this chapter includes, in part, Avogadro,<sup>150</sup> CP2K,<sup>151</sup> Matplotlib,<sup>109</sup> NumPy,<sup>110</sup> pandas,<sup>111</sup> pySerial, SciPy,<sup>112</sup> Statsmodels,<sup>152</sup> and Python-VXI11.



## 5.0 Oligopeptide-Based Piezoelectric Materials: Understanding Electromechanical Coupling in Molecules

This chapter is adapted from a manuscript in preparation for submission to the *Journal of Physical Chemistry C* as an invited perspective; it is a work in progress. It is a collaborative effort with Caroline M. Chun, Giuseppe Cassone, Nathaniel C. Miller, and Geoffrey R. Hutchison in which I carried out the device scale piezoelectric measurements and wrote large portions of the manuscript; C.M.C. carried out the piezo force microscopy based piezoelectric measurements, designed and executed the DFT calculations, and wrote part of the manuscript; G.C. designed and executed the *ab initio* molecular dynamics simulations; N.C.M. wrote the original text on which parts of the manuscript are based; and G.R.H. wrote part of the manuscript and conceived and directed the project.

### 5.1 Introduction

The piezoelectric effect, which linearly interconverts electrostatic response and mechanical distortion, is comprised of the direct effect in which mechanical stress generates an electric charge and the converse effect in which an applied electric field produces a mechanical distortion (Figure 5.1). Traditional inorganic, crystalline piezoelectrics see a wide range of uses from ultrasounds to microactuators to barbeque lighters. While the mechanism behind the piezoelectric effect is well understood in inorganic crystals, much uncertainty remains in the realm of biopiezoelectrics. Since the piezoelectric effect was first confirmed in

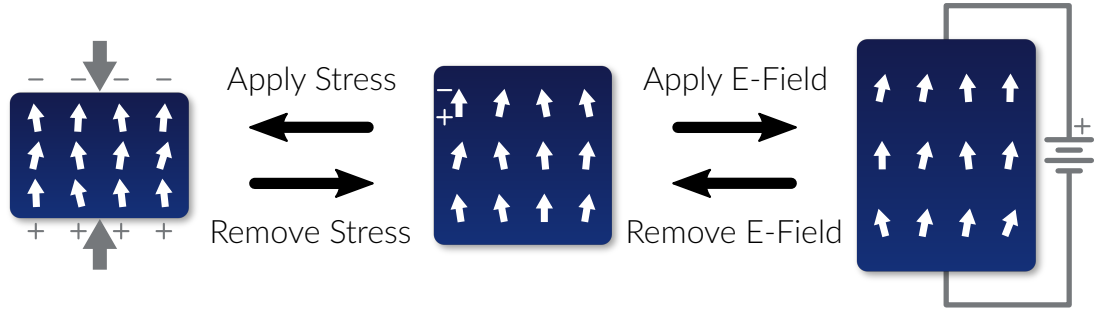


Figure 5.1: Schematic of the piezoelectric effect from left to right: the direct piezoelectric effect, steady state, and converse piezoelectric effect. The arrows represent individual dipoles.

biological tissues more than half a century ago,<sup>153</sup> piezoelectric activity measured in bones,<sup>153</sup> muscles,<sup>154</sup> and other biological materials<sup>155</sup> has led to questions as to the molecular origins of piezoelectric response.

Fundamentally, piezoelectric response requires a polar material undergoing stress, typically a mechanical distortion or electrical potential. Traditional examples of piezoelectric materials include lead zirconate titanate (PZT), quartz, and various polymers such as polyvinylidene difluoride (PVDF) while more recent, unusual discoveries range from viruses<sup>50</sup> to onion skins<sup>125</sup> to fish bladders<sup>156</sup> and shrimp shells.<sup>127</sup> Although intriguing, devices made from bulk natural materials do not significantly aid in growing a fundamental understanding of the piezoelectric mechanism in biomaterials. In recent years, the breadth of piezoelectric materials and devices has grown significantly from the traditional scope of ceramics and semicrystalline polymer films to include various composites, natural biomaterials, and molecularly engineered devices, including 2D- and bio-materials. Much of this research has focused on developing better flexible devices with the hope of matching or exceeding the piezoelectric response of traditional ceramics without the innate physical shortcomings of these hard, brittle materials. Composite approaches often involve embedding ceramic particles in flexible materials while maintaining polar alignment and force transmission; these devices rely on repackaging traditional piezoelectric materials. Devices made from natural biomaterials rely on a trial-and-error approach and are sometimes as simple as applying electrodes to a plant

or animal sample. Reducing materials down to a two-dimensional layer, introduces polar order to many materials where it is not present in the bulk state (e.g., MoS<sub>2</sub>); additionally, the single atomic layer leaves molecules accessible to further surface modification and the potential to engineer greater piezoelectric response.<sup>157</sup> Many amino acids, one of the basic building blocks of life, form single crystalline piezoelectrics; more complex materials can be bioengineered from this toolkit including polypeptides, nanotubes, proteins, and nearly all other piezoactive biomaterials.<sup>38</sup>

We believe that engineering self-assembled monolayers (SAMs) holds great potential in developing practical, biocompatible piezoelectric sensors and further elucidating the mechanism behind biopiezoelectricity. In a monolayer, the attachment of the molecule to a surface inherently breaks symmetry and generates a polar environment leading to an intrinsically piezoelectric material.<sup>117</sup> Since many molecules are also polar, a SAM represents a new environment to understand the structure–function relationships underlying piezoelectric response of molecules, find new electromechanical materials with high response, and develop new categories of piezoelectric devices.

A key challenge remains for developing accurate and reproducible methods to reliably determine the piezoelectric response of a given molecular material. At present, three general measurement categories exist: device-scale electromechanical characterization, nanoscale scanning-probe characterization, and computational prediction using electronic structure methods. Each method has its own sources of error, so comparing methods is important in determining the true piezoelectric response needed for fundamental understanding of the mechanism. As mentioned above, a wide range of biological materials that exhibit piezoelectric response are under current study. Key to further elucidating the mechanism behind the piezoelectric effect in biological materials is identifying a uniform, tailorable scaffold that can be precisely engineered and quantified to determine the effect of tweaks down to the molecular level. In this perspective we will focus on the applications of each characterization method as applied to well-defined oligopeptide monolayers.

## 5.2 Background

Several key figures of merit arise for piezoelectric response, primarily the piezoelectric charge constant ( $d_{ij}$ ) and voltage constant ( $g_{ij}$ ). Here  $i$  is the direction of the applied stressor and  $j$  is the direction of the resulting response. Subscript values of 1, 2, and 3 represent the  $X$ ,  $Y$ , and  $Z$  axes, respectively while 4, 5, and 6 represent shear about those axes. For example, when both the stress and developed strain are along the  $Z$ -axis, the piezoelectric charge coefficient is denoted as  $d_{33}$  while applied stress along the  $X$ -axis leading to developed shear strain along the  $Y$ -axis is denoted as  $d_{15}$ .

In piezoelectric materials, the stress is related to the electric field by a third order tensor; the elastic state of the material is defined by the second order tensors of stress and strain while the electrical state is defined by the vector quantities of electric field and electric displacement. All piezoelectric properties can be determined from these four values.<sup>17</sup> The most commonly reported piezoelectric constant is the charge constant ( $d_{ij}$ ) which, depending on units, relates induced charge with stress or displacement with applied electric field. When reporting on the direct effect, units are often reported as pC/N whereas when reporting on the converse effect, units of pm/V; both sets of units are equivalent. Based on the piezoelectric coupling constant, it can be shown that:

$$d_{ij} \leq \sqrt{\frac{\varepsilon_{ij}}{k_{ij}}} \quad (5.1)$$

where  $\varepsilon_{ij}$  is the relative permittivity and  $k_{ij}$  is the modulus. Thus, for organic materials with low dielectric constant, a key design principle is to yield a low elastic modulus to maximize piezoelectric response. In essence, upon compression of a polar piezo material, the film generates surface charge, becoming a charged capacitor.

A less reported but related metric is the piezoelectric voltage constant ( $g_{ij}$ ) with units of Vm/N; it relates voltage response to applied stress and is related to the charge constant by

the relative permittivity as follows:

$$g_{ij} = \frac{1}{\sqrt{k_{ij}\epsilon_{ij}}} \quad (5.2)$$

For this purpose, a small elastic modulus and small dielectric constant yield a large piezoelectric voltage constant. Consequently, organic SAM piezoelectric materials should have significantly greater  $g_{33}$  than corresponding inorganic ceramics such as PZT or crystalline PVDF, both of which have higher elastic modulus and permittivity. The voltage constant is important for sensing applications as large voltages can be easily and accurately detected. Unfortunately, direct measurements of the voltage constant are often lacking in the literature, and, when it does appear, it is often converted from the charge constant by dividing by the dielectric permittivity. Direct measurements of the voltage constant are desired for low frequency sensing applications, however, as permittivities measured at higher frequencies do not always apply to the quasi-static regime. Much like the piezoelectric charge constant  $d_{ij}$  is connected to short-circuit current, the piezoelectric voltage constant  $g_{ij}$  is connected to the open-circuit voltage.

Early investigations into the piezoelectricity of biomaterials involved single amino acid crystals. The structural dependence of piezoelectricity is emphasized through electromechanical characterizations and simulations. The simplest amino acid glycine, which has polymorphs, is extensively studied:  $\alpha$ -glycine (with an inversion center) does not display piezoelectricity, yet  $\beta$ - and  $\gamma$ -glycine are piezoelectric due to their non-centrosymmetry (Figure 5.2).

Guerin et al. report that the net dipole moment and van der Waals packing influence piezoelectric coefficients of amino acid crystals.<sup>30</sup> The crystal's electrical dipole moment is generated by the shift in atoms under stress. The molecular packing shifts the alignment of electric dipoles, and the net polarization is present for molecules that lack an inversion center. They hypothesized that soft materials (low elastic constant) with high packing density and high molecular dipole moment can increase the piezoelectric coefficient. When polymorphs

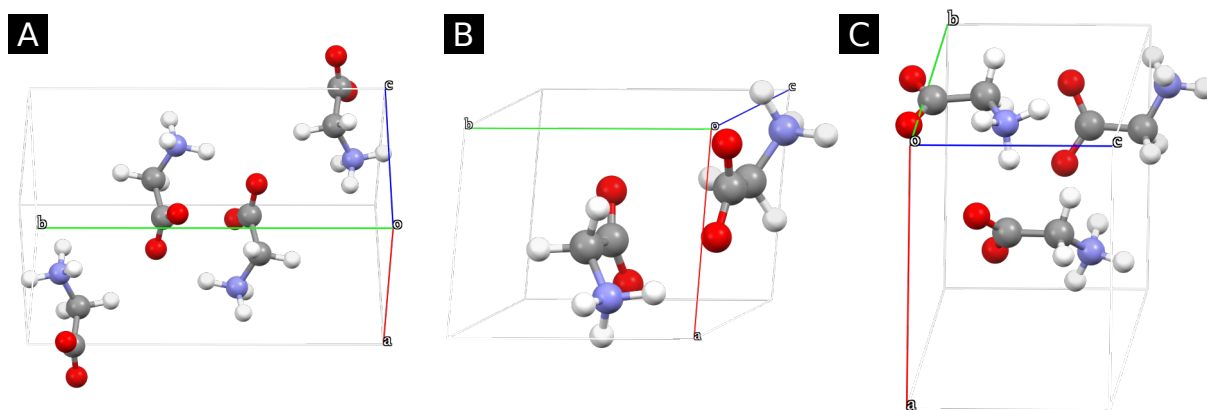


Figure 5.2: Unit cells of (A)  $\alpha$ -, (B)  $\beta$ -, and (C)  $\gamma$ -polymorphs of glycine.  $\alpha$ -Glycine crystallizes into the centrosymmetric  $P2_1/c$  space group while  $\beta$ - and  $\gamma$ -glycine crystallize into the noncentrosymmetric  $P2_1$  and  $P3_2$  space groups, respectively.<sup>30</sup>

of glycine are compared ( $\beta$ - and  $\gamma$ -glycine),  $\beta$ -glycine has the highest shear piezoelectric response ( $d_{16} = 178 \text{ pm/V}$ ), whereas  $\gamma$ -glycine has lower response ( $d_{33} = 9.93 \text{ pm/V}$ ) and  $\alpha$ -glycine (centrosymmetric) exhibits no piezoelectricity. Since the relative permittivity of  $\beta$ - and  $\gamma$ -glycine is only  $\sim 2\text{--}3$ , the piezoelectric voltage constant ( $g_{ij}$ ) is high, which opens up possibilities for biological piezoelectric devices.<sup>30</sup> The observed change in the domain, as well as the hysteresis loop in piezo force microscopy (PFM), demonstrate that  $\gamma$ -glycine is also ferroelectric; molecular dynamics simulations suggest that, by controlling the electric field, glycine's degree of polarization can be selectively modified in nanoscale.<sup>158</sup>

Furthermore, the formation of crystalline films from single crystals of amino acids offers more possibilities to tailor biological piezoelectric materials. L-leucine films have a density functional theory (DFT) calculated piezoelectric voltage constant ( $g_{22}$ ) of  $0.4 \text{ Vm/N}$  and calculated piezoelectric charge coefficients varying from  $d_{23} = 1.5 \text{ pC/N}$  to  $d_{34} = 20 \text{ pC/N}$ .<sup>159</sup> A commercial piezoelectric tester provides the average  $d_{33}$  as  $1.57 \text{ pC/N}$  for the upright position and  $-1.52 \text{ pC/N}$  for the inverted one. Since poling is not necessary for amino acid crystalline films and because the calculated voltage constant is greater than that of inorganic ceramics ( $0.25 \text{ Vm/N}$ ), the researchers proposed L-leucine films for potential device applications.<sup>159</sup>

In addition to simple amino acid crystals and films, amino acid derivatives have also been investigated. Wojtaś et al. examined inorganic–organic hybrid crystals: [H- $\beta$ -(3-Pyridyl)-Ala-OH][ClO<sub>4</sub>] and [H- $\beta$ -(4-Pyridyl)-Ala-OH][ClO<sub>4</sub>]<sup>160</sup> as well as [H- $\beta$ -(2-pyridyl)-Ala-OH][BF<sub>4</sub>] and [H- $\beta$ -(2-pyridyl)-Ala-OH][ClO<sub>4</sub>].<sup>161</sup> It is argued that [3PyAla][ClO<sub>4</sub>]’s higher piezoelectric response ( $d_{25} = 39$  pm/V;  $d_{22} = 18$  pm/V) compared to that of [4PyAla][ClO<sub>4</sub>] ( $d_{25} = 20$  pm/V;  $d_{22} = 6$  pm/V) is caused by intramolecular and intermolecular interactions.<sup>160</sup>  $\Pi$ -interactions and hydrogen bonds introduce rigidity to the molecular structure and lower the piezoelectric response. Also, selecting a different inorganic system results in different space groups upon crystallization. [H- $\beta$ -(2-pyridyl)-Ala-OH][ClO<sub>4</sub>] forms a spiral channel through hydrogen bonding and bears some resemblance to dipeptides.<sup>161</sup>

The structure of molecules plays a key role in determining the function. This relationship is also applicable to piezoelectric materials. For example, the PIEZO channel, which operates by mechanotransduction, relies heavily on the shape of protein aggregates. Energy harvesters made up of piezoelectric materials also depend on the structure. Thus, it is natural that, to understand the origin of piezoelectricity, we need to know how piezoelectricity works in organic materials. In turn, this will help to advance a fundamental understanding of how piezoelectricity originates (how microscale properties—intermolecular forces—carries onto bulk properties) as well as the design principles for synthesizing or building piezoelectric organic materials. From previous works on piezoelectric organic materials, it was found that the polarization direction of the overall structure; the orientation and strength of individual molecules’ dipole moments; intermolecular and intramolecular forces; and structure influence the magnitude of piezoelectric response.

The direction of polarization impacts the strength of the piezoelectric effect. The polarization of diphenylalanine (FF) microrods is controllable during growth by changing the direction of the applied electric field.<sup>162</sup> The maximum  $d_{33}$  was 17.9 pm/V, with power generation of 3.3 nW/cm<sup>2</sup>. The direction and strength of dipole moment influence piezoelectric response. In small amino acid crystals, namely  $\beta$ - and  $\gamma$ -glycine, piezoelectricity was measured experi-

mentally and computationally.<sup>30</sup> The relative permittivity of glycine molecules give insight into the overall dipole moment. Glycine polymorphs are not as polarized as perovskites are, yet the low permittivity of polymorphs (approximately 2) gives rise to high strain. As a result, they are favorable for harnessing energy for electronic devices.  $\beta$ -glycine, which is less packed (a smaller number of molecules in a unit cell per volume density) than  $\alpha$ -glycine is, exhibited a higher piezoelectric response than  $\alpha$ -glycine.<sup>30</sup> DFT calculations of piezoelectricity in a single-molecule investigate how the dipole moment along the  $Z$ -axis of a molecular spring is correlated to the converse piezoelectric effect.<sup>130</sup> In general, the regiochemical isomers of [6]helicene and phenanthrenes have higher  $d_{33}$  as the dipole moment is increased. However, since [6]helicene isomers have a low correlation between the two parameters, while the dipole moment contributes some degree to the strength of the piezoelectric response, it may not be the predominant factor. Other variables, such as intramolecular and intermolecular forces, as well as functional group substitutions, should also be considered to examine the origin of the piezoelectric effect in organic materials.<sup>130</sup>

The compactness of a molecule per volume is influenced by intramolecular and intermolecular forces. The intramolecular forces, as well as the intermolecular forces (the van der Waals forces, hydrogen bonding, and others) impact piezoelectric response. Hydrogen bonding affects the molecular arrangement by stabilization. The effect of hydrogen bonding on the piezoelectric response of amino acid derivatives has been investigated using PFM and DFT calculations. Although [H-(2-Pyridyl)-Ala-OH][BF<sub>4</sub>] (or [2PyAla][BH<sub>4</sub>]) crystals have hydrogen bonds between the hydrogen of the amino group and fluorine, vibrations of the BF<sub>4</sub> group cause weaker hydrogen bonding than that of [2PyAla][ClO<sub>4</sub>].<sup>161</sup> Coincidentally, the PFM measurements show that [2PyAla][BH<sub>4</sub>] has higher piezoelectric responses ( $d_{15}$  41 pm/V;  $d_{33}$  19.2 pm/V) than those of [2PyAla][ClO<sub>4</sub>] ( $d_{15}$  3 pm/V) and LiNbO<sub>3</sub> ( $d_{33}$  17 pm/V). [2PyAla][BH<sub>4</sub>] with weaker hydrogen bonding has a stronger piezoelectric response, yet whether hydrogen bonding is singlehandedly responsible for such a relationship is inconclusive.<sup>161</sup> A related study compares amino acid-perchlorate derivatives: [3PyAla][ClO<sub>4</sub>],



[4PyAla][ClO<sub>4</sub>], and [2PyAla][ClO<sub>4</sub>]. The 2-pyridyl analog’s rigidity is attributed to its seven intermolecular hydrogen bonds (versus four in [3PyAla][ClO<sub>4</sub>] and [4PyAla][ClO<sub>4</sub>]) and favorable donor–acceptor alignment.<sup>160</sup> The interaction between the pyridyl ring and the Cl–O bond is more significant in the 4-pyridyl derivative than in the 3-pyridyl analog. Also,  $d_{33}$  of the least rigid [3PyAla][ClO<sub>4</sub>] is the highest (39 pm/V), followed by 20 pm/V for [4PyAla][ClO<sub>4</sub>], and 3 pm/V for [2PyAla][ClO<sub>4</sub>]. The values of  $d_{25}$  also have the same order (18 pm/V for [3PyAla][ClO<sub>4</sub>]; 6 pm/V for [4PyAla][ClO<sub>4</sub>]; 0 pm/V for [2PyAla][ClO<sub>4</sub>]), implying that molecular packing and hydrogen bonding can contribute toward piezoelectric response.<sup>160</sup> In addition to hydrogen bonding, weaker interaction (van der Waals repulsion) also influences piezoelectric response.<sup>130</sup> In the computational study, as a single helicene molecule is compressed, the repulsion prevents the helicene from deforming too much. On the other hand, upon expansion, the molecule can polarize further, such that it stretches more. Such nonlinear behavior at the two extremes of field strengths suggests that the linear model of deformation (as a function of the electric field) would benefit from factoring in other parameters.<sup>130</sup>

For amino acid crystals, having low elastic constants resulted in a higher piezoelectric response, indicating that softer materials exhibit higher piezoelectricity.<sup>30</sup> In addition to small organic crystals, more complex organic materials (peptide nanotubes) have been also studied.<sup>163</sup> Peptide nanotubes (PNTs) formed by dipeptides show a significant piezoelectric response that appears to increase linearly as the external diameter of PNTs gets larger ( $d_{15}$  35 pm/V for 100 nm diameter;  $d_{15}$  60 pm/V for 200 nm nanotubes). Since the inner diameter is not known, however, more information about the structure of PNTs is needed to conclude the effect of external diameter.<sup>163</sup> Dipeptides can also form microrods.<sup>162</sup> As mentioned previously, the change in polarization can be achieved. The positive electric field (along the perpendicular axis relative to the substrate) places the NH<sub>3</sub><sup>+</sup> group toward the surface, whereas the negative electric field reveals the COO<sup>−</sup> end to the air. This control over alignment opens up possibilities of functionalizing microrods.<sup>162</sup> Furthermore, the dipeptide

FF self-assemblies can form various types of structures that display different piezoelectric responses.<sup>164</sup> In water solvent, FF forms hexagonal microtubes that exhibit a piezoelectric response of about  $d_{\text{eff}} = 60 \text{ pm/V}$ . In contrast, orthorhombic FF crystals, which are formed by using ethylene glycol solvent during self-assembly, have a lower response of  $d_{\text{eff}} = 40 \text{ pm/V}$ . This demonstrates that, even if the building block is the same, the morphological difference of the assembled crystal impacts the piezoelectric effect.<sup>164</sup> In the past two decades of piezoelectric organic materials research, small amino acid crystals and nanostructures derived from diphenylalanine have been primarily investigated. A study of piezoelectricity in peptides and peptoids reveals that peptides have higher  $d_{33}$ , but the structural differences among peptides do not appear to affect the piezoelectric response significantly.<sup>131</sup> However, the impact of side groups on peptides should not be disregarded completely, as there is a new methodology called DC-sweep DART-PFM to measure soft organic materials more effectively using probes with low spring constant.<sup>82</sup> A summary of the piezoelectric response observed in organic materials is found in Table 5.1.

Beyond piezoelectric response, several related electromechanical effects can arise, particularly in nanoscale materials. First, electrostriction is the nonlinear coupling between an applied electric field stress and material response. This quadratic response, of developed strain under an applied electrical stress, is present in many dielectric materials. In these cases, the application of stress causes the unaligned dipoles of the material to become increasingly aligned with the increasing magnitude of the applied stress; this stress is relieved by deformation of the material.<sup>97,165</sup> This effect, while present in piezoelectric materials, is generally small and inconsequential in comparison to the piezoelectric effect, whose linear nature distinguishes it from electrostriction.

Flexoelectricity is a non-linear coupling between an applied mechanical stress and material response in which a stress-strain gradient is established by the non-uniform deformation of a material. This gradient induces electromechanical coupling by either breaking the centrosymmetry of a material or bringing the dipoles into a net alignment. Unlike piezoelectricity

Table 5.1: Piezoelectric coefficients of organic materials. The following abbreviations are used: DFT is density functional theory; GGA is generalized gradient approximation; PBE and B3LYP are DFT functionals; PFM is piezo force microscopy; DART-PFM is dual AC resonance tracking-PFM; FF is dipheynlalanine; CS-AFM is current sensing atomic force microscopy; and SAM is self-assembled monolayer.

Material (State)	Piezoelectric Coefficient	Method	Ref.
$\beta$ -glycine (single crystal)	$d_{16} = (178 \pm 11) \text{ pm/V}$	resonance impedance	[30]
$\beta$ -glycine (single crystal)	$d_{16} = 195 \text{ pm/V}$	DFT (GGA)	[30]
$\gamma$ -glycine (single crystal)	$d_{33} = 9.93 \text{ pm/V}$	commercial $d_{33}$ tester	[30]
$\gamma$ -glycine (single crystal)	$d_{11} = 1.6 \text{ pm/V}$ $d_{22} = -1.1 \text{ pm/V}$	DFT (GGA)	[30]
$\gamma$ -glycine (single crystal)	$d_{11} = 1.7 \text{ pm/V}$ $d_{22} = -1.1 \text{ pm/V}$	commercial $d_{33}$ tester	[30]
$\gamma$ -glycine (single crystal)	$d_{33} = 10 \text{ pm/V}$	PFM	[158]
L-proline (single crystal)	$d_{14} = 3.35 \text{ pC/N}$ $d_{25} = -0.09 \text{ pC/N}$ $d_{36} = 0.4 \text{ pC/N}$	DFT via PBE (GGA)	[166]
hydroxy-L- proline (single crystal)	$d_{14} = 3.72 \text{ pC/N}$ $d_{25} = -27.75 \text{ pC/N}$ $d_{36} = 4.55 \text{ pC/N}$	DFT via PBE (GGA)	[166]
L-alanine (single crystal)	$d_{14} = -6.26 \text{ pC/N}$ $d_{25} = -3.78 \text{ pC/N}$ $d_{36} = 6.30 \text{ pC/N}$	DFT via PBE (GGA)	[166]

Table 5.1: (continued)

Material (State)	Piezoelectric Coefficient	Method	Ref.
hydroxy-L- proline (single crystal)	$d_{25} = (25 \pm 5) \text{ pC/N}$	resonance impedance	[166]
L-leucine (single crystal)	$d_{34} = 20 \text{ pC/N}$	DFT via PBE (GGA)	[159]
L-leucine (crystalline film)	$d_{\text{eff-upright}} = 1.57 \text{ pC/N}$ $d_{\text{eff-invert}} = -1.52 \text{ pC/N}$	commercial $d_{33}$ meter	[159]
DL-alanine (single crystal)	$d_{33} = 9.1 \text{ pm/V}$	PFM	[37]
L-amino acids (crystalline films)	$d_{14}$ up to $-6.26 \text{ pm/V}$ $d_{25}$ up to $-27.75 \text{ pm/V}$ $d_{36}$ up to $-11.40 \text{ pm/V}$	DFT via PBE (GGA)	[39]
[3PyAla][ClO <sub>4</sub> ] (single crystal)	$d_{25} = 39 \text{ pm/V}$ $d_{22} = 18 \text{ pm/V}$	PFM	[160]
[4PyAla][ClO <sub>4</sub> ] (single crystal)	$d_{25} = 20 \text{ pm/V}$ $d_{22} = 6 \text{ pm/V}$	PFM	[160]
[2PyAla][ClO <sub>4</sub> ] (single crystal)	$d_{25} = 3 \text{ pm/V}$ $d_{22} = 0 \text{ pm/V}$	PFM	[160]
[2PyAla][BF <sub>4</sub> ] (single crystal)	$d_{15} = (41.0 \pm 1.0) \text{ pm/V}$ $d_{33} = (19.2 \pm 0.3) \text{ pm/V}$	PFM	[161]
[2PyAla][ClO <sub>4</sub> ] (single crystal)	$d_{15} = (3.0 \pm 0.3) \text{ pm/V}$	PFM	[161]

Table 5.1: (continued)

Material (State)	Piezoelectric Coefficient	Method	Ref.
modified FF peptide (nanotubes)	$d_{15} = (33.7 \pm 0.7) \text{ pm/V}$	PFM	[167]
modified FF peptide (nanofibrils)	$d_{15} = (1.7 \pm 0.5) \text{ pm/V}$	PFM	[167]
FF peptide (nanotubes)	$d_{15} \approx 60 \text{ pm/V}$	PFM	[163]
FF peptide (microrods)	$d_{33} = 17.9 \text{ pm/V}$	PFM	[162]
cyclic tetra- $\beta$ - peptide derived (nanotubes)	$d_{33} =$ $(1.17 \pm 0.15) \text{ pm/V}$	PFM	[168]
FF peptide (microribbons)	$d_{\text{eff}} = (40 \pm 5) \text{ pm/V}$	PFM	[164]
cyclic hexapeptide (nanotubes)	$d_{33} = 2 \text{ pC/N} - 6 \text{ pC/N}$	CS-AFM	[169]
poly- $\gamma$ -benzyl- L-glutamate (PBLG) (grafted film)	$d = 0.740 \text{ pm/V} -$ $1.323 \text{ pm/V}$	Nomarski optical interferometry	[170]

Table 5.1: (continued)

Material (State)	Piezoelectric Coefficient	Method	Ref.
substituted [6]helicene (single molecule)	$d_{33} = 48.8 \text{ pm/V}$	DFT with B3LYP	[130]
phenanthrene derivative (single molecule)	$d_{33} = 59.7 \text{ pm/V}$	DFT with B3LYP	[130]
peptide (SAMs)	$d_{33}$ up to $(1.75 \pm 0.32) \text{ pm/V}$	DART-PFM	[131]
peptoid (SAMs)	$d_{33}$ up to $(1.12 \pm 0.23) \text{ pm/V}$	DART-PFM	[131]
dodecanethiol (SAM)	$d_{33} =$ $(1.12 \pm 0.25) \text{ pm/V}$	DART-PFM	[131]

and electrostriction, flexoelectricity is size-dependent and ranges from an insignificant effect in large bulk scale materials, to a sizable effect in some nanoscale materials such as lipid bilayers.<sup>97</sup>

Finally, the electrostatic or triboelectric effect in a material results from the Coulombic force generated between two separated charges. This effect can occur when two different materials are brought into close contact with each other generating a local electric field. The electrostatic effect can contribute to the magnitude of the measured piezoelectric effect but can be deconvoluted from the measurement due to its non-linearity and small

contribution to the overall response.<sup>97</sup> In relation to the linear piezoelectric effect, these other electrostatic contributions can be detected and mitigated due to their non-linear nature and often inconsequential relative magnitude.

### 5.3 Model Oligopeptide System

Building upon our recently published work on oligopeptide SAM based piezoelectric devices, herein we present a model oligopeptide system and examine the effect of molecular level changes through device scale characterization, PFM, and computational investigations. We examine helical thiol-containing oligopeptides ranging in length from seven to thirteen amino acids (Figure 5.3). For our experimental investigations, these SAMs are grown from solution on gold substrates (Figure 5.4) whereas our computational investigations are gas-phase single-molecule predictions. Peptide sequences include cysteine (C), six to twelve alanines (A), and, optionally, a substitution of one tyrosine (Y), phenylalanine (F), or the unnatural amino acid 4-cyano-phenylalanine (denoted X). This allows for us to examine the effects of sequence length, direction, and substitution as well as to compare measurements and predictions between our three methods.

### 5.4 Device Scale Characterization

Piezoelectric materials ultimately need to be scaled up such that they can be easily handled and implemented in real-world applications. In the lab, this usually means producing devices in the square centimeter range. Several methods exist for quantifying the piezoelectric charge constant of such devices: the static method, the quasi-static method, and the resonant method. The basic principles of the static and quasi-static direct methods are the same, a

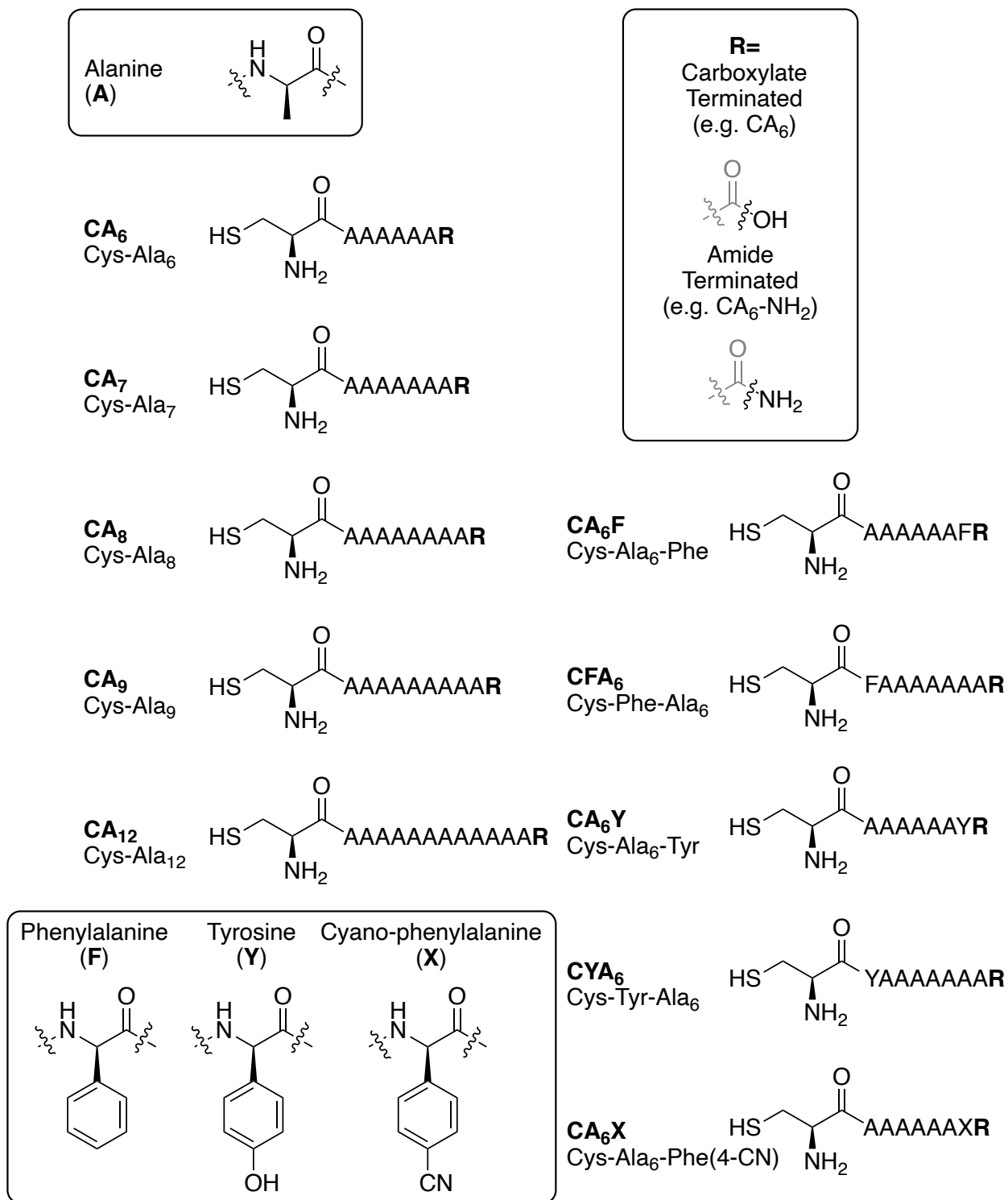


Figure 5.3: Schematic diagram of oligopeptides studied in model oligopeptide system.



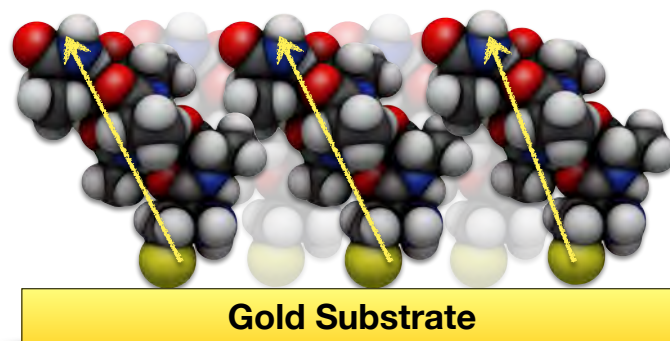


Figure 5.4: Model of oligopeptide SAM on gold substrate.

force is applied to the sample and the resultant charge response due to the direct effect is measured; the ratio of charge to force gives the charge constant. The quasi-static method offers improved accuracy as quicker, repetitive deformations minimize measurement interference, drift, and leakage. In the resonant method, the sample is excited by an oscillating electric field resulting in mechanical deformations due to the converse effect; based on the frequency which produces maximum deformation and the dimensions of the sample, the charge constant can be calculated.

These piezoelectric measurement techniques—traditionally applied to ceramics—present special challenges when soft, deformable materials are to be measured. The quasi-static method is most commonly applied using a “ $d_{33}$  meter” (sometimes referred to as a Berlincourt meter) which generally applies a 10 N preload force followed by 0.25 N compressions at a frequency of  $\sim 100$  Hz.<sup>76,77</sup> These meters cannot accurately measure materials that recover from deformations at rates near or slower than the compression frequency as well as materials that deform by significant amounts, such as foams. The resonant method has similar limitations as it requires a material with precisely known, relatively unchanging dimensions where electrical strain cannot be relieved by internal deformations. Luckily, quasi-static measurements of soft materials can be accurately measured using a measurement setup different from that of commercial  $d_{33}$  meters. The device can be gently compressed using a stepper motor while the resulting current is measured and integrated to calculate the charge; the speed and travel

of the compressions can be tuned to the device. For improved accuracy, a range of forces can be applied such that the charge constant can be derived through linear regression of the force and charge values. Similarly, the piezoelectric voltage constant can be obtained by measuring the open-circuit voltage instead of the short-circuit current. While the mechanical setup of such a testing system is simple, it does require more precise electronics than a  $d_{33}$  meter for accurately measuring the electrical response.

In an earlier systematic study of organic based, soft piezoelectric devices, we doped poly(dimethylsiloxane) (PDMS) foams with various polar, small organic molecules and examined the effects of dopant concentration and dopant dipole moment on the piezoelectric response.<sup>65</sup> Based on Equation 5.1 mentioned on page 74, one can see that the piezoelectric charge constant is dependent on an electrical component, the permittivity, and a mechanical component, the modulus; each of these components can be tuned separately. Increasing the dipole moment by tuning the dopant or increasing the dipole concentration by increasing the dopant amount should increase the permittivity and, therefore, the charge constant; indeed, we saw an increase in piezoelectric response until a saturation point by increasing the dopant dipole moment as well as an increase in response by increasing the dopant concentration. Separately, we tuned the mechanical properties of our PDMS foams; we tuned the modulus by changing the curing temperature of the PDMS. Decreasing the modulus of the foams, the denominator in Equation 5.1, led to an increase in piezoelectric response, as expected. While this system proves the relations between dipoles, modulus, and piezoelectric response, it does not allow us to easily examine effects down to the molecular level.

Our model oligopeptide system improves on the shortcomings of the PDMS foams by allowing for molecular level tunability; herein we expand upon device scale results of this model system. Several possible molecular level changes to the oligopeptide sequence tune the molecule’s resultant piezoelectric response: the sequence direction, the sequence length, and the presence of differing amino acid substituents. As shown in Figure 5.5(A), reversing the order of the amino acids in the oligopeptide sequence does not significantly alter the

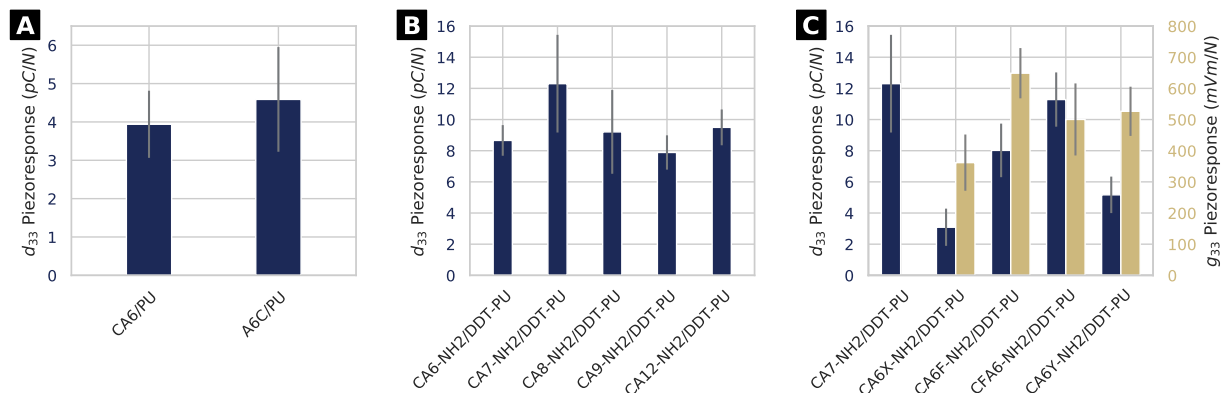


Figure 5.5: Measured direct piezoelectric constants of model oligopeptide system measured on the device scale. (A) Direction effect on piezoelectric charge constant ( $d_{33}$ ). (B) Length effect on  $d_{33}$ . (C) Substituent effect on  $d_{33}$ .

resultant piezoelectric response. Similarly, altering the sequence length also does not appear to significantly affect the response (Figure 5.5(B)). Finally, adding a different amino acid substituent to the chain is able to tune the response, although not always in easily predictable ways. As seen in Figure 5.5(C), adding a phenylalanine (F) to the oligopeptide does not appear to have a significant effect whereas adding a tyrosine (Y) results in a decrease in response. The unnatural amino acid cyano-phenylalanine (X) decreases the piezoelectric response more pronouncedly than the tyrosine does; computations, discussed in Section 5.6, show that the cyano group aligns opposite to the direction of the macrodipole, thereby decreasing the overall response. Predicting these molecular effects of the oligopeptide sequence on the piezoelectric response are complicated by changes in the SAM; altering the sequence can change how the oligopeptide stands and packs on the gold surface, complicating prediction efforts. We directly measured both the piezoelectric charge ( $d_{33}$ ) and voltage ( $g_{33}$ ) constants; they are related by the relative permittivity such that  $g_{33} = \frac{d_{33}}{\epsilon_r \epsilon_0}$ , where  $\epsilon_r$  is the relative permittivity of the material and  $\epsilon_0$  is the vacuum permittivity.<sup>25</sup> Figure C.1 correlates our measurements of these constants and gives a relative permittivity of 2.91 for our oligopeptide based devices; this is in line with the lower end of literature values for polyurethane which serves as the conformal dielectric layer in the devices.<sup>171,172</sup>

## 5.5 Piezo-Force Microscopy

Determining the converse piezoelectric response of a material requires the precise quantification of the mechanical response of the material to an applied electric field. Traditional atomic force microscopy (AFM), a technique initially developed for mapping nanoscale morphological variations, can accurately quantify the mechanical deformations and properties of materials.<sup>173,174</sup> Numerous functional AFM methods have since been developed to expand the technique’s usefulness and applications, including PFM where an applied electric field is paired with mechanical measurements to measure the piezoelectric response induced by the applied voltage.<sup>174–178</sup> Due to crosstalk between the measurement feedback loops, classical PFM suffers from poor sensitivity; dual AC resonance tracking (DART), developed by Kalinin, introduces a bias voltage that solves many of PFM’s shortcomings and allows for more quantitative converse piezoelectric measurements due to greatly improved sensitivity.<sup>81,173,175,177–181</sup> A remaining obstacle to accurate quantitative DART-PFM measurements is the elimination of electrostatic signals due to interactions between the AFM tip and the sample surface. The band excitation (BE) method looks to overcome these distortions by exciting the lever at multiple frequencies surrounding the fundamental frequency to help alleviate topological induced shifts to the fundamental frequency.<sup>182</sup> More recent work has looked to minimize these distortions—albeit only in certain cases—through innovative lever designs or the use of high spring-constant levers.<sup>97,183–186</sup> New techniques are needed to accurately quantify the converse piezoelectric effect, particularly in soft, biomaterials.

In order to overcome these short comings in measuring soft organic and biomaterials, we have developed a DC-Sweep DART-PFM method whereby electrostatic contributions are eliminated instead of merely minimized.<sup>82</sup> Previous methods, such as the use of high spring-constant levers, perform best when the elastic modulus of the material is significantly greater than that of the lever; unfortunately, in soft organic and biomaterials where the modulus is small in comparison to the lever, the lever simply deforms the target surface

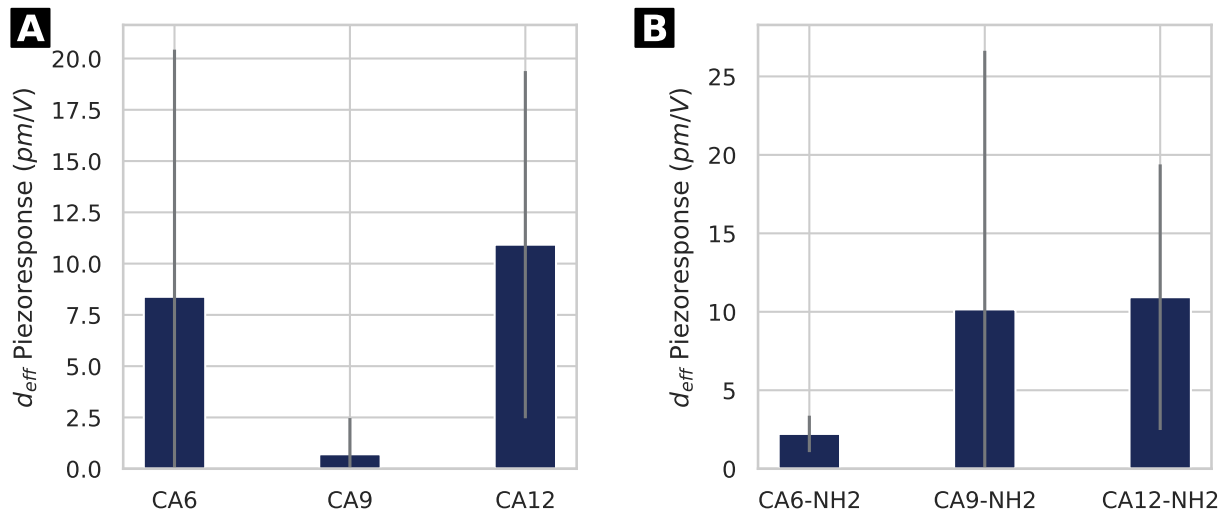


Figure 5.6: Measured converse piezoelectric constants of model oligopeptide system measured using DART-PFM. (A) Length effect on carboxylate-terminated peptides. (B) Length effect on amide-terminated peptides. Error bars represent standard error for the  $d_{\text{eff}}$  regression.

leading negating the sensitivity enhancements garnered by DART and BE techniques. By sweeping an applied DC field under a fixed AC field, we can calculate and subtract the electrostatic component of the tip response thereby allowing for the use of low spring constant levers necessary for good sensitivity.

Collection has begun on PFM measurements of the oligopeptides using our DC-sweep DART-PFM method.<sup>82</sup> Initial PFM results, presented in Figure 5.6, indicate somewhat decent correlation with the device scale measurements presented in Section 5.4 (see Figures 5.7 and C.3 for correlations). More results are needed before conclusions can be drawn.

## 5.6 Computational Investigations

Gas-phase single-molecule predictions were performed using DFT methods where the electric field was set to be in complete alignment with the molecular axis (Figure 5.8). Calculations were performed where the length change was calculated using the distance between either [C]

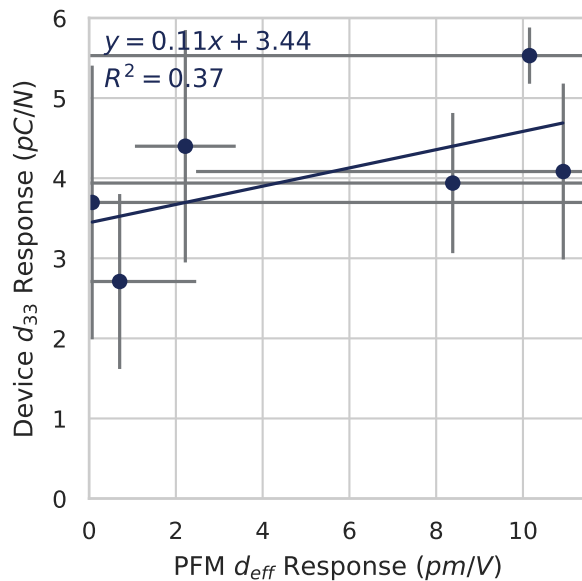


Figure 5.7: Correlation of piezoelectric response between PFM measurements and device scale measurements. For device scale measurements, the results with unfunctionalized PU coated PCBs are used (e.g., CA<sub>X</sub>/PU).

the N-terminus and the carbonyl carbon of the C-terminus or [O] the N-terminus and the carbonyl oxygen of the C-terminus; Figure C.2 shows that there is good agreement between the methods. The B3LYP functional was originally examined, but found to produce poor results. A switch to the  $\omega$ B97X-D<sub>3</sub> functional improved results, but correlation with the device scale experimental results in Section 5.4 (Figures 5.9 and C.4) and PFM results in Section 5.5 (Figure 5.10) was still relatively poor. The negative correlations between the B3LYP calculations and experimental results show that the method does a particularly poor job at modeling the system. The newer  $\omega$ B97X-D<sub>3</sub> functional shows superior performance due to its better treatment of electrostatics. We turned to *ab initio* molecular dynamics solutions to help explain the discrepancies between experiment and computation (Figures C.5–C.10). These simulations revealed that more than one dominant helix may be present. Poor correlation is expected if the DFT calculations were not run on the predominant helix or if multiple helices with greatly differing response are present. More work is needed to

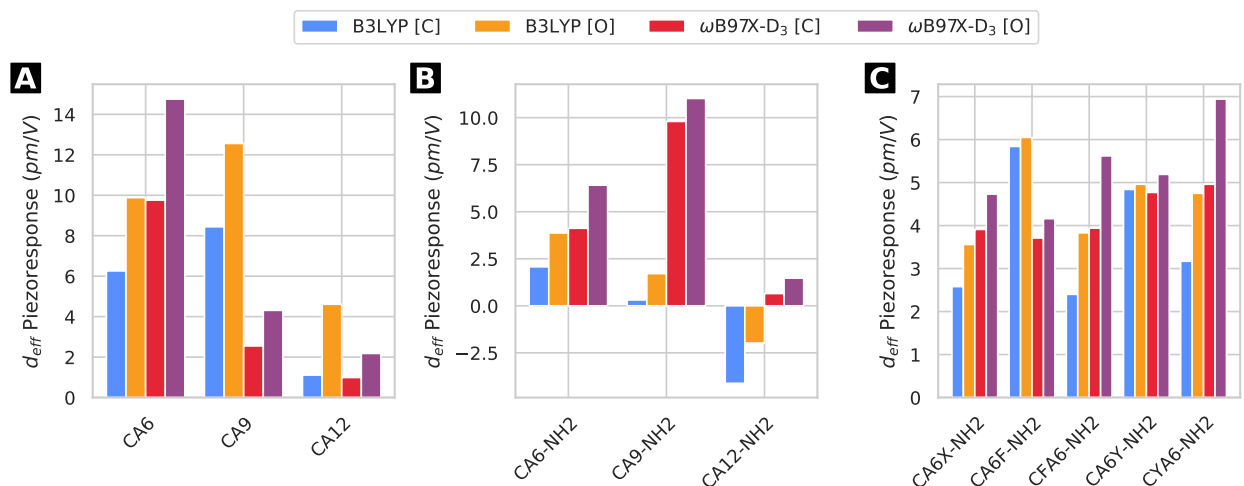


Figure 5.8: Converse piezoelectric constants of model oligopeptide system calculated using DFT. (A) Length effect on carboxylate-terminated peptides. (B) Length effect on amide-terminated peptides. (C) Substituent effect on amide-terminated peptides. B3LYP and  $\omega$ B97-XD functionals were used where the length change was calculated using the distance between either [C] the N-terminus and the carbonyl carbon of the C-terminus or [O] the N-terminus and the carbonyl oxygen of the C-terminus.

improve computational modeling of the piezoelectric oligopeptide system. More experimental data should help guide the refinement of computational methods which may then potentially used to predict better performing oligopeptide sequences.

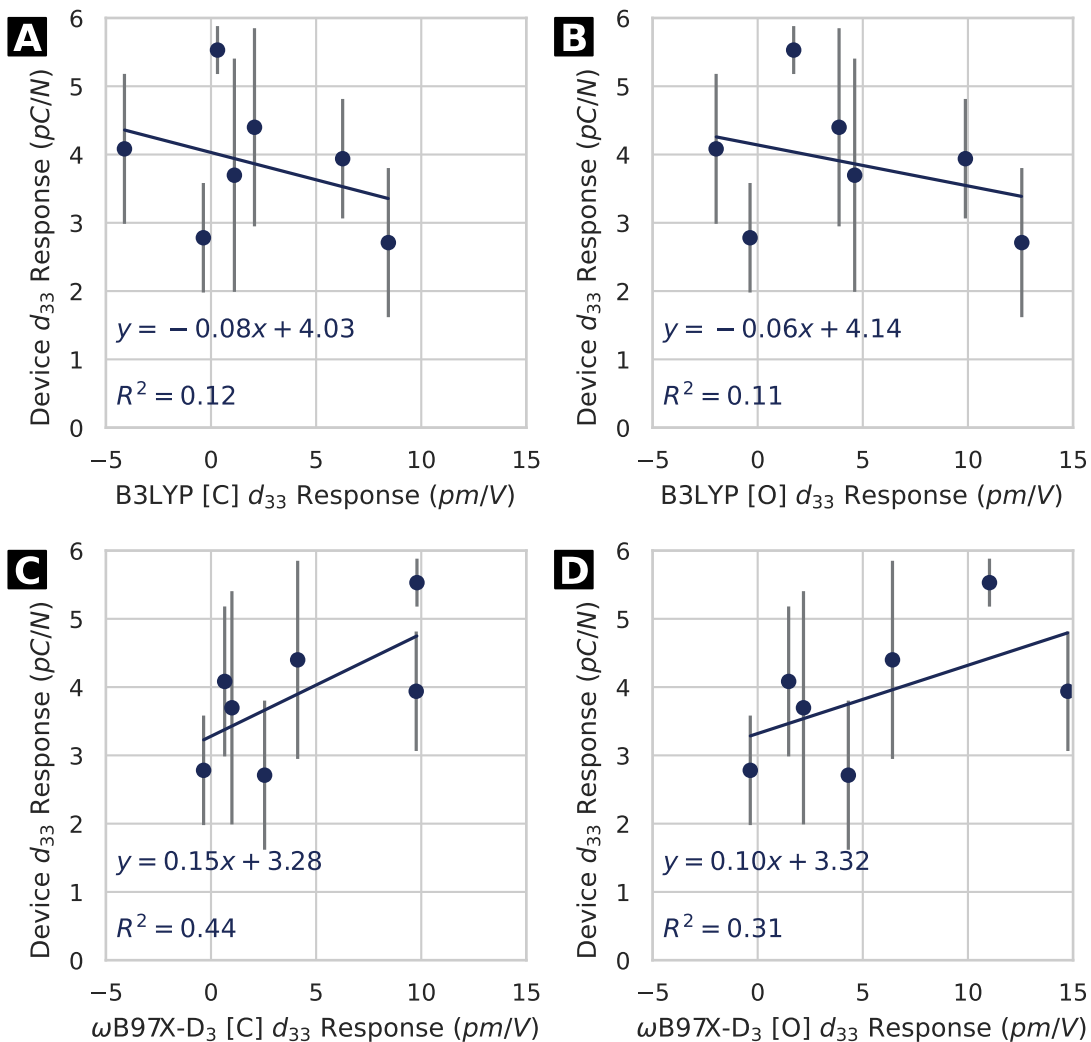


Figure 5.9: Correlation of piezoelectric response between DFT calculations and device scale measurements. For device scale measurements, the results with unfunctionalized PU coated PCBs are used (e.g., CA<sub>X</sub>/PU). B3LYP and  $\omega$ B97-XD functionals were used where the length change was calculated using the distance between either [C] the N-terminus and the carbonyl carbon of the C-terminus or [O] the N-terminus and the carbonyl oxygen of the C-terminus.



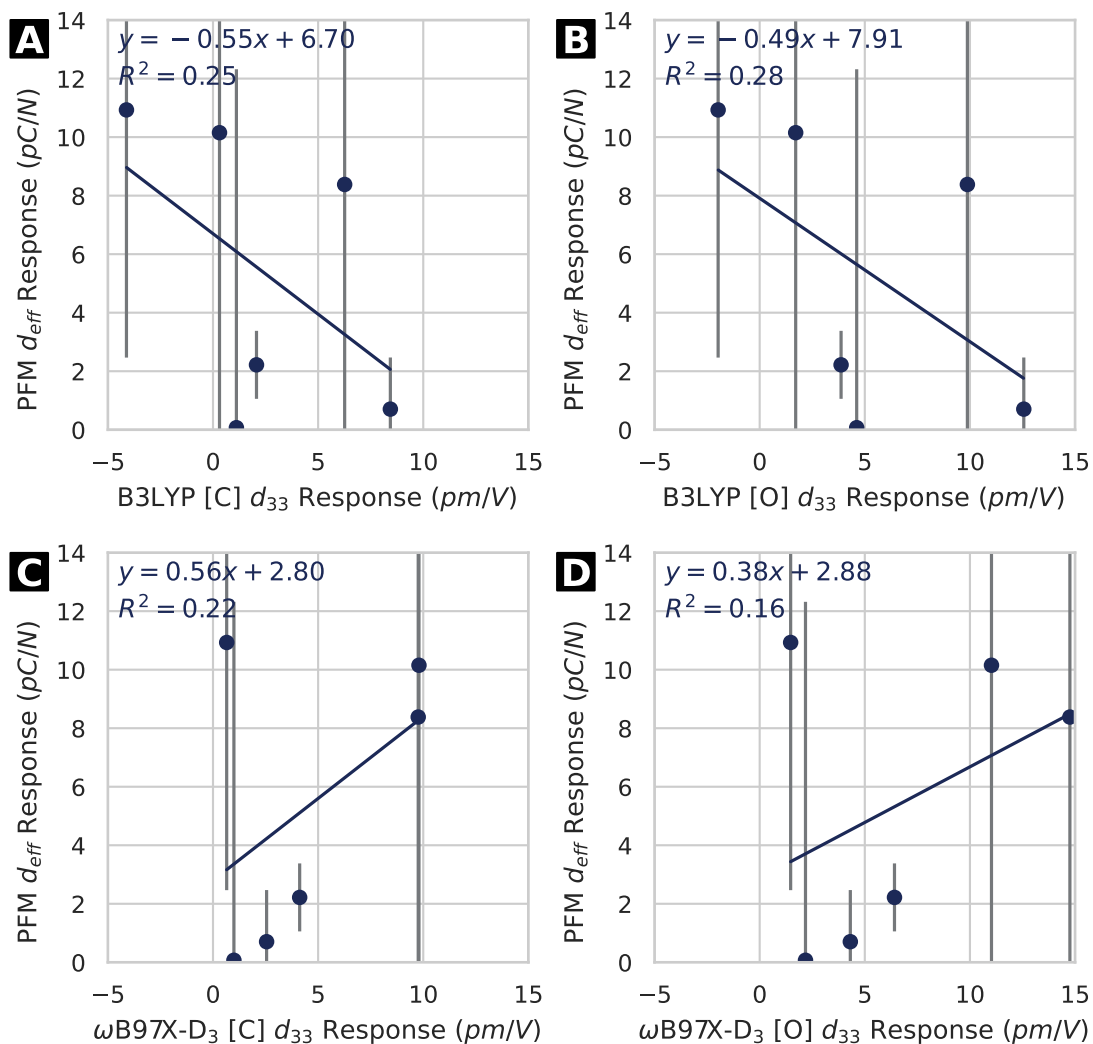


Figure 5.10: Correlation of piezoelectric response between DFT calculations and PFM measurements. B3LYP and  $\omega$ B97-XD functionals were used where the length change was calculated using the distance between either [C] the N-terminus and the carbonyl carbon of the C-terminus or [O] the N-terminus and the carbonyl oxygen of the C-terminus.

## 6.0 Double-Wave Method Ferroelectric Measurements of a Corannulene Derivative

This chapter is a collaborative effort with Allison M. Rice and Nathaniel C. Miller in which I designed, implemented, carried out, and analyzed a double-wave method for ferroelectric measurements of self-assembled monolayers (SAMs) of a potentially ferroelectric corannulene derivative—4,4',4'',4'''-(dibenzo[*ghi,mno*]fluoranthene-1,2,5,6-tetrayl)tetrabenzoic acid (H<sub>4</sub>DFT); A.M.R., formerly of the Shustova group at the University of South Carolina, developed methods for and carried out the synthesis of the H<sub>4</sub>DFT molecule studied; and N.C.M. developed optimized deposition methods, measured the piezoelectric response using dual AC resonance tracking piezo force microscopy (DART-PFM), and carried out scanning Kelvin probe force microscopy (SKPFM) ferroelectric measurements of the SAMs.

### 6.1 Introduction

Ferroelectrics are a class of materials which possess a switchable spontaneous polarization; they are a subset of piezoelectrics which exhibit a permanent dipole moment that can be reversed through the application of an external electric field.<sup>187</sup> Several distinct types of polarization behavior exist (Figure 6.1). In a standard linear dielectric, the polarization changes linearly with changing electric field. In a paraelectric material, transitory dielectric polarizations develop with applied electric field resulting in non-linear polarization changes about the origin. Finally, in a ferroelectric material, these polarizations are semi-permanent;

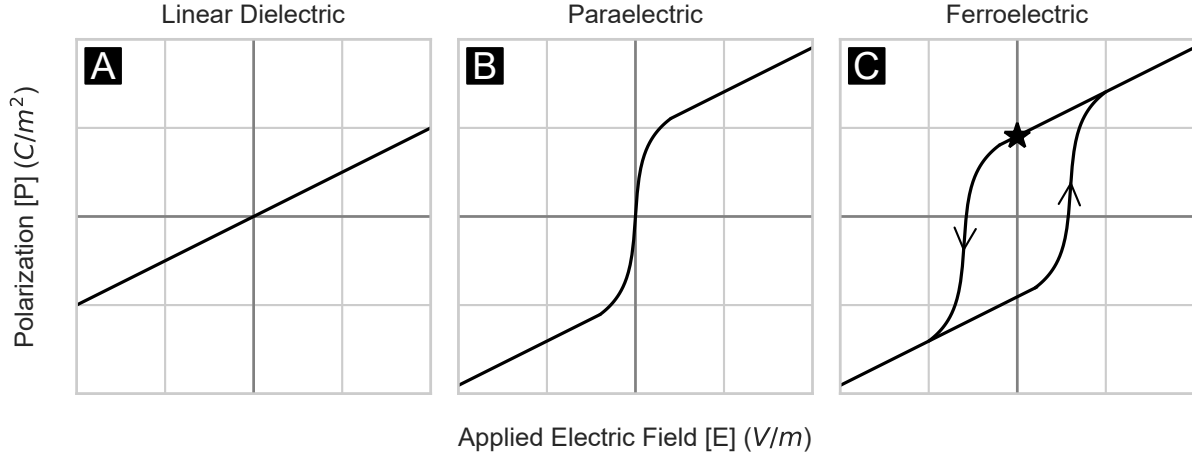


Figure 6.1: Types of polarization–electric field (P–E) curves: (A) linear dielectric, (B) paraelectric, and (C) ferroelectric. The star in panel (C) represents the positive spontaneous polarization.

they exhibit “memory.” A voltage is applied to switch the polarization states and these multiple polarization states result in hysteresis in the polarization–electric field (P–E) curve.

The P–E curve, or loop, (Figure 6.1C) is a good starting point for analyzing the ferroelectric behavior of a material. The existence of hysteresis is a promising initial indicator of ferroelectricity, and one can derive several figures of merit from the curve including the spontaneous polarization and coercive field strength.<sup>188</sup> The spontaneous polarization ( $P_s$ ) is a measure of the ferroelectric strength and is the point where the linear region (or extrapolation thereof) intersects the y-axis (indicated with a star in Figure 6.1C). The polarization at the y-axis is the remanent<sup>‡</sup> polarization ( $P_r$ ); it is usually approximately equal to  $P_s$  in crystals but somewhat lower in ceramics.<sup>3</sup> The saturation polarization ( $P_{sat}$ ) is the polarization in regions where the hysteresis loop has closed in on itself. The coercive field strength is the minimum applied electric field strength needed to completely flip the polarization state; it is approximately the voltage at which the vertical portion of the P–E curve crosses the x-axis. Generally, the hysteresis loop will not have a vertical portion if switching is incomplete.

<sup>‡</sup>While essentially equivalent to *remnant*, *remanent* is the technical term used to describe residual magnetism and is used here as the field of (ferro)magnetism is the source of much piezoelectric and ferroelectric terminology due to the many parallels.

Resistors and lossy capacitors also have open P–E hysteresis loops, but these loops are generally rounded at voltage extremes whereas ferroelectric loops close off at saturation. There are several additional nonferroelectric effects present at the nanoscale that can cause hysteresis loops to be observed including effects due to charge injection, Vegard strain, and Joule heating.<sup>189</sup> For certain materials, ferroelectric hysteresis can also be observed optically by monitoring domain movements and switching. P–E loops, like most ferroelectric properties, are generally temperature, frequency, and stress dependent, so it is important to keep in mind a material’s intended use conditions when performing evaluative measurements.

Most ferroelectrics lose their ferroelectric properties above the Curie, or transition, temperature ( $T_C$ ), similar to how most piezoelectrics lose their fixed polarization above  $T_C$ . While not unique, a significant attribute of ferroelectrics is their anomalous behavior near  $T_C$ .<sup>187</sup> Most noteworthy of these abnormalities is in the permittivity ( $\varepsilon$ ) which rises sharply with temperature to a peak at  $T_C$ . Above  $T_C$ , the permittivity of a ferroelectric decreases, often following the Curie–Weiss law ( $\varepsilon = \frac{C}{T-T_C}$ , where  $C$  is the Curie constant).<sup>187</sup> Other anomalous properties may include changes to the piezoelectric constants, specific heat, and electrocaloric coefficient near  $T_C$ .<sup>187</sup>

There are many useful applications of ferroelectric materials, including those due to their commonly high permittivity values. The high permittivity leads to ferroelectrics being among the best piezoelectric transducers since the high permittivity leads to a high electromechanical coupling factor; the high permittivity also helps to produce good capacitors.<sup>187</sup> Often, the most desirable properties of ferroelectrics occur near  $T_C$ ; therefore, much effort has gone into “room-temperature” ceramic ferroelectrics which have been tuned by carefully combining multiple ferroelectric components along with other additives to preform well near ambient temperatures. It is also often desirable to widen the peak of the desired property such that the device is not nearly as temperature sensitive.

Applications of ferroelectrics vary widely and range from dielectric bolometers<sup>190</sup> to potential biomedical uses<sup>191</sup> to photovoltaics<sup>192</sup> and energy storage.<sup>193</sup> Most of these applica-

tions take advantage of more general materials properties that are enhanced in ferroelectric materials near the Curie temperature. One long-standing research interest that takes direct advantage of fundamental ferroelectric switching, however, is applying ferroelectrics towards use as nonvolatile computer memories.<sup>194</sup> There are three ways that the state of a ferroelectric memory can be read out: (1) as a charge read out during the switching or non-switching of a capacitor, (2) as a shift in the I–V curve of a field effect transistor due to the polarization state of the ferroelectric gate dielectric, and (3) as the current tunneling directly through a thin capacitor.<sup>194</sup> Capacitance-based ferroelectric memories are the oldest and mostly widely studied. They are read in a destructive manner by applying a bias voltage across the capacitor and measuring the resulting charge; domains that are flipped in the process will yield much greater charge than those already in the end state. Integrating ferroelectrics into the gate stack of field effect transistors overcomes many shortcomings of capacitor based ferroelectric memories, including enabling nondestructive readout through examination of the resulting I–V curve. Finally, use of ferroelectric tunneling junctions allow for the direct readout of the ferroelectric state. The recent development of methods to reliably produce very thin ferroelectrics has revived interest in further exploring this method. Despite the considerable promise of and research interest in ferroelectric based nonvolatile memories, they have largely stayed relegated to the lab due to cost and technological limitations that have, so far, left them inferior to more traditional memories.

### **6.1.1 Single-Molecule Ferroelectric Bowls**

“Bowl-like” corannulene derivatives hold considerable promise as single-molecule ferroelectrics. Most ferroelectrics are crystalline, and the polarization is switched by flipping the position of an atom in the lattice through a small energy maximum. Polymer based ferroelectrics, on the other hand, are switched by rotating the orientation of the polymer chains. Corannulene molecular bowls, however, hold promise to function as ferroelectrics through a conforma-

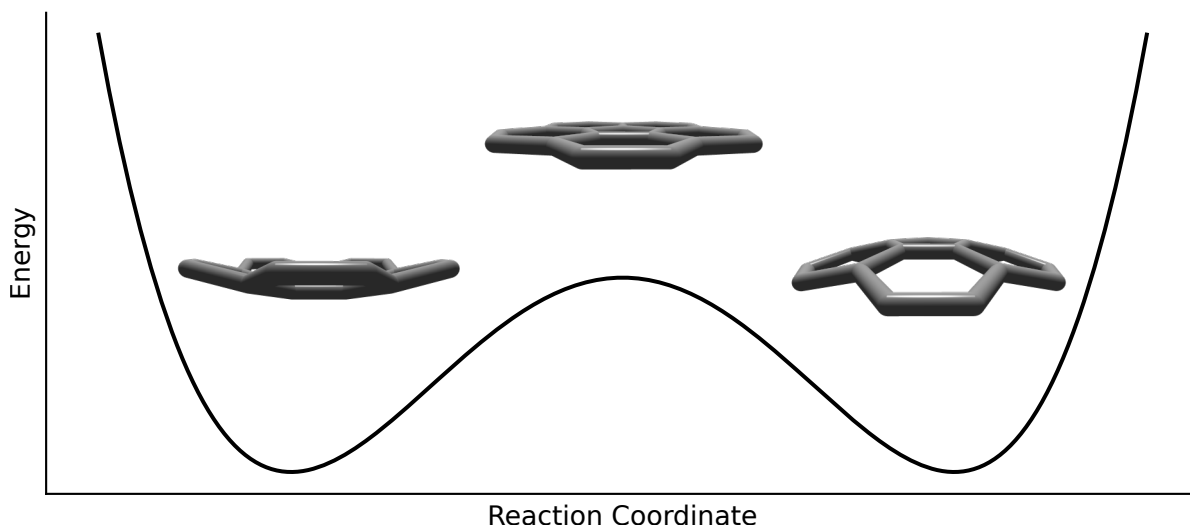


Figure 6.2: Schematic of corannulene bowl-to-bowl inversion. An example fourth-order polynomial potential energy well is shown below the 3D models. As the bowl is inverted, it passes through a small, strain-induced energy maximum; therefore, the two bowls are the preferred conformations.

tional change—bowl-to-bowl inversion (Figure 6.2). Quan, of our group, computationally predicted that bowl-like corannulenes and similar aromatic “buckybowl” molecules exhibit piezoelectric and ferroelectric properties<sup>128</sup> while Miller, also of our group, experimentally demonstrated their piezoelectric response via dual AC resonance tracking piezo force microscopy (DART-PFM) and produced some evidence of ferroelectricity via scanning Kelvin probe force microscopy (SKPFM) methods.<sup>195</sup> Other, similar bowl-to-bowl ferroelectric inversions have been observed experimentally.<sup>196</sup> As a switchable single molecule, these molecular bowls hold promise for memory applications due to their intrinsically small size—they are “conformational memory.”

The height of the bowl-to-bowl inversion energy and thermal barrier of these molecules is key for experimental realization, as the inversion voltage must be below the dielectric breakdown voltage. Corannulene bowls have a fourth-order relationship between bowl depth and inversion energy, meaning that shallow bowls are necessary for practical applications.<sup>128,197</sup> Quan computationally showed that shallower bowls tend to be more flexible which leads to

higher piezoelectric coefficients. He also showed that substituting strong electron withdrawing or donating groups onto the rim of the bowl results in a lower inversion energy by destabilizing the ground state and only has a minimal effect on bowl depth. The substituents can also serve added benefits, as, for example, acid groups can serve as anchor points to oxide substrates.

### 6.1.2 Double-Wave Method

Developed by Fukunaga and Noda,<sup>198</sup> the double-wave method allows for quick, accurate measurements of ferroelectric P–E hysteresis loops where the hysteresis component can be extracted automatically without the need to manually make assumptions about what needs to be removed.\*\*<sup>198</sup> A raw P–E hysteresis loop consists of an amalgamation of ferroelectric, dielectric, and conductive components.<sup>3,198</sup> Traditionally, the non-ferroelectric components were subtracted out manually through measurement circuit modifications or through post-processing simulations based on various assumptions such that a reasonable loop was obtained.<sup>198</sup> In the double-wave method, the extraneous components are directly removed. An optional preparation pulse flips domains into the same polarization state; then, two identical positive triangle wave voltage pulses are applied followed by two negative ones (Figure 6.3). The current measured from the first pulse of each pair contains the ferroelectric component—the “memory”—as well as the extraneous components, while the second pulse of each pair only contains the extraneous components as the ferroelectric state has already been flipped. The pure ferroelectric component is obtained by simply subtracting the second pulse from the first pulse. While initially implemented using a Sawyer–Tower circuit<sup>200</sup> and partial sinusoidal waves, modern source-measure units (SMUs) can approximate triangle waves and perform the necessary pulses and measurements internally.<sup>198,201</sup> SMUs generally have less drift than a Sawyer–Tower circuit and are advantageous for low-frequency measurements, but, deleteriously, electrical interference from electromagnetically noisy environments can have a

---

\*\*Strictly speaking, these are electrical displacement–electric field (D–E) loops, but, since  $P = D - \epsilon_0 E$  and  $D \gg \epsilon_0 E$  for most ferroelectrics, the terms are often used interchangeably.<sup>199</sup>

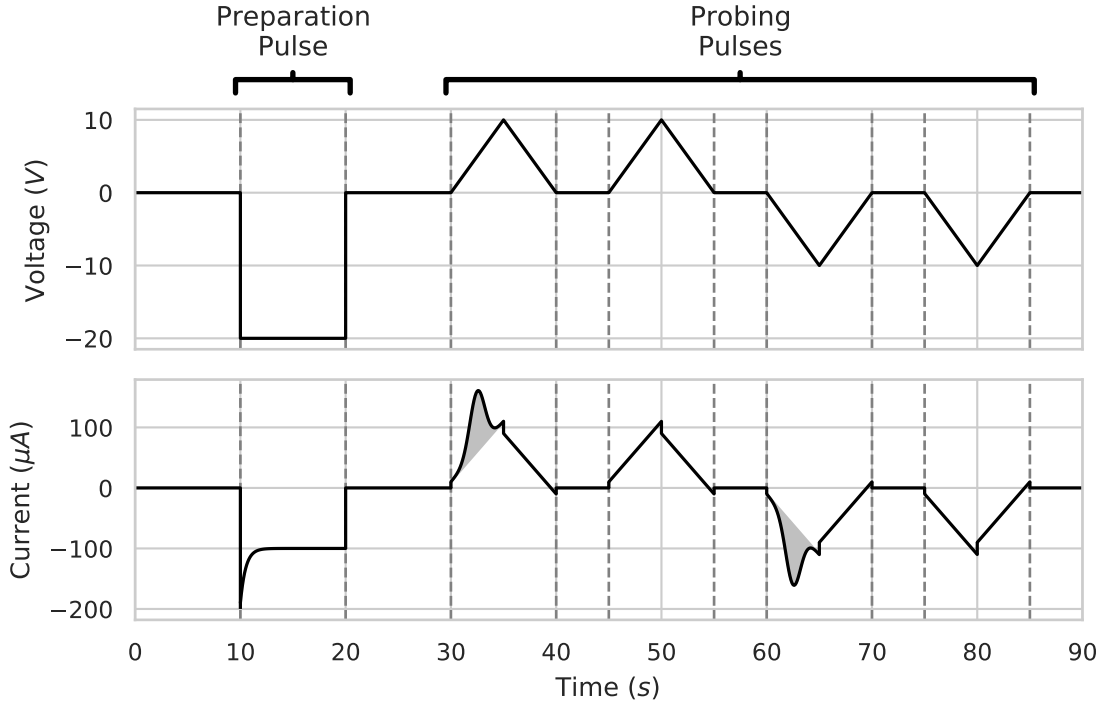


Figure 6.3: Double-wave method example.<sup>††</sup>(Top) Example applied voltage pulses. An optional preparation pulse (of equal or greater magnitude than the probing pulses) flips domains into the same state. Then, pairs of positive and negative probing pulses are applied. (Bottom) Example measured current resulting from the applied voltage potential. The shoulder (shaded region) on the first peak of the pair is the ferroelectric component; the second peak only contains the displacement (vertical offset) and leakage (slope) currents.

much larger effect on the signal.<sup>199</sup> The double-wave method is related to the positive-up negative-down (PUND) method except that the double-wave method uses triangle waves instead of square waves to minimize displacement currents.<sup>202</sup> Despite the advantages of the double-wave method in largely eliminating dielectric and conductive components from hysteresis loops, care must still be taken as several pitfalls still remain which can lead to false conclusions about ferroelectric behavior.

<sup>††</sup>Figure adapted from reference [201].



### 6.1.3 EGaIn Electrodes

Eutectic gallium-indium (EGaIn) electrodes are conformal electrodes suitable for direct electrical measurements of SAMs. First introduced by the Whitesides group<sup>203</sup> and consisting of a 3:1 ratio (w/w) of gallium and indium, they take advantage of the material’s room-temperature fluid-metal properties. Crucially, this mixture is a liquid at room temperature that holds its shape; this allows it to be formed into metastable cones with micrometer-diameter tips. Combined with its high electrical conductivity, it is able to make low-contact-resistance interfaces with materials such as SAMs. It is an ideal electrode for studying SAMs because it makes small-area, conformal, non-damaging contact; the small contact area helps to minimize the effect of monolayer defects and prevent electrical shorts.<sup>203</sup> EGaIn electrodes also have the added benefits of being able to be formed without special equipment and being nontoxic.

## 6.2 Materials and Methods

### 6.2.1 Materials

Ethanol (200 proof) was obtained from Decon Labs. 1-Pyrenecarboxylic acid (97%) (PCA), gallium-indium eutectic (Ga 75.5%/In 24.5%,  $\geq 99.99\%$  trace metals basis) (EGaIn), and indium tin oxide (ITO) coated glass substrates (surface resistivity  $30\ \Omega/\text{sq}$ – $60\ \Omega/\text{sq}$ ) were obtained from Sigma-Aldrich. 4,4',4'',4'''-(dibenzo[*ghi,mno*]fluoranthene-1,2,5,6-tetrayl)tetra-benzoic acid (H<sub>4</sub>DFT) was synthesized via a previously outlined method and provided by a collaborator.<sup>204</sup> All chemicals were used as received.

### 6.2.2 Sample Preparation

In order to prepare self-assembled monolayers (SAMs) of the target molecules, ITO substrates were first cleaned by subjecting them to ultrasonication in ethanol for at least 30 min and then drying them under nitrogen flow. Next, a solution of the target molecule (1 mM PCA and 0.125 mM H<sub>4</sub>DFT) was drop-cast onto the substrate. The sample was then placed in a vacuum desiccator for at least 1 h to dry prior to testing.

### 6.2.3 Measurement Setup

Measurements were taken using a Keithley SourceMeter 2614 source-measure unit controlled via a custom Python script. The positive lead was connected to the needle of the EGaIn electrode while the negative lead was connected to the substrate. The EGaIn electrode was prepared by lowering a blunt 26 G needle into a drop of EGaIn on a gold substrate and carefully withdrawing it such that a cone of EGaIn was drawn from the drop and remained on the tip of the needle. Depending on the measurement conditions, the substrate either rested on a temperature controlled plate inside a metal probe station or under an inert nitrogen atmosphere inside a glove box. When the probe station was used, the temperature was controlled by the probe station using a combination of circulation of chilled fluid and resistive electric heat; when the glove box was used, the temperature was lowered by placing dry ice in contact with the outside of the glove box directly underneath the sample. The temperature was measured using a thermocouple temperature probe taped to the aluminum block on which the sample substrate rested. While a sharp cone was easily drawn under atmospheric conditions, the dry, inert atmosphere of the glove box altered the surface tension of the EGaIn resulting in a considerably shorter, rounder cone (Figure 6.4). The surface of

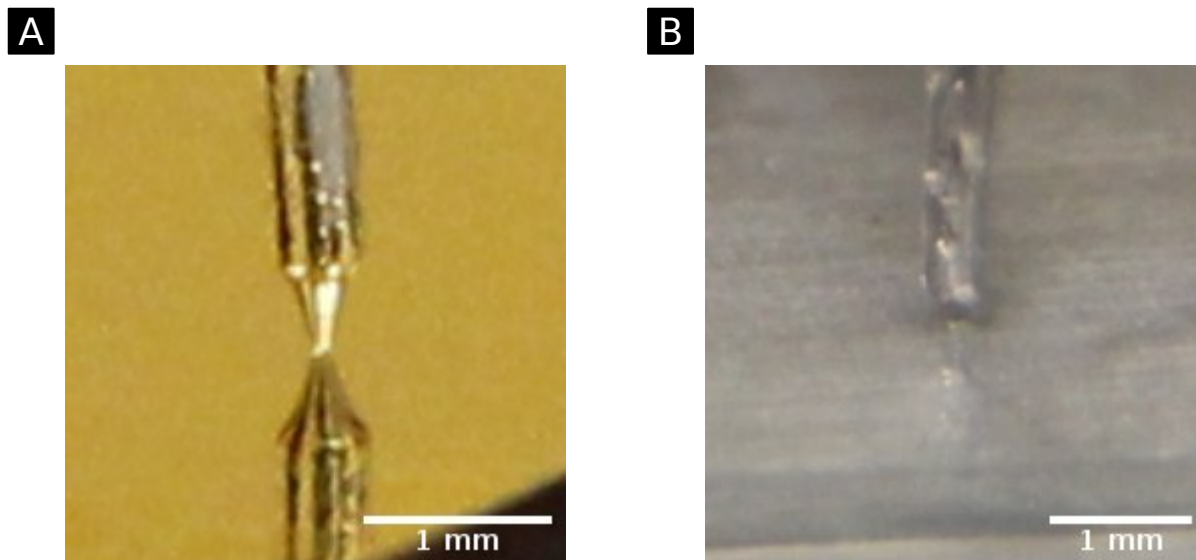


Figure 6.4: EGaIn electrode measurement setup. (A) Sharp conical tip drawn under atmospheric conditions (shown over gold substrate for clarity). (B) Blunt tip drawn under inert conditions.

EGaIn electrodes normally consists of a film of water coating a layer of gallium oxides;<sup>203</sup> the lack of moisture and oxygen in the glove box likely greatly reduces these layers leading to the altered drawing behavior.

#### 6.2.4 Ferroelectric Measurements

Ferroelectric measurements were taken using the double-wave method. This consisted of a negative preparation pulse being applied to the sample followed by two identical positive triangle wave pulses and two identical negative triangle wave pulses (Figure 6.3). The voltage applied ranged from 1 V to 20 V where the preparation pulse (usually 10 V or 20 V) was at or above the maximum voltage of the triangle waves. Generally, 16 sets of 1 s duration pulses were applied over the course of  $\sim 100$  s, although other pulse lengths and numbers of repetitions were also examined. Analysis was performed using a Python script (see minimum working example, Appendix D.1). In order to determine the resultant charge, the current for the second pulse of each pair of triangle waves was subtracted from the first pulse of the

pair and the difference integrated. The resultant charge was plotted as a function of applied voltage to produce charge–voltage loops which are qualitatively equivalent to P–E loops (the y-axis is scaled since charge is not divided by electrode area and the x-axis is scaled because applied voltage is not divided by electrode separation).

### 6.3 Results and Discussion

We set out to study the possible ferroelectric and piezoelectric properties of monolayers of bowl-like molecules. 4,4',4'',4'''-(Dibenzo[*ghi,mno*]fluoranthene-1,2,5,6-tetrayl)tetrabenzoic acid (H<sub>4</sub>DFT; Figure 6.5) was chosen as a model buckybowl system due to its synthetic accessibility and acid substituents that allow for anchoring of the molecule to an ITO substrate. Miller optimized deposition parameters to ensure uniform coverage with minimal aggregation and studied the resulting monolayers using piezo force microscopy techniques.<sup>195</sup> Using DART-PFM he showed an effective piezoelectric charge constant ( $d_{\text{eff}}$ ) of 26.49 pm/V on ITO for H<sub>4</sub>DFT. As a control, 1-pyrenecarboxylic acid (PCA; Figure 6.6) was used due to its similar  $\pi$ -conjugated system and acid attachment; it showed a  $d_{\text{eff}}$  of only 0.291 pm/V, showing that the piezoelectric response of H<sub>4</sub>DFT likely comes from its molecular bowl conformation. Next, he used SKPFM to examine the ferroelectric response. The resulting surface potential–applied field plots showed hysteresis, lending credence to the monolayer’s ferroelectric nature. Once again, PCA was used as a control and showed little to no change in surface potential, even at the maximum applied fields. Due to the minimally open hysteresis loop and temperature dependence of ferroelectrics, he performed additional scans at other temperatures; the surface potential changed with temperature as expected, which helped to eliminate redox mechanisms as a potential source of the hysteresis. The purpose of this work was to test for evidence of ferroelectricity in H<sub>4</sub>DFT through use of bulk-scale P–E loop measurements.

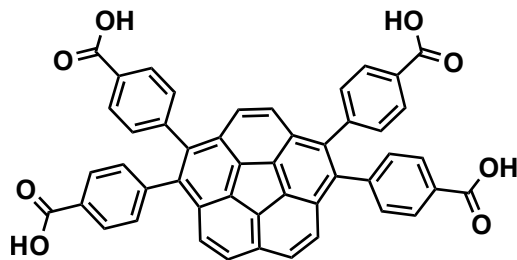


Figure 6.5: 4,4',4'',4'''-(Dibenzo[*ghi,mno*]fluoranthene-1,2,5,6-tetrayl)tetrabenzoic acid ( $H_4DFT$ ) structure.

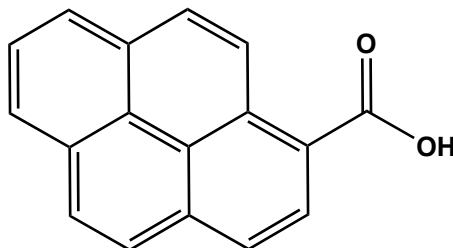


Figure 6.6: 1-Pyrenecarboxylic acid (PCA) structure.

Sample current–voltage and charge–voltage loops are presented in Figure 6.7.<sup>‡‡</sup> The parameters of  $\sim 1$  s duration probing pulses with 16 sets of pulses per scan were chosen as they were found to be a good balance between noise and drift; shorter pulse durations lead to noisier data while drift started to become a problem with longer overall scan durations. Most scans were recorded at  $\sim 15^\circ\text{C}$  as that temperature yielded the most consistent results. One immediately notices that, generally, the charge loop is not continuous; that is, the positive and negative voltage sweeps do not yield equal but opposite charge. Additionally, the loops do not scale with increased applied voltage as would be expected for a ferroelectric. In a traditional P–E loop, a straight line is seen at low field; it begins to open up above a threshold voltage value. As the field increases further, the characteristic square shape develops before eventually closing off as high fields after the saturation polarization is reached. The observed loop, however, generally shrinks in height with increasing voltage while growing in width and maintaining approximately the same overall shape. PCA, which is not expected to be

<sup>‡‡</sup>The data presented herein is a best attempt at showing the most common behavior for a given set of conditions; there was, however, a large spread of data variability across the measurements.

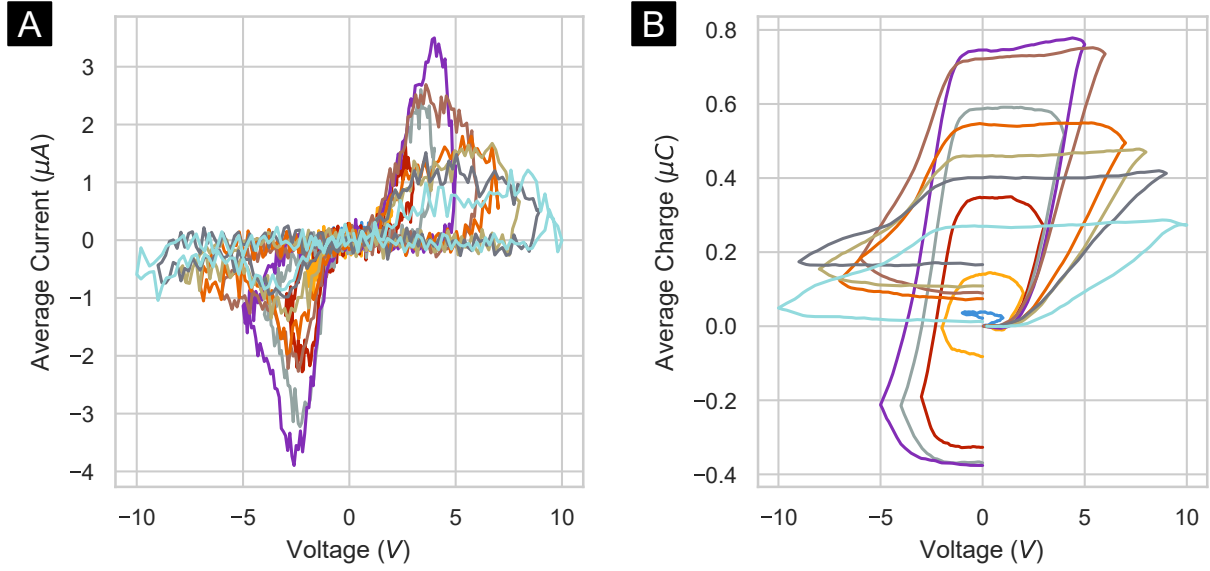


Figure 6.7: Sample (A) current-voltage and (B) charge-voltage curves for  $\text{H}_4\text{DFT}$  up to 10 V. Each curve is the average of 16 consecutive sets of probing pulses recorded after a  $-10$  V preparation pulse at  $13.7^\circ\text{C}$ .

ferroelectric, was measured as a control (Figure 6.8). It displays similar behavior to the  $\text{H}_4\text{DFT}$  although the current-voltage loops are less symmetric; the negative half of the curve shows a curve downward at fields more negative than  $-5$  V and a separate distinct peak between  $-5$  V and  $-1$  V. To further explore the effect of voltage, scans of  $\text{H}_4\text{DFT}$  were taken where voltages were swept up to 20 V (Figure 6.9). Here, the current-voltage curves begin to exhibit behavior similar to that seen with PCA, while the charge-voltage curves take on a more rounded shape—the charge is no longer constant on the backside of the pulse as the voltage is decreased and there is still no evidence of saturation.

Since ferroelectric response is often very temperature sensitive, measurements were taken under an array of temperatures. As seen in Figure 6.10, temperature affected the magnitude of recorded charge but did not significantly alter the shape of the charge-voltage loops. At temperatures of  $\sim 25^\circ\text{C}$  and  $\sim 35^\circ\text{C}$ , larger voltages resulted in large charge increases which were more heavily weighted towards the positive voltage sweep. The curves measured at  $\sim 5^\circ\text{C}$  were much noisier due to the lower magnitude of charge produced. Charge generally

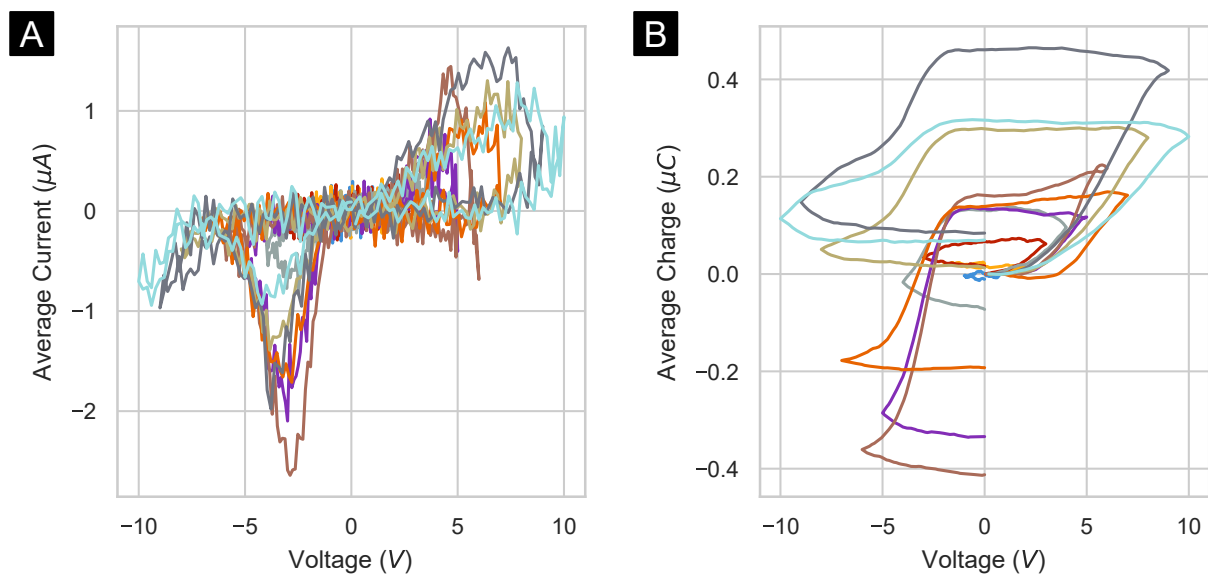


Figure 6.8: Sample (A) current–voltage and (B) charge–voltage curves for PCA control. Each curve is the average of 16 consecutive sets of probing pulses recorded after a  $-10\text{ V}$  preparation pulse at  $13.9^\circ\text{C}$ .

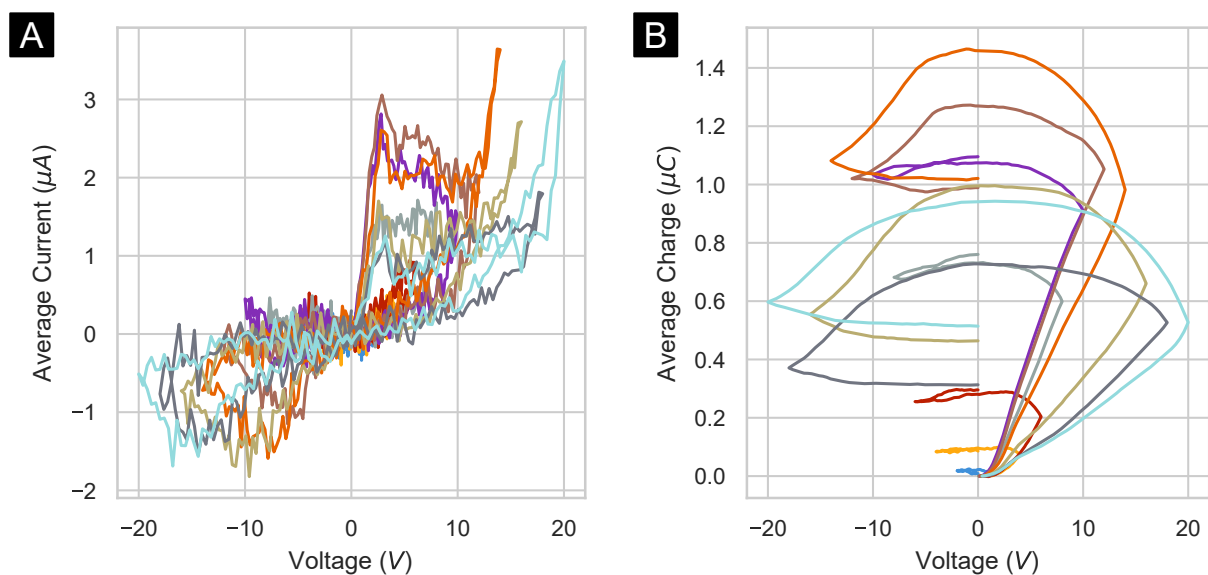


Figure 6.9: Sample (A) current–voltage and (B) charge–voltage curves for  $\text{H}_4\text{DFT}$  up to 20 V. Each curve is the average of 16 consecutive sets of probing pulses recorded after a  $-20\text{ V}$  preparation pulse at  $13.3^\circ\text{C}$ .

increased with temperature, with the maximum charge increasing two orders of magnitude as the temperature increased from  $\sim 5^\circ\text{C}$  to  $\sim 35^\circ\text{C}$ . Increases in current leakage with temperature are expected, but the double-wave method should eliminate that effect. A change in ferroelectric character with temperature is normally associated with a change in loop shape, which was not observed.

Ferroelectric switching is not always near instantaneous. If probing pulses are too short to adequately switch a given material, resulting measurements may behave unusually. The effect of probing pulse speed on  $\text{H}_4\text{DFT}$  is examined in Figure 6.11. The left pane shows the current trace for each of the probing speeds; the traces are similar across the speeds. For most measurements, the height of the first probing pulse of a set is greater than the second pulse, and the peaks from the positive voltage pulses (first set) are greater in magnitude than those from the negative pulses (second set). This behavior is different than what is expected for ferroelectrics measured using the double-wave method; the height of both peaks in a set is expected to be the same, while the switching current should be seen as a left shoulder in the first peak of the set. The current–voltage (middle pane) and charge–voltage (right pane) curves show somewhat differing behavior with pulse duration where the  $\sim 10\text{ s}$  and  $\sim 0.1\text{ s}$  pulses show more closed off, less symmetric loops.

Next, we turn towards a more detailed examination of voltage pulses and the resulting current traces. Figure 6.12 shows the current traces for a number of different preparation and probing pulse sequences: (A)  $-10\text{ V}$  preparation pulse followed by two  $5\text{ V}$  and two  $-5\text{ V}$  probing pulses, (B)  $-10\text{ V}$  preparation pulse followed by three  $5\text{ V}$  and three  $-5\text{ V}$  probing pulses, (C) no preparation pulse followed by three  $5\text{ V}$  and three  $-5\text{ V}$  probing pulses, and (D)  $10\text{ V}$  preparation pulse followed by three  $-5\text{ V}$  and three  $5\text{ V}$  probing pulses. When sets of three pulses were used, the height of the second and third current peaks were generally shorter than the first but were both of approximately equal magnitude; this indicates that something additional is occurring when the first pulse of a given polarity is applied. When no preparation pulse is applied, the magnitude difference between the first and second pulses



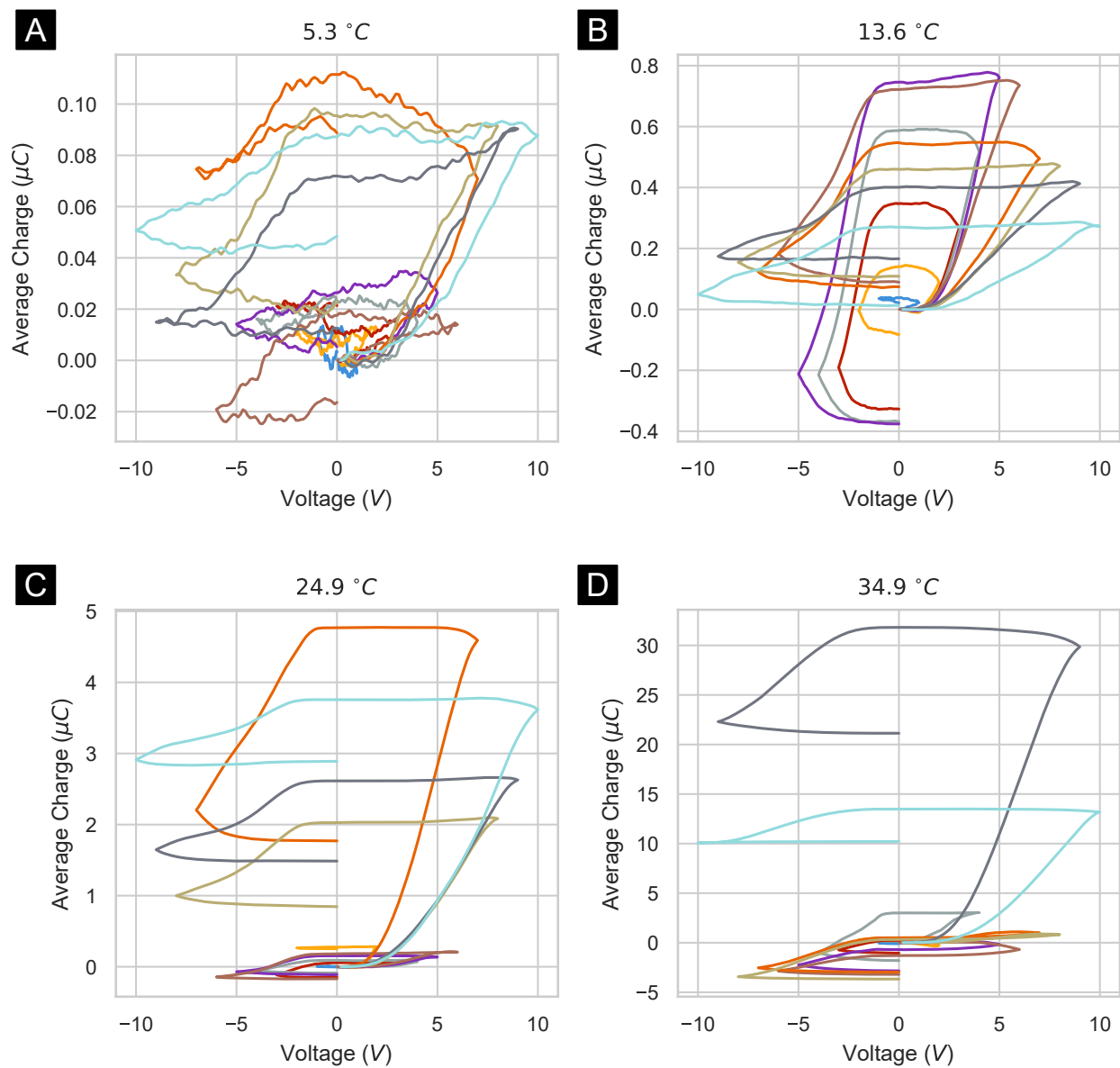


Figure 6.10: Sample charge-voltage curves for  $H_4DFT$  at different temperatures. Scans were taken at (A)  $5.3^\circ C$ , (B)  $13.6^\circ C$ , (C)  $24.9^\circ C$ , and (D)  $34.9^\circ C$ . Each curve is the average of 16 consecutive scans recorded after a  $-10$  V preparation pulse.

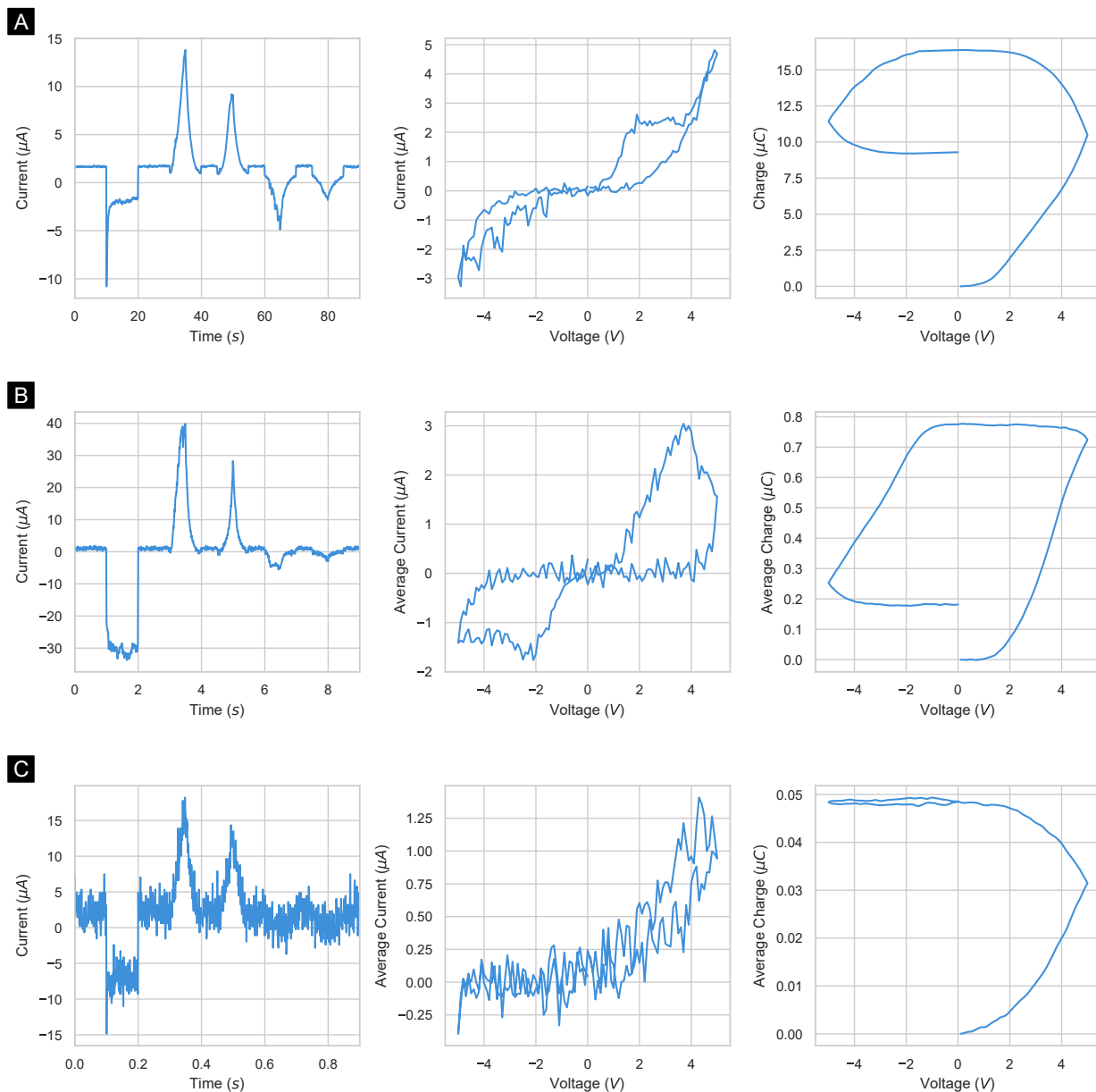


Figure 6.11: Effect of pulse speed on  $H_4$ DFT measurements. Current-time (left), current-voltage (middle), and charge-voltage (right) plots are shown for (A)  $\sim 10$  s, (B)  $\sim 1$  s, and (C)  $\sim 0.1$  s pulses. The current-voltage and charge-voltage plots are averages of (A) 1, (B) 16, and (C) 256 sets of pulses. A preparation pulse of (A)  $-10$  V, (B)  $-10$  V, and (C)  $-5$  V was applied followed by two  $5$  V and two  $-5$  V probing pulses. All measurements were taken at  $\sim 15^\circ C$ .

is smaller; this is expected as the domains were not all fully aligned to begin with. When the pulse polarity is reversed, the current polarity is simply flipped.<sup>§§</sup> Also of note when examining current traces, is that the magnitude of the current peaks generally decreases over the course of the first few sets of pulses before stabilizing (Figure 6.13).

Finally, the samples and measurement apparatus were moved into a glove box with an inert nitrogen atmosphere to help rule out any redox effects of surface moisture. These results are presented in Figure 6.14. For measurements taken at ambient temperatures, no significant changes were observed compared to atmospheric conditions. The lack of humidity allowed us to use dry ice to further cool the samples to  $\sim -20^\circ\text{C}$ ; measurements at this temperature resulted in much smoother curves. Measurements of the PCA control under the inert atmosphere were more unusual (Figure 6.15); at ambient temperatures, the current peak from the second probing pulse of each set of positive pulses was the larger of the two, resulting in a butterfly-like current–voltage curve, while at colder temperatures, the current–voltage loop was more typical save that it contained sharper peaks. The magnitude of the currents in the glove box measurements are not directly comparable to the ones taken under atmospheric conditions as the inert environment affects the drawing behavior of the EGaIn electrodes resulting in a considerably blunter tip and therefore larger contact area.

Besides ferroelectricity, redox behavior is another potential source of hysteresis in the measurements. In the literature,  $\text{H}_4\text{DFT}$  was previously shown to be redox active when part of a crystalline hybrid scaffold.<sup>204</sup> In a cyclic voltammetry experiment in that environment, it underwent one irreversible reduction at a peak potential of  $-1.64\text{ V}$  versus a saturated calomel reference electrode; this is similar to the behavior of related benzoic acids. Similarly, PCA was shown in cyclic voltammetry experiments to undergo an irreversible oxidation.<sup>205</sup> Irreversible redox behavior might help explain the observed data in the current–voltage and charge–voltage loops for  $\text{H}_4\text{DFT}$  and PCA; the observed scans may, in fact, be a convolution of ferroelectric and redox behavior.

---

<sup>§§</sup>The larger negative peaks in Figure 6.12(D) are simply due to the particular sample and measurement; it was recorded immediately after the current trace in Figure 6.12(C) without the sample being disturbed.

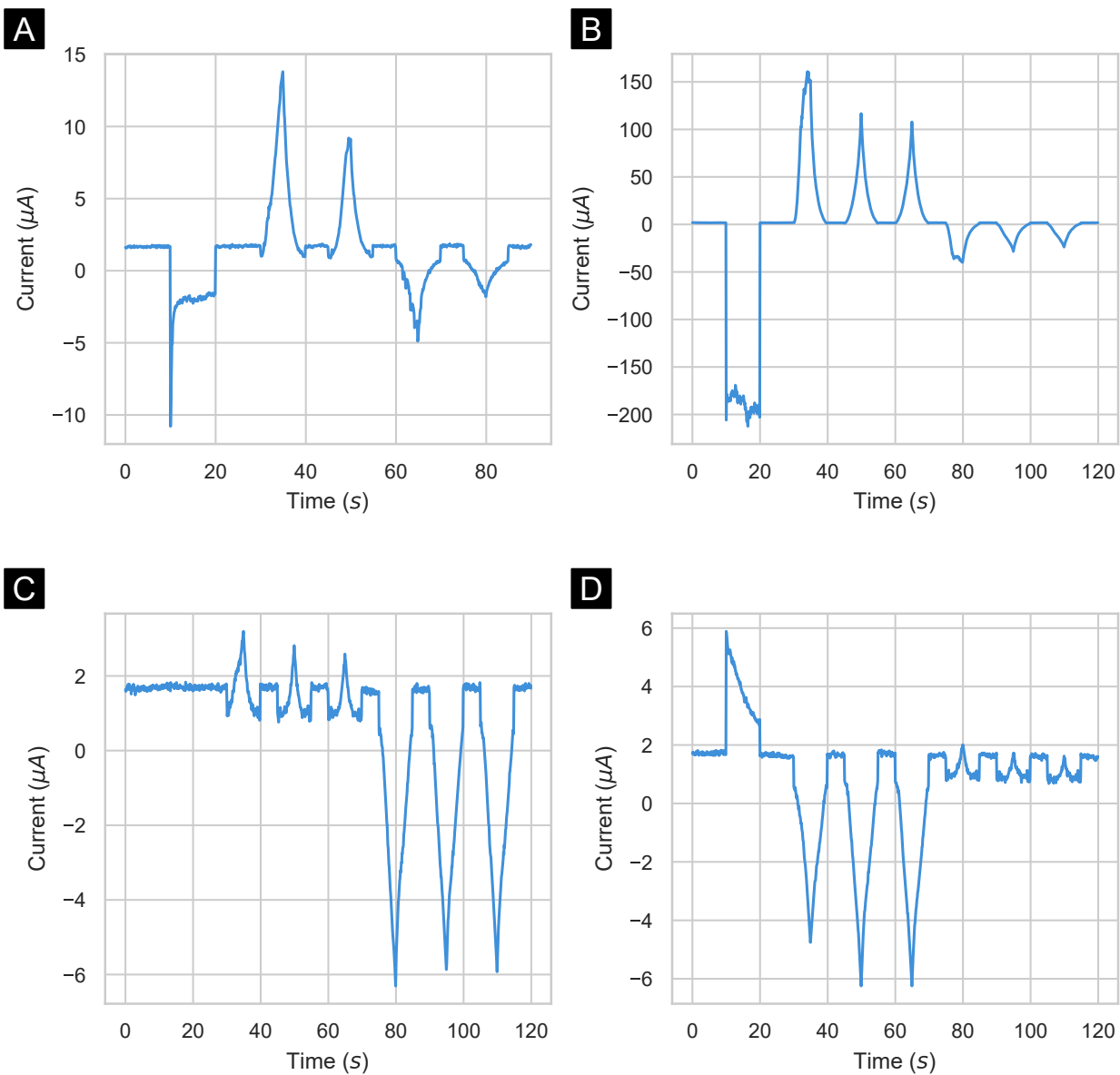


Figure 6.12: Sample current–time traces for  $H_4DFT$  under different pulse sequences. (A) Current trace under normal conditions. (B) Current trace under triplet pulse conditions. (C) Current trace under triplet pulse conditions without a preparation pulse. (D) Current trace under triplet pulse conditions with the pulse polarity reversed. All measurements were taken at  $\sim 15^\circ C$ , the preparation pulse, if present, was 10 V in magnitude, and the probing pulses were 5 V in magnitude. A slower pulse duration of  $\sim 10$  s was used.

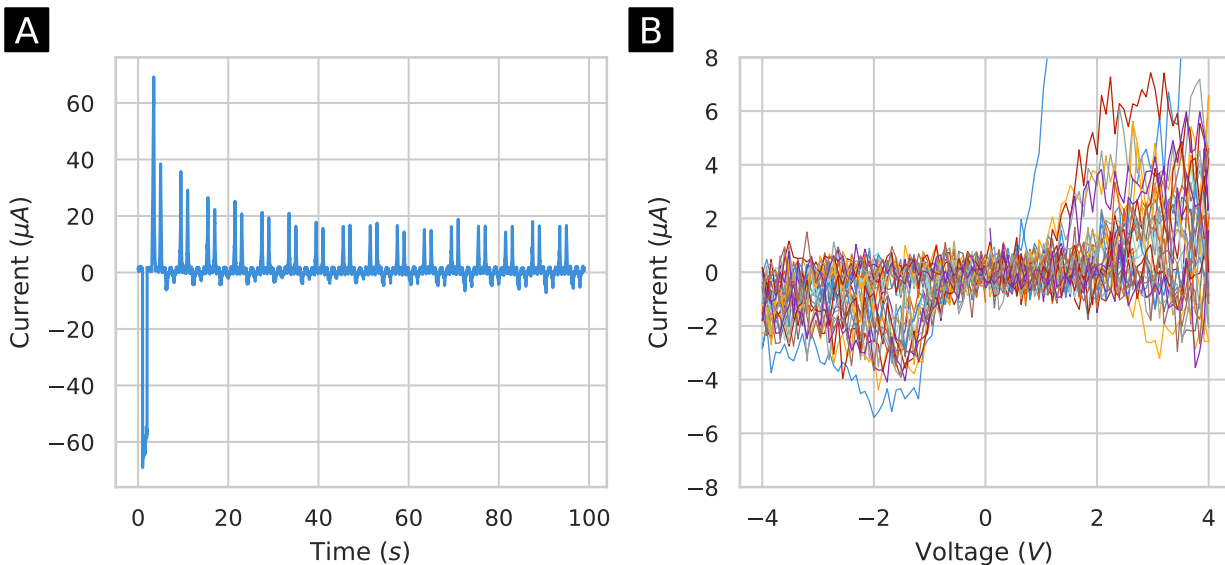


Figure 6.13: Sample current behavior for  $\text{H}_4\text{DFT}$  over time. (A) Current trace for complete measurement of preparation pulse and all 16 sets of probing pulses. (B) Current–voltage loops for each individual set of probing pulses. Measurements were taken at  $14.1^\circ\text{C}$  with a  $-10\text{ V}$  preparation pulse and  $4\text{ V}$  in magnitude probing pulses.

## 6.4 Conclusions

Double-wave method current–voltage and charge–voltage loops were measured under a variety of conditions in an attempt to gather additional evidence of the potentially ferroelectric nature of the bowl-like molecule  $\text{H}_4\text{DFT}$ . Unfortunately, while these scans showed hysteresis, the loops did not respond to changing conditions as would be expected for a ferroelectric material. While the material may still be ferroelectric as predicted, interference from redox behavior or other effects prevented the use of P–E loops as clear evidence of ferroelectricity. In the future, monolayers of  $\text{H}_4\text{DFT}$  can be reexamined for other potential evidence of ferroelectricity, and it may even be possible to produce archetypal P–E loops using a different measurement setup

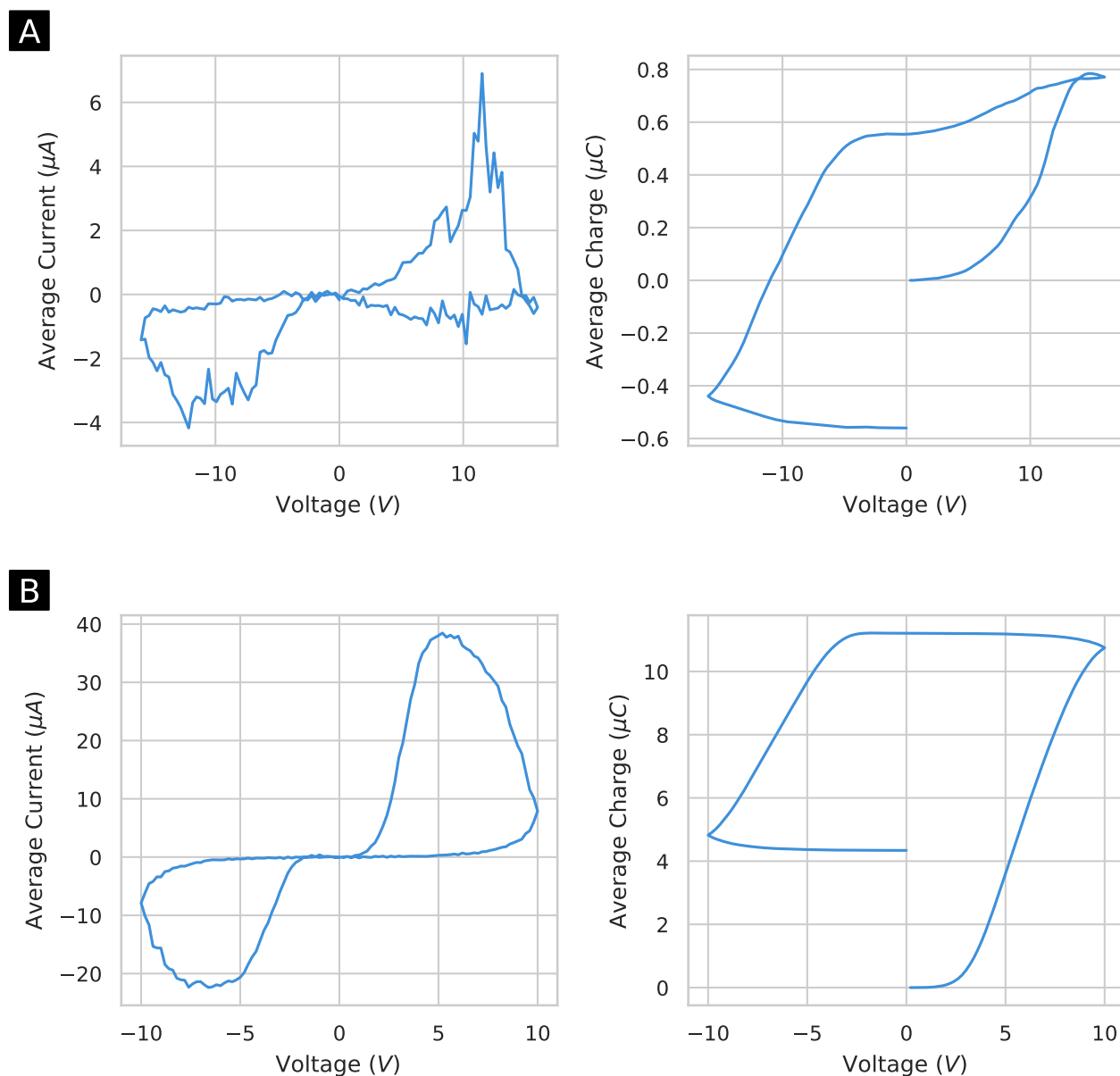


Figure 6.14: Current–voltage (left) and charge–voltage (right) curves for  $\text{H}_4\text{DFT}$  measured under inert conditions. Measurements were taken at (A)  $\sim 20^\circ\text{C}$  with a  $-20\text{ V}$  preparation pulse and (B)  $\sim -10^\circ\text{C}$  with a  $-10\text{ V}$  preparation pulse. All measurements were taken inside a glove box under an inert nitrogen atmosphere and consist of the average of 16 sets of pulses.

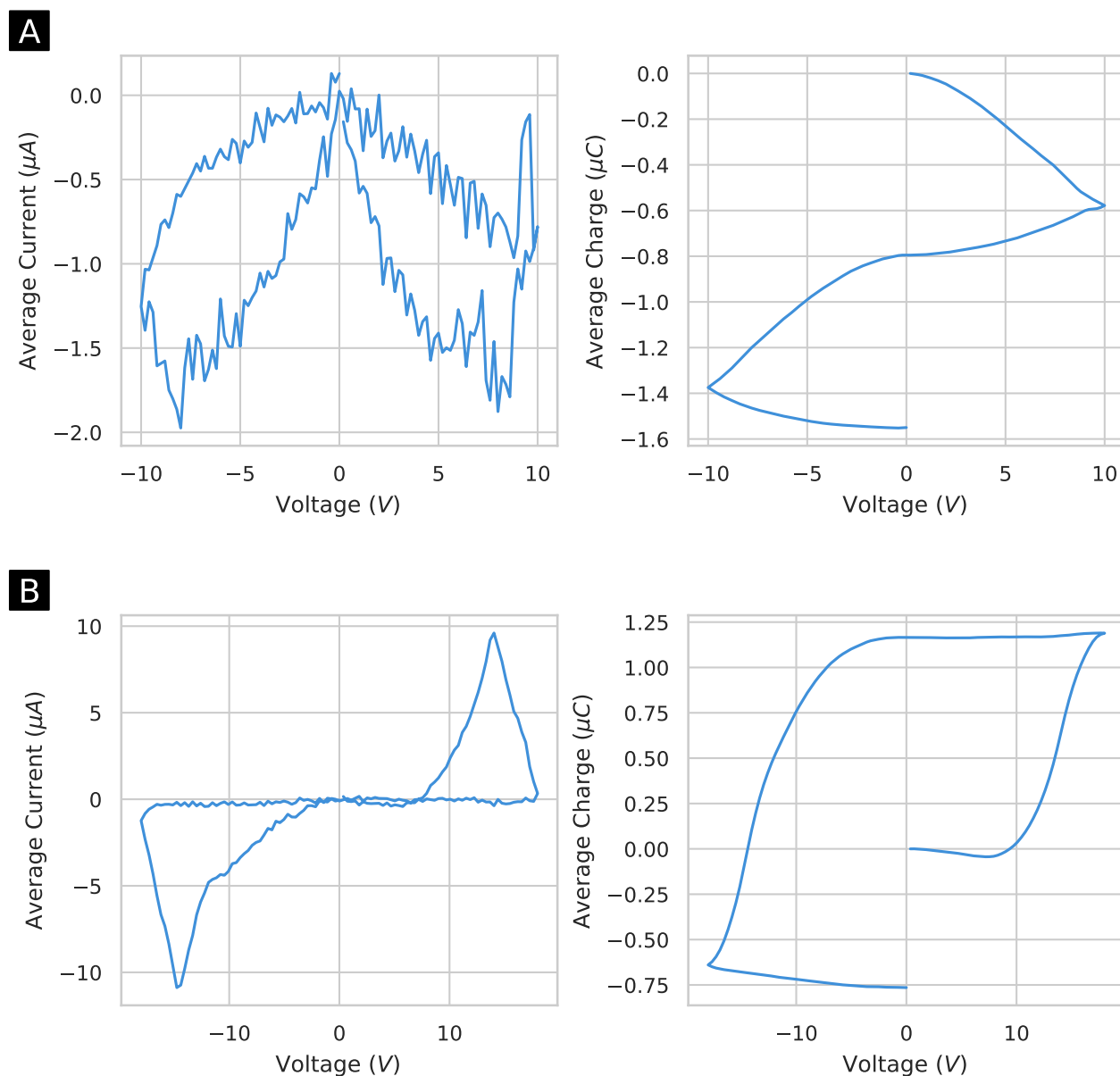


Figure 6.15: Current–voltage (left) and charge–voltage (right) curves for PCA control measured under inert conditions. Measurements were taken at (A)  $\sim 20^\circ\text{C}$  with a  $-20\text{ V}$  preparation pulse and (B)  $\sim -15^\circ\text{C}$  with a  $-20\text{ V}$  preparation pulse. All measurements were taken inside a glove box under an inert nitrogen atmosphere and consist of the average of 16 sets of pulses.

such as using a traditional Sawyer–Tower circuit to reduce noise and increase measurement frequency. Monolayers of bowl-like molecules hold significant potential as single-molecule ferroelectrics and are deserving of further study.

## 6.5 Acknowledgment

Software used in this chapter includes, in part, Avogadro,<sup>150</sup> Matplotlib,<sup>109</sup> NumPy,<sup>110</sup> pandas,<sup>111</sup> pySerial, SciPy,<sup>112</sup> and Python-VXI11. The color cycle used in the figures is courtesy of Matthew Petroff.



## 7.0 Conclusions and Future Directions

### 7.1 Conclusions

Piezoelectric materials research began with the study of single crystals, before moving on to polycrystalline and ceramic materials. Now, as we near the sesquicentennial of their discovery, a new paradigm of molecularly engineered piezoelectrics is beginning to emerge. This dissertation presented several frameworks where rational design was applied towards the further understanding of the molecular origins of the piezoelectric effect in organic and biomolecular materials. It began by introducing the history and basic concepts of piezoelectricity and related phenomena, before moving on to a discussion of measurement methods, especially those best suited for the characterization of this growing subset of soft materials and devices. Next, frameworks to study molecular effects on bulk piezoelectric response based on (1) the use of polar, small organic molecule dopants dispersively adhered to a poly(dimethylsiloxane) (PDMS) foam scaffold and (2) self-assembled monolayers (SAMs) of oligopeptides were presented. Subsequently, the bulk, device scale oligopeptide results were compared with those due to piezo force microscopy (PFM) and computational modeling. Lastly, ferroelectricity was explored with regards to hysteretic current–voltage loops for a bowl-like corannulene derivative.

Piezoelectric response is contingent on both the dielectric and mechanical properties of a material, meaning that overall response should be tunable based on either of these parameters. PDMS foams, discussed in Chapter 3, were chosen as a simple, tunable scaffold on which polarity could be controllably imparted through the dipole moment, concentration, and degree of alignment of deposited dopant molecules. The PDMS foams were produced from sugar and table salt templates where the foam’s compressive modulus was dependent

on both the template and curing temperature used. The foams were then saturated with solutions of polar small organic molecules and placed under a high voltage electric field; after the solvent evaporated, foams coated with poled, dispersively attached molecules remained. The poling field, dopant identity, and concentration of the dopant solution was varied. The piezoelectric responses of these foam based devices were tested in a quasi-static manner.

The results show that, generally, the piezoelectric response increased with increased poling field, increased with increased dopant dipole moment until a saturation point was reached, and increased with decreased compressive modulus. Results for the effect of dopant solution concentration on piezoelectric response were less conclusive. In agreement with these data, increased poling fields are expected to produce a greater degree of dopant dipole alignment, while greater dipole moment and alignment should result in greater permittivity and, hence, greater piezoelectric response. Softer materials lead to more deformation per unit of applied force, leading to a higher piezoelectric response. The maximum piezoelectric charge constant ( $d_{33}$ ) obtained was 153 pC/N. The results of this work prove that, when successfully decoupled, the electrical and mechanical components of piezoelectric response can be tuned independently. Additionally, this decoupling provided a platform to easily examine the effects of different molecules, in order to better predict molecular response.

SAMs provide a method to easily and reliably achieve polar order without the use of electrical poling. As presented in Chapter 4, oligopeptide SAMs are piezoelectrically active. Devices made using these oligopeptide SAMs have several inherent advantages in that they are intrinsically piezoelectric and can be produced through solution processing. Since specific peptide sequences can be synthesized, the role of sequence on piezoelectric response can be examined experimentally to aid in the rational design of these molecular piezoelectrics. Gold-thiol SAMs were grown on printed circuit boards (PCBs) from solutions of cysteine-containing oligopeptides. Device assemblies consisted of the SAM functionalized PCB facing a polyurethane coated PCB and were tested in a quasi-static manner. The polymer coating provided conformal contact between the PCBs, thereby minimizing PCB-to-PCB

inconsistencies and allowing for consistent, reproducible contact. Sealed devices—including flexible ones—were also produced by assembling the device before the polyurethane cured; this helped to prevent the reversible atmospheric degradation of piezoelectric response.

The piezoelectric charge and voltage constants of the oligopeptide SAM devices were both measured directly. While the piezoelectric voltage constant can be obtained from the charge constant and permittivity, measuring the voltage constant directly, by means of recording the open-circuit voltage, provides a more accurate picture of these devices in low-frequency sensing applications. Since sensing applications normally rely upon voltage signals rather than current signals, the piezoelectric voltage constant is a more meaningful figure of merit in such cases. While the measured charge constants of oligopeptide SAMs were modest, excellent piezoelectric voltage constants ( $g_{33}$ ) up to 2 Vm/N—some of the highest ever recorded—were obtained. Thinner polyurethane layers led to larger voltage constants, as did functionalizing the polyurethane coated PCB with a linear alkanethiol. Since the calculated induced electric field is based on the overall device thickness, it is unsurprising that decreasing the thickness improved response. The effect of the alkanethiol is more surprising and less understood, but its influence on response could be related to potential organizing effects in conjunction with the polyurethane. From a molecular design perspective, the effect of peptide sequence on piezoelectric response, unfortunately, was less conclusive. Response decayed relatively quickly after the samples were removed from the desiccator; this was solved by the use of sealed devices, although somewhat at the expense of initial response. The potential of this technology for flexible touch sensing applications was demonstrated by a flexible device prototype which produced nearly 6 V in response to gentle bending action.

While important for practical applications, device scale measurements do not necessarily provide the clearest picture of the underlying piezoelectric mechanisms, as they are more likely to be convoluted by other electromechanical and electrostatic effects. Therefore, Chapter 5 introduced other ways to study the piezoelectric workings of the oligopeptide system. It is somewhat complicated to obtain the true converse piezoelectric response of soft materials

using PFM due to electrostatic interactions between the tip and the surface, but this can be largely overcome by utilizing the newly developed DC-sweep DART-PFM method. As with most things in chemistry, computational modeling also provides helpful insights. Problems, however, remain in identifying the best computational methods for studying these complex systems. For the density functional theory (DFT) calculations, the B3LYP functional initially used gave poor results; they were improved somewhat by switching to the  $\omega$ B97 functional. Another issue in relating these single molecule calculations in vacuum to practical application is that the *ab initio* molecular dynamics simulations showed that more than one dominant helix may be present in the oligopeptides. While more work is necessary, all three methods will ultimately provide valuable insights in the rational design of oligopeptide based piezoelectrics.

Closely related to piezoelectricity, ferroelectricity has the ability to impart “memory” onto molecules. Chapter 6 presented current–voltage measurements examining the potentially ferroelectric nature of a bowl-like corannulene derivative (abbreviated H<sub>4</sub>DFT). SAMs of the molecules were deposited on indium tin oxide (ITO) coated substrates and the electrical response was measured using an eutectic gallium-indium (EGaIn) electrode via a double-wave method (DWM). The current–voltage measurements obtained showed hysteresis for both the H<sub>4</sub>DFT and the 1-pyrenecarboxylic acid control. The hysteresis loops strayed from standard ferroelectric behavior as they were asymmetrical and did not close off at higher voltages. Although the data did not show evidence of ferroelectricity, it does not mean that the molecules are not ferroelectric, and other methods, potentially employed in the future, may show more promising results.

The work presented herein shows the potential of molecularly based piezoelectrics, and, furthermore, it shows that principles of rational design can be used to iteratively improve piezoelectric response and theoretical understanding of these systems. These materials hold potential as piezoelectric energy harvesters and sensors with advantageous features, including being low cost, easy to manufacture, biocompatible, flexible, and, in the case of the

oligopeptide SAMs, poling free. With the present results as a good foundation, more work is needed to better understand their intricacies, in order to improve and optimize these systems towards their full potential.

## 7.2 Future Directions

With several proven frameworks in place, there are numerous future directions possible towards bettering our understanding and improving the piezoelectric response of molecularly engineered materials. These include more precise manufacturing methods for optimizing the response, reliability, and longevity of existing devices; examining a wider array of piezoelectrically active elements; and developing improved calculation methods to help predict better molecular designs. The solid existing foundation, paired with these promising pathways to improvement, means that there is a bright future for molecularly engineered piezoelectrics.

Elastomers and foams hold piezoelectric potential, as small amounts of force can produce large deformations and charge movements. The PDMS foams, described in Chapter 3, helped to prove the concept but suffer from poor long-term stability due to the weak nature of the dopant's dispersive attachment to the polymer matrix. Developing covalent attachment methods should greatly improve the long term polar alignment and stability of the response. Furthermore, integrating polar substituents into the molecular backbone of a cross-linked polymer should boost response by incorporating the polar elements into the matrix through which the compressive force is transmitted. This can potentially be accomplished in a variety of ways, including, using polar cross-linkers, short-chain substituents, or bound ions. Other materials improvements include changes to the foam matrix used to decrease the pore size, increase the uniformity, and decrease the modulus. The rotation caused by pore deformation

upon compression pulls some of the polar dopants out of alignment. This effect can be minimized by utilizing a foam with smaller, more uniform pores. Finally, since modulus is inversely linked to piezoelectric response, using a softer foam should produce a larger response.

Having already proven its piezoelectric sensing ability, the model oligopeptide SAM system holds great promise for improvement. From a materials standpoint, current limiting factors include the thickness and uniformity of the conformal polyurethane layer, as well as the surface roughness of the gold surface on the printed circuit boards (PCBs). The current materials were selected due to their low cost and practicality. While not as readily accessible on a lab scale as aerosol cans and spin-coating, many improved methods of depositing highly-uniform, ultra-thin polymer films exist. While it may not actually boost the overall magnitude of the voltage signal, a thinner polymer coating would improve the piezoelectric charge constant of the overall device. The PCB used proved very practical for lab-scale testing but suffers from visible surface roughness. Switching to a smoother gold substrate, paired with a thinner, more uniform polymer coating, should serve to increase piezoelectric response and greatly improve sample-to-sample consistency, ideally to an extent such that sequence effects can be readily distinguished.

Computational investigations have the potential to provide key insights for new synthetic directions. Currently work is focusing on improving computational parameters such that they more closely agree with the experimental results of the oligopeptide devices. If reasonable agreement can be found between modeling and experiment, computational modeling can then be expanded to identify new candidates for experimental study. The process can then repeat ad infinitum. As the number of oligopeptides studied as a device, by PFM, and by computation grows, more is learned about the workings of the system and its piezoelectric response. Another avenue of potential SAM exploration involves mixed monolayers where

island structures within the SAM can potentially amplify stresses and, thereby, increase piezoelectric response. These different methods of analysis work together to inform each other and grow our knowledge base, ideally leading to better piezoelectrics.

# Appendix A: Supplementary Information for Highly Tunable Molecularly Doped Flexible Poly(dimethylsiloxane) Foam Piezoelectric Energy Harvesters

## A.1 Supplementary Figures

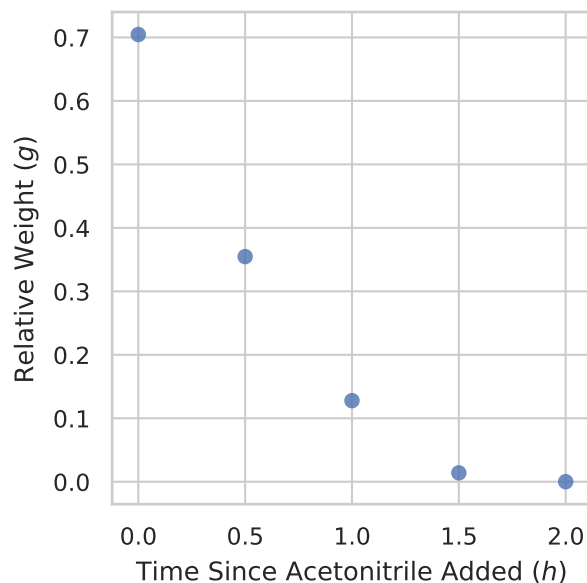


Figure A.1: Evaporation rate of acetonitrile in PDMS foam. Weights are relative to the weight of the PDMS foam sample before 1 mL of acetonitrile was added.



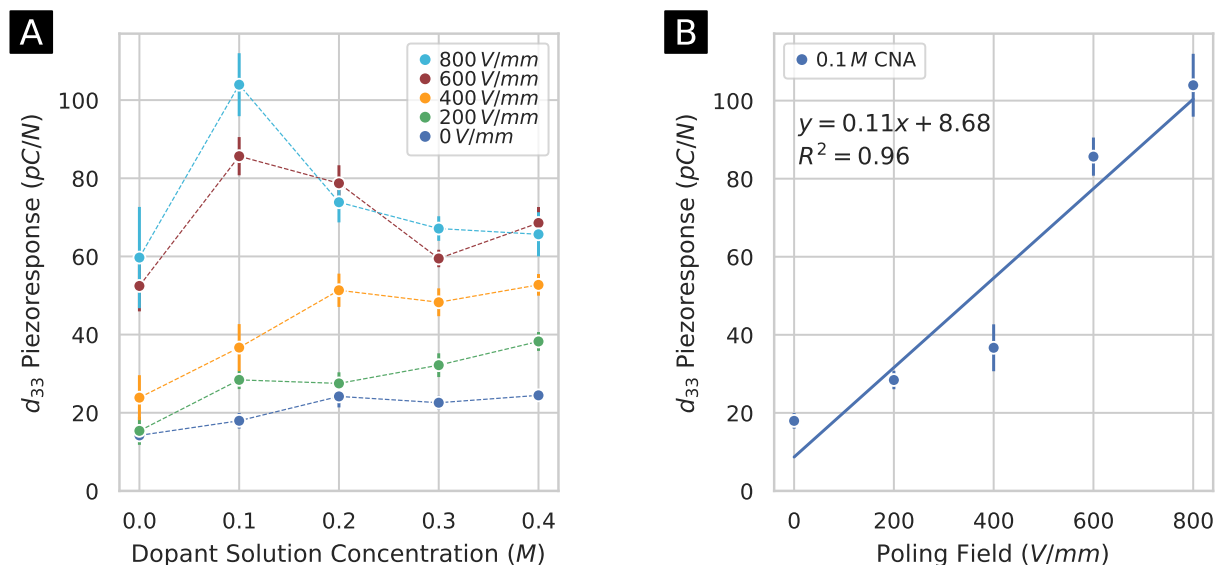


Figure A.2: Effect of dopant concentration and poling field on piezoelectric response up to 10 N. (A) The piezoelectric response as a function of added CNA dopant solution concentration over an array of poling fields using force values up to 10 N. (B) The 0.1 M CNA dopant solution subset showing the piezoelectric response increasing as a function of poling field. Error bars represent standard error across at least four samples.

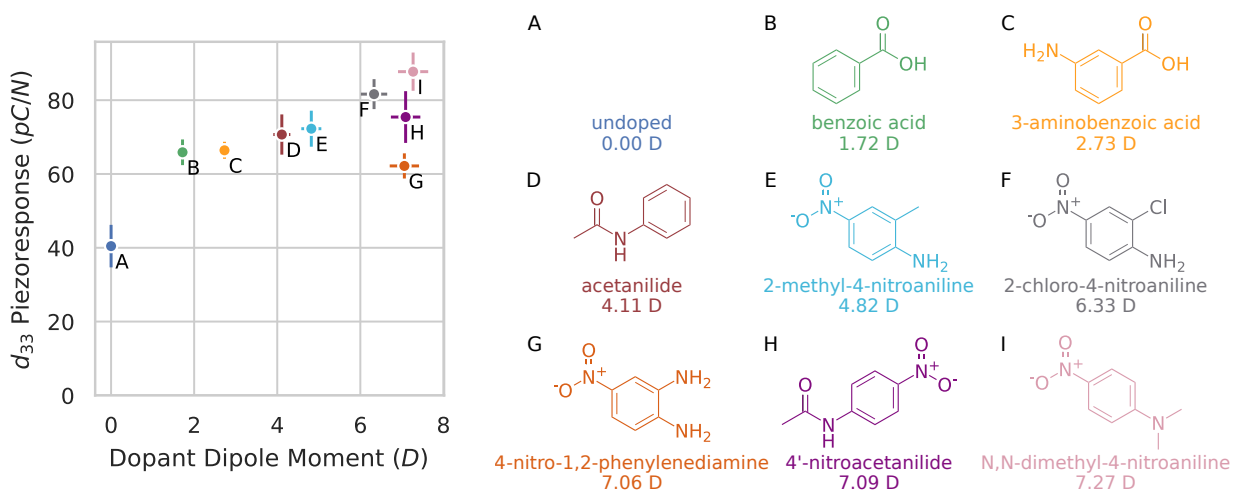


Figure A.3: Effect of dopant on piezoelectric response up to 10 N. Piezoelectric response as a function of dopant dipole moment for samples poled at 600 V/mm after being doped with a 0.1 M solution using force values up to 10 N. Dipole moments are experimental values in dioxane taken from the literature.<sup>104–107</sup> X-axis error bars are 5%; Y-axis error bars represent standard error across at least four samples.

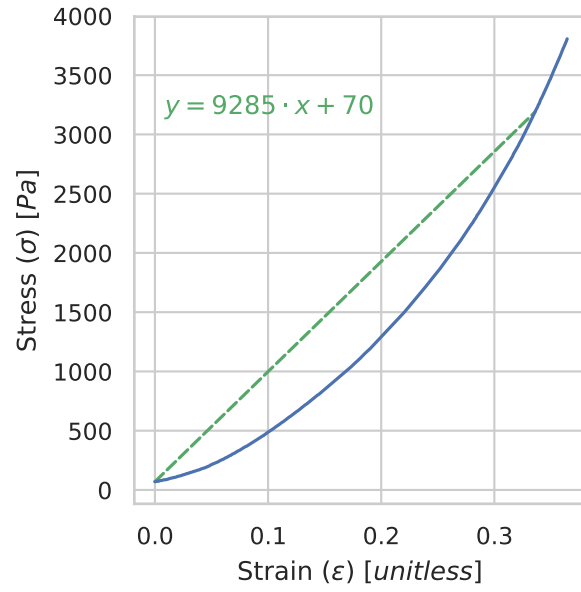


Figure A.4: Stress–strain curve for sugar templated PDMS foam. Compressive modulus is the slope of the secant (dashed green line) taken from zero strain to the strain corresponding to 10 N of applied force.

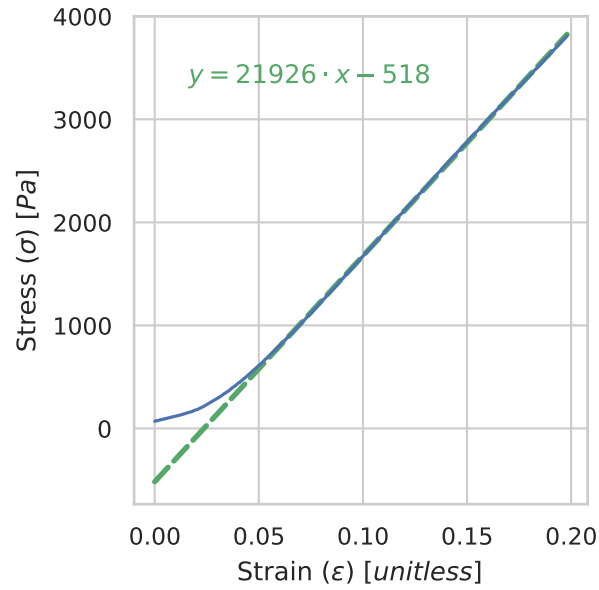


Figure A.5: Stress–strain curve for a salt templated PDMS foam cured at room temperature. Compressive modulus is the slope of the linear region (dashed green line).

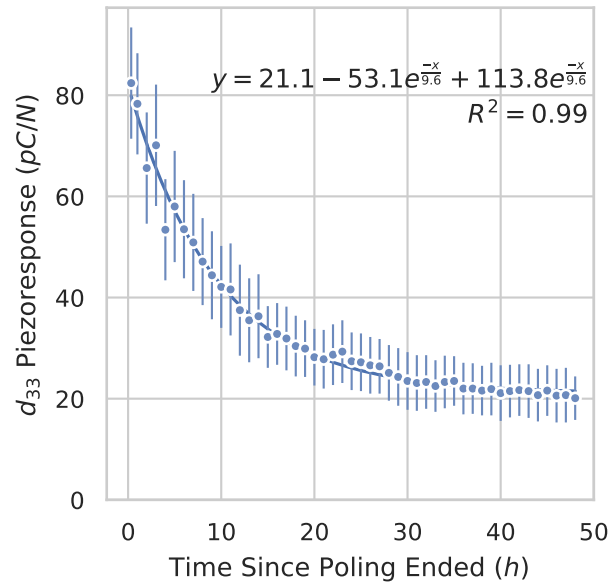


Figure A.6: Decay in piezoelectric response over time for a PDMS foam sample doped with 0.4 M CNA and poled at 800 V/mm.

## A.2 Peak Finding Python Script

The following Python script was used to identify force and current peaks to calculate the piezoelectric charge constant. The script is also available online at <https://doi.org/10.1021/acsaem.9b01061> and <https://doi.org/10.26434/chemrxiv.7562456.v3>.

```
1  #!/usr/bin/env python
2
3  #Python 2.7
4  import os
5  import math
6  import glob
7
8  #integrate area using a combination of triangles and trapezoids
9  #returns sum of all positive areas within given range
10     #'initial' -> initial index, 'final' -> final index
11  def exactPosArea(initial, final, time, data):
12
13     area = 0.0
14
15     for i in range(initial, final):
16
17         if ( i + 1 ) >= len(data):
18
19             break
20
21         data_init = float(data[i])
22         data_fin = float(data[i + 1])
23
24         dt = float(time[i + 1]) - float(time[i])
25
26         #if two consecutive points have opposite signs (from - to + OR + to -)
27
28         if (data_init > 0) ^ (data_fin > 0):
29
30             #'zero_inter' -> point where line between data points of opposite
31
32             #signs crosses zero
33
34             zero_inter = abs(dt * (max(data_init,data_fin) / (abs(data_fin) \
35
36                 + abs(data_init))))
```

```

25         if 0.5 * zero_inter * (data_init) > 0:
26             area += 0.5 * zero_inter * (data_init)
27         if 0.5 * zero_inter * (data_fin) > 0:
28             area += 0.5 * zero_inter * (data_fin)
29     else:     #trapezoidal method
30         if 0.5 * (data_init + data_fin) * (dt) > 0:
31             area += 0.5 * (data_init + data_fin) * (dt)
32     return area
33
34     #calculate standard deviation of dataset 'data'
35     def standardDev(data, data_avg):
36         std_tmp = 0.0
37         for i in range(len(data)):
38             std_tmp += pow((data[i] - data_avg),2)
39         return math.sqrt(std_tmp / len(data))
40
41     #calculate the average of dataset 'data'
42     def avg(data):
43         return sum([float(i) for i in data]) / len(data)
44
45     #open data file, calculate / analyze data, write to analysis file
46     def main(path):
47         print(path),
48         with open(os.path.abspath(path), 'r') as fl:
49             time = []
50             force = []
51             current = []
52
53         for lines in fl:

```

```

54         entries = lines.split()
55         if len(entries) > 5:
56             continue
57         #take time, current, and force values from text data
58         time.append(float(entries[0]))
59         current.append(float(entries[2]))
60         force.append(float(entries[3]))
61
62         #average force and current for first 25 data points
63         force_avg25 = avg(force[:25])
64         current_avg25 = avg(current[:25])
65
66         #calculate standard deviation of force and current for first 25 data
67         #points
68         force_std = standardDev(force[:25], force_avg25)
69         current_std = standardDev(current[:25], current_avg25)
70
71         #calculate threshold value for force and current using first 25 data
72         #points
73         force_baseline = force_avg25 + 3*force_std
74         current_baseline = current_avg25 + 3*current_std
75
76         #creates list of lists holding all time values for which force
77         #is above baseline
78         force_times = []
79         active_force = []
80         i = 0
81         while i < len(force):
82             while force[i] > force_baseline:

```

```

83         active_force.append(time[i])
84         i += 1
85     if active_force != []:
86         force_times.append(active_force)
87         active_force = []
88     i += 1
89
90     #remove all forces with length one(1) or less
91     for i in force_times:
92         if len(i) <= 1:
93             force_times.remove(i)
94
95     #remove final data point to avoid errors with force applied during final
96     #time area
97     del force_times[len(force_times) - 1]
98
99     #finds the max force applied for each interval of active force
100    max_forces = []
101    for intervals in force_times:
102        tmp_max = 0
103        for times in intervals:
104            if force[time.index(times)] > tmp_max:
105                tmp_max = force[time.index(times)]
106        max_forces.append(tmp_max)
107
108    #calculate each delay between end of force and current going above
109    #baseline
110    delay_from_end = []
111    for i in force_times:

```

```

112         force_end_time = i[-1]
113         end_time_index = time.index(force_end_time)
114         while ( current[end_time_index] < current_baseline ):
115             end_time_index += 1
116             if end_time_index >= len(current):
117                 break
118         if not end_time_index >= len(current):
119             delay_from_end.append(time[end_time_index] - force_end_time)
120
121     if len(delay_from_end) > 0:
122         avg_delay_from_end = avg(delay_from_end)
123         std_delay_from_end = standardDev(delay_from_end, avg_delay_from_end)
124     if len(delay_from_end) <= 0:
125         avg_delay_from_end = 0
126         std_delay_from_end = 0
127
128     #calculate delay between start of force and current going over baseline
129     delay_from_start = []
130     for i in force_times:
131         end_time_index = time.index(i[0])
132         while ( current[end_time_index] < current_baseline ):
133             end_time_index += 1
134             if end_time_index >= len(current):
135                 break
136         if not end_time_index >= len(current):
137             delay_from_start.append(time[end_time_index] - i[0])
138
139     if len(delay_from_start) > 0:
140         avg_delay_from_start = avg(delay_from_start)

```



```

141         std_delay_from_start = standardDev(delay_from_start, \
142             avg_delay_from_start)
143     if len(delay_from_start) <= 0:
144         avg_delay_from_start = 0
145         std_delay_from_start = 0
146
147     #CALCULATE AREA UNDER CURRENT V. TIME CURVES
148
149     #area from start of force using only positive current values
150     posArea = []
151     max_currents = []
152     if len(force_times) > 0:
153         for i in force_times:
154             #calculate area beyond force curve until the mean of 3
155             #consecutive currents is greater than the baseline
156             final_index = time.index(i[-1]) + 3
157             avg3 = float('inf')
158             iteration = 0
159             #'avg3' -> most recent three current values, beginning after end
160             #of force
161             while ( avg3 > 0 ):
162                 avg3 = avg(current[time.index(i[-1]) + iteration : \
163                     final_index])
164                 final_index += 1
165                 iteration += 1
166                 posArea.append(exactPosArea(time.index(i[0]), final_index, \
167                     time, current))
168     else:
169         final_index = 0

```

```

170
171     #calculate peak current values in time period after applied force
172     tmp_max = 0
173     for i in range(time.index(i[0]), final_index):
174         if ( i + 1 ) >= len(current):
175             break
176         if current[i] > tmp_max:
177             tmp_max = current[i]
178     max_currents.append(tmp_max)
179
180     #remove all area and force values corresponding to where the area equals
181     #zero
182      #(zero area corresponds to a non-significant force, only slightly above
183      #baseline)
184     tmp = 0
185     while tmp < len(posArea):
186         if posArea[tmp] == 0.0:
187             del posArea[tmp]
188             del max_forces[tmp]
189             tmp -= 1
190         tmp += 1
191
192     #remove forces and currents such that all corrected forces are relevant
193      #(remove any forces < 0.5 N)
194     tmp = 0
195     while tmp < len(max_forces):
196         if (max_forces[tmp] - force_avg25) < 0.5:
197             del max_forces[tmp]
198             del posArea[tmp]

```

```

199         tmp -= 1
200         tmp += 1
201
202         #write results of analysis to a new file in the same location with
203         #the same name, appended by '_analysis.txt'
204         write_target_dir = os.path.abspath(path)[: -4] + '_analysis.txt'
205         with open(write_target_dir, 'w') as newFile:
206             #column headers
207             newFile.write('Applied Force\t')
208             newFile.write('Corrected Force\t')
209             newFile.write('Charge <positive only>\t')
210             newFile.write('\n')
211
212             #data
213             for i in range(len(max_forces)):
214                 newFile.write(str(max_forces[i]) + '\t')
215                 newFile.write(str(max_forces[i] - force_avg25) + '\t')
216                 newFile.write(str(posArea[i]) + '\t')
217                 newFile.write('\n')
218             if len(max_forces) < 5:
219                 print('Warning! Less than 5 data points.')
220             else:
221                 print('')
222
223         #####
224
225         rootdir = os.path.abspath(raw_input('Enter Starting Directory: '))
226
227         #case if data text file path is entered directly

```

```

228 if rootdir.endswith('.txt') and not rootdir.endswith('analysis.txt'):
229     main(rootdir)
230
231 #case if folder containing data files is entered
232 else:
233     os.chdir(os.path.abspath(rootdir))
234
235 #used to break out of excess loops if 'rootdir' contains data text files
236 end_break = False
237
238 #go through each day's folder within the overall data folder
239 for f in glob.iglob('*'):
240     #error catch if individual data folders are selected
241     if '.' not in f:
242         os.chdir(os.path.abspath(f))
243     else:
244         end_break = True
245     #go through each data text file and perform calculations
246     for t in sorted(glob.iglob('*.txt')):
247         #catch to bypass analysis text files located in the same folder
248         if not t.endswith('analysis.txt'):
249             main(t)
250
251 #reset current working directory to the root directory in order to
252 #move onto the next file
253     os.chdir(rootdir)
254     #break out of excess loops
255     if end_break:
256         break

```

# Appendix B: Supplementary Information for

## Intrinsically Polar Piezoelectric

## Self-Assembled Oligopeptide Monolayers

### B.1 ANOVA

Analysis of Variance (ANOVA) was used to determine if different effects have statistical significance. The ANOVA calculations were performed using LibreOffice Calc (v. 6.4.5.2) software, and the results are presented in Tables B.1–B.12.

Table B.1: ANOVA charge constant results for DDT-PU PCBs. The data do not show a statistically significant effect between tests of the piezoelectric charge constant ( $d_{33}$ ) using different DDT-PU coated PCBs.

Group	Count	Sum	Mean	Variance	
$d_{33}$ DDT-PU PCB 1	16	130.04	8.13	16.86	
$d_{33}$ DDT-PU PCB 2	19	147.41	7.76	13.06	
$d_{33}$ DDT-PU PCB 3	18	165.79	9.21	21.68	
Source of Variation	SS	df	MS	F	P-value
Between Groups	20.76	2	10.38	0.61	0.55
Within Groups	856.62	50	17.13		

Table B.2: ANOVA charge constant results for PU PCBs. The data do not show a statistically significant effect between tests of the piezoelectric charge constant ( $d_{33}$ ) using different PU coated PCBs.

Group	Count	Sum	Mean	Variance	
$d_{33}$ PU PCB 1	15	58.76	3.92	4.59	
$d_{33}$ PU PCB 2	13	57.01	4.39	6.19	
Source of Variation	SS	df	MS	F	P-value
Between Groups	1.25	1	1.53	0.29	0.60
Within Groups	138.46	26	5.33		

Table B.3: ANOVA charge constant results for thin PU PCBs. The data show a statistically significant effect between tests of the piezoelectric charge constant ( $d_{33}$ ) using different thin PU coated PCBs.

Group	Count	Sum	Mean	Variance	
$d_{33}$ Thin PU PCB 1	14	116.61	8.33	14.96	
$d_{33}$ Thin PU PCB 2	14	55.09	3.94	2.65	
$d_{33}$ Thin PU PCB 3	4	34.03	8.51	2.52	
Source of Variation	SS	df	MS	F	P-value
Between Groups	154.91	2	77.45	9.50	0.000 67
Within Groups	236.54	29	8.17		

Table B.4: ANOVA charge constant results for carboxylate-terminated versus amide-terminated peptides. The data appear to show a statistically significant effect (P-value<0.05) between tests of the piezoelectric charge constant ( $d_{33}$ ) using carboxylate-terminated and amide-terminated peptides.

Group	Count	Sum	Mean	Variance	
$d_{33}$ Carboxylate-Terminated Peptides	61	369.62	6.06	11.07	
$d_{33}$ Amide-Terminated Peptides	52	395.13	7.60	19.82	
Source of Variation	SS	df	MS	F	P-value
Between Groups	66.52	1	66.52	4.41	0.038
Within Groups	1675.00	111	15.09		

Table B.5: ANOVA charge constant results for carboxylate-terminated peptides. The data do not show a statistically significant effect between tests of the piezoelectric charge constant ( $d_{33}$ ) using different length carboxylate-terminated peptides.

Group	Count	Sum	Mean	Variance	
$d_{33}$ CA <sub>6</sub>	14	70.78	5.06	7.44	
$d_{33}$ A <sub>6</sub> C	14	80.03	5.72	5.91	
$d_{33}$ CA <sub>9</sub>	16	104.47	6.53	16.34	
$d_{33}$ CA <sub>12</sub>	16	106.44	6.65	14.44	
Source of Variation	SS	df	MS	F	P-value
Between Groups	24.85	3	8.28	0.73	0.54
Within Groups	635.19	56	11.34		

Table B.6: ANOVA charge constant results for amide-terminated peptides. The data do not show a statistically significant effect between tests of the piezoelectric charge constant ( $d_{33}$ ) using different length amide-terminated peptides.

Group	Count	Sum	Mean	Variance	
$d_{33}$ CA <sub>6</sub> -NH <sub>2</sub>	14	102.39	7.31	17.44	
$d_{33}$ CA <sub>9</sub> -NH <sub>2</sub>	18	135.32	7.52	18.75	
$d_{33}$ CA <sub>12</sub> -NH <sub>2</sub>	14	87.76	6.27	9.06	
Source of Variation	SS	df	MS	F	P-value
Between Groups	13.43	2	6.71	0.44	0.65
Within Groups	663.22	43	15.42		

Table B.7: ANOVA charge constant results for DDT-PU versus PU coated PCBs. The data show a statistically significant effect between tests of the piezoelectric charge constant ( $d_{33}$ ) using unfunctionalized and DDT functionalized PU coated PCBs.

Group	Count	Sum	Mean	Variance	
$d_{33}$ DDT-PU	46	365.69	7.95	12.90	
$d_{33}$ PU	28	115.77	4.13	5.18	
Source of Variation	SS	df	MS	F	P-value
Between Groups	253.32	1	253.32	25.32	0.000 003 4
Within Groups	720.31	72	10.00		

Table B.8: ANOVA charge constant results for normal thickness versus thinner thickness PU coated PCBs. The data show a statistically significant effect between tests of the piezoelectric charge constant ( $d_{33}$ ) using PCBs coated with normal thickness PU and thinner thickness PU.

Group	Count	Sum	Mean	Variance	
$d_{33}$ Normal PU	28	115.77	4.13	5.18	
$d_{33}$ Thin PU	32	205.73	6.43	12.63	
Source of Variation	SS	df	MS	F	P-value
Between Groups	78.61	1	78.61	8.58	0.0049
Within Groups	531.44	58	9.16		

Table B.9: ANOVA voltage constant results for DDT-PU PCBs. The data show a statistically significant effect between tests of the piezoelectric voltage constant ( $g_{33}$ ) using different DDT-PU coated PCBs.

Group	Count	Sum	Mean	Variance	
$g_{33}$ DDT-PU PCB 1	14	11 714	837	99 346	
$g_{33}$ DDT-PU PCB 2	14	6396	457	35 136	
$g_{33}$ DDT-PU PCB 3	16	7603	475	31 404	
Source of Variation	SS	df	MS	F	P-value
Between Groups	1 309 918	2	654 959	12.10	0.000 074
Within Groups	2 219 335	41	54 130		

Table B.10: ANOVA voltage constant results for PU PCBs. The data do not show a statistically significant effect between tests of the piezoelectric voltage constant ( $g_{33}$ ) using different PU coated PCBs.

Group	Count	Sum	Mean	Variance	
$g_{33}$ PU PCB 1	14	6566	469	52 126	
$g_{33}$ PU PCB 2	14	6543	467	58 555	
Source of Variation	SS	df	MS	F	P-value
Between Groups	18.66	1	18.66	0.000 34	0.99
Within Groups	1 438 852	26	55 340		



Table B.11: ANOVA voltage constant results for thin PU PCBs. The data show a statistically significant effect between tests of the piezoelectric voltage constant ( $g_{33}$ ) using different thin PU coated PCBs.

Group	Count	Sum	Mean	Variance	
$g_{33}$ Thin PU PCB 1	16	33 812	2113	1 742 123	
$g_{33}$ Thin PU PCB 2	16	16 132	1008	160 542	
$g_{33}$ Thin PU PCB 3	8	7671	959	416 999	
Source of Variation	SS	df	MS	F	P-value
Between Groups	12 087 411	2	6 043 705	7.11	0.0024
Within Groups	31 458 975	37	850 243		

Table B.12: ANOVA voltage constant results for normal thickness versus thinner thickness PU coated PCBs. The data show a statistically significant effect between tests of the piezoelectric voltage constant ( $g_{33}$ ) using PCBs coated with normal thickness PU and thinner thickness PU.

Group	Count	Sum	Mean	Variance	
$g_{33}$ Normal PU	28	13 110	468	53 292	
$g_{33}$ Thin PU	40	57 615	1440	1 116 574	
Source of Variation	SS	df	MS	F	P-value
Between Groups	15 566 850	1	15 566 850	22.84	0.000 010
Within Groups	44 985 256	66	681 595		

## B.2 Supplementary Figures on Piezoelectric Response

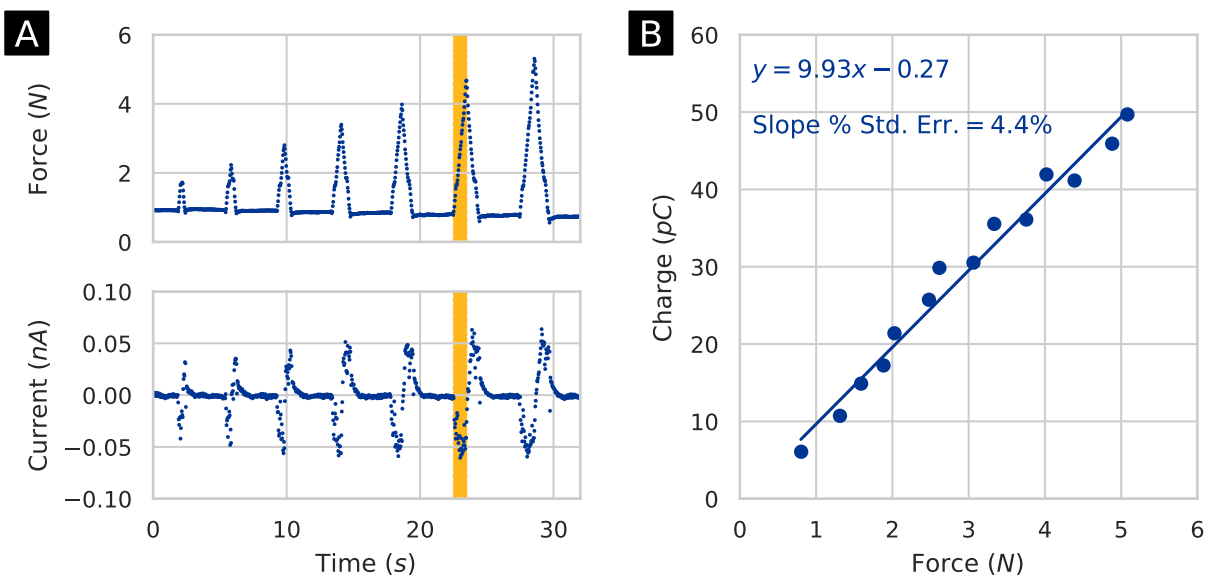


Figure B.1: Process by which the piezoelectric charge constant ( $d_{33}$ ) is obtained. (A) Simultaneous measurement of force and short-circuit current over time. The gold shading represents the time over which the current is integrated to calculate charge; the absolute value of the charge is then used. (B) Charge–force plot for a CA6-NH<sub>2</sub>/DDT-PU PSAM device showing a  $d_{33}$  of 9.93 pC/N.

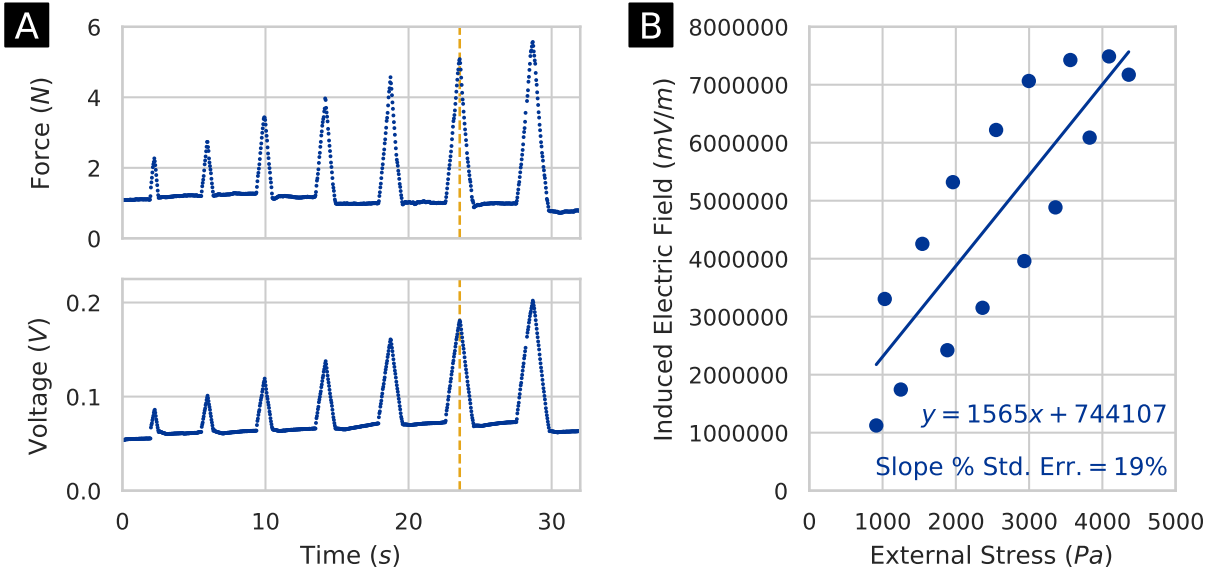


Figure B.2: Process by which the piezoelectric voltage constant ( $g_{33}$ ) is obtained. (A) Simultaneous measurement of force and open-circuit voltage over time; the baseline of the measured voltage is first corrected for measurement drift. The dashed gold line shows corresponding force and voltage peaks. (B) Induced electric field–external stress plot for a CA12-NH<sub>2</sub>/thin-PU PSAM device showing a  $g_{33}$  of 1565 mVm/N. Induced electric field is calculated by dividing voltage by sample thickness; external stress is calculated by dividing applied force by electrode area.

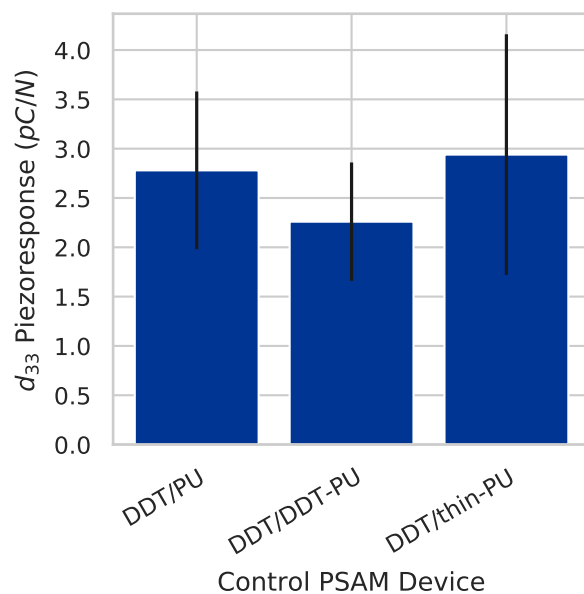


Figure B.3: Piezoelectric charge constant ( $d_{33}$ ) values for 1-dodecanethiol (DDT) control PSAM devices. Control values are less than 3 pC/N. Error bars represent standard error across multiple samples.

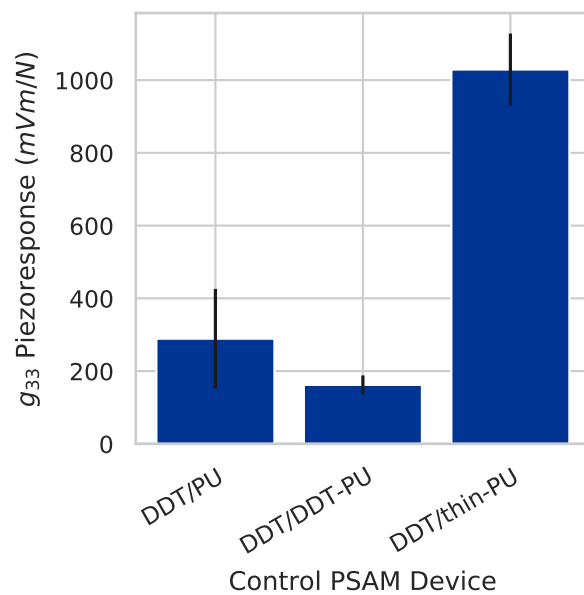


Figure B.4: Piezoelectric voltage constant ( $g_{33}$ ) values for 1-dodecanethiol (DDT) control PSAM devices. Control values for normal thickness PU devices are less than 300 mVm/N. Error bars represent standard error across multiple samples.

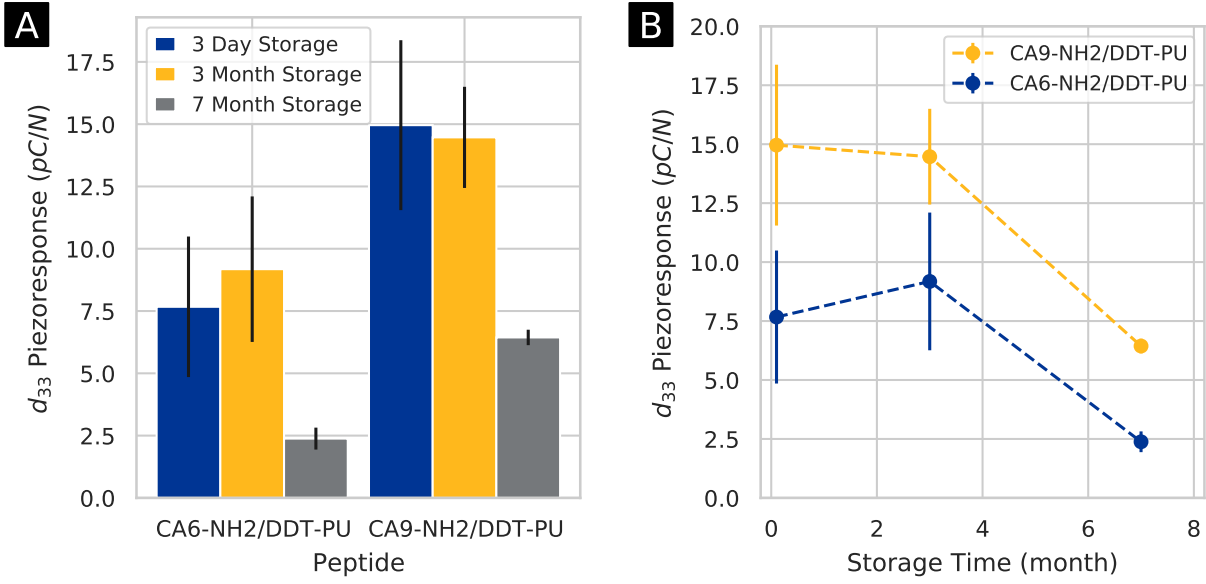


Figure B.5: Long term storage stability of samples showing they retain piezoelectric response over several months of storage in a vacuum desiccator. (A) Response grouped by sample. (B) Response as a function of storage time. Error bars represent standard error across multiple tests.

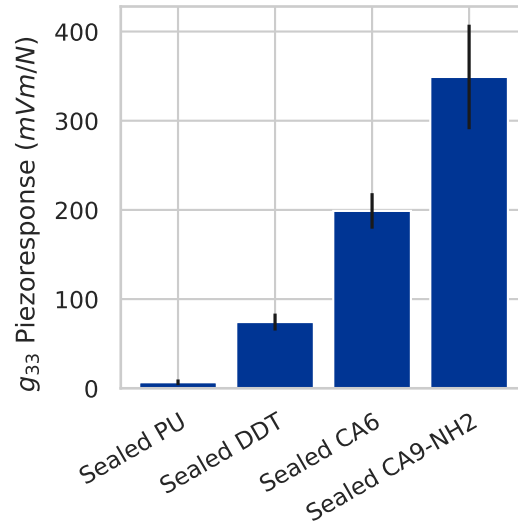


Figure B.6: The piezoelectric voltage constants ( $g_{33}$ ) of sealed PSAM devices. The  $g_{33}$  of sealed PSAM devices is similar to that of other samples despite the thinner PU layer; the  $d_{33}$  is much lower (not shown); and the stability is much better. Error bars represent standard error across multiple tests.

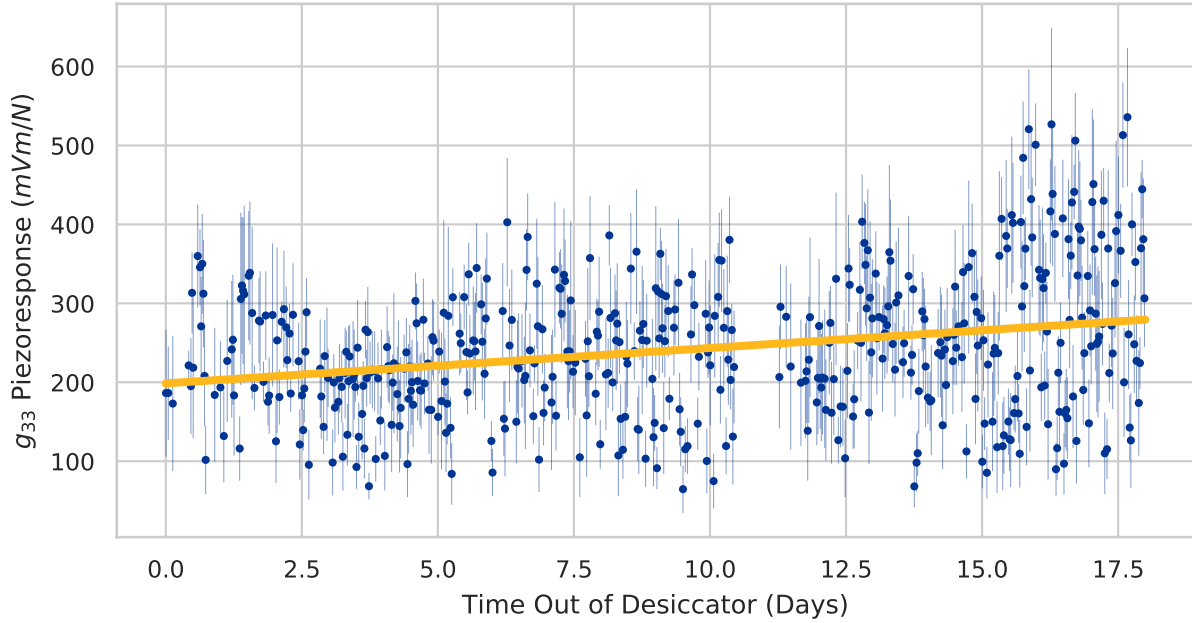


Figure B.7: Stability of sealed PSAM devices showing that they retain response over 18 d and approximately 900 test cycles under ambient conditions. The increase in response over time is due, in part, to the gradual decrease of preload force due to the nature of the testing setup. Data were excluded around day 11 due to HVAC instability. Error bars represent standard error is the slope of the robust linear regression for each individual test.

### B.3 Supplementary Note: Computational Details and Discussion

The piezoelectric response of carboxylate/amide-terminated peptides is ultimately dependent on the strength of the H-bonds constituting their own  $\alpha$ -helices, whose lengths are defined in Figure B.8.

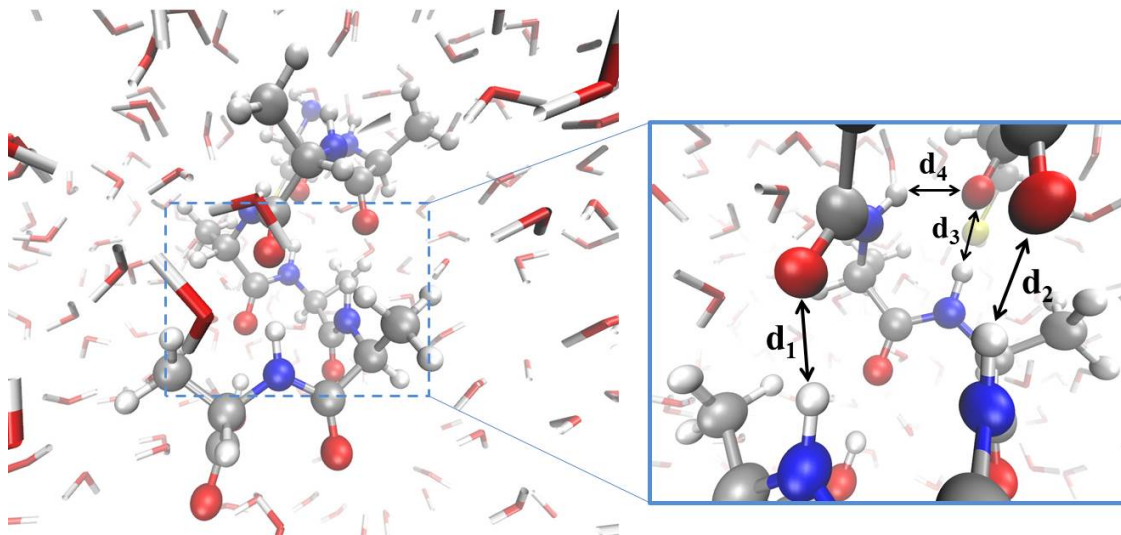


Figure B.8: Atomistic visualization of the carboxylate-terminated peptide  $CA_6$  in liquid water from room-temperature *ab initio* molecular dynamics simulations. In the inset, a magnification displaying the definition of the four crucial interatomic distances ( $d_1$ ,  $d_2$ ,  $d_3$ ,  $d_4$ ) determining the  $\alpha$ -helix structure is shown. Equivalent definitions also hold for the amide-terminated peptide  $CA_6-NH_2$  structure. Red, grey, yellow, blue, and white coloring refer to oxygen, carbon, sulfur, nitrogen, and hydrogen atoms, respectively.

In order to atomistically monitor the behavior of carboxylate-terminated peptides  $CA_6$  and amide-terminated peptides  $CA_6-NH_2$ , a series of *ab initio* molecular dynamics (AIMD) simulations at room conditions and under the effect of different field intensities was executed. As shown in Figure B.9, in the zero-field regime and at room temperature, the four  $NH \cdots O$  internal distances of the  $CA_6$  species exhibit values statistically falling within the range of typical strong-to-moderate H-bonds (*i.e.*,  $\sim [1.7 - 3.2]$  Å), with the exception of  $d_4$  which also

probes longer distances. This latter represents the weakest interatomic bond—among those defining the  $\alpha$ -helix—since it shares the acceptor oxygen atom with the bond defined as  $d_3$  (Figure B.8). This way, the  $\alpha$ -helix structure of  $CA_6$  is essentially determined by the H-bonds identified by  $d_1$ ,  $d_2$ , and  $d_3$ . On the other hand, the probability distributions characterizing all four internal H-bonds of the amide-terminated peptide  $CA_6-NH_2$  exhibit broader distributions than their counterparts in the  $CA_6$  species, indicating that amide-terminated  $\alpha$ -helices are less rigid than the carboxylate-terminated ones. In fact, both  $d_1$  and  $d_3$  distributions are slightly broader in  $CA_6-NH_2$  with respect to their homologues in  $CA_6$ , as shown in Figure B.9. Moreover, the weakest H-bond of the  $CA_6$  peptide, identified by  $d_4$ , develops into very feeble interatomic interactions, exhibiting distances beyond the typical lengths of very weak H-bonds (*i.e.*,  $\sim 4$  Å). Nevertheless, the most prominent difference is recorded for the H-bond defined as  $d_2$ . Whereas in the  $CA_6$  peptide structure such a bond exhibits lengths which are ascribable to H-bonds with a predominantly covalent character (*i.e.*,  $\sim 2$  Å), in the amide-terminated  $CA_6-NH_2$  species the same bond shows lengths typical of very weak H-bonds or even being purely electrostatic in nature. Those microscopic aspects are crucial not only in interpreting the results concerning the electric-field-induced effects on the  $\alpha$ -helices of the peptides shown in Figures B.10 and B.11, but also in the understanding of the larger piezoelectric response of the amide-terminated peptides with respect to their carboxylate-terminated counterparts emerging from experiments.

A series of analyses on the crucial H-bonds defining the  $\alpha$ -helix was executed. As shown in Figure B.10, the application of electric field strengths on the order of 0.5 V/nm perturbs the internal H-bonds of the  $CA_6$  structure. In fact, one of the four bonds characterizing the  $\alpha$ -helix (*i.e.*,  $d_1$ ) starts exploring larger distances. However, all the remaining probability distributions associated with the other H-bonds are not significantly altered by the field action, as shown in Figure B.10. Such a finding highlights, once again, the robustness of the structure of the carboxylate-terminated peptide  $CA_6$ . On the other hand, a field intensity of



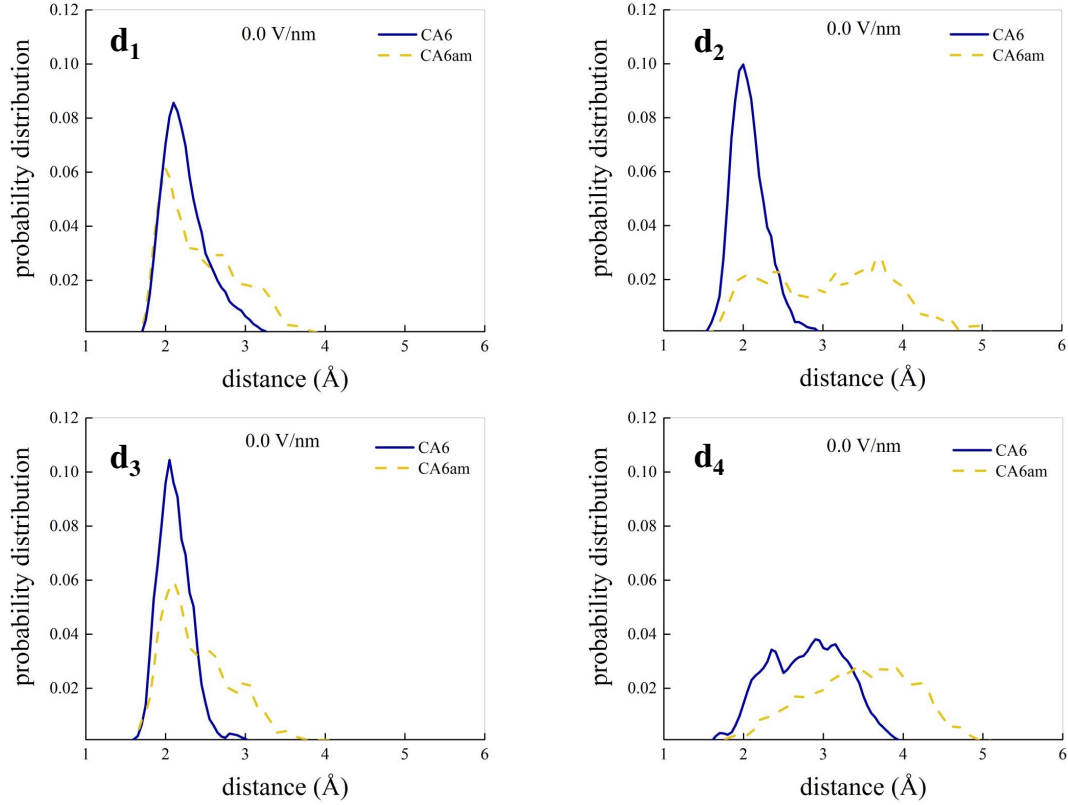


Figure B.9: Probability distributions of the lengths of the four H-bonds characterizing the  $\alpha$ -helix structure of the carboxylate-terminated peptide (CA<sub>6</sub>; solid blue curves) and the amide-terminated peptide (CA<sub>6am</sub>; dashed yellow curves), as determined by *ab initio* molecular dynamics simulations in the zero-field regime (*i.e.*,  $E = 0.0$  V/nm). For the distances definition, please refer to Figure B.8.

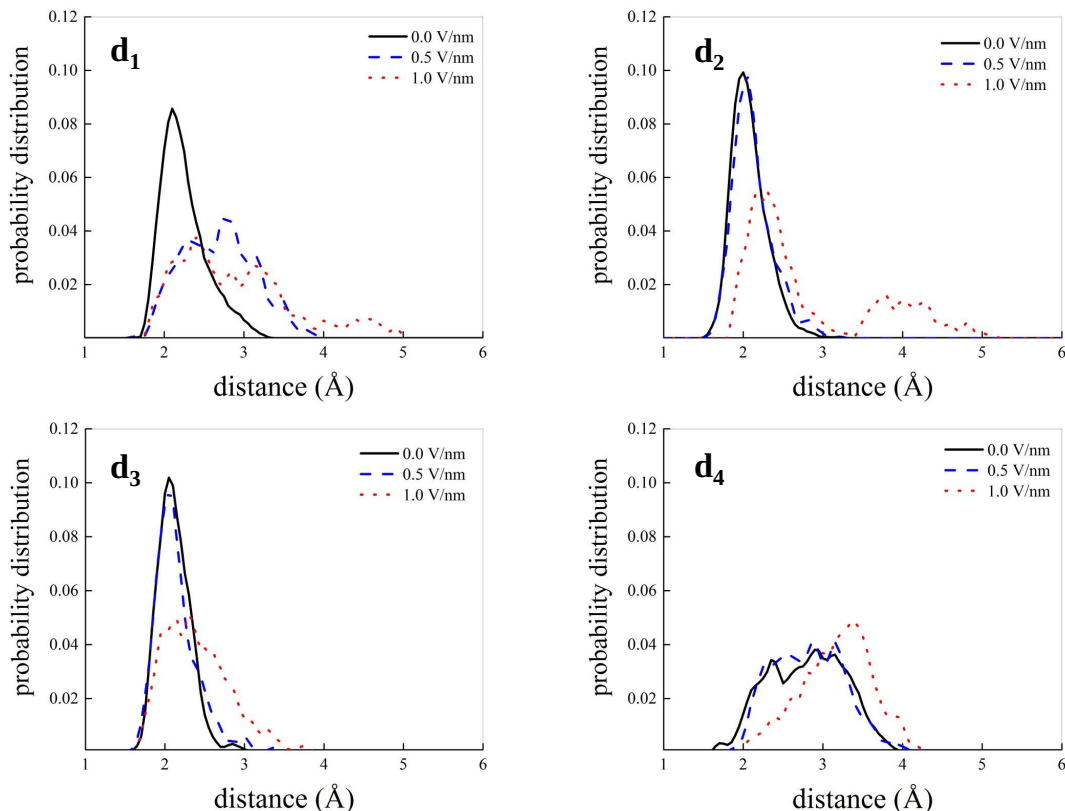


Figure B.10: Probability distributions of the lengths of the four H-bonds characterizing the  $\alpha$ -helix structure of the carboxylate-terminated peptide  $CA_6$  in the zero-field regime (solid black curves) and at field strengths of 0.5 V/nm (dashed blue curves) and 1.0 V/nm (dotted red curves), as determined by *ab initio* molecular dynamics simulations. For the distances definition, please refer to Figure B.8.

1.0 V/nm is able to almost completely break the  $\alpha$ -helix structure, leaving partially intact only the H-bond identified as  $d_3$  and the weakest (and very weak) intermolecular bond defined as  $d_4$ , as shown in Figure B.10.

As previously mentioned, in the zero-field regime the structure of the amide-terminated peptide  $CA_6-NH_2$  is less rigid than its own carboxylate-terminated counterpart. The weaker internal H-bonds constituting the  $\alpha$ -helix render the  $CA_6-NH_2$  structure more sensitive to the application of external electrostatic potential gradients. In fact, a field strength of 0.5 V/nm is already able to largely affect most of the lengths of the bonds under investigation, as shown in Figure B.11.

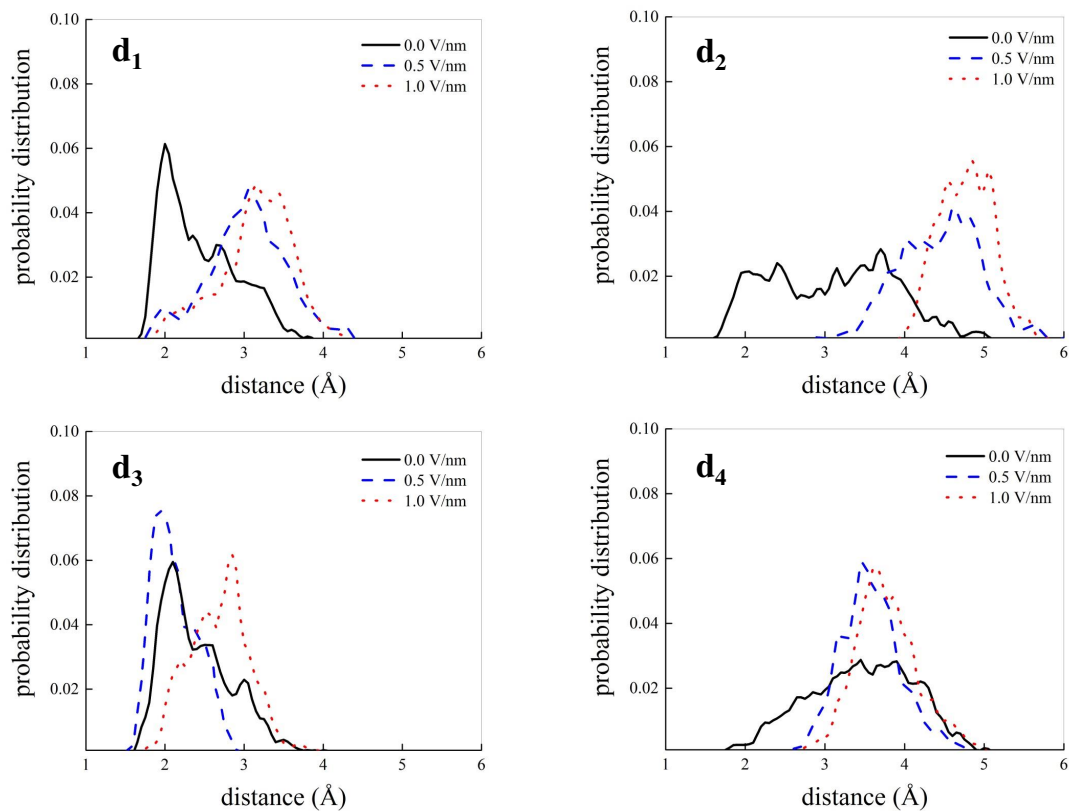


Figure B.11: Probability distributions of the lengths of the four H-bonds characterizing the  $\alpha$ -helix structure of the amide-terminated peptide  $\text{CA}_6\text{-NH}_2$  in the zero-field regime (solid black curves) and at field strengths of 0.5 V/nm (dashed blue curves) and 1.0 V/nm (dotted red curves), as determined by *ab initio* molecular dynamics simulations. For the distances definition, please refer to Figure B.8.

## B.4 AFM Images of PCB Substrate

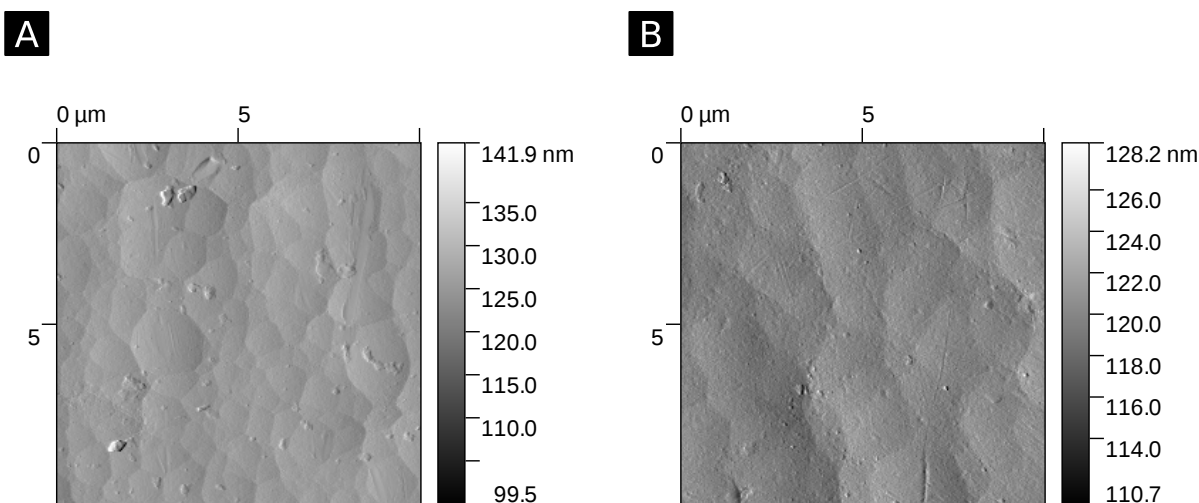


Figure B.12: AFM amplitude scans of PCBs. (A) Bare, unfunctionalized PCB with a height RMS roughness of 68 nm. (B) CA<sub>6</sub> functionalized PCB with a height RMS roughness of 52 nm.

## B.5 Minimum Working Example of Voltage Peak Finding Python Script

The following is a minimum working example of the Python script used to identify force and voltage peaks to calculate the piezoelectric voltage constant. The script is also available online at <https://github.com/hutchisonlab/g33-piezoelectric-constant> and <https://doi.org/10.26434/chemrxiv.13151069.v1>.

```

1  #!/usr/bin/env python3
2
3  import numpy as np
4  import pandas as pd
5  import statsmodels.api as sm
6  from scipy.stats import linregress
7  from scipy.signal import find_peaks
8
9  # Load data
10 a = pd.pandas.read_csv('data.txt', delimiter='\t')
11
12 # Correct baseline
13 x = a.iloc[30:530]['Time (s)']
14 y = a.iloc[30:530]['VoltageB (V)']
15 slope, intercept, r_value, p_value, std_err = linregress(x, y)
16 a['Corrected Voltage'] = a['VoltageB (V)'] - slope * a['Time (s)']
17 baseline = np.mean(a.iloc[30:530]['Corrected Voltage'])
18 a['Corrected Voltage'] = a['Corrected Voltage'] - baseline
19
20 # Identify Force and Voltage Peaks
21 # Average initial force
22 force_avg = np.mean(a.iloc[30:530]['ForceA (N)'])
23 force_std = np.std(a.iloc[30:530]['ForceA (N)'])
24 # Calculate force baseline
25 force_baseline = force_avg + 3*force_std + 0.2
26 # Calculate force peaks
27 force_peaks, force_properties = find_peaks(a['ForceA (N)'],
28      height=force_baseline, distance=100, prominence=0)
29 force_index = a['ForceA (N)'].index[force_peaks]

```

```

30 force_times = a.iloc[force_index]['Time (s)']
31 force_times = force_times.values
32 force_values = a['ForceA (N)'].values[force_peaks]
33 force_values_rel = force_properties['prominences']
34 # Calculate voltage peaks
35 voltage_peaks, voltage_properties = \
36     find_peaks(a.iloc[530:]['Corrected Voltage'], distance=100, prominence=0)
37 voltage_index = a.iloc[530:]['Corrected Voltage'].index[voltage_peaks]
38 voltage_times = a.iloc[voltage_index]['Time (s)']
39 voltage_times = voltage_times.values
40 voltage_values = a.iloc[530:]['Corrected Voltage'].values[voltage_peaks]
41 voltage_values_rel = voltage_properties['prominences']
42
43 # Process results
44 area = 0.035 * 0.035 # meters
45 separation = 0.00004 # meters
46 x = force_values_rel / area
47 y = voltage_values_rel * 1000 / separation
48 # Calculate robust linear regression
49 x_rlm = sm.add_constant(x)
50 huber_t = sm.RLM(y, x_rlm, M=sm.robust.norms.HuberT())
51 hub_results = huber_t.fit()
52 # Calculate slope percent standard error
53 percent_std_err = hub_results.bse[1] / hub_results.params[1] * 100
54 slope = hub_results.params[1]
55 intercept = hub_results.params[0]
56 print('Response\tIntercept\tSlope-Percent-Standard-Error\t')
57 print(str(slope) + '\t' + str(intercept) + '\t' + str(percent_std_err))

```

# Appendix C: Supplementary Information for

## Oligopeptide-Based Piezoelectric Materials:

### Understanding Electromechanical Coupling in Molecules

#### C.1 Materials and Methods

##### C.1.1 Peptide Devices

In brief, oligopeptide self-assembled monolayers were grown from  $0.1 \text{ mol dm}^{-3}$  solution by soaking the gold-coated printed circuit board (PCB) for 48 h. A peptide functionalized PCB was placed facing either an unfunctionalized polyurethane (PU) coated PCB or a 1-dodecanethiol (DDT) functionalized PCB. This assembly was then subjected to various compression forces while either the resulting short-circuit current or open-circuit voltage was measured. The current was integrated and the piezoelectric charge constant ( $d_{33}$ ) was calculated from the slope of the linear fit of charge versus applied force. Similarly, voltage was converted to electric field by dividing by sample thickness; the result was plotted against applied force to obtain the piezoelectric voltage constant ( $g_{33}$ ). Linear fits were calculated using robust linear regression with the Huber's T norm. Full experimental details are available in our previous work;<sup>67</sup> some data is reused while additional data was collected in an analogous manner. Peptides used for newly reported measurements (CFA6-NH<sub>2</sub>, CA6F-NH<sub>2</sub>, CYA6-NH<sub>2</sub>, CA6Y-NH<sub>2</sub>, CA6X-NH<sub>2</sub>, CA7-NH<sub>2</sub>, and CA8-NH<sub>2</sub>) were obtained from Anaspec (unpurified grade, used without further purification).

### C.1.2 PFM Measurements

Piezo force microscopy (PFM) measurements were taken using our DC-sweep DART-PFM method.<sup>82</sup> Voltage offsets of  $\pm 0.5$  V,  $\pm 1$  V,  $\pm 1.5$  V, and  $\pm 2$  V were used.

### C.1.3 Computational Methods

Density functional theory (DFT) calculations were run using Gaussian 16. Oligopeptides were initially optimized using the B3LYP functional with the 6-31G(d) basis set. Calculations were then run using either the B3LYP or  $\omega$ B97X-D<sub>3</sub> functional both with the Def2SVP basis set. *Ab initio* molecular dynamics simulations were performed similar to those in our previous work.<sup>67</sup>



## C.2 Supporting Figures

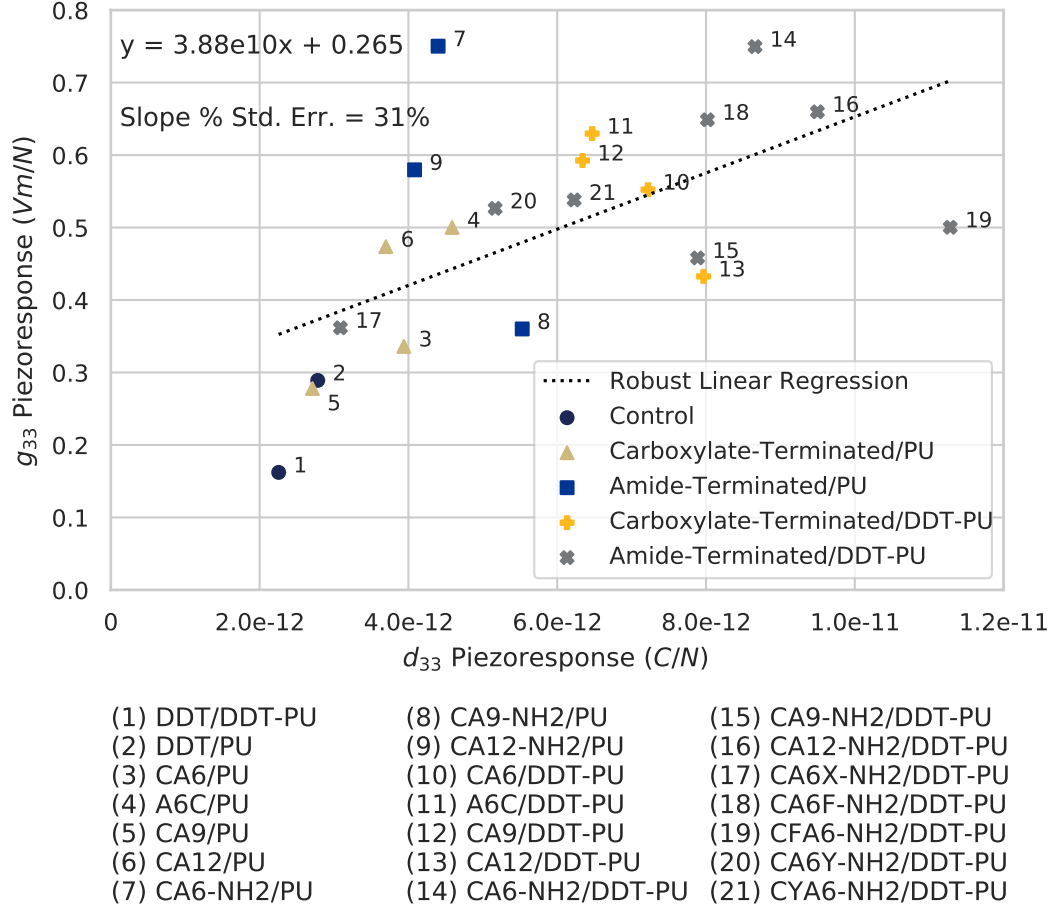


Figure C.1: Relationship between measured piezoelectric charge and voltage constants for peptide self-assembled monolayer (PSAM) devices. The dotted line is a robust linear regression of the data (calculated using the statsmodels Python package<sup>152</sup> with Huber's T norm) and can be used to calculate the effective relative permittivity of the devices. Since the piezoelectric charge and voltage constants are related by the relative permittivity, the slope of the linear fit is equal to the inverse of the absolute permittivity, so  $\varepsilon = \varepsilon_r \varepsilon_0 = \frac{1}{\text{slope}}$  and  $\varepsilon_r = \frac{1}{\varepsilon_0 \cdot \text{slope}}$  where  $\varepsilon$  is the absolute permittivity,  $\varepsilon_r$  is the relative permittivity, and  $\varepsilon_0$  is the vacuum permittivity. The data give a relative permittivity value for the PSAM devices of 2.91.

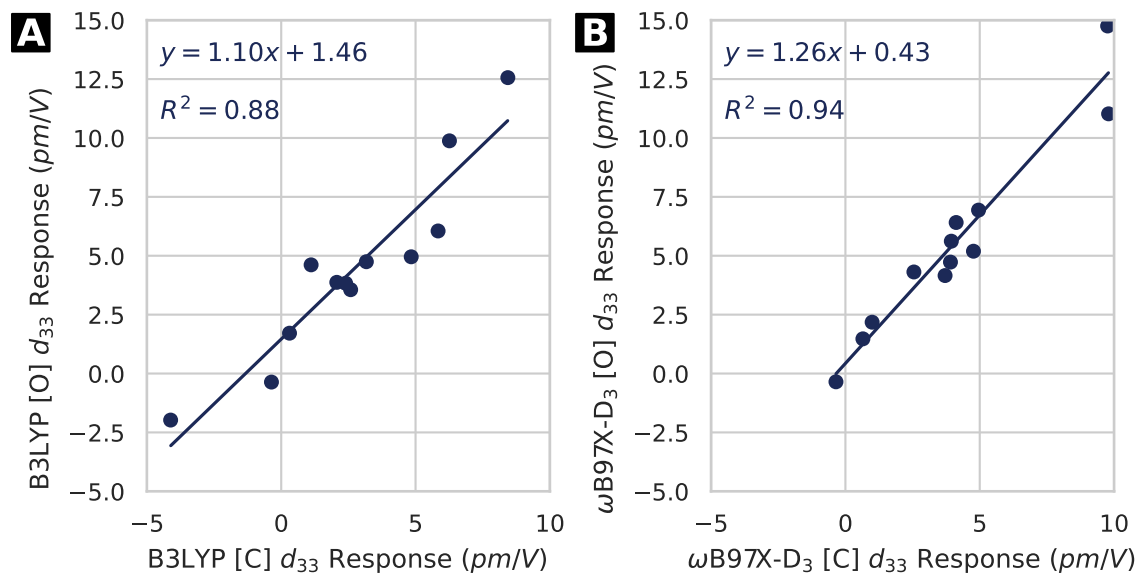


Figure C.2: Correlation between calculations made using the different measurement reference points. B3LYP and  $\omega$ B97-XD functionals were used where the length change was calculated using the distance between either [C] the N-terminus and the carbonyl carbon of the C-terminus or [O] the N-terminus and the carbonyl oxygen of the C-terminus.

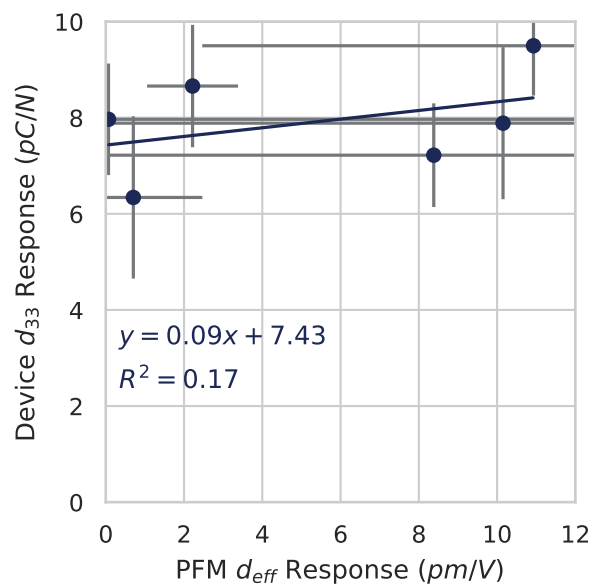


Figure C.3: Correlation of piezoelectric response between PFM measurements and device scale measurements. For device scale measurements, the results with dodecanethiol (DDT)-functionalized PU coated PCBs are used (e.g., CA<sub>X</sub>/DDT-PU).

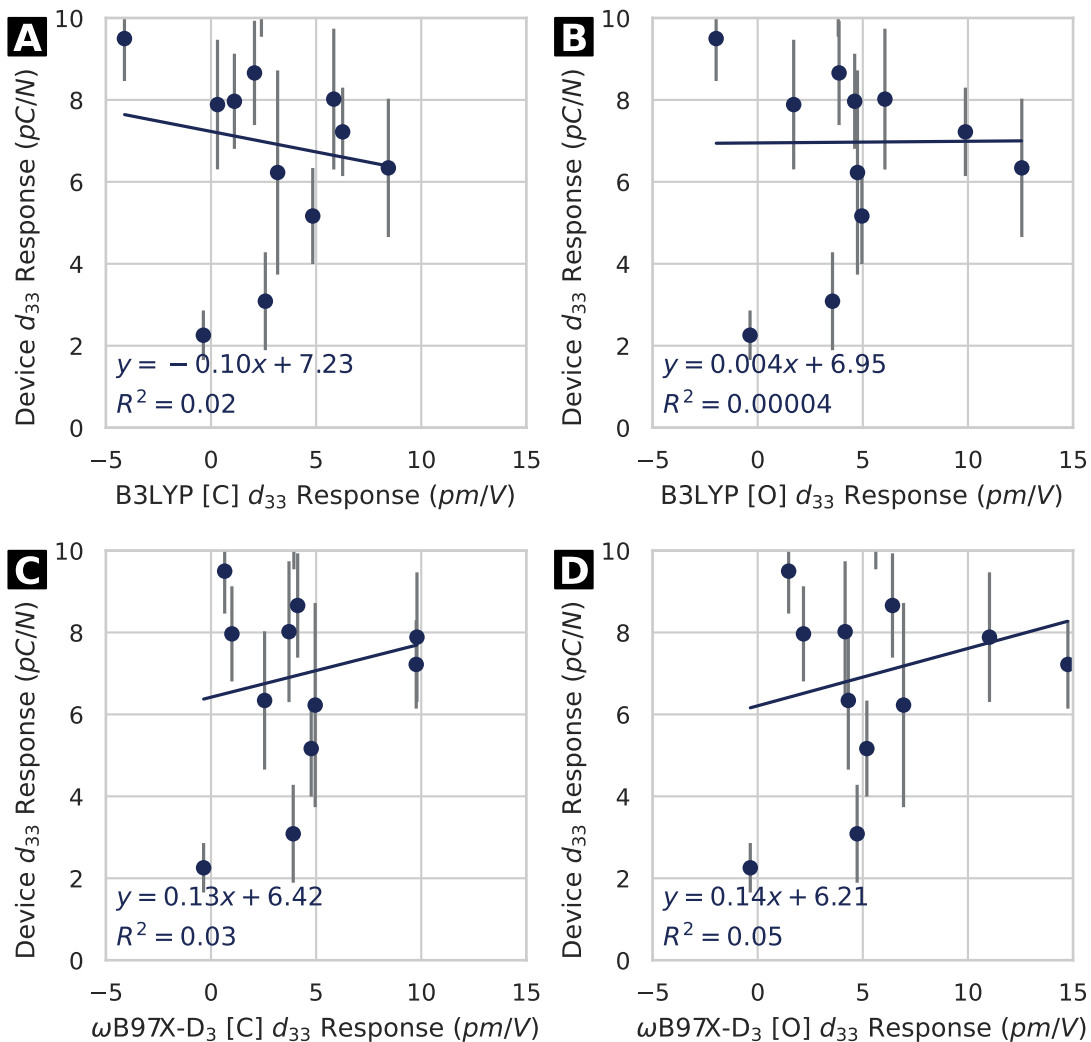


Figure C.4: Correlation of piezoelectric response between DFT calculations and device scale measurements. For device scale measurements, the results with dodecanethiol (DDT)-functionalized PU coated PCBs are used (e.g., CA<sub>X</sub>/DDT-PU). B3LYP and  $\omega$ B97-XD functionals were used where the length change was calculated using the distance between either [C] the N-terminus and the carbonyl carbon of the C-terminus or [O] the N-terminus and the carbonyl oxygen of the C-terminus.

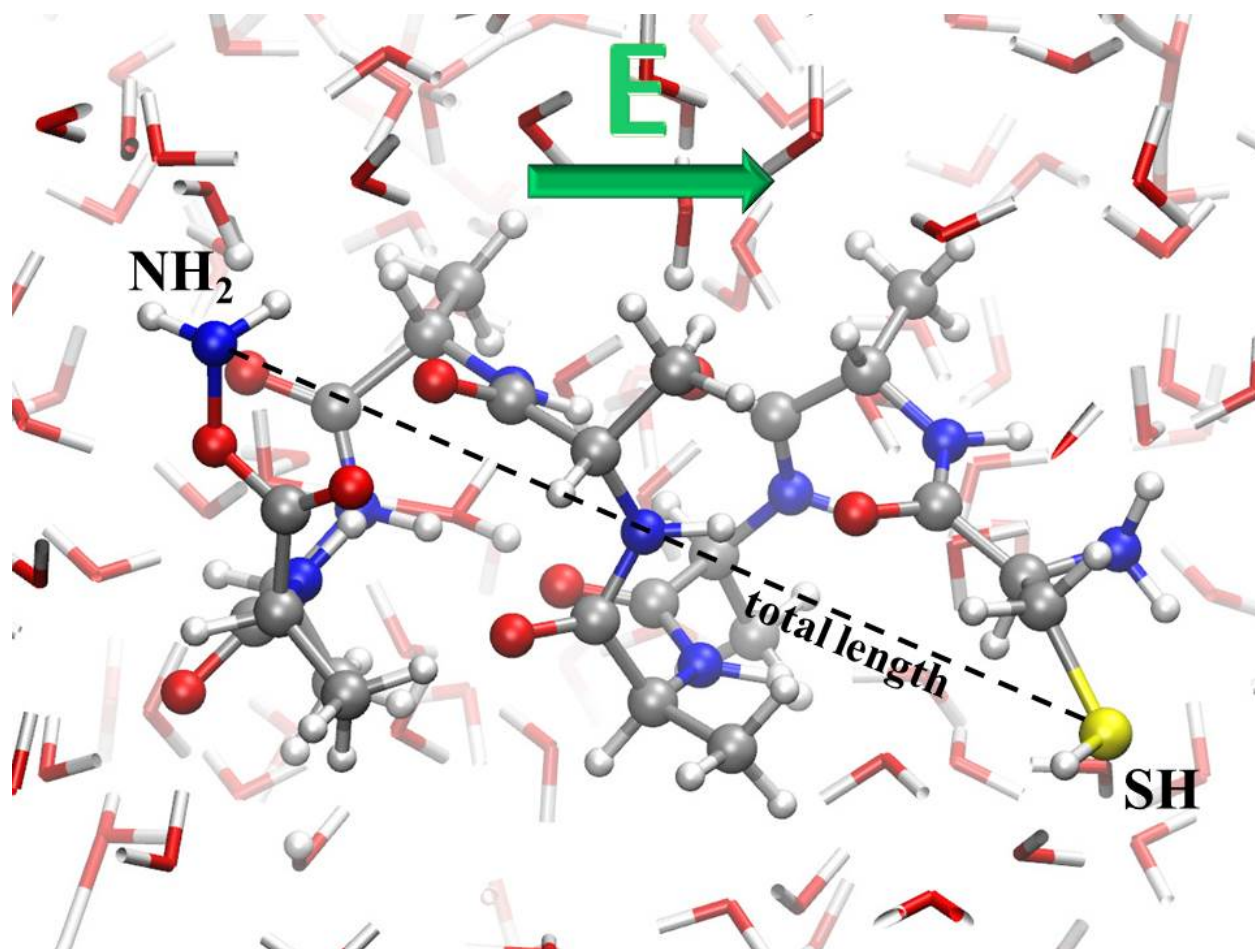


Figure C.5: Atomistic visualization of the amide-terminated peptide CA<sub>7</sub>-NH<sub>2</sub> in liquid water from room-temperature *ab initio* molecular dynamics simulations. The total length of the peptide is calculated as being the distance between the the sulfur on the cysteine of the N-terminus and amide nitrogen of the C-terminus. The direction of the applied electric field is also indicated. Red, grey, yellow, blue, and white coloring refer to oxygen, carbon, sulfur, nitrogen, and hydrogen atoms, respectively.

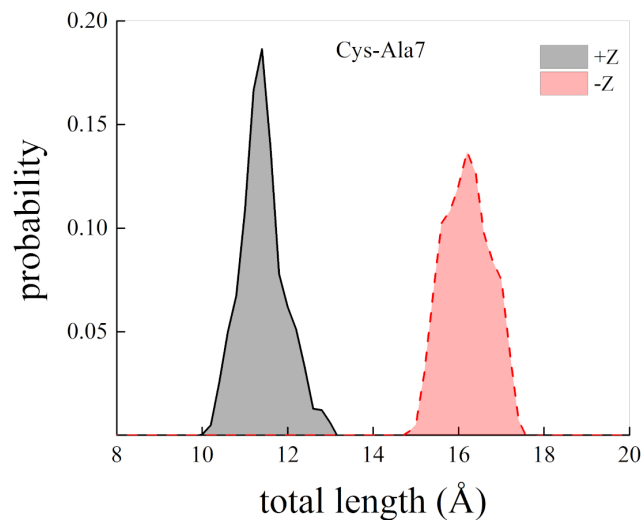


Figure C.6: Probability distributions of the length of the structure of the amide-terminated peptide CA<sub>7</sub>-NH<sub>2</sub> at field strengths of 1.0 V/nm (+Z) (solid curve) and -1.0 V/nm (-Z) (dashed curve), as determined by *ab initio* molecular dynamics simulations. For the distances definition, please refer to Figure C.5. Note the multiple dominant helices.

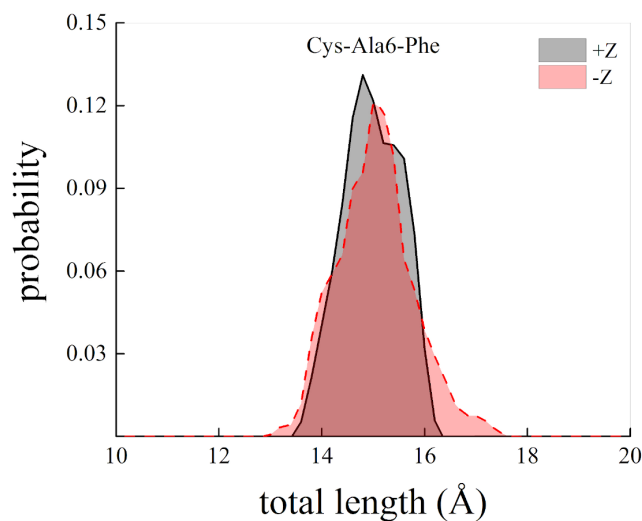


Figure C.7: Probability distributions of the length of the structure of the amide-terminated peptide CA<sub>6</sub>F-NH<sub>2</sub> at field strengths of 1.0 V/nm (+Z) (solid curve) and -1.0 V/nm (-Z) (dashed curve), as determined by *ab initio* molecular dynamics simulations. For the distances definition, please refer to Figure C.5.

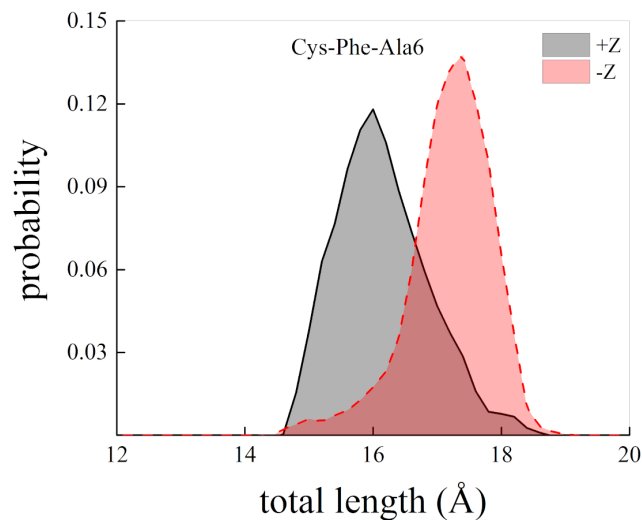


Figure C.8: Probability distributions of the length of the structure of the amide-terminated peptide CFA<sub>6</sub>-NH<sub>2</sub> at field strengths of 1.0 V/nm (+Z) (solid curve) and −1.0 V/nm (−Z) (dashed curve), as determined by *ab initio* molecular dynamics simulations. For the distances definition, please refer to Figure C.5. Note the multiple dominant helices.

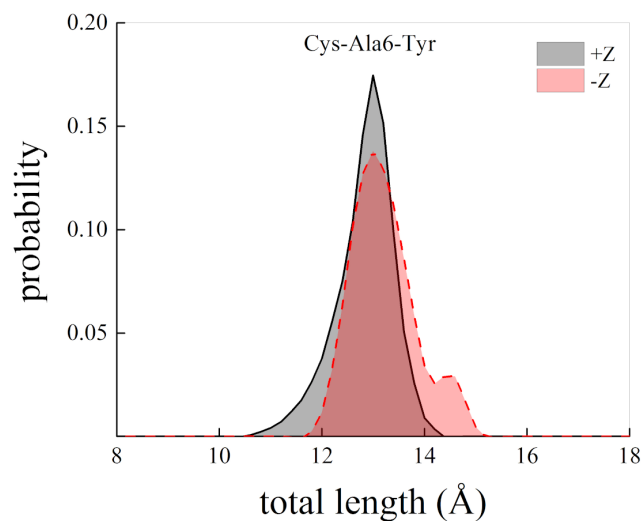


Figure C.9: Probability distributions of the length of the structure of the amide-terminated peptide CA<sub>6</sub>Y-NH<sub>2</sub> at field strengths of 1.0 V/nm (+Z) (solid curve) and −1.0 V/nm (−Z) (dashed curve), as determined by *ab initio* molecular dynamics simulations. For the distances definition, please refer to Figure C.5.

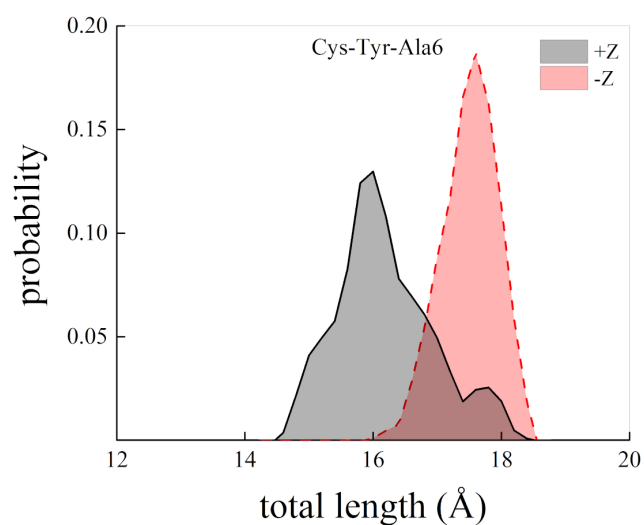


Figure C.10: Probability distributions of the length of the structure of the amide-terminated peptide  $\text{CYA}_6\text{-NH}_2$  at field strengths of  $1.0 \text{ V/nm}$  (+Z) (solid curve) and  $-1.0 \text{ V/nm}$  (-Z) (dashed curve), as determined by *ab initio* molecular dynamics simulations. For the distances definition, please refer to Figure C.5. Note the multiple dominant helices.

# Appendix D: Supplementary Information for Double-Wave Method Ferroelectric Measurements of a Corannulene Derivative

## D.1 Minimum Working Example of Ferroelectric Analysis Python Script

The following is a minimum working example of the Python script used to convert current traces into current-voltage and charge-voltage loops.

```
1  #!/usr/bin/env python3
2
3  import numpy as np
4  import pandas as pd
5
6  # Load data
7  file = 'data-file-name'
8  a = pd.pandas.read_csv(file + '.csv')
9
10 # Set parameters
11 numberTests = 16
12 maxVoltage = 10
13
14 # Calculate voltage steps
15 voltage = []
16 for i in range(50):
```



```

17     voltage.append((i + 1) * (maxVoltage / 50))
18     for i in range(50):
19         voltage.append(maxVoltage - (i + 1) * (maxVoltage / 50))
20     for i in range(50):
21         voltage.append(-(i + 1) * (maxVoltage / 50))
22     for i in range(50):
23         voltage.append(-maxVoltage + (i + 1) * (maxVoltage / 50))
24
25     # Make main dataframe
26     data = pd.DataFrame(a.iloc[np.r_[300:400,600:700]]['Time (s)'])
27     data.reset_index(drop=True,inplace=True)
28
29     voltagedf = pd.DataFrame(voltage,columns=['Voltage (V)'])
30     data['Voltage (V)'] = voltagedf['Voltage (V)']
31
32     # Loop through current data for each test
33     for i in range(numberTests):
34         # Combine positive peaks
35         x0 = a.iloc[300 + 600 * i:400 + 600 * i]['Time (s)']
36         yA0 = a.iloc[300 + 600 * i:400 + 600 * i]['CurrentA (I)']
37         yB0 = a.iloc[450 + 600 * i:550 + 600 * i]['CurrentA (I)']
38
39         y0 = []
40
41         zip_object0 = zip(yA0,yB0)
42         for yA0_i, yB0_i in zip_object0:
43             y0.append(yA0_i-yB0_i)
44
45         # Combine negative peaks

```

```

46     x1 = a.iloc[600 + 600 * i:700 + 600 * i]['Time (s)']
47     yA1 = a.iloc[600 + 600 * i:700 + 600 * i]['CurrentA (I)']
48     yB1 = a.iloc[750 + 600 * i:850 + 600 * i]['CurrentA (I)']
49
50     y1 = []
51
52     zip_object1 = zip(yA1,yB1)
53     for yA1_i, yB1_i in zip_object1:
54         y1.append(yA1_i-yB1_i)
55
56     # Combine postive and negative peaks into one list
57     for j in y1:
58         y0.append(j)
59
60     # Make df and add to data
61     df = pd.DataFrame(y0,columns=['test' + str(i + 1)])
62     data['test' + str(i + 1)] = df['test' + str(i + 1)]
63
64     # Average current
65     col = data.loc[:, 'test1': 'test' + str(numberTests)]
66     data['Average Current (A)'] = col.mean(axis=1)
67
68     # Calculate charge
69     data['Average Charge (C)'] = np.nan
70     data.at[0, 'Average Charge (C)'] = 0
71     for i in range(1,len(data.index)):
72         data.at[i, 'Average Charge (C)'] = data.iloc[i-1]['Average Charge (C)'] \
73             + (data.iloc[i-1]['Average Current (A)'] + \
74                 data.iloc[i]['Average Current (A)']) / 2 * (data.iloc[i]['Time (s)'] \

```

```

75         - data.iloc[i-1]['Time (s)'])
76
77     # Correct shift between positive and negative voltage
78     shift = data.iloc[100]['Average Charge (C)'] \
79         - data.iloc[99]['Average Charge (C)']
80     for i in range(100,len(data.index)):
81         data.at[i,'Average Charge (C)'] = data.iloc[i]['Average Charge (C)'] \
82             - shift
83
84     # Save processed data
85     data.to_csv(file + '-charge-current.csv', \
86         columns=['Voltage (V)','Average Current (A)','Average Charge (C)'])

```

# Bibliography

- [1] Williams, B. P.; Lo, W.-S.; Morabito, J. V.; Young, A. P.; Tsung, F.; Kuo, C.-H.; Palomba, J. M.; Rayder, T. M.; Chou, L.-Y.; Sneed, B. T.; Liu, X.-Y.; Lamontagne, L. K.; Petroff, C. A.; Brodsky, C. N.; Yang, J.; Andoni, I.; Li, Y.; Zhang, F.; Li, Z.; Chen, S.-Y.; Gallacher, C.; Li, B.; Tsung, S.-Y.; Pu, M.-H.; Tsung, C.-K. Tailoring Heterogeneous Catalysts at the Atomic Level: In Memoriam, Prof. Chia-Kuang (Frank) Tsung. *ACS Appl. Mater. Interfaces* DOI: 10.1021/acsami.1c08916.
- [2] Böttcher, C. J. F.; van Belle, O. C.; Bordewijk, P.; Rip, A. *Theory of Electric Polarization*, 2nd ed.; Elsevier Scientific Publishing Company: New York, 1973; DOI: 10.1016/C2009-0-15579-4.
- [3] Jaffe, B.; Cook, W. R.; Jaffe, H. *Piezoelectric Ceramics*; Academic Press: New York, 1971; DOI: 10.1016/B978-0-12-379550-2.50007-7.
- [4] Cady, W. G. *Piezoelectricity: An Introduction to the Theory and Applications of Electromechanical Phenomena in Crystals*, new revised ed.; Dover Publications: New York, 1964; Vol. one.
- [5] Atkins, P.; de Paula, J. *Physical Chemistry*, 9th ed.; W. H. Freeman and Company: New York, 2010.
- [6] Megson, T. H. G. *Structural and Stress Analysis*, 2nd ed.; Elsevier Butterworth-Heinemann: New York, 2005.
- [7] Sadd, M. H. *Elasticity: Theory, Applications, and Numerics*; Elsevier Butterworth-Heinemann: New York, 2005; DOI: 10.1016/B978-0-12-605811-6.X5000-3.
- [8] Clemitson, I. R. *Polyurethane Casting Primer*; CRC Press Taylor & Francis Group: New York, 2012.
- [9] Choi, S.-J.; Kwon, T.-H.; Im, H.; Moon, D.-I.; Baek, D. J.; Seol, M.-L.; Duarte, J. P.; Choi, Y.-K. A Polydimethylsiloxane (PDMS) Sponge for the Selective Absorption of Oil from Water. *ACS Appl. Mater. Interfaces* **2011**, *3*, 4552–4556, DOI: 10.1021/am201352w.
- [10] Curie, P.; Curie, J. Développement, par pression, de l'électricité polaire dans les cristaux hémihédres à faces inclinées. *Comptes Rendus* **1881**, *91*, 294–295, DOI: 10.3406/bulmi.1880.1564.
- [11] Hankel, W. G. Über die aktino- und piezoelektrischen eigenschaften des bergkrystalles und ihre beziehung zu den thermoelektrischen. *Abh. Söchs.* **1881**, *12*, 457–547.
- [12] Arnau, A.; Soares, D. In *Piezoelectric Transducers and Applications*, 2nd ed.; Vives, A. A., Ed.; Springer Berlin Heidelberg: Berlin, 2008; pp 1–38, DOI: 10.1007/978-3-540-77508-9\_1.

- [13] Lippmann, G. Principe de conservation de l'électricité, ou second principe de la théorie des phénomènes électriques. *J. Phys. Theor. Appl.* **1881**, 10, 381–394, DOI: 10.1051/jphysap:0188100100038100.
- [14] Voigt, W. *Lehrbuch der Kristallphysik (mit Ausschluss der Kristalloptik)*; B. G. Teubner: Leipzig, 1910; DOI: 10.1007/978-3-663-15884-4.
- [15] Cady, W. G. The Piezo-Electric Resonator in Proceedings of the American Physical Society. *Phys. Rev.* **1921**, 17, 531, DOI: 10.1103/PhysRev.17.508.
- [16] *Standards on Piezoelectric Crystals: Recommended Terminology*; The Institute of Radio Engineers: New York, 1945.
- [17] Standards on Piezoelectric Crystals, 1949. *Proc. IRE* **1949**, 37, 1378–1395, DOI: 10.1109/JRPROC.1949.229975.
- [18] Helke, G.; Lubitz, K. In *Piezoelectricity: Evolution and Future of a Technology*; Heywang, W., Lubitz, K., Wersing, W., Eds.; Springer: Berlin, 2008; Vol. 114; Chapter 4, pp 89–130, DOI: 10.1007/978-3-540-68683-5.
- [19] Savchuk, G. K.; Letko, A. K. Crystal structure of lead zirconate titanate ceramics prepared using ultrasonic processing. *Inorg. Mater.* **2017**, 53, 226–232, DOI: 10.1134/S0020168517020121.
- [20] Pinin/Wikimedia Commons. Perovskite structure of PZT. <https://commons.wikimedia.org/wiki/File:Perovskite.svg> (accessed Nov 8, 2017).
- [21] Bowen, C. R.; Kim, H. A.; Weaver, P. M.; Dunn, S. Piezoelectric and ferroelectric materials and structures for energy harvesting applications. *Energy Environ. Sci.* **2014**, 7, 25–44, DOI: 10.1039/c3ee42454e.
- [22] Halperin, C.; Mutchnik, S.; Agronin, A.; Molotskii, M.; Urenski, P.; Salai, M.; Rosenman, G. Piezoelectric Effect in Human Bones Studied in Nanometer Scale. *Nano Lett.* **2004**, 4, 1253–1256, DOI: 10.1021/nl049453i.
- [23] Hayward, G.; Bennett, J.; Hamilton, R. A theoretical study on the influence of some constituent material properties on the behavior of 1-3 connectivity composite transducers. *J. Acoust. Soc. Am.* **1995**, 98, 2187–2196, DOI: 10.1121/1.413333.
- [24] Kepler, R. G.; Anderson, R. A. Piezoelectricity in polymers. *Crit. Rev. Solid State Mater. Sci.* **1980**, 9, 399–447, DOI: 10.1080/10408438008243576.
- [25] IEEE Standard on Piezoelectricity. *ANSI/IEEE Std 176-1987* **1988**, 1–66, DOI: 10.1109/IEEESTD.1988.79638.
- [26] Bechmann, R. Elastic and Piezoelectric Constants of Alpha-Quartz. *Phys. Rev.* **1958**, 110, 1060–1061, DOI: 10.1103/PhysRev.110.1060.

- [27] Newnham, R.; Bowen, L.; Klinker, K.; Cross, L. Composite piezoelectric transducers. *Mater. Des.* **1980**, *2*, 93–106, DOI: 10.1016/0261-3069(80)90019-9.
- [28] Berlincourt, D.; Jaffe, H. Elastic and Piezoelectric Coefficients of Single-Crystal Barium Titanate. *Phys. Rev.* **1958**, *111*, 143–148, DOI: 10.1103/PhysRev.111.143.
- [29] Uchino, K. In *Advanced Piezoelectric Materials*; Uchino, K., Ed.; Woodhead Publishing Series in Electronic and Optical Materials; Woodhead Publishing, 2010; pp 318–346, DOI: 10.1533/9781845699758.1.318.
- [30] Guerin, S.; Stapleton, A.; Chovan, D.; Mouras, R.; Gleeson, M.; McKeown, C.; Noor, M. R.; Silien, C.; Rhen, F. M. F.; Kholkin, A. L.; Liu, N.; Soulimane, T.; Tofail, S. A. M.; Thompson, D. Control of piezoelectricity in amino acids by supramolecular packing. *Nat. Mater.* **2017**, *17*, 180–186, DOI: 10.1038/nmat5045.
- [31] Stracke, A.; Bayer, A.; Zimmermann, S.; Wendorff, J. H.; Wirges, W.; Bauer-Gogonea, S.; Bauer, S.; Gerhard-Multhaupt, R. Relaxation behaviour of electrically induced polar orientation and of optically induced non-polar orientation in an azo-chromophore side group polymer. *J. Phys. D: Appl. Phys.* **1999**, *32*, 2996–3003, DOI: 10.1088/0022-3727/32/23/304.
- [32] Moody, M. J.; Marvin, C. W.; Hutchison, G. R. Molecularly-doped polyurethane foams with massive piezoelectric response. *J. Mater. Chem. C* **2016**, *4*, 4387–4392, DOI: 10.1039/c6tc00613b.
- [33] Moulson, A. J.; Herbert, J. M. *Electroceramics: Materials, properties, and applications*; Chapman and Hall: New York, 1990.
- [34] Ballato, A. In *Piezoelectricity: Evolution and Future of a Technology*; Heywang, W., Lubitz, K., Wersing, W., Eds.; Springer: Berlin, 2008; Vol. 114; Chapter 2, pp 9–35, DOI: 10.1007/978-3-540-68683-5.
- [35] Momosaki, E. A brief review of progress in quartz tuning fork resonators. Proceedings of International Frequency Control Symposium. 1997; pp 552–565, DOI: 10.1109/FREQ.1997.638700.
- [36] Guerin, S.; Stapleton, A.; Chovan, D.; Mouras, R.; Gleeson, M.; McKeown, C.; Noor, M. R.; Silien, C.; Rhen, F. M. F.; Kholkin, A. L.; Liu, N.; Soulimane, T.; Tofail, S. A. M.; Thompson, D. Control of piezoelectricity in amino acids by supramolecular packing. *Nat. Mater.* **2017**, *17*, 180–186, DOI: 10.1038/nmat5045.
- [37] Guerin, S.; O'Donnell, J.; Haq, E. U.; McKeown, C.; Silien, C.; Rhen, F. M. F.; Soulimane, T.; Tofail, S. A. M.; Thompson, D. Racemic Amino Acid Piezoelectric Transducer. *Phys. Rev. Lett.* **2019**, *122*, 047701, DOI: 10.1103/PhysRevLett.122.047701.
- [38] Kim, D.; Han, S. A.; Kim, J. H.; Lee, J.-H.; Kim, S.-W.; Lee, S.-W. Biomolecular Piezoelectric Materials: From Amino Acids to Living Tissues. *Adv. Mater. (Weinheim, Ger.)* **2020**, *32*, 1906989, DOI: 10.1002/adma.201906989.

- [39] Guerin, S.; Tofail, S. A. M.; Thompson, D. Longitudinal Piezoelectricity in Orthorhombic Amino Acid Crystal Films. *Crystal Growth Des.* **2018**, *18*, 4844–4848, DOI: 10.1021/acs.cgd.8b00835.
- [40] Tilley, R. J. D. *Perovskites: Structure-Property Relationships*; John Wiley & Sons: West Sussex, UK, 2016.
- [41] Horchidan, N.; Ciomaga, C.; Frunza, R.; Capiani, C.; Galassi, C.; Mitoseriu, L. A comparative study of hard/soft PZT-based ceramic composites. *Ceram. Int.* **2016**, *42*, 9125–9132, DOI: 10.1016/j.ceramint.2016.02.179.
- [42] Kim, K.; Zhu, W.; Qu, X.; Aaronson, C.; McCall, W. R.; Chen, S.; Sirbulu, D. J. 3D Optical Printing of Piezoelectric Nanoparticle–Polymer Composite Materials. *ACS Nano* **2014**, *8*, 9799–9806, DOI: 10.1021/nm503268f.
- [43] Wang, F.; Mai, Y.-W.; Wang, D.; Ding, R.; Shi, W. High quality barium titanate nanofibers for flexible piezoelectric device applications. *Sens. Actuators, A* **2015**, *233*, 195–201, DOI: 10.1016/j.sna.2015.07.002.
- [44] Anton, S.; Farinholt, K.; Erturk, A. Piezoelectret foam–based vibration energy harvesting. *J. Intell. Mater. Syst. Struct.* **2014**, *25*, 1681–1692, DOI: 10.1177/1045389X14541501.
- [45] Bauer, S.; Bauer, F. In *Piezoelectricity: Evolution and Future of a Technology*; Heywang, W., Lubitz, K., Wersing, W., Eds.; Springer: Berlin, 2008; Vol. 114; Chapter 4, pp 157–177, DOI: 10.1007/978-3-540-68683-5.
- [46] Crossley, S.; Whiter, R. A.; Kar-Narayan, S. Polymer-based nanopiezoelectric generators for energy harvesting applications. *Mater. Sci. Tech.* **2014**, *30*, 1613–1624, DOI: 10.1179/1743284714Y.00000000605.
- [47] Nguyen, D.-N.; Yu, S. M.; Moon, W. Electrospinning of poly( $\gamma$ -benzyl- $\alpha$ ,L-glutamate) microfibers for piezoelectric polymer applications. *J. Appl. Polym. Sci.* **2018**, *135*, 46440, DOI: 10.1002/app.46440.
- [48] Kabir, E.; Khatun, M.; Nasrin, L.; Raihan, M. J.; Rahman, M. Pure  $\beta$ -phase formation in polyvinylidene fluoride (PVDF)-carbon nanotube composites. *J. Phys. D: Appl. Phys.* **2017**, *50*, 163002, DOI: 10.1088/1361-6463/aa5f85.
- [49] Vallem, V.; Sargolzaeiaval, Y.; Ozturk, M.; Lai, Y.-C.; Dickey, M. D. Energy Harvesting and Storage with Soft and Stretchable Materials. *Adv. Mater.* **2021**, *33*, 2004832, DOI: 10.1002/adma.202004832.
- [50] Lee, B. Y.; Zhang, J.; Zueger, C.; Chung, W.-J.; Yoo, S. Y.; Wang, E.; Meyer, J.; Ramesh, R.; Lee, S.-W. Virus-based piezoelectric energy generation. *Nat. Nanotechnol.* **2012**, *7*, 351–356, DOI: 10.1038/nnano.2012.69.

- [51] Dagdeviren, C.; Joe, P.; Tuzman, O. L.; Park, K.-I.; Lee, K. J.; Shi, Y.; Huang, Y.; Rogers, J. A. Recent progress in flexible and stretchable piezoelectric devices for mechanical energy harvesting, sensing and actuation. *Extreme Mech. Lett.* **2016**, *9*, 269 – 281, DOI: 10.1016/j.eml.2016.05.015.
- [52] Ma, L. L.; Chen, W. J.; Zheng, Y. In *Handbook of Mechanics of Materials*; Schmauder, S., Chen, C.-S., Chawla, K. K., Chawla, N., Chen, W., Kagawa, Y., Eds.; Springer Singapore: Singapore, 2019; pp 549–589, DOI: 10.1007/978-981-10-6884-3\_18.
- [53] Uchino, K. *Ferroelectric Devices*; Marcel Dekker: New York, 2000.
- [54] Cady, W. G. *Piezoelectricity: An Introduction to the Theory and Applications of Electromechanical Phenomena in Crystals*, new revised ed.; Dover Publications: New York, 1964; Vol. two.
- [55] Sessler, G. M. In *Electrets*, second enlarged ed.; Sessler, G. M., Ed.; Springer-Verlag: New York, 1987; pp 13–80, DOI: 10.1007/3540173358\_10.
- [56] Kestelman, V. N.; Pinchuk, L. S.; Goldade, V. A. *Electrets in Engineering: Fundamentals and Applications*; Kluwer Academic Publishers: Boston, 2000; DOI: 10.1007/978-1-4615-4455-5.
- [57] Li, J.; Shepelin, N. A.; Sherrell, P. C.; Ellis, A. V. Poly(dimethylsiloxane) for Triboelectricity: From Mechanisms to Practical Strategies. *Chem. Mater.* **2021**, *33*, 4304–4327, DOI: 10.1021/acs.chemmater.1c01275.
- [58] Tressler, J. F.; Alkoy, S.; Newnham, R. E. Piezoelectric Sensors and Sensor Materials. *J. Electroceram.* **1998**, *2*, 257–272, DOI: 10.1023/a:1009926623551.
- [59] Akdogan, E. K.; Allahverdi, M.; Safari, A. Piezoelectric composites for sensor and actuator applications. *IEEE Trans. Ultrason. Ferroelectr. Freq. Control* **2005**, *52*, 746–775, DOI: 10.1109/TUFFC.2005.1503962.
- [60] Newnham, R. E.; Safari, A.; Giniewicz, J.; Fox, B. H. Composite piezoelectric sensors. *Ferroelectrics* **1984**, *60*, 15–21, DOI: 10.1080/00150198408017505.
- [61] Newnham, R.; Skinner, D.; Cross, L. Connectivity and piezoelectric-pyroelectric composites. *Mater. Res. Bull.* **1978**, *13*, 525–536, DOI: 10.1016/0025-5408(78)90161-7.
- [62] IRE Standards on Piezoelectric Crystals: Determination of the Elastic, Piezoelectric, and Dielectric Constants—The Electromechanical Coupling Factor, 1958. *Proc. IRE* **1958**, *46*, 764–778, DOI: 10.1109/JRPROC.1958.286778.
- [63] Berlincourt, D. A.; Cmolik, C.; Jaffe, H. Piezoelectric Properties of Polycrystalline Lead Titanate Zirconate Compositions. *Proc. IRE* **1960**, *48*, 220–229, DOI: 10.1109/JRPROC.1960.287467.
- [64] Newman, B. A.; Scheinbeim, J. I.; Sen, A. The effect of plasticizer on the piezoelectric properties of unoriented polyvinylidene fluoride films. *Ferroelectrics* **1984**, *57*, 229–241, DOI: 10.1080/00150198408012765.



- [65] Petroff, C. A.; Bina, T. F.; Hutchison, G. R. Highly Tunable Molecularly Doped Flexible Poly(dimethylsiloxane) Foam Piezoelectric Energy Harvesters. *ACS Appl. Energy Mater.* **2019**, *2*, 6484–6489, DOI: 10.1021/acsaem.9b01061.
- [66] Ulman, A. Formation and Structure of Self-Assembled Monolayers. *Chem. Rev.* **1996**, *96*, 1533–1554, DOI: 10.1021/cr9502357.
- [67] Petroff, C. A.; Cassone, G.; Šponer, J.; Hutchison, G. R. Intrinsically Polar Piezoelectric Self-Assembled Oligopeptide Monolayers. *Adv. Mater.* **2021**, *33*, 2007486, DOI: 10.1002/adma.202007486.
- [68] IRE Standards on Piezoelectric Crystals—The Piezoelectric Vibrator: Definitions and Methods of Measurement, 1957. *Proc. IRE* **1957**, *45*, 353–358, DOI: 10.1109/JRPROC.1957.278371.
- [69] IRE Standards on Piezoelectric Crystals: Measurements of Piezoelectric Ceramics, 1961. *Proc. IRE* **1961**, *49*, 1161–1169, DOI: 10.1109/JRPROC.1961.287860.
- [70] IEEE Standard on Piezoelectricity. *ANSI/IEEE Std 176-1978* **1978**, 1–58, DOI: 10.1109/IEEESTD.1978.8941331.
- [71] Tsujiura, Y.; Kawabe, S.; Kurokawa, F.; Hida, H.; Kanno, I. Comparison of effective transverse piezoelectric coefficients  $e_{31,f}$  of  $\text{Pb}(\text{Zr,Ti})\text{O}_3$  thin films between direct and converse piezoelectric effects. *Jpn. J. Appl. Phys.* **2015**, *54*, 10NA04, DOI: 10.7567/jjap.54.10na04.
- [72] Drdlik, D.; Zeman, D.; Tofel, P.; Chlup, Z.; Hadraba, H.; Drdlikova, K. A comparative study of direct and indirect evaluation of piezoelectric properties of electrophoretically deposited (Ba, Ca) (Zr, Ti) $\text{O}_3$  lead-free piezoceramics. *Ceram. Int.* **2021**, *47*, 2034–2042, DOI: 10.1016/j.ceramint.2020.09.035.
- [73] Fu, J. Y.; Liu, P. Y.; Cheng, J.; Bhalla, A. S.; Guo, R. Optical measurement of the converse piezoelectric  $d_{33}$  coefficients of bulk and microtubular zinc oxide crystals. *Appl. Phys. Lett.* **2007**, *90*, 212907, DOI: 10.1063/1.2742587.
- [74] Broitman, E.; Soomro, M. Y.; Lu, J.; Willander, M.; Hultman, L. Nanoscale piezoelectric response of ZnO nanowires measured using a nanoindentation technique. *Phys. Chem. Chem. Phys.* **2013**, *15*, 11113–11118, DOI: 10.1039/C3CP50915J.
- [75] Mason, W. P.; Jaffe, H. Methods for Measuring Piezoelectric, Elastic, and Dielectric Coefficients of Crystals and Ceramics. *Proc. IRE* **1954**, *42*, 921–930, DOI: 10.1109/JRPROC.1954.274752.
- [76] Erhart, J.; Burianová, L. What is really measured on a  $d_{33}$ -meter? *J. Eur. Ceram. Soc.* **2001**, *21*, 1413–1415, DOI: 10.1016/S0955-2219(01)00030-9.
- [77] Stewart, M.; Battrick, W.; Cain, M. G. *Measuring piezoelectric  $d_{33}$  coefficients using the direct method.*; National Physical Laboratory, 2001.

- [78] IEEE Standard Definitions and Methods of Measurement for Piezoelectric Vibrators. *IEEE Std 177* **1966**, DOI: 10.1109/IEEESTD.1966.120168.
- [79] Uchino, K. In *Ultrasonic transducers: Materials and design for sensors, actuators and medical applications*; Nakamura, K., Ed.; Woodhead Publishing: Philadelphia, 2012; Chapter 3, pp 70–116.
- [80] Güthner, P.; Dransfeld, K. Local poling of ferroelectric polymers by scanning force microscopy. *Appl. Phys. Lett.* **1992**, *61*, 1137–1139, DOI: 10.1063/1.107693.
- [81] Rodriguez, B. J.; Callahan, C.; Kalinin, S. V.; Proksch, R. Dual-frequency resonance-tracking atomic force microscopy. *Nanotechnol.* **2007**, *18*, 475504, DOI: 10.1088/0957-4484/18/47/475504.
- [82] Miller, N. C.; Grimm, H. M.; Horne, W. S.; Hutchison, G. R. Accurate electromechanical characterization of soft molecular monolayers using piezo force microscopy. *Nanoscale Adv.* **2019**, *1*, 4834–4843, DOI: 10.1039/C9NA00638A.
- [83] Argin, M.; Karady, G. G. Characterization of Polyurethane Foam Dielectric Strength. *IEEE Trans. Dielectr. Electr. Insul.* **2008**, *15*, 350–356, DOI: 10.1109/TDEI.2008.4483452.
- [84] Wang, Z. L. Towards Self-Powered Nanosystems: From Nanogenerators to Nanopiezotronics. *Adv. Funct. Mater.* **2008**, *18*, 3553–3567, DOI: 10.1002/adfm.200800541.
- [85] Dagdeviren, C.; Yang, B. D.; Su, Y.; Tran, P. L.; Joe, P.; Anderson, E.; Xia, J.; Doraiswamy, V.; Dehdashti, B.; Feng, X.; Lu, B.; Poston, R.; Khalpey, Z.; Ghaffari, R.; Huang, Y.; Slepian, M. J.; Rogers, J. A. Conformal piezoelectric energy harvesting and storage from motions of the heart, lung, and diaphragm. *Proc. Natl. Acad. Sci. U.S.A.* **2014**, *111*, 1927–1932, DOI: 10.1073/pnas.1317233111.
- [86] Mader, G.; Meixner, H.; Kleinschmidt, P. Temperature and stress dependence of Young’s modulus in semiconducting barium titanate ceramics. *J. Appl. Phys.* **1985**, *58*, 702–704, DOI: 10.1063/1.336185.
- [87] Webber, K.; Aulbach, E.; Key, T.; Marsilius, M.; Granzow, T.; Rödel, J. Temperature-dependent ferroelastic switching of soft lead zirconate titanate. *Acta Mater.* **2009**, *57*, 4614–4623, DOI: 10.1016/j.actamat.2009.06.037.
- [88] Yan, Y.; Zhou, J. E.; Maurya, D.; Wang, Y. U.; Priya, S. Giant piezoelectric voltage coefficient in grain-oriented modified PbTiO<sub>3</sub> material. *Nat. Commun.* **2016**, *7*, 13089, DOI: 10.1038/ncomms13089.
- [89] Lee, J.-H.; Heo, K.; Schulz-Schönhagen, K.; Lee, J. H.; Desai, M. S.; Jin, H.-E.; Lee, S.-W. Diphenylalanine Peptide Nanotube Energy Harvesters. *ACS Nano* **2018**, *12*, 8138–8144, DOI: 10.1021/acsnano.8b03118.

- [90] Zhang, Y.; Jeong, C. K.; Yang, T.; Sun, H.; Chen, L.-Q.; Zhang, S.; Chen, W.; Wang, Q. Bioinspired elastic piezoelectric composites for high-performance mechanical energy harvesting. *J. Mater. Chem. A* **2018**, *6*, 14546–14552, DOI: 10.1039/C8TA03617A.
- [91] Ma, S.; Jin, L.; Huang, X.; Riziotis, C.; Huang, R.; Zhang, C.; Lu, J.; Yang, W. Nanogenerators Begin to Light Up: A Novel Poling-Free Piezoelectric System with Multicolor Photoluminescence as an Efficient Mechatronics Development Platform. *Adv. Mater. Interfaces* **2018**, *5*, 1800587, DOI: 10.1002/admi.201800587.
- [92] McCall, W. R.; Kim, K.; Heath, C.; La Pierre, G.; Sirbulu, D. J. Piezoelectric Nanoparticle–Polymer Composite Foams. *ACS Appl. Mater. Interfaces* **2014**, *6*, 19504–19509, DOI: 10.1021/am506415y.
- [93] Maity, K.; Garain, S.; Henkel, K.; Schmeißer, D.; Mandal, D. Natural Sugar-Assisted, Chemically Reinforced, Highly Durable Piezoorganic Nanogenerator with Superior Power Density for Self-Powered Wearable Electronics. *ACS Appl. Mater. Interfaces* **2018**, *10*, 44018–44032, DOI: 10.1021/acsami.8b15320.
- [94] Swallowe, G. M. In *Mechanical Properties and Testing of Polymers: An A–Z Reference*; Swallowe, G. M., Ed.; Springer Netherlands: Dordrecht, 1999; pp 242–247, DOI: 10.1007/978-94-015-9231-4\_52.
- [95] *Technical Data Sheet: SYLGARD 184 Silicone Elastomer*; 2017; The Dow Chemical Company; Form No. 11-3184-01 C.
- [96] Tang, Y.; Zheng, Q.; Chen, B.; Ma, Z.; Gong, S. A new class of flexible nanogenerators consisting of porous aerogel films driven by mechanoradicals. *Nano Energy* **2017**, *38*, 401–411, DOI: 10.1016/j.nanoen.2017.06.022.
- [97] Chae, I.; Jeong, C. K.; Ounaies, Z.; Kim, S. H. Review on Electromechanical Coupling Properties of Biomaterials. *ACS Appl. Bio Mater.* **2018**, *1*, 936–953, DOI: 10.1021/acsabm.8b00309.
- [98] Baytekin, H. T.; Baytekin, B.; Grzybowski, B. A. Mechanoradicals Created in “Polymeric Sponges” Drive Reactions in Aqueous Media. *Angew. Chem., Int. Ed.* **2012**, *51*, 3596–3600, DOI: 10.1002/anie.201108110.
- [99] Groom, C. R.; Bruno, I. J.; Lightfoot, M. P.; Ward, S. C. The Cambridge Structural Database. *Acta Crystallogr., Sect. B: Struct. Sci., Cryst. Eng. Mater.* **2016**, *72*, 171–179, DOI: 10.1107/S2052520616003954.
- [100] Sim, G. A.; Robertson, J. M.; Goodwin, T. H. The crystal and molecular structure of benzoic acid. *Acta Crystallogr.* **1955**, *8*, 157–164, DOI: 10.1107/S0365110X55000601.
- [101] Williams, P. A.; Hughes, C. E.; Lim, G. K.; Kariuki, B. M.; Harris, K. D. M. Discovery of a New System Exhibiting Abundant Polymorphism: m-Aminobenzoic Acid. *Cryst. Growth Des.* **2012**, *12*, 3104–3113, DOI: 10.1021/cg3003178.

- [102] Brown, C. J. Further refinement of the crystal structure of acetanilide. *Acta Crystallogr.* **1966**, *21*, 442–445, DOI: 10.1107/S0365110X66003128.
- [103] Coles, S. L.; Threlfall, T. L.; Hursthouse, M. B. N-(4-Nitrophenyl)acetamide. 2009; <http://ecrystals.chem.soton.ac.uk/1383/>.
- [104] Vaughan, W. E., Ed. *Digest of Literature of Dielectrics*; National Academy of Sciences: Washington, 1973; Vol. 37.
- [105] Luts'kii, A. E.; Kondratenko, B. P. Intramolecular Hydrogen Bond and Dipole Moments of Organic Compounds. IV. Nitro- and Acetylacetanilides. *J. Gen. Chem. USSR* **1959**, *29*, 2041–2044.
- [106] McClellan, A. L. *Tables of Experimental Dipole Moments*; W. H. Freeman: San Francisco, 1963.
- [107] Millefiori, S.; Favini, G.; Millefiori, A.; Grasso, D. Electronic spectra and structure of nitroanilines. *Spectrochim. Acta, Part A* **1977**, *33*, 21–27, DOI: 10.1016/0584-8539(77)80143-8.
- [108] Liu, M.; Sun, J.; Chen, Q. Influences of heating temperature on mechanical properties of polydimethylsiloxane. *Sens. Actuators, A* **2009**, *151*, 42–45, DOI: 10.1016/j.sna.2009.02.016.
- [109] Hunter, J. D. Matplotlib: A 2D Graphics Environment. *Comput. Sci. Eng.* **2007**, *9*, 90–95, DOI: 10.1109/MCSE.2007.55.
- [110] Van Der Walt, S.; Colbert, S. C.; Varoquaux, G. The NumPy Array: A Structure for Efficient Numerical Computation. *Comput. Sci. Eng.* **2011**, *13*, 22, DOI: 10.1109/MCSE.2011.37.
- [111] McKinney, W. Data Structures for Statistical Computing in Python. Proceedings of the 9th Python in Science Conference. 2010; pp 56 – 61, DOI: 10.25080/Majora-92bf1922-00a.
- [112] Virtanen, P. et al. SciPy 1.0: fundamental algorithms for scientific computing in Python. *Nat. Methods* **2020**, *17*, 261–272, DOI: 10.1038/s41592-019-0686-2.
- [113] Briscoe, J.; Dunn, S. Piezoelectric nanogenerators — a review of nanostructured piezoelectric energy harvesters. *Nano Energy* **2015**, *14*, 15–29, DOI: 10.1016/j.nanoen.2014.11.059.
- [114] Uchino, K. Piezoelectric actuators 2006: Expansion from IT/robotics to ecological/energy applications. *J. Electroceram.* **2007**, *20*, 301–311, DOI: 10.1007/s10832-007-9196-1.
- [115] Ramadan, K. S.; Sameoto, D.; Evoy, S. A review of piezoelectric polymers as functional materials for electromechanical transducers. *Smart Mater. Struct.* **2014**, *23*, 033001, DOI: 10.1088/0964-1726/23/3/033001.

- [116] Li, H.; Tian, C.; Deng, Z. D. Energy harvesting from low frequency applications using piezoelectric materials. *Appl. Phys. Rev.* **2014**, *1*, 041301, DOI: 10.1063/1.4900845.
- [117] Stetsovykh, O.; Mutombo, P.; Švec, M.; Šámal, M.; Nejedlý, J.; Čísařová, I.; Vázquez, H.; Moro-Lagares, M.; Berger, J.; Vacek, J.; Stará, I. G.; Starý, I.; Jelínek, P. Large Converse Piezoelectric Effect Measured on a Single Molecule on a Metallic Surface. *J. Am. Chem. Soc.* **2018**, *140*, 940–946, DOI: 10.1021/jacs.7b08729.
- [118] Hosseini, E. S.; Manjakkal, L.; Shakthivel, D.; Dahiya, R. Glycine–Chitosan-Based Flexible Biodegradable Piezoelectric Pressure Sensor. *ACS Appl. Mater. Interfaces* **2020**, *12*, 9008–9016, DOI: 10.1021/acsami.9b21052.
- [119] Safari, A.; Akdogan, E. K. Rapid Prototyping of Novel Piezoelectric Composites. *Ferroelectrics* **2006**, *331*, 153–179, DOI: 10.1080/00150190600737727.
- [120] Chen, X.; Ware, H. O. T.; Baker, E.; Chu, W.; Hu, J.; Sun, C. The Development of an All-polymer-based Piezoelectric Photocurable Resin for Additive Manufacturing. *Procedia CIRP* **2017**, *65*, 157 – 162, DOI: 10.1016/j.procir.2017.04.025, 3rd CIRP Conference on BioManufacturing.
- [121] Kumar, B. P.; Kumar, H.; Kharat, D. Effect of porosity on dielectric properties and microstructure of porous PZT ceramics. *Mater. Sci. Eng., B* **2006**, *127*, 130 – 133, DOI: 10.1016/j.mseb.2005.10.003.
- [122] Wan, W.; Luo, J.; e Huang, C.; Yang, J.; Feng, Y.; Yuan, W.-X.; Ouyang, Y.; Chen, D.; Qiu, T. Calcium copper titanate/polyurethane composite films with high dielectric constant, low dielectric loss and super flexibility. *Ceram. Int.* **2018**, *44*, 5086–5092, DOI: 10.1016/j.ceramint.2017.12.108.
- [123] Zak, A.; Gan, W.; Majid, W. A.; Darroudi, M.; Velayutham, T. Experimental and theoretical dielectric studies of PVDF/PZT nanocomposite thin films. *Ceram. Int.* **2011**, *37*, 1653–1660, DOI: 10.1016/j.ceramint.2011.01.037.
- [124] Bairagi, S.; Ghosh, S.; Ali, S. W. A fully sustainable, self-poled, bio-waste based piezoelectric nanogenerator: electricity generation from pomelo fruit membrane. *Sci. Rep.* **2020**, *10*, DOI: 10.1038/s41598-020-68751-3.
- [125] Maiti, S.; Kumar Karan, S.; Lee, J.; Kumar Mishra, A.; Bhusan Khatua, B.; Kon Kim, J. Bio-waste onion skin as an innovative nature-driven piezoelectric material with high energy conversion efficiency. *Nano Energy* **2017**, *42*, 282 – 293, DOI: 10.1016/j.nanoen.2017.10.041.
- [126] Ghosh, S. K.; Mandal, D. High-performance bio-piezoelectric nanogenerator made with fish scale. *Appl. Phys. Lett.* **2016**, *109*, 103701, DOI: 10.1063/1.4961623.
- [127] Ghosh, S. K.; Mandal, D. Bio-assembled, piezoelectric prawn shell made self-powered wearable sensor for non-invasive physiological signal monitoring. *Appl. Phys. Lett.* **2017**, *110*, 123701, DOI: 10.1063/1.4979081.

- [128] Quan, X.; Madura, J. D.; Hutchison, G. R. Self-Assembled Monolayer Piezoelectrics: Electric-Field Driven Conformational Changes. 2017; <https://arxiv.org/abs/1706.08993>.
- [129] Love, J. C.; Estroff, L. A.; Kriebel, J. K.; Nuzzo, R. G.; Whitesides, G. M. Self-Assembled Monolayers of Thiolates on Metals as a Form of Nanotechnology. *Chem. Rev.* **2005**, *105*, 1103–1170, DOI: 10.1021/cr0300789.
- [130] Quan, X.; Marvin, C. W.; Seebald, L.; Hutchison, G. R. Single-Molecule Piezoelectric Deformation: Rational Design from First-Principles Calculations. *J. Phys. Chem. C* **2013**, *117*, 16783–16790, DOI: 10.1021/jp404252v.
- [131] Marvin, C. W.; Grimm, H. M.; Miller, N. C.; Horne, W. S.; Hutchison, G. R. Interplay among Sequence, Folding Propensity, and Bio-Piezoelectric Response in Short Peptides and Peptoids. *J. Phys. Chem. B* **2017**, *121*, 10269–10275, DOI: 10.1021/acs.jpcb.7b10085.
- [132] Yang, M.-M.; Luo, Z.-D.; Mi, Z.; Zhao, J.; E, S. P.; Alexe, M. Piezoelectric and pyroelectric effects induced by interface polar symmetry. *Nature* **2020**, *584*, 377–381, DOI: 10.1038/s41586-020-2602-4.
- [133] Gayatri, N. N. D.; Hutchison, G. Origins of Negative and Positive Electromechanical Response of Oligopeptide Piezoelectrics. 2019; <https://doi.org/10.26434/chemrxiv.9985205.v1>.
- [134] Chen, H. D.; Udayakumar, K. R.; Cross, L. E.; Bernstein, J. J.; Niles, L. C. Dielectric, ferroelectric, and piezoelectric properties of lead zirconate titanate thick films on silicon substrates. *J. Appl. Phys. (Melville, NY, U. S.)* **1995**, *77*, 3349–3353, DOI: 10.1063/1.358621.
- [135] Goh, W.; Yao, K.; Ong, C. Effects of microstructure on the properties of ferroelectric lead zirconate titanate (PZT) thin films. *Appl. Phys. A: Mater. Sci. Process.* **2005**, *81*, 1089–1093, DOI: 10.1007/s00339-004-2964-8.
- [136] Hutter, J.; Iannuzzi, M.; Schiffmann, F.; VandeVondele, J. CP2K: atomistic simulations of condensed matter systems. *Wiley Interdiscip. Rev.: Comput. Mol. Sci.* **2014**, *4*, 15–25, DOI: 10.1002/wcms.1159.
- [137] VandeVondele, J.; Krack, M.; Mohamed, F.; Parrinello, M.; Chassaing, T.; Hutter, J. QUICKSTEP: Fast and accurate density functional calculations using a mixed Gaussian and plane waves approach. *Comput. Phys. Commun.* **2005**, *167*, 103 – 128, DOI: 10.1016/j.cpc.2004.12.014.
- [138] King-Smith, R. D.; Vanderbilt, D. Theory of polarization of crystalline solids. *Phys. Rev. B* **1993**, *47*, 1651–1654, DOI: 10.1103/PhysRevB.47.1651.
- [139] Resta, R. Macroscopic polarization in crystalline dielectrics: the geometric phase approach. *Rev. Mod. Phys.* **1994**, *66*, 899–915, DOI: 10.1103/RevModPhys.66.899.

- [140] Berry, M. V. Quantal phase factors accompanying adiabatic changes. *Proc. R. Soc. London, Ser. A* **1984**, *392*, 45–57, DOI: 10.1098/rspa.1984.0023.
- [141] Umari, P.; Pasquarello, A. *Ab initio* Molecular Dynamics in a Finite Homogeneous Electric Field. *Phys. Rev. Lett.* **2002**, *89*, 157602, DOI: 10.1103/PhysRevLett.89.157602.
- [142] Krack, M. Pseudopotentials for H to Kr optimized for gradient-corrected exchange-correlation functionals. *Theor. Chem. Acc.* **2005**, *114*, 145–152, DOI: 10.1007/s00214-005-0655-y.
- [143] Becke, A. D. Density-functional exchange-energy approximation with correct asymptotic behavior. *Phys. Rev. A* **1988**, *38*, 3098–3100, DOI: 10.1103/PhysRevA.38.3098.
- [144] Grimme, S.; Antony, J.; Ehrlich, S.; Krieg, H. A consistent and accurate *ab initio* parametrization of density functional dispersion correction (DFT-D) for the 94 elements H-Pu. *J. Chem. Phys.* **2010**, *132*, 154104, DOI: 10.1063/1.3382344.
- [145] Grimme, S.; Ehrlich, S.; Goerigk, L. Effect of the damping function in dispersion corrected density functional theory. *J. Comput. Chem.* **2011**, *32*, 1456–1465, DOI: 10.1002/jcc.21759.
- [146] Lin, I.-C.; Seitsonen, A. P.; Tavernelli, I.; Rothlisberger, U. Structure and Dynamics of Liquid Water from *ab Initio* Molecular Dynamics—Comparison of BLYP, PBE, and revPBE Density Functionals with and without van der Waals Corrections. *J. Chem. Theory Comput.* **2012**, *8*, 3902–3910, DOI: 10.1021/ct3001848.
- [147] Bankura, A.; Karmakar, A.; Carnevale, V.; Chandra, A.; Klein, M. L. Structure, Dynamics, and Spectral Diffusion of Water from First-Principles Molecular Dynamics. *J. Phys. Chem. C* **2014**, *118*, 29401–29411, DOI: 10.1021/jp506120t.
- [148] Gillan, M. J.; Alfè, D.; Michaelides, A. Perspective: How good is DFT for water? *J. Chem. Phys.* **2016**, *144*, 130901, DOI: 10.1063/1.4944633.
- [149] Bussi, G.; Donadio, D.; Parrinello, M. Canonical sampling through velocity rescaling. *J. Chem. Phys.* **2007**, *126*, 014101, DOI: 10.1063/1.2408420.
- [150] Hanwell, M. D.; Curtis, D. E.; Lonie, D. C.; Vandermeersch, T.; Zurek, E.; Hutchison, G. R. Avogadro: an advanced semantic chemical editor, visualization, and analysis platform. *J. Cheminf.* **2012**, *4*, DOI: 10.1186/1758-2946-4-17.
- [151] Kühne, T. D. et al. CP2K: An electronic structure and molecular dynamics software package - Quickstep: Efficient and accurate electronic structure calculations. *J. Chem. Phys.* **2020**, *152*, 194103, DOI: 10.1063/5.0007045.
- [152] Seabold, S.; Perktold, J. Statsmodels: Econometric and Statistical Modeling with Python. Proceedings of the 9th Python in Science Conference. 2010; pp 92 – 96, DOI: 10.25080/Majora-92bf1922-011.

- [153] Fukada, E.; Yasuda, I. On the Piezoelectric Effect of Bone. *J. Phys. Soc. Jpn.* **1957**, *12*, 1158–1162, DOI: 10.1143/JPSJ.12.1158.
- [154] Fukada, E.; Ueda, H. Piezoelectric Effect in Muscle. *Jap. J. Appl. Phys.* **1970**, *9*, 844–845, DOI: 10.1143/jjap.9.844.
- [155] Fukada, E.; Hara, K. Piezoelectric Effect in Blood Vessel Walls. *J. Phys. Soc. Jap.* **1969**, *26*, 777–780, DOI: 10.1143/JPSJ.26.777.
- [156] Ghosh, S. K.; Mandal, D. Efficient natural piezoelectric nanogenerator: Electricity generation from fish swim bladder. *Nano Energy* **2016**, *28*, 356–365, DOI: 10.1016/j.nanoen.2016.08.030.
- [157] Hinchet, R.; Khan, U.; Falconi, C.; Kim, S.-W. Piezoelectric properties in two-dimensional materials: Simulations and experiments. *Mater. Today* **2018**, *21*, 611–630, DOI: 10.1016/j.mattod.2018.01.031.
- [158] Heredia, A.; Meunier, V.; Bdikin, I. K.; Gracio, J.; Balke, N.; Jesse, S.; Tselev, A.; Agarwal, P. K.; Sumpter, B. G.; Kalinin, S. V.; Kholkin, A. L. Nanoscale Ferroelectricity in Crystalline  $\gamma$ -Glycine. *Adv. Funct. Mater.* **2012**, *22*, 2996–3003, DOI: 10.1002/adfm.201103011.
- [159] O'Donnell, J.; Sarkar, S. M.; Guerin, S.; Borda, G. G.; Silien, C.; Soulimane, T.; Thompson, D.; O'Reilly, E.; Tofail, S. A. M. Piezoelectricity in the proteinogenic amino acid L-leucine: A novel piezoactive bioelectret. *IEEE Trans. Dielectr. Electr. Insul.* **2020**, *27*, 1465–1468, DOI: 10.1109/TDEI.2020.008908.
- [160] Wojtaś, M.; Kinzhybalo, V.; Bdikin, I.; Kholkin, A. L. Crystal Structure and Strong Piezoelectricity of New Amino Acid Based Hybrid Crystals: [H- $\beta$ -(3-Pyridyl)-Ala-OH][ClO<sub>4</sub>] and [H- $\beta$ -(4-Pyridyl)-Ala-OH][ClO<sub>4</sub>]. *Cryst. Growth Des.* **2019**, *19*, 2583–2593, DOI: 10.1021/acs.cgd.8b01611.
- [161] Wojtaś, M.; Gagor, A.; Kholkin, A. L. Strong piezoelectricity in [H- $\beta$ -(2-pyridyl)-Ala-OH][BF<sub>4</sub>] and [H- $\beta$ -(2-pyridyl)-Ala-OH][ClO<sub>4</sub>] — new amino acid based hybrid crystals. *J. Mater. Chem. C* **2016**, *4*, 7622–7631, DOI: 10.1039/C6TC02206E.
- [162] Nguyen, V.; Zhu, R.; Jenkins, K.; Yang, R. Self-assembly of diphenylalanine peptide with controlled polarization for power generation. *Nat. Commun.* **2016**, *7*, 13566, DOI: 10.1038/ncomms13566.
- [163] Kholkin, A.; Amdursky, N.; Bdikin, I.; Gazit, E.; Rosenman, G. Strong Piezoelectricity in Bioinspired Peptide Nanotubes. *ACS Nano* **2010**, *4*, 610–614, DOI: 10.1021/nn901327v.
- [164] Safaryan, S.; Slabov, V.; Kopyl, S.; Romanyuk, K.; Bdikin, I.; Vasilev, S.; Zelenovskiy, P.; Shur, V. Y.; Uslamin, E. A.; Pidko, E. A.; Vinogradov, A. V.; Kholkin, A. L. Diphenylalanine-Based Microribbons for Piezoelectric Applications via Inkjet Printing. *ACS Appl. Mater. Interfaces* **2018**, *10*, 10543–10551, DOI: 10.1021/acsami.7b19668.



- [165] Cheong, L.-Z.; Zhao, W.; Song, S.; Shen, C. Lab on a tip: Applications of functional atomic force microscopy for the study of electrical properties in biology. *Acta Biomater.* **2019**, *99*, 33–52, DOI: 10.1016/j.actbio.2019.08.023.
- [166] Guerin, S.; Syed, T. A. M.; Thompson, D. Deconstructing collagen piezoelectricity using alanine-hydroxyproline-glycine building blocks. *Nanoscale* **2018**, *10*, 9653–9663, DOI: 10.1039/C8NR01634H.
- [167] Ryan, K.; Beirne, J.; Redmond, G.; Kilpatrick, J. I.; Guyonnet, J.; Buchete, N.-V.; Kholkin, A. L.; Rodriguez, B. J. Nanoscale Piezoelectric Properties of Self-Assembled Fmoc-FF Peptide Fibrous Networks. *ACS Appl. Mater. Interfaces* **2015**, *7*, 12702–12707, DOI: 10.1021/acsami.5b01251.
- [168] Tabata, Y.; Takagaki, K.; Uji, H.; Kimura, S. Piezoelectric property of bundled peptide nanotubes stapled by bis-cyclic- $\beta$ -peptide. *J. Pept. Sci.* **2019**, *25*, e3134, DOI: 10.1002/psc.3134.
- [169] Tabata, Y.; Uji, H.; Imai, T.; Kimura, S. Two one-dimensional arrays of naphthyl and anthryl groups along peptide nanotubes prepared from cyclic peptides comprising  $\alpha$ - and  $\beta$ -amino acids. *Soft Matter* **2018**, *14*, 7597–7604, DOI: 10.1039/C8SM01627E.
- [170] Jaworek, T.; Neher, D.; Wegner, G.; Wieringa, R. H.; Schouten, A. J. Electromechanical Properties of an Ultrathin Layer of Directionally Aligned Helical Polypeptides. *Science* **1998**, *279*, 57–60, DOI: 10.1126/science.279.5347.57.
- [171] Montesano, L. Room Temperature-Curing Polyurethane Casting Compounds. *Ind. Eng. Chem. Prod. Res. Dev.* **1964**, *3*, 133–137, DOI: 10.1021/i360010a015.
- [172] Hirota, S.; Saito, S.; Nakajima, T. Dielectric loss in nylon 6, nylon 12 and 4,6-polyurethane in very low frequency range. *Kolloid-Z. Z. Polym.* **1966**, *213*, 109–115, DOI: 10.1007/BF01552519.
- [173] Kalinin, S. V.; Rodriguez, B. J.; Jesse, S.; Karapetian, E.; Mirman, B.; Eliseev, E. A.; Morozovska, A. N. Nanoscale Electromechanics of Ferroelectric and Biological Systems: A New Dimension in Scanning Probe Microscopy. *Annu. Rev. Mater. Res.* **2007**, *37*, 189–238, DOI: 10.1146/annurev.matsci.37.052506.084323.
- [174] Rabe, U. In *Applied Scanning Probe Methods II: Scanning Probe Microscopy Techniques*; Bhushan, B., Fuchs, H., Eds.; Springer Berlin Heidelberg: Berlin, 2006; pp 37–90, DOI: 10.1007/3-540-27453-7\_2.
- [175] Balke, N.; Maksymovych, P.; Jesse, S.; Kravchenko, I. I.; Li, Q.; Kalinin, S. V. Exploring Local Electrostatic Effects with Scanning Probe Microscopy: Implications for Piezoresponse Force Microscopy and Triboelectricity. *ACS Nano* **2014**, *8*, 10229–10236, DOI: 10.1021/nn505176a.
- [176] Christman, J. A.; Woolcott, R. R.; Kingon, A. I.; Nemanich, R. J. Piezoelectric measurements with atomic force microscopy. *Appl. Phys. Lett.* **1998**, *73*, 3851–3853, DOI: 10.1063/1.122914.

- [177] Kalinin, S. V.; Bonnell, D. A. Imaging mechanism of piezoresponse force microscopy of ferroelectric surfaces. *Phys. Rev. B* **2002**, *65*, 125408, DOI: 10.1103/PhysRevB.65.125408.
- [178] Kalinin, S. V.; Karapetian, E.; Kachanov, M. Nanoelectromechanics of piezoresponse force microscopy. *Phys. Rev. B* **2004**, *70*, 184101, DOI: 10.1103/PhysRevB.70.184101.
- [179] Gruverman, A.; Kalinin, S. V. Piezoresponse force microscopy and recent advances in nanoscale studies of ferroelectrics. *J. Mater. Sci.* **2006**, *41*, 107–116, DOI: 10.1007/s10853-005-5946-0.
- [180] Jesse, S.; Baddorf, A. P.; Kalinin, S. V. Dynamic behaviour in piezoresponse force microscopy. *Nanotechnol.* **2006**, *17*, 1615–1628, DOI: 10.1088/0957-4484/17/6/014.
- [181] Jesse, S.; Mirman, B.; Kalinin, S. V. Resonance enhancement in piezoresponse force microscopy: Mapping electromechanical activity, contact stiffness, and Q factor. *Appl. Phys. Lett.* **2006**, *89*, 022906, DOI: 10.1063/1.2221496.
- [182] Jesse, S.; Kalinin, S. V. Band excitation in scanning probe microscopy: sines of change. *J. Phys. D: Appl. Phys.* **2011**, *44*, 464006, DOI: 10.1088/0022-3727/44/46/464006.
- [183] Balke, N.; Maksymovych, P.; Jesse, S.; Herklotz, A.; Tselev, A.; Eom, C.-B.; Kravchenko, I. I.; Yu, P.; Kalinin, S. V. Differentiating Ferroelectric and Nonferroelectric Electromechanical Effects with Scanning Probe Microscopy. *ACS Nano* **2015**, *9*, 6484–6492, DOI: 10.1021/acs.nano.5b02227.
- [184] Calahorra, Y.; Smith, M.; Datta, A.; Benisty, H.; Kar-Narayan, S. Mapping piezoelectric response in nanomaterials using a dedicated non-destructive scanning probe technique. *Nanoscale* **2017**, *9*, 19290–19297, DOI: 10.1039/C7NR06714C.
- [185] Gomez, A.; Puig, T.; Obradors, X. Diminish electrostatic in piezoresponse force microscopy through longer or ultra-stiff tips. *Appl. Surf. Sci.* **2018**, *439*, 577–582, DOI: 10.1016/j.apsusc.2018.01.080.
- [186] Kim, S.; Seol, D.; Lu, X.; Alexe, M.; Kim, Y. Electrostatic-free piezoresponse force microscopy. *Sci. Rep.* **2017**, *7*, 41657, DOI: 10.1038/srep41657.
- [187] Burfoot, J. C. *Ferroelectrics: An Introduction to the Physical Principles*; D. Van Nostrand Company: Princeton, NJ, 1967; Chapter 1, pp 1–12.
- [188] Fatuzzo, E.; Merz, W. J. *Ferroelectricity*; John Wiley & Sons: New York, 1967; Chapter 2, pp 5–104.
- [189] Vasudevan, R. K.; Balke, N.; Maksymovych, P.; Jesse, S.; Kalinin, S. V. Ferroelectric or non-ferroelectric: Why so many materials exhibit “ferroelectricity” on the nanoscale. *Appl. Phys. Rev.* **2017**, *4*, 021302, DOI: 10.1063/1.4979015.
- [190] Whatmore, R. W.; Osbond, P. C.; Shorrocks, N. M. Ferroelectric materials for thermal IR detectors. *Ferroelectrics* **1987**, *76*, 351–367, DOI: 10.1080/00150198708016956.

- [191] Blázquez-Castro, A.; García-Cabañes, A.; Carrascosa, M. Biological applications of ferroelectric materials. *Appl. Phys. Rev.* **2018**, *5*, 041101, DOI: 10.1063/1.5044472.
- [192] Yuan, Y.; Xiao, Z.; Yang, B.; Huang, J. Arising applications of ferroelectric materials in photovoltaic devices. *J. Mater. Chem. A* **2014**, *2*, 6027–6041, DOI: 10.1039/C3TA14188H.
- [193] Ma, W.; Zhu, Y.; Marwat, M. A.; Fan, P.; Xie, B.; Salamon, D.; Ye, Z.-G.; Zhang, H. Enhanced energy-storage performance with excellent stability under low electric fields in BNT–ST relaxor ferroelectric ceramics. *J. Mater. Chem. C* **2019**, *7*, 281–288, DOI: 10.1039/C8TC04447C.
- [194] Mikolajick, T.; Schroeder, U.; Slesazek, S. The Past, the Present, and the Future of Ferroelectric Memories. *IEEE Transactions on Electron Devices* **2020**, *67*, 1434–1443, DOI: 10.1109/TED.2020.2976148.
- [195] Miller, N. C. Exploration of Nanoscale Electromechanical Couplings. Ph.D. dissertation, University of Pittsburgh, Pittsburgh, Pennsylvania, 2020.
- [196] Furukawa, S.; Wu, J.; Koyama, M.; Hayashi, K.; Hoshino, N.; Takeda, T.; Suzuki, Y.; Kawamata, J.; Saito, M.; Akutagawa, T. Ferroelectric columnar assemblies from the bowl-to-bowl inversion of aromatic cores. *Nat. Commun.* **2021**, *12*, 768, DOI: 10.1038/s41467-021-21019-4.
- [197] Seiders, T. J.; Baldrige, K. K.; Grube, G. H.; Siegel, J. S. Structure/Energy Correlation of Bowl Depth and Inversion Barrier in Corannulene Derivatives: Combined Experimental and Quantum Mechanical Analysis. *J. Am. Chem. Soc.* **2001**, *123*, 517–525, DOI: 10.1021/ja0019981.
- [198] Fukunaga, M.; Noda, Y. New Technique for Measuring Ferroelectric and Antiferroelectric Hysteresis Loops. *J. Phys. Soc. Jpn.* **2008**, *77*, 064706, DOI: 10.1143/JPSJ.77.064706.
- [199] Stewart, M.; Cain, M. G.; Weaver, P. In *Characterisation of Ferroelectric Bulk Materials and Thin Films*; Cain, M. G., Ed.; Springer Netherlands: Dordrecht, 2014; pp 1–14, DOI: 10.1007/978-1-4020-9311-1\_1.
- [200] Sawyer, C. B.; Tower, C. H. Rochelle Salt as a Dielectric. *Phys. Rev.* **1930**, *35*, 269–273, DOI: 10.1103/PhysRev.35.269.
- [201] Gorbunov, A. V.; Garcia Iglesias, M.; Guilleme, J.; Cornelissen, T. D.; Roelofs, W. S. C.; Torres, T.; González-Rodríguez, D.; Meijer, E. W.; Kemerink, M. Ferroelectric self-assembled molecular materials showing both rectifying and switchable conductivity. *Sci. Adv.* **2017**, *3*, DOI: 10.1126/sciadv.1701017.
- [202] Khikhlovskiy, V.; Gorbunov, A. V.; van Breemen, A. J.; Janssen, R. A.; Gelinck, G. H.; Kemerink, M. Multi-bit organic ferroelectric memory. *Org. Electron.* **2013**, *14*, 3399–3405, DOI: 10.1016/j.orgel.2013.09.006.

- [203] Chiechi, R.; Weiss, E.; Dickey, M.; Whitesides, G. Eutectic Gallium–Indium (EGaIn): A Moldable Liquid Metal for Electrical Characterization of Self-Assembled Monolayers. *Angew. Chem., Int. Ed.* **2008**, *47*, 142–144, DOI: 10.1002/anie.200703642.
- [204] Fellows, W. B.; Rice, A. M.; Williams, D. E.; Dolgoplova, E. A.; Vannucci, A. K.; Pellechia, P. J.; Smith, M. D.; Krause, J. A.; Shustova, N. B. Redox-Active Corannulene Buckybowls in a Crystalline Hybrid Scaffold. *Angew. Chem., Int. Ed.* **2016**, *55*, 2195–2199, DOI: 10.1002/anie.201509557.
- [205] Bachman, J. C.; Kavian, R.; Graham, D. J.; Kim, D. Y.; Noda, S.; Nocera, D. G.; Shao-Horn, Y.; Lee, S. W. Electrochemical polymerization of pyrene derivatives on functionalized carbon nanotubes for pseudocapacitive electrodes. *Nat. Commun.* **2015**, *6*, DOI: 10.1038/ncomms8040.